

# GEMS & GEMOLOGY

SUMMER 2022  
VOLUME LVIII

THE QUARTERLY JOURNAL OF THE GEMOLOGICAL INSTITUTE OF AMERICA



Diamonds from Guyana

Surface Features of Ekanite from Sri Lanka

A Study of Gems from Napoleon III's Crown

A New Source of Amber in Vietnam



p. 146



p. 170



p. 184



p. 219



p. 226



p. 266

## EDITORIAL

### 137 Diamonds from Guyana, Ekanite from Sri Lanka, a New Amber Source in Vietnam, and More...

*Duncan Pay*

## FEATURE ARTICLES

### 138 A Look at Diamonds and Diamond Mining in Guyana

*Roy Bassoo and Kenneth Befus*

Reports on diamonds from Guyana's alluvial deposits, including mining history and practices.

### 156 The Shape of Ekanite

*Lutz Nasdala, K.A. Geeth Sameera, G.W.A. Rohan Fernando, Manfred Wildner, Chutimun Chanmuang N., Gerlinde Habler, Annalena Erlacher, and Radek Škoda*

Discusses the unusual surface characteristics of ekanite from secondary deposits in Sri Lanka.

### 168 A Gemological and Spectroscopic Study with Mobile Instruments of "Emeralds" from the Coronation Crown of Napoleon III

*Stefanos Karamelas, Eloïse Gaillou, Annabelle Herreweghe, Farida Maouche, Ugo Hennebois, Sophie Leblan, Bérengère Meslin Sainte Beuve, Michel Lechartier, Didier Nectoux, and Aurélien Delaunay*

An examination of 45 gems from the coronation crown of Napoleon III, using nondestructive mobile spectroscopic and gemological testing methods.

### 184 Characteristics of Newly Discovered Amber from Phu Quoc, Vietnam

*Le Ngoc Nang, Pham Trung Hieu, Lam Vinh Phat, Pham Minh Tien, Ho Nguyen Tri Man, and Ha Thuy Hang*

Offers the first detailed summary of amber from the Vietnamese island of Phu Quoc and a comparison with Baltic, Dominican, and Burmese material.

### 196 Natural Radioactivity in Select Serpentinite-Related Nephrite Samples: A Comparison with Dolomite-Related Nephrite

*Dariusz Malczewski, Michał Sachanbiński, and Maria Dziurawicz*

Uses gamma-ray spectrometry to directly measure internal radioactivity in green nephrite from deposits in Poland, Russia, Canada, and New Zealand.

## REGULAR FEATURES

### 214 Lab Notes

Orange benitoite • Set of blue "rough" stones • Type IIb De Beers Cullinan Blue diamond • Green diamond with unusual radiation stains • 10 ct HPHT-treated CVD-grown diamond • Reported *Cassis* pearl from Florida • RFID device in South Sea bead cultured pearl necklaces • A star and cat's-eye color-change sapphire • Bicolor cuprian tourmaline

### 226 G&G Micro-World

Apatite cluster in emerald • Blue apatite in garnet • Large diamond in diamond • Network of etch channels in diamond • Eye pattern in rock • Filler patterns in fracture-filled emerald • Flux synthetic beryl overgrowth • "Boomerang" in topaz • Quarterly Crystal: Cinnabar in fluorite

### 234 Colored Stones Unearthed

A look at inclusions in gemstones and what they mean for gemologists and geoscientists.

### 244 Gem News International

Aquamarine with unusual etch features • Topaz in red beryl • Cat's-eye omphacite *fei cui* jade • Three-rayed asterism in quartz • Zircon with strong photochromic effect • Myne London • Glass-and-quartz triplet imitating emerald • Heated ruby: A costly mistake • Yellow sapphires with unstable color • Spring 2022 auction highlights • The Big Find: Fifty years of Maine tourmaline • *Brilliance* at the Natural History Museum of Los Angeles County • American diamonds at the Smithsonian • The GIA Alumni Collective

## Editorial Staff

### Editor-in-Chief

Duncan Pay

### Managing Editor

Stuart D. Overlin  
soverlin@gia.edu

### Editor

Brooke Goedert

### Editorial Coordinator

Erica Zaidman

### Editors, Lab Notes

Thomas M. Moses  
Shane F. McClure

### Editors, Micro-World

Nathan Renfro  
Elise A. Skalwold  
John I. Koivula

### Editors, Gem News

Gagan Choudhary  
Christopher M. Breeding  
Guanghai Shi

### Editors, Colored Stones Unearthed

Aaron C. Palke  
James E. Shigley

### Editor, Diamond Reflections

Evan M. Smith

### Contributing Editors

James E. Shigley  
Raquel Alonso-Perez

### Editor-in-Chief Emeritus

Alice S. Keller

### Technical Editors

Tao Z. Hsu  
Jennifer Stone-Sundberg

### Assistant Editor

Erin Hogarth

## Production Staff

### Creative Director

Faizah Bhatti

### Production and Multimedia Specialist

Michael Creighton

### Photo/Video Producer

Kevin Schumacher

### Photographer

Robert Weldon

### Multimedia Associate

Christopher Bonine

### Video Production

Albert Salvato

## Editorial Review Board

### Ahmadjan Abduriyim

Tokyo, Japan

### Timothy Adams

San Diego, California

### Edward W. Boehm

Chattanooga, Tennessee

### James E. Butler

Washington, DC

### Alan T. Collins

London, UK

### Sally Eaton-Magaña

Carlsbad, California

### John L. Emmett

Brush Prairie, Washington

### Emmanuel Fritsch

Nantes, France

### Eloïse Gaillou

Paris, France

### Al Gilbertson

Carlsbad, California

### Gaston Giuliani

Nancy, France

### Lee A. Groat

Vancouver, Canada

### Yunbin Guan

Pasadena, California

### Peter Heaney

University Park, Pennsylvania

### Richard W. Hughes

Bangkok, Thailand

### Jaroslav Hyršl

Prague, Czech Republic

### Dorrit Jacob

Canberra, Australia

### A.J.A. (Bram) Janse

Perth, Australia

### Mary L. Johnson

San Diego, California

### Stefanos Karamelas

Paris, France

### Lore Kiefert

Lucerne, Switzerland

### Simon Lawson

Maidenhead, UK

### Ren Lu

Wuhan, China

### Thomas M. Moses

New York, New York

### Laura Otter

Canberra, Australia

### Aaron C. Palke

Carlsbad, California

### Ilene Reinitz

Chicago, Illinois

### Nathan Renfro

Carlsbad, California

### Benjamin Rondeau

Nantes, France

### George R. Rossman

Pasadena, California

### Sudarat Saeseaw

Bangkok, Thailand

### Karl Schmetzer

Petershausen, Germany

### Andy Shen

Wuhan, China

### Guanghai Shi

Beijing, China

### James E. Shigley

Carlsbad, California

### Elisabeth Strack

Hamburg, Germany

### Nicholas Sturman

Bangkok, Thailand

### D. Brian Thompson

Florence, Alabama

### Fanus Viljoen

Johannesburg, South Africa

### Wuyi Wang

New York, New York

### Christopher M. Welbourn

Reading, UK

### Chunhui Zhou

New York, New York

### J.C. (Hanco) Zwaan

Leiden, The Netherlands

# GEMS & GEMOLOGY®

gia.edu/gems-gemology

### Customer Service

(760) 603-4200  
gandg@gia.edu



### Subscriptions

Copies of the current issue may be purchased for \$29.95 plus shipping. Subscriptions are \$79.99 for one year (4 issues) in the U.S. and \$99.99 elsewhere. Canadian subscribers should add GST. Discounts are available for renewals, group subscriptions, GIA alumni, and current GIA students. To purchase print subscriptions, visit [store.gia.edu](http://store.gia.edu) or contact Customer Service. For institutional rates, contact Customer Service.

### Database Coverage

*Gems & Gemology's* impact factor is 2.045, according to the 2021 Journal Citation Reports by Clarivate Analytics (issued June 2022). *G&G* is abstracted in Thomson Reuters products (Current Contents: Physical, Chemical & Earth Sciences and Science Citation Index—Expanded, including the Web of Knowledge) and other databases. For a complete list of sources abstracting *G&G*, go to [gia.edu/gems-gemology](http://gia.edu/gems-gemology), and click on "Publication Information."

### Manuscript Submissions

*Gems & Gemology*, a peer-reviewed journal, welcomes the submission of articles on all aspects of the field. Please see the Author Guidelines at [gia.edu/gems-gemology](http://gia.edu/gems-gemology) or contact the Managing Editor. Letters on articles published in *G&G* are also welcome. Please note that Field Reports, Lab Notes, Gem News International, Micro-World, Colored Stones Unearthed, Diamond Reflections, and Charts are not peer-reviewed sections but do undergo technical and editorial review.

### Copyright and Reprint Permission

Abstracting is permitted with credit to the source. Libraries are permitted to photocopy beyond the limits of U.S. copyright law for private use of patrons. Instructors are permitted to reproduce isolated articles and photographs/images owned by *G&G* for noncommercial classroom use without fee. Use of photographs/images under copyright by external parties is prohibited without the express permission of the photographer or owner of the image, as listed in the credits. For other copying, reprint, or republication permission, please contact the Managing Editor.

*Gems & Gemology* is published quarterly by the Gemological Institute of America, a nonprofit educational organization for the gem and jewelry industry.

Postmaster: Return undeliverable copies of *Gems & Gemology* to GIA, The Robert Mouawad Campus, 5345 Armada Drive, Carlsbad, CA 92008.

Our Canadian goods and service registration number is 126142892RT.

Any opinions expressed in signed articles are understood to be opinions of the authors and not of the publisher.

## About the Cover

*This 95.5 × 64.0 mm figure of a grizzly bear with a freshly caught salmon is carved from Canadian nephrite jade from the Polar Jade mine in northwest British Columbia. The measurement of natural radioactivity concentrations in nephrite from Canada and other major sources is the subject of a feature article from this issue. Photo by Robert Weldon/GIA; courtesy of Jade West Group (Blaine, Washington).*

Printing is by L+L Printers, Carlsbad, CA.

GIA World Headquarters The Robert Mouawad Campus 5345 Armada Drive Carlsbad, CA 92008 USA  
© 2022 Gemological Institute of America All rights reserved. ISSN 0016-626X



# Diamonds from Guyana, Ekanite from Sri Lanka, a New Amber Source in Vietnam, and More...



Welcome to the Summer issue of *Gems & Gemology*! This installment is packed with interesting new content, including five feature articles ranging from reports on new and lesser-known gem sources to a study of the emeralds once embedded in the crown of Napoleon III.

In our lead article, Roy Bassoo and Kenneth Befus explore diamonds and diamond mining in Guyana. Drawing on their own observations of diamonds from various alluvial deposits, coupled with government reports, datasets, and historical accounts, the authors provide an overview of diamond production and mining practices in Guyana, along with findings on color, morphology, nitrogen content, and luminescence.

*“...an overview of diamond production and mining practices in Guyana, along with findings on color...”*

Our second article investigates the uneven shapes and surface features of ekanite from Sri Lanka. Lutz Nasdala and his team analyze ekanite fragments and ekanite-containing specimens of rock discovered near Ampegama, comparing the samples to those from other Sri Lankan sources to identify the processes that led to the distinctive shape and surface features.

As part of an ongoing effort to research gemstones of historical significance, Stefanos Karampelas and coauthors present their analysis of 45 “emeralds” formerly set in the coronation crown of Napoleon III. Using nondestructive mobile spectroscopic and gemological means at Mines Paris - PSL, they verified that 41 of these 45 gems were emeralds, likely of Colombian provenance, while the remaining four were glass containing iron and/or copper.

Next, a team led by Le Ngoc Nang examines the gemological properties and commercial potential of a newly discovered amber source on Phu Quoc island in Vietnam. They conclude that based on the high quality of the amber and the wide distribution of the host rock on the island, Vietnam’s only known amber locality may have a promising future in the market.

In our final article, Dariusz Malczewski and colleagues present their study on natural radioactivity in nephrite. After examining 11 serpentinite-related nephrite samples from Poland, Russia, Canada, and New Zealand, the authors determined that there is no radiological risk to handling nephrite and that the levels of the radioactive isotopes studied are very low.

Our regular columns deliver interesting finds from around the world. Highlights from the *Lab Notes* section include a very rare large bright orange benitoite, the famed De Beers Cullinan Blue diamond, and pearls embedded with RFID devices. In *Micro-World*, the inner beauty of gems comes alive with an impressive blue apatite inclusion in garnet, eye-visible etch channels in a natural diamond, and a rock fragment exhibiting a very realistic eye pattern. *Gem News International* keeps you up to date with the latest developments, including unusual chatoyancy in omphacite *fei cui* jade, a company with a mission to support women in the gem trade, testing of color instability in yellow sapphire, and a museum exhibit celebrating a major tourmaline discovery in Maine. *Colored Stones Unearthed* returns to cover inclusions in gems, explaining how they form, how they are studied, and what they mean for gemologists and geoscientists.

Finally, we invite you to join our Facebook group at [www.facebook.com/groups/giagemsgemology](https://www.facebook.com/groups/giagemsgemology). Since its launch in February 2020, our growing community has surpassed 25,000 members. Thank you for your continued support and interest in *G&G*!

Duncan Pay | Editor-in-Chief | [dpay@gia.edu](mailto:dpay@gia.edu)

# A LOOK AT DIAMONDS AND DIAMOND MINING IN GUYANA

Roy Bassoo and Kenneth Befus

Diamonds have been mined in Guyana for more than 130 years and are traded in major diamond centers in Belgium, Israel, and the United Arab Emirates. Notwithstanding this long history, the primary source rocks of Guyana's diamonds remain a mystery. The diamonds are likely detrital material derived from sedimentary rocks of the Roraima Supergroup, but a primary igneous, kimberlitic source has not been eliminated. Diamond exploration and mining in Guyana remain a mostly artisanal endeavor. In a similar fashion, scientific studies have rarely addressed these diamonds' provenance and formation, and very few were aimed at a gemological audience. Here we present a detailed gemological description of Guyana's diamonds to serve as a comparison with other diamond populations in the Guiana Shield and globally. We use our direct observations of diamonds from various alluvial deposits in Guyana. We combine government reports and datasets as well as historical accounts to provide an overview of diamond production and mining practices in Guyana. Details concerning color, morphology, nitrogen content, and luminescence are also included.

Situated on the northern edge of South America, Guyana (figure 1) is the continent's only English-speaking nation. Originally, Guyana was populated by the first nations of Akawaio, Carib, Patamona, Lokono, Macushi, Pemon, Waiwai, Wapishana, and Warao. Dutch, French, and finally English colonialism brought advances in agriculture and technology. Sadly, these advances were also intertwined with the violent history of transatlantic slavery and indentured servitude. Laborers from Ghana, Togo, India, China, and Portugal were brought to Guyana, either by force or voluntarily. The colonial economy was based on the cultivation of sugarcane throughout the nineteenth and twentieth centuries. Guyana's legacy of colonialism has been one of violence, racism, and poverty, which peaked during the social upheavals of the 1960s (Spencer, 2007). It has been difficult for Guyana to fully divorce itself from its colonial past. However, Guyana today is a peaceful and diverse mix of cultures and ethnic groups from around the world. This little melting pot of different languages, clothing styles, cuisines, traditional dance, and music has

birthed a culture that is distinctly Guyanese (Rodney, 1981; Ishmael, 2013; <https://guyanatourism.com>).

Guyana's population is concentrated near the coastal deltas. Most of the population is engaged in agriculture, as the tropical climate, flat terrains, and fertile soils support sugarcane and rice cultivation. The scenery becomes increasingly pristine as one moves inland. Cultivated plains and infrastructure give way to tropical rainforests and rolling hills car-

## In Brief

- Guyana has contributed to the global supply of diamonds for more than 130 years.
- Guyanese diamonds are prized for their clarity and green colors.
- Morphology and luminescence suggest that recycled paleoplacer diamonds and more recent primary diamonds coexist in the same deposit.
- Guyana's alluvial deposits host not only diamonds and gold but also underexploited ruby, sapphire, and topaz.

peted by the Amazon jungle. The country's western boundary is dominated by the towering, flat-topped *tepuis* of the Roraima Mountains (figure 2). It is within the mountainous northwest where most of the diamond deposits are located. The lead author,

See end of article for About the Authors and Acknowledgments.

GEMS & GEMOLOGY, Vol. 58, No. 2, pp. 138–155,

<http://dx.doi.org/10.5741/GEMS.58.2.138>

© 2022 Gemological Institute of America

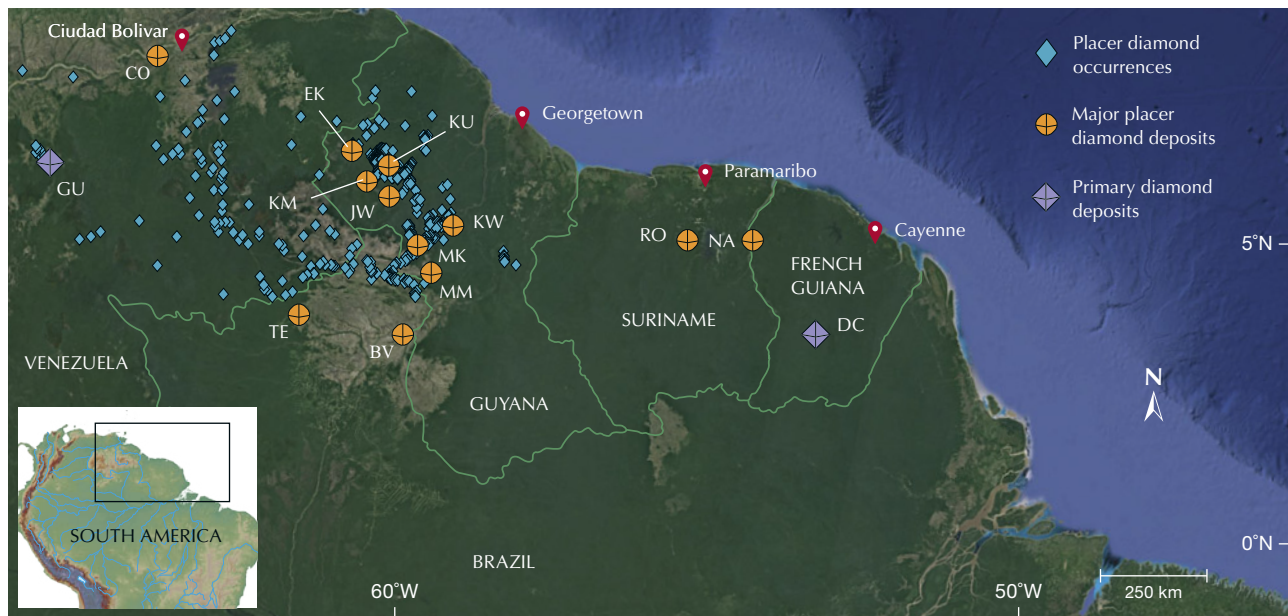


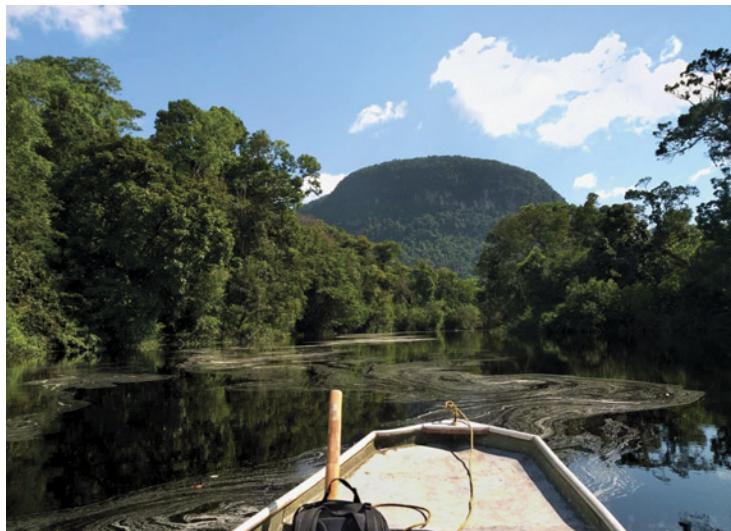
Figure 1. Google Earth satellite image of northern South America showing various diamond occurrences in Brazil (BV—Boa Vista, TE—Tepequém), Venezuela (CO—Los Coquitos, GU—Guaniamo), Guyana (EK—Ekereku, JW—Jawalla, KM—Kamarang, KU—Kurupung, KW—Konawaruk, MK—Maikwak, MM—Monkey Mountain), Suriname (NA—Nassau, RO—Rosebel), and French Guiana (DC—Dachine).

a Guyanese native, grew up hearing about jungle diamonds found deep in the mountainous interior, a topic that sparked his imagination and scientific curiosity.

Geologically, the diamond-bearing rocks that occur in the country's interior are part of the Guiana Shield, which is exposed over ~3,000,000 km<sup>2</sup> along

the northern margin of the Amazonian Craton (figure 3). The evolution of the Guiana Shield was dominated by episodes of accretionary mountain-building events during Archean to Proterozoic times, evidenced by outcrops of quartzite, schists, gneisses, greenstone belts, and amphibolites (Tassinari, 1997; Reis et al., 2000; Fraga et al., 2009; Kroonenberg et

Figure 2. Left: Roraima Mountain tepuis (elevation ~2000 m) near the source of the Kurupung River in Guyana. Right: Outcrop of Roraima Supergroup rocks. Photos by Kenneth Befus.



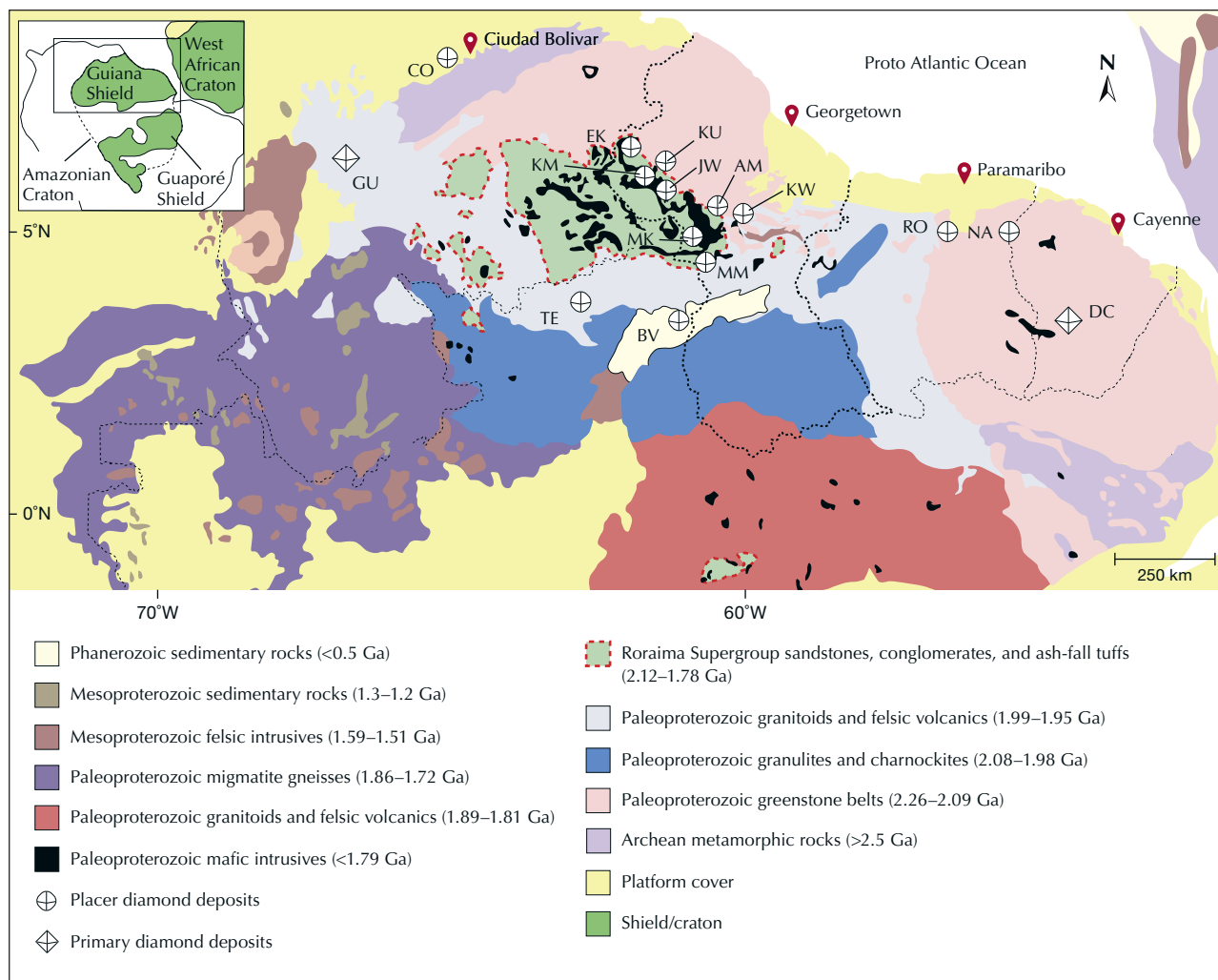


Figure 3. Modern simplified geologic map of the Guiana Shield. The Amazonian Craton consists of the Guiana and Guaporé Shield, separated by fluvial cover of the Amazon drainage basin (Gibbs and Barron, 1993; Kroonenberg et al., 2016). Note the current extent of the Roraima Supergroup (red dashed border), from which most diamonds of the Guiana Shield are derived (AM—Amatuk, BV—Boa Vista, CO—Los Coquitos, DC—Dachine, EK—Ekereku, GU—Guianimo, JW—Jawalla, KM—Kamarang, KU—Kurupung, KW—Konawaruk, MK—Maikwak, MM—Monkey Mountain, NA—Nassau, RO—Rosebel, TE—Tepequém). Modified from Kroonenberg et al. (2016) and references therein.

al., 2016). In western Guyana, the basement rocks of the Guiana Shield are unconformably overlain by the Roraima Supergroup, which is an interbedded, 2300 m thick sequence of sandstones, conglomerates, and ash-fall tuffs with an age of 2.12–1.78 Ga (billions of years), deposited from rocks eroding from earlier greenstone terranes (Priem et al., 1973; Santos et al., 2003). Paleoproterozoic mafic dikes of the Avanavero Suite crosscut the entire Roraima Supergroup sequence.

Throughout much of the Phanerozoic (the time since the Cambrian ~541 million years ago), the region has been a stable craton, only modified by erosion and

deposition of sedimentary sequences. The Upper Proterozoic was marked by a period of uplift with no evidence of sedimentation (Gibbs and Barron, 1993). Since the late Triassic, drainage patterns and depositional systems have evolved in response to faulting and rifting associated with the opening of the Atlantic Ocean. Where cratonic igneous and metamorphic rocks are buried, Guyana's jungle interior is underlain by a complex network of high alluvial, terrace, alluvial flat, riverbed, buried channel, and plateau deposits (figure 4). These repeated cycles of erosion and deposition have led to complex diamond placer deposits with variable provenances and timing.



Figure 4. Top: Buried alluvial diamond deposit underlying a fine-grained aeolian sand deposit, with Guyanese geotechnician Nigel Blackman standing for scale. Photo by Roy Bassoo. Bottom: Close-up view of an alluvial deposit. Photo by Uwe Van Dijk.



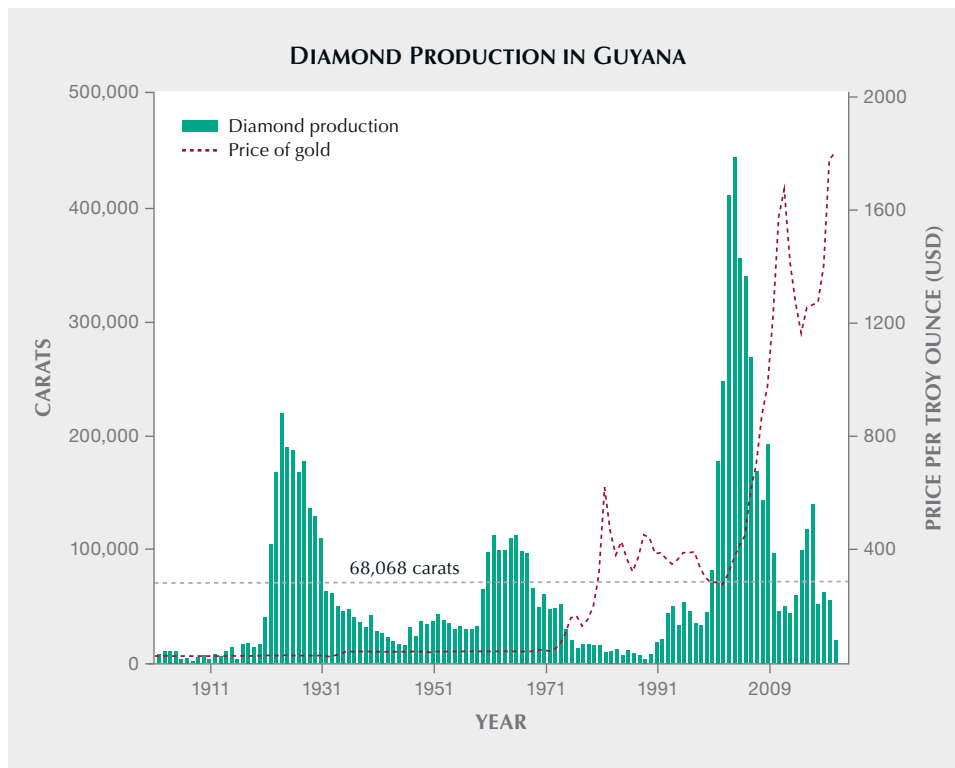


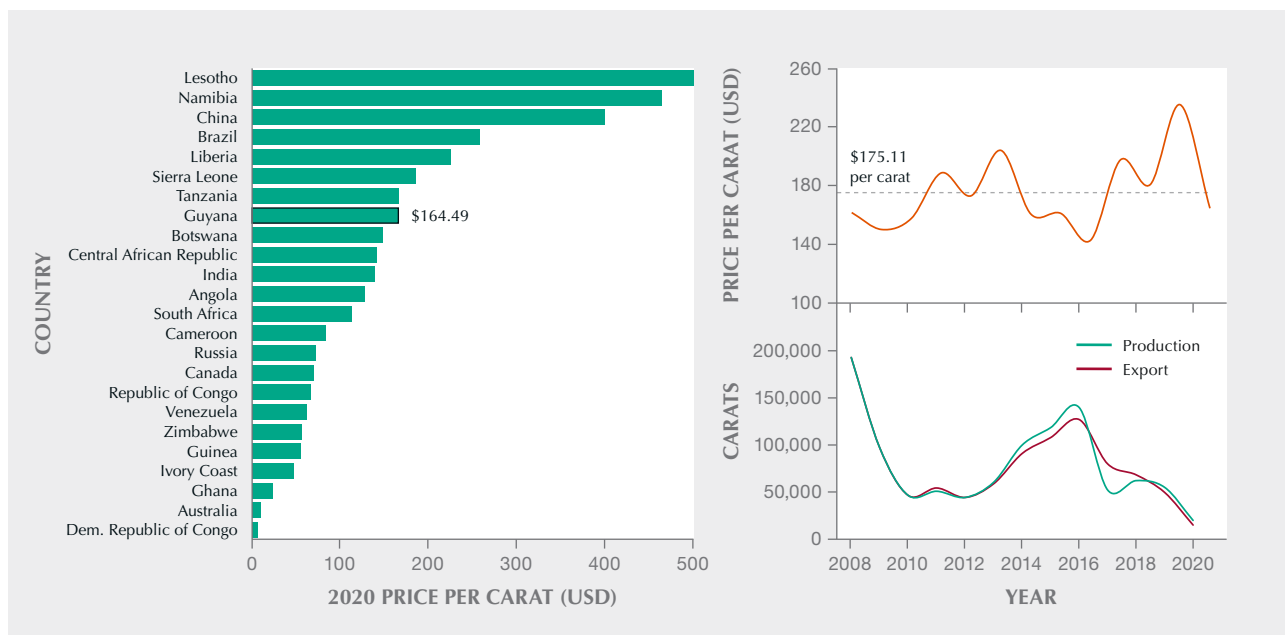
Figure 5. Diamond production (green bars) in Guyana (Kimberley Process Rough Diamond Statistics, n.d.) and price of gold (dashed red line) per troy ounce (National Mining Association, n.d.). Also plotted is the historical average production per year (gray dashed line).

### GUYANA'S DIAMOND PRODUCTION

According to the Guyana Bureau of Statistics, mining accounted for ~12% of the country's GDP from 2000

to 2019. Gold is by far the most important mineral resource, accounting for ~82% of all exported ore resources by monetary value. Diamonds are third most

Figure 6. Global price per carat value of diamond-producing countries for 2020 (left). Guyana's historical diamond price per carat and average price per carat indicated by the gray dashed line (top right) and exports versus production (bottom right) (Kimberley Process Rough Diamond Statistics, n.d.).



important and currently account for 2% of all exported ore materials (second is bauxite at 16%). Historically, diamond production is intimately tied to gold mining because both tend to be found in the same alluvial deposits. When gold prices are low, miners tend to extract more diamonds, which is one explanation for the cyclical nature of diamond production in Guyana (figure 5).

Although it is not well publicized, Guyana has contributed to the global supply of diamonds for more than 130 years. Their trade name has been “British diamonds,” hinting at the country’s colonial past (Persaud, 2010). In the twenty-first century, Guyana’s declared diamond production has averaged ~68,000 carats per year (figure 5). In 2004, Guyana recorded its highest production to date of 445,540 carats. From 2008 to 2012, there was a steady decline in production, likely exacerbated by financial challenges associated with the 2008 global financial crisis. After 2012, there was a steady increase in diamond production. Production today, however, remains relatively low, which can be attributed to rising gold prices (figure 5). With a historical average price per carat of US\$175 (figure 6), Guyana’s diamonds remain fairly profitable when compared to the global average price per carat of US\$151 in 2020 (figure 6, left). They fall within the per-carat price range of diamonds from Sierra Leone (US\$186) and Botswana (US\$148) (figure 6). Declared diamonds are taxed at a 3% royalty and 2% withholding tax (Guyana Geology and Mines Commission, <https://ggmc.gov.gy/law/all>).

There remains room for expansion and increased production. Marketing is one such possible avenue to growth. From the 1920s to the 1980s, Guyana’s production was limited mostly to rough diamond sales in the UK, Trinidad, and Barbados (Lee, 1981). Since the 1990s, a growing number of Guyanese-owned and operated manufacturing houses have started to polish and set diamonds into beautiful pieces (figure 7).

### DIAMOND MINING IN GUYANA

Diamond exploration has been driven mostly by Guyanese artisanal miners who prospect along riverbanks for unconventional, and locally specific, detrital indicator minerals to which they ascribe fanciful names. “Sweetman,” “cantankerer,” “blue jacket,” and “tin” refer to waterworn quartz, ruby, sapphire, and rutile, respectively (figure 8). Other diamond indicator minerals include topaz, jasper, zircon, il-



*Figure 7. This brownish yellow diamond from Guyana, a 1.01 ct pear brilliant measuring 7.39 × 5.19 × 3.62 mm, is set beneath a colorless round brilliant diamond. Photo by Nathan Renfro; courtesy of Michelle Bassoo.*

menite, gold, tourmaline, minor garnet, and chromite (figure 8). The Guyana Geology and Mines Commission (GGMC) is the regulatory body that oversees mining, safety, environmental protection, and education in diamond mining and geology. Although this resource is available, most miners are not well educated in prospecting or alluvial processes. Instead, they frequently rely on anecdotal evidence and superstition, only prospecting in areas that have produced diamonds in the past. The result is that the discovery and exploitation of new diamond deposits is very rare. Regardless, production has continued to provide income for artisanal miners for more than 100 years since the first discovery of diamonds in 1887 on the Potaro River (Lee, 1981).



Figure 8. Top left: Washed alluvial gravel sample in a batel (a gold panning tool made of iron with a riffled interior). Top right: Accessory minerals found with Guyana diamonds, including rounded quartz, jasper, and rutile (field of view 17 cm). Photos by Uwe Van Dijk. Recovered corundum (bottom left) and topaz (bottom right) of various colors. Photos by Roy Bassoo.

Artisanal mining in Guyana was born in the decades after the abolition of slavery in 1838. Many freed slaves of predominantly West African heritage sought a livelihood away from the sugar plantations and their former slave owners (Josiah, 2011).

Prospecting and hand mining for gold and diamonds in the relatively unexplored and undeveloped interior offered both literal and metaphorical independence. Toward the end of the nineteenth century, these artisanal miners were called “pork knockers”

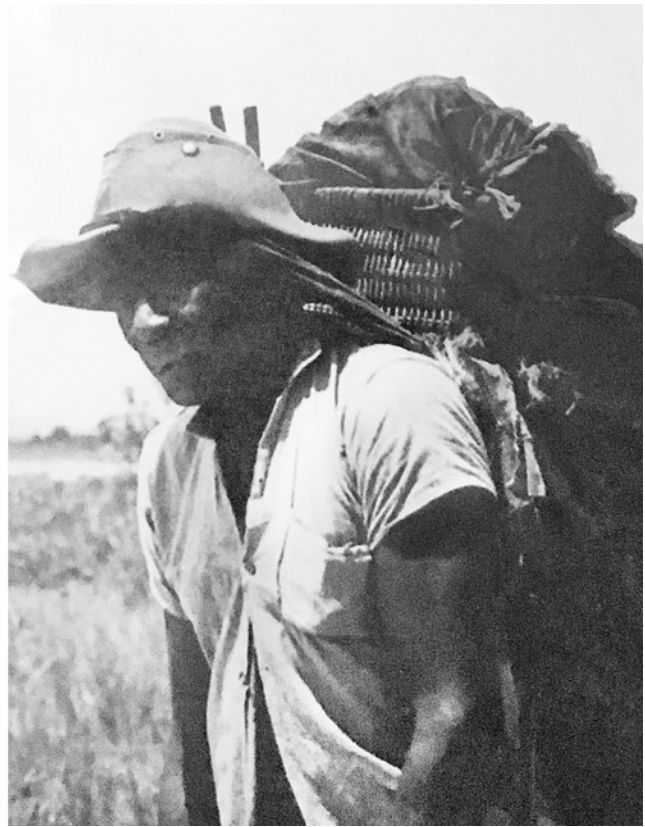


Figure 9. Wood carving (left) and historical photograph (right) of an unknown early twentieth-century Afro-Guyanese “pork knocker” at the Guyana National Museum, which shows how little capital investment was required to pursue economic independence. To his left is a small sluice box for filtering gold and diamonds from sediment called a “tom and box” (Lee, 1981). Notice he carries on his head an iron batel of conical shape and rifled interior used not only for panning but also to protect the wearer from the sun. He also carries cooking utensils, a cutlass, and a handcrafted wooden pipe for smoking. Worn just below his left knee is a red cotton cloth, believed to protect against rheumatoid arthritis and ensure good fortune. The wariishi secured to his head is handwoven from palm fronds and serves as a supply basket. Photos by Roy Bassoo.

(figure 9). This nickname is likely a creolization of “pork noshers,” a label applied to artisanal miners because of their consumption of salted and cured pork. It is theorized that a predominantly Jewish diamond merchant class coined this term (J. Krakowsky, pers. comm., 2019). Legendary pork knockers, spinning tales of fist-sized diamonds and hills topped with gold, have stirred the public’s imagination. The stories of Makantali, who wore all white and flung money into the air when arriving at the port of Bartica, and Gold Dawg, who became the first person in his village to own a car (Bascom, 1996), add enchantment to the mining industry in Guyana even today.

Artisanal “pork knocking” today is typically a small-scale, independent or cooperative effort. Operations are conducted on a tribute basis, where an artisanal miner receives a share of the proceeds. These

miners divert water channels using mud and wood dams. Pickaxes and shovels are used to move prospective diamond gravels into manmade ponds screened with 0.2–1.0 cm sieves. Sediment <0.2 cm is discarded into the holding ponds. The artisanal miners also excavate small pits of 6–7 m depth that are shored up using cut timber (Lee, 1981). Larger groups of miners may form collectives and syndicates. Alternatively, claim owners contract small teams to prospect alluvial deposits. Individual miners are sometimes paid a salary, but diamonds are often used as currency in the jungle for purchasing fuel, services, and food (Persaud, 2010). Complementary activities that support the mining industry include food service, bookkeeping, and cleaning. Larger-scale ventures rely upon heavy equipment and techniques borrowed from the gold industry. Placer deposits are removed by an excavator and formed



Figure 10. Top: Hydraulic mining of alluvial deposits. Photo by Roy Bassoo. Bottom: Examining a sieve “wash” for diamonds. Photo by James Herbison.



Figure 11. A campsite of artisanal miners. Photos by Roy Bassoo.

into a slurry using hydraulic techniques, and this slurry is then pumped to a sluice box and jig to extract both gold and diamonds (figures 10–12). Heavy minerals, including diamond, are then handpicked from the rest of the washed and sieved minerals and stored for sale (see video at [www.gia.edu/gems-gemology/summer-2022-diamonds-from-guyana](http://www.gia.edu/gems-gemology/summer-2022-diamonds-from-guyana)).

In the early years, a “bush trader” ventured into the field to sell food, liquor, and equipment in exchange for diamonds. This practice has evolved to become more stationary, where a bush trader owns a property near a port town specifically for transactions. Today, miners often carry their own diamond parcels to the capital city of Georgetown, visiting different brokers to gather quotes before confirming a sale. The

economics of the diamond trade in Guyana are influenced heavily by market fluctuations, fuel supply, and the rainy season. Heavy rains in May–June and September–October significantly limit mining activity. In the offseason, miners seek alternative forms of employment in the construction, security, or food service industries. However, off-season unemployment is widespread (J. Krakowsky, pers. comm., 2019). Miners are often poorly educated on the relative value of individual diamonds in their parcels, tending to rely solely on carat weight as the metric of value. There is a need for educational outreach in this regard, where an improved understanding of how rough diamonds are manufactured into cut diamonds would improve the negotiating position of local miners.

Figure 12. A typical small- to medium-scale diamond mining operation in Guyana using a diamond jig attached to a sluice box. Photo by Roy Bassoo.





Figure 13. Top left: Guyanese diamonds recovered by artisanal mining. Top right: Gem-quality Guyanese diamonds. Photos by Kenneth Befus. Bottom: Selected specimens highlighting color and morphology. Photo by Nathan Renfro.

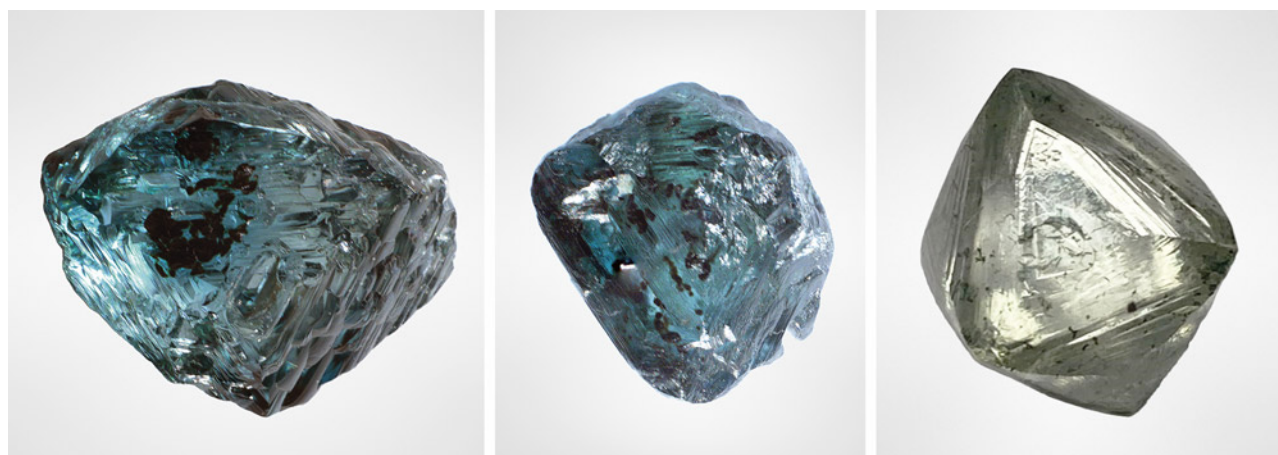


Figure 14. Left and center: Two greenish blue Guyanese diamonds (~0.27 and ~0.10 ct) from the GIA collection, donated by Roger Krakowsky. Photos by Roy Bassoo. Right: A larger diamond with a green skin (~6 ct). Photo by James Krakowsky.

## GUYANA'S DIAMONDS

**Color and Size.** Economically viable diamonds in Guyana are small, mostly ranging from 0.1 to 0.4 ct. Diamonds with sizes up to 10 ct have been found but are uncommon. The largest gem-quality stones ever recovered were 56.75 and 42 ct, found in the Ewang region in 1926 and in the Perenong region in 2001, respectively (Persaud, 2010). Polished Guyanese diamonds are predominantly near-colorless, with approximately 93% of them G–J and 7% K–M, and very rarely in white or near-opaque bodycolors (J. Krakowsky, pers. comm., 2019).

Of special note, many of Guyana's rough diamonds (~42%) display green to green-blue skins or green spotting that covers up to ~100% of the surface area (figure 13). While diamonds with a green bodycolor are rare (figure 14) (Bassoo et al., 2021), they are relatively abundant in Guyana compared to other sources such as Brazil, Ghana, and Zimbabwe (Breeding et al., 2018). Guyana has a relatively higher abundance of green diamonds because the placer diamonds may have resided within the sedimentary environment for up to two billion years (Bassoo et al., 2021). Diamonds thus may accumulate radioactive damage over hundreds of millions of years. Alpha, beta, and gamma radiation from nearby radioactive minerals such as zircon, monazite, and potassium feldspar created vacancy and interstitial defects in the diamonds. Photoluminescence spectroscopy reveals these vacancy defects to have a zero phonon line (ZPL) at 741 nm and are classed as the GR1 or neutral vacancy ( $V^0$ ) defect. Vacancy defects absorb in the red portion of the visible spectrum and, in the presence of nitrogen

defects, reflect/transmit green wavelengths. Furthermore, the type of radiation influences the intensity and depth of green color penetration in the diamond, with gamma radiation creating the deepest penetration of green color and alpha radiation the least (Breeding et al., 2018; Eaton-Magaña et al., 2018).

**Morphology and Surface Textures.** Guyana's diamonds range in crystal shape from octahedral to dodecahedral and occasionally display flattened cuboid forms. Twinned diamonds and aggregates are rare. Fine stepped, lamellar trigonal faces are common, whereas flat faces and sharp edges are not. Resorption textures such as terraces, teardrop hillocks, and dissolution pits are found in 95% of the diamonds (figure 15). Flat-bottom dissolution pits including trigons account for ~69% of all dissolution pits and frequently penetrate into the {111} crystal faces (Bassoo et al., 2021). Most of the octahedral diamonds have resorbed edges and can be fully resorbed to dodecahedrons. Late-stage etching features such as corrosion sculptures, shallow depressions, ruts, and glossy surfaces are observed in two-thirds of the diamonds.

Edge abrasion, found in 44% of the abraded diamonds, is the most commonly observed surface texture (figure 15). Most Guyanese diamonds have some degree of surface abrasion from minor scratches and edge abrasion. Some have no apparent surface abrasion, however. This distinction subdivides Guyana's diamonds into 85% abraded and 15% non-abraded (Bassoo et al., 2021). Abraded diamonds may reflect an older population with a long history of repeated transport within streams and



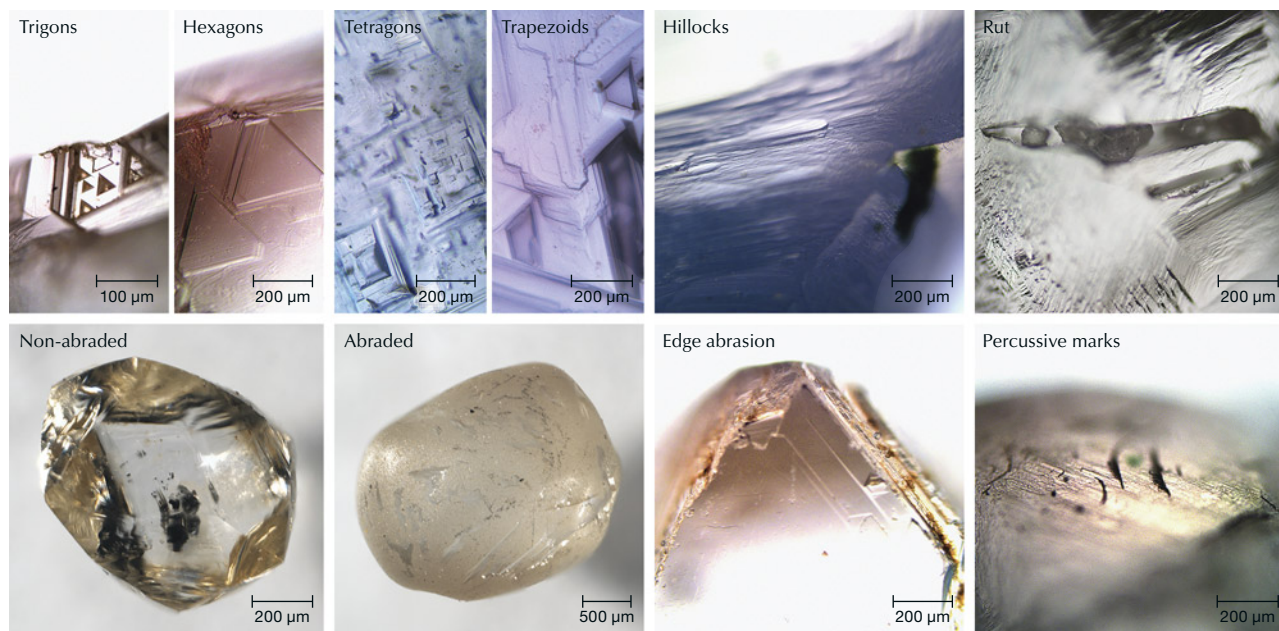
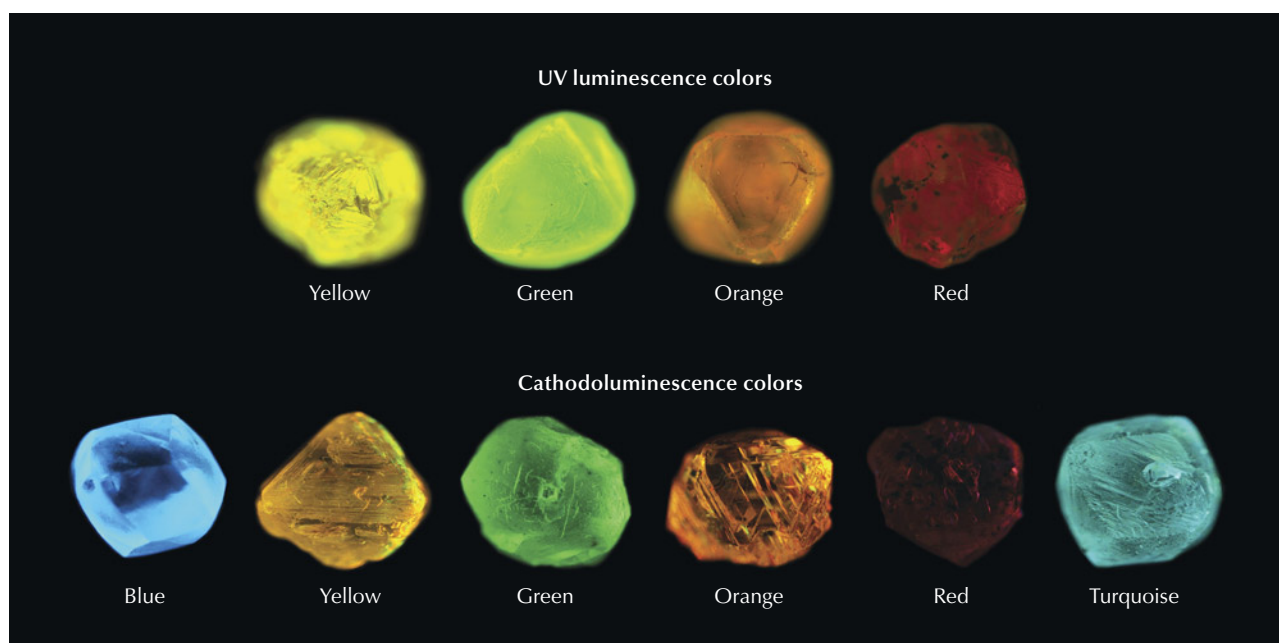


Figure 15. Examples of Guyanese diamond surface morphology. Photos by Roy Bassoo.

rivers. Non-abraded diamonds may reflect a shorter distance and/or time of transport. Alternatively, the 15% non-abraded population may be derived from undiscovered kimberlites or lamproites (Bassoo et al., 2021). Abraded and non-abraded diamonds also display differences in luminescence.

**Luminescence.** Guyana’s diamonds display luminescence colors of blue, green, orange, yellow, red, and turquoise (figure 16) (Bassoo et al., 2021). Of 472 diamonds, the abraded diamonds dominantly show green to turquoise (~60%) and some blue (~20%) cathodoluminescence responses. Non-abraded dia-

Figure 16. Luminescence responses of Guyana’s diamonds. UV luminescence (280–315 nm) response colors (top) and cathodoluminescence response colors (bottom). Photos by Roy Bassoo.



monds cathodoluminesce predominantly blue (~60%) and moderate green to turquoise (~25%). Ultraviolet (UV) luminescence (280–315 nm) also yields a distinction between abraded and non-abraded samples. Abraded diamonds luminesce green (~85%) predominantly with very minor orange, red, and yellow (~8%). In contrast, ~50% of the non-abraded diamonds show green UV luminescence, and a larger proportion (~45%) exhibit none at all.

Cathodoluminescence spectroscopy reveals defect changes preserved within diamonds that have resided within metasedimentary rocks for billions of years. Cathodoluminescence spectroscopy is a technique that can be used to infer primary or secondary diamond sources. Most kimberlite-derived diamonds have a blue luminescence response (Bulanova, 1995; Lindblom et al., 2005). Blue luminescence is often related to the N3 defect (ZPL ~503 nm), which consists of three nitrogen atoms surrounding a vacancy (Clark et al., 1992; Shigley and Breeding, 2013). Metamorphosed paleoplacers, such as those in Guyana, tend to preserve a smaller population of blue luminescent diamonds compared to green and other luminescence response colors (Bruce et al., 2011; Kopylova et al., 2011). Green luminescence could be related to the H3 to H4 defect, consisting of more complex arrangements of four nitrogen atoms surrounding two vacancies (H3) or two nitrogen atoms separated by a vacancy (H4) (Shigley and Breeding, 2013). A change from blue lu-

minescence to green or other colors corresponding with a shift in ZPL from ~503 nm to higher wavenumbers has been observed in diamonds from unmetamorphosed and metamorphosed rocks, respectively (Iakoubovskii and Adriaenssens, 1999; Collins et al., 2005; Bruce et al., 2011). The Roraima Supergroup, from which Guyana's abraded diamonds are likely derived, has been metamorphosed to zeolite and greenschist facies (Beyer et al., 2015). This observation may explain the relative proportion of blue to green luminescence response colors of Guyanese diamonds.

**Composition and Inclusions.** The carbon isotope composition ( $\delta^{13}\text{C}$ ) of Guyanese diamonds ranges from -2.8 to -16.1‰, similar to that of Brazilian diamonds (Tappert et al., 2006). The carbon isotopic composition of Guyana's diamonds indicates they formed from upper mantle rocks (Bassoo et al., 2021). Nitrogen contents can be as high as ~2000 ppm, with >50% being type IaAB (figure 17). A small percentage (~9%) are type IaB, having more nitrogen platelets. Type IIa and IaA diamonds are of similar abundances, within 6% of each other. No type IIb or Ib diamonds have been reported. The nitrogen type and concentration were used to derive a residence temperature of ~1120°C, indicating that Guyanese diamonds are lithospheric (Bassoo et al., 2021). Inclusion composition also indicates an upper mantle origin.

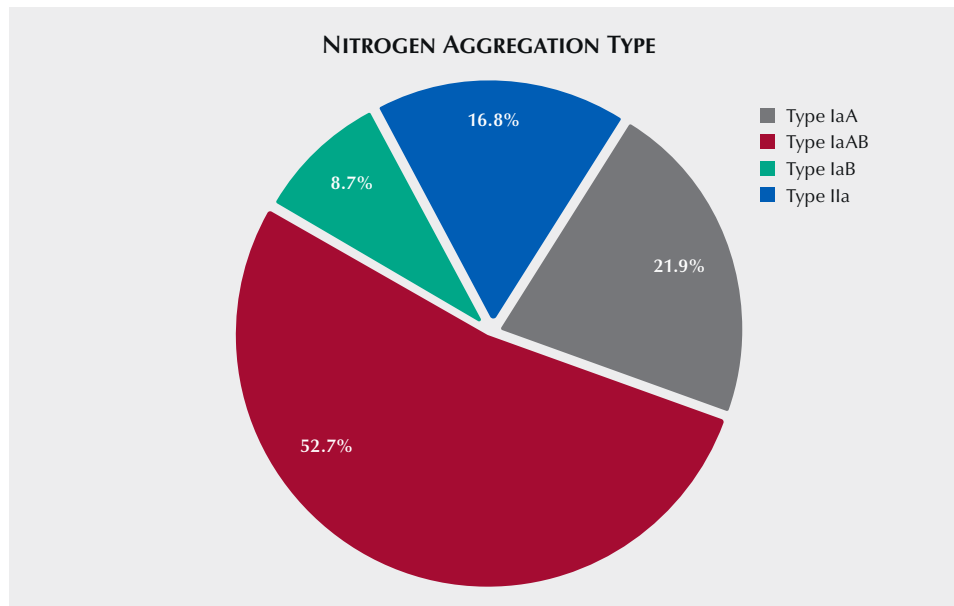


Figure 17. Distribution of nitrogen type in Guyanese diamonds (Bassoo et al., 2021).

Inclusions occur in ~15% of the diamonds and have been identified by comparing their Raman spectra with those in the RRUFF spectra database (Lafuente et al., 2016; Bassoo et al., 2021). Most of the inclusions in Guyanese diamonds consist of forsterite, enstatite, and chromite, indicating the diamonds formed from peridotitic upper mantle rocks. There are some diamonds that contain rutile, coesite, and clinopyroxene, and these are interpreted to have formed from eclogitic upper mantle rocks (Bassoo et al., 2021). Raman thermobarometry of entrapped olivine and Cr-pyrope inclusions indicates internal pressures of ~6.2 GPa, again lending evidence to their formation in the upper mantle (Bassoo and Befus, 2021). Guyana's diamonds are typical of peridotitic to eclogitic cratonic diamonds.

## COMPARISONS TO OTHER DIAMONDS FROM NORTHERN SOUTH AMERICA

Guyana's diamonds are part of a larger story about the evolution of cratons and residence within sedimentary systems. Their morphological and geochemical features compare and distinguish them from other diamonds of the Guiana Shield in northern South America (figure 18). Important deposits occur in Brazil, Venezuela, Suriname, and French Guiana.

Alluvial diamonds are mined in Brazil and Suriname. In the Guiana Shield portion of northern Brazil, diamonds are recovered from alluvial terraces shed from conglomerates of the Tepequém Formation (Santos et al., 2003; Reis et al., 2017). The diamonds are generally 2–3 mm in size and occur in a flattened octahedral to dodecahedral form. They are colorless to gray, oftentimes resorbed, and contain peridotitic-type inclusions such as forsterite (Araújo et al., 2011). The Tepequém Formation represents a regional high-energy, depositional basin that was a diamond sink, synchronous with emplacement by several episodes of kimberlite volcanism within the Guiana Shield during the middle Paleoproterozoic (>2.0 Ga) (Santos et al., 2003; Schulze et al., 2006). In Suriname, alluvial diamonds are thought to be derived from rocks of the Rosebel Formation (Naipal et al., 2020). These are colorless to brown to slightly green, and green skins are common (figure 18, top). Resorption textures including trigons and frosting are common, and inclusions such as forsterite and enstatite are peridotitic. French Guiana is also home to primary diamond-bearing igneous sources, but these are metamorphosed ultramafic and pyroclastic shoshonites or lamprophyres found in the Dachine

region. These diamonds are very small (~1 mm), grayish yellow to brown, irregular to cuboid (figure 18, middle), and mostly contain sulfide inclusions (Cartigny, 2010; Smith et al., 2016).

Alluvial diamond data from Venezuela is difficult to assess because illegal mining and smuggling are prevalent (e.g., Blore, 2006). Also, most alluvial deposits are located in inaccessible parts of the Amazon jungle near the Brazil and Guyana borders, where isolated Amerindian tribes such as the Yanomami are leery of outsiders (Heylman, 2001). Further west in Venezuela is the Guaniamo area, where there exists a unique deposit of primary diamond-bearing kimberlite dikes (Capdevila et al., 1999; Channer et al., 2001; Kaminsky et al., 2000, 2004; Smith et al., 2016). Guaniamo diamonds are small, ranging from 1 to 2 mm, and colorless to gray with common green skins, frequently occurring in resorbed dodecahedrons and octahedrons (figure 18, bottom). Diamonds from Guaniamo contain inclusions of the predominantly eclogitic variety, including almandine garnet, clinopyroxene, rutile, ilmenite, pyrrhotite, and coesite (Taylor, 1999; Kaminsky et al., 2000).

## CONCLUSIONS

Guyana's diamonds are found in gravels along the eastern edge of the Roraima Supergroup. Most originate as paleoplacers from as yet unknown rocks of the Roraima Supergroup. Similar alluvial diamonds are found in nearby Venezuela, Brazil, and Suriname, suggesting the Roraima is a common source. Indeed, these paleoplacers represent a regional diamond terrane with a lateral extent of at least 450,000 km<sup>2</sup>. Diamonds from Guyana are of scientific interest because they are survivors of >2 Ga of weathering and erosion. As such, they are >2 billion-year-old xenocrysts from the mantle, brought to the surface by some of the earth's oldest kimberlite or lamproite eruptions. They are an important source of information on the cratonic root of northern South America during the Paleoproterozoic (Schulze et al., 2006; Bassoo and Befus, 2021).

There is opportunity for expanded economic use of Guyana's diamonds. Although small, they are valued for their lack of color and their clarity, especially as melee stones. Artisanal mining practices result in a relatively low price point, and they are not subject to prohibitive taxation. With continued exploration efforts, new paleoplacer deposits are sure to be discovered. The discovery of a primary kimberlite deposit should not be expected, but abrasion and

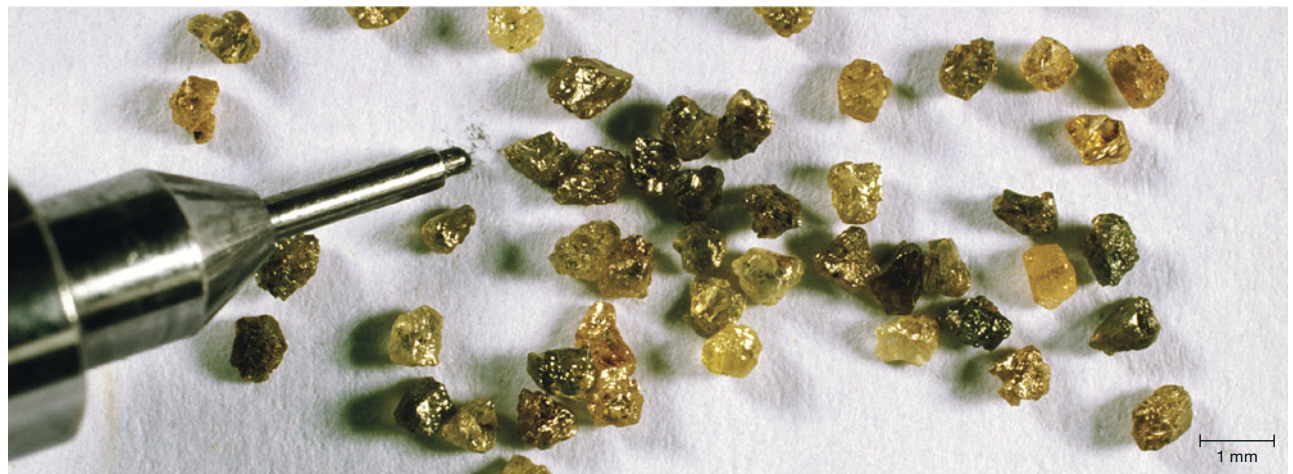


Figure 18. Top: Diamonds (0.10–2.12 ct) from Suriname; from Naipal et al. (2020). Middle: French Guiana diamonds; from Cartigny (2010). Bottom: Alluvial diamonds from Guaniamo, Venezuela. Photo by Maha Tannous; courtesy of Ric Taylor.

luminescence information could indicate that some stones have experienced little transport and thermal alteration. We also recognize an opportunity for the exploration and improved recovery of other gemstones. Ruby, sapphire, and topaz are considered indicator minerals for gold and diamonds. There is no

common knowledge regarding their quality or sources. Tourmaline is also present but has only been documented as schorl. Such diverse gem and mineral wealth bodes well for future discoveries in this English-speaking nation with an established gemstone mining and trade network.

#### ABOUT THE AUTHORS

*Dr. Bassoo is a Guyanese geoscientist and consulting geologist who is currently a postdoctoral researcher at GIA in Carlsbad, California. Dr. Befus is a petrologist and volcanologist who serves as a professor of geology at Baylor University in Waco, Texas.*

#### ACKNOWLEDGMENTS

*The authors sincerely thank James Krakowsky (general manager of Kays Diamond Enterprise Ltd.) for his gemological input and samples donated for study. Gordon Nestor (manager at the Guyana Geology and Mines Commission) provided valuable logistical support. We are grateful to Jim Shigley of GIA for his encouragement to prepare this article for the gemological community. We also thank Rachele Turnier and Aaron Palke of GIA for their assistance in identifying corundum specimens.*

#### REFERENCES

- Araújo D.P., Santos R.V., Souza V., Chemale F., Dantas E. (2011) Diamantes Serra do Tepequém: Resultados preliminares. *12th Simpósio da Amazônia*, October 2–5, 2011, Boa Vista, Roraima, Brazil.
- Bascom H. (1996) *Makantali*. Carifesta XI, Georgetown, Guyana.
- Bassoo R., Befus K. (2021) Composition of the sub-cratonic mantle of the Guiana Shield inferred from diamond-hosted inclusions. *Geochemistry, Geophysics, Geosystems*, Vol. 22, No. 6, <http://dx.doi.org/10.1029/2021GC009841>
- Bassoo R., Befus K., Liang P., Forman S., Sharman G. (2021) Deciphering the enigmatic origin of Guyana's diamonds. *American Mineralogist*, Vol. 106, No. 1, pp. 54–68, <http://dx.doi.org/10.2138/am-2020-7486>
- Beyer S.R., Hiatt E.E., Kyser K., Drever G.L., Marlatt J. (2015) Stratigraphy, diagenesis and geological evolution of the Paleoproterozoic Roraima Basin, Guyana: Links to tectonic events on the Amazon Craton and assessment for uranium mineralization potential. *Precambrian Research*, Vol. 267, pp. 227–249, <http://dx.doi.org/10.1016/j.precamres.2015.06.017>
- Blore S.G., Ed. (2006) The lost world: Diamond mining and smuggling in Venezuela. *Partnership Africa Canada, Ottawa, Occasional Paper*, Vol. 16, 20 pp.
- Breeding C.M., Eaton-Magaña S., Shigley J.E. (2018) Natural-color green diamonds: A beautiful conundrum. *G&G*, Vol. 54, No. 1, pp. 2–27, <http://dx.doi.org/10.5741/GEMS.54.1.2>
- Bruce L.F., Kopylova M.G., Longo M., Ryder J., Dobrzynetskaya L.F. (2011) Luminescence of diamonds from metamorphic rocks. *American Mineralogist*, Vol. 96, No. 1, pp. 14–22, <http://dx.doi.org/10.2138/am.2011.3467>
- Bulanova G.P. (1995) The formation of diamond. *Journal of Geochemical Exploration*, Vol. 53, No. 1–3, pp. 1–23, [http://dx.doi.org/10.1016/0375-6742\(94\)00016-5](http://dx.doi.org/10.1016/0375-6742(94)00016-5)
- Capdevila R., Arndt N., Letendre J., Sauvage J.F. (1999) Diamonds in volcanoclastic komatiite from French Guiana. *Nature*, Vol. 399, No. 6735, pp. 456–458, <http://dx.doi.org/10.1038/20911>
- Cartigny P. (2010) Mantle related carbonados? Geochemical insights from diamonds from the Dachine komatiite (French Guiana). *Earth and Planetary Science Letters*, Vol. 296, No. 3–4, pp. 329–339, <http://dx.doi.org/10.1016/j.epsl.2010.05.015>
- Channer D.M.D., Egorov A., Kaminsky F. (2001) Geology and structure of the Guaniamo diamondiferous kimberlite sheets, south-west Venezuela. *Revista Brasileira de Geociências*, Vol. 31, No. 4, pp. 615–630, <http://dx.doi.org/10.25249/0375-7536.2001314615630>
- Clark C.D., Collins A.T., Woods G.S. (1992) Absorption and luminescence spectroscopy. In J.E. Field, Ed., *The Properties of Natural and Synthetic Diamond*. Academic Press, London, pp. 35–69.
- Collins A., Connor A., Ly C.-H., Shareef A. (2005) High-temperature annealing of optical centers in type-I diamond. *Journal of Applied Physics*, Vol. 97, No. 8, article no. 083517, <http://dx.doi.org/10.1063/1.1866501>
- Eaton-Magaña S., Breeding C.M., Shigley J.E. (2018) Natural-color blue, gray, and violet diamonds: Allure of the deep. *G&G*, Vol. 54, No. 2, pp. 112–131, <http://dx.doi.org/10.5741/GEMS.54.2.112>
- Fraga L.M., Macambira M.J.B., Dall'Agnol R., Costa J.B.S. (2009) 1.94–1.93 Ga charnockitic magmatism from the central part of the Guyana Shield, Roraima, Brazil: Single-zircon evaporation data and tectonic implications. *Journal of South American Earth Sciences*, Vol. 27, No. 4, pp. 247–257, <http://dx.doi.org/10.1016/j.jsames.2009.02.007>
- Gibbs A.K., Barron C.N. (1993) *The Geology of the Guiana Shield*. Oxford University Press, New York.
- Heylman E.B. (2001) Placer diamonds in Venezuela. *International California Mining Journal*, Vol. 70, No. 7, pp. 21–23.
- Iakoubovskii K., Adriaenssens G.J. (1999) Photoluminescence in CVD diamond films. *Physica Status Solidi (a)*, Vol. 172, No. 1, pp. 123–129, [http://dx.doi.org/10.1002/\[SICI\]1521-396X\(199903\)172:1%3C123::AID-PSSA123%3E3.0.CO;2-E](http://dx.doi.org/10.1002/[SICI]1521-396X(199903)172:1%3C123::AID-PSSA123%3E3.0.CO;2-E)
- Ishmael O. (2013) *The Guyana Story: From Earliest Times to Independence*. Xlibris, Bloomington, Indiana.
- Josiah B. (2011) *Migration, Mining, and the African Diaspora:*

- Guyana in the Nineteenth and Twentieth Centuries*. Palgrave Macmillan, Basingstoke, UK.
- Kaminsky F.V., Zakharchenko O.D., Griffin W.L., Channer D.M.DeR., Khacchatryan-Blinova G.K. (2000) Diamond from the Guaniamo area, Venezuela. *Canadian Mineralogist*, Vol. 38, No. 6, pp. 1347–1370, <http://dx.doi.org/10.2113/gscanmin.38.6.1347>
- Kaminsky F.V., Sablukov S.M., Sablukova L.I., Channer D.M.D. (2004) Neoproterozoic “anomalous” kimberlites of Guaniamo, Venezuela: Mica kimberlites of “isotopic transitional” type. *Lithos*, Vol. 76, No. 1-4, pp. 565–590, <http://dx.doi.org/10.1016/j.lithos.2004.03.035>
- Kimberley Process Rough Diamond Statistics (n.d.) Public Statistics Area, [https://kimberleyprocessstatistics.org/public\\_statistics](https://kimberleyprocessstatistics.org/public_statistics)
- Kopylova M.G., Afanasiev V.P., Bruce L.F., Thurston P.C., Ryder J. (2011) Metaconglomerate preserves evidence for kimberlite, diamondiferous root and medium grade terrane of a pre-2.7 Ga Southern Superior protocraton. *Earth and Planetary Science Letters*, Vol. 312, No. 1-2, pp. 213–225, <http://dx.doi.org/10.1016/j.epsl.2011.09.057>
- Kroonenberg S.B., de Roever E.W.F., Fraga L.M., Reis N.J., Faraco T., Lafon J.-M., Cordani U., Wong Th.E. (2016) Paleoproterozoic evolution of the Guiana Shield in Suriname: A revised model. *Netherlands Journal of Geosciences*, Vol. 95, No. 4, pp. 491–522, <http://dx.doi.org/10.1017/njg.2016.10>
- Lafuente B., Downs R.T., Yang H., Stone N. (2016) The power of databases: The RRUFF project. In T. Armbruster and R.M. Danisi, Eds., *Highlights in Mineralogical Crystallography*. W. de Gruyter GmbH, Berlin, pp. 1–29.
- Lee R.J. (1981) Diamond production in Guyana. *Journal of Gemmology*, Vol. 17, No. 7, pp. 465–479.
- Lindblom J., Hölsä J., Papunen H., Häkkänen H. (2005) Luminescence study of defects in synthetic as-grown and HPHT diamonds compared to natural diamonds. *American Mineralogist*, Vol. 90, No. 2-3, pp. 428–440, <http://dx.doi.org/10.2138/am.2005.1681>
- Naipal R., Zwaan J.C., Kroonenberg S.B., Kriegsman L.M., Mason P.R.D. (2020) Diamonds from the Nassau Mountains, Suriname. *Journal of Gemmology*, Vol 37, No. 2, pp. 180–191.
- National Mining Association (n.d.) Historical gold prices – 1833 to present, [http://www.nma.org/pdf/g\\_prices.pdf](http://www.nma.org/pdf/g_prices.pdf)
- Persaud K. (2010) The diamond industry and exploration for diamonds in Guyana. Guyana Geology and Mines Commission.
- Priem H.N.A., Boelrijk N.A.I.M., Hebeda E.H., Verdurmen E.A.Th., Verschure R.H. (1973) Age of the Precambrian Roraima formation in northeastern South America: Evidence from isotopic dating of Roraima pyroclastic volcanic rocks in Suriname. *GSA Bulletin*, Vol. 84, No. 5, pp. 1677–1684, [http://dx.doi.org/10.1130/0016-7606\(1973\)84%3C1677:AOT-PRF%3E2.0.CO;2](http://dx.doi.org/10.1130/0016-7606(1973)84%3C1677:AOT-PRF%3E2.0.CO;2)
- Reis N.J., de Faria M.S.G., Fraga L.M., Haddad R.C. (2000) Orosirian calc-alkaline volcanism and the Orocaima event in the northern Amazonian Craton, eastern Roraima State. *Revista Brasileira de Geociências*, Vol. 30, No. 3, pp. 380–383.
- Reis N.J., Nadeau S., Fraga L.M., Betiello L.M., Faraco M.T.L., Reece J., Lachhman D., Ault R. (2017) Stratigraphy of the Roraima Supergroup along the Brazil-Guyana border in the Guiana Shield, Northern Amazonian Craton—Results of the Brazil-Guyana Geology and Geodiversity Mapping Project. *Brazilian Journal of Geology*, Vol. 47, No. 1, pp. 43–57, <http://dx.doi.org/10.1590/2317-4889201720160139>
- Rodney W. (1981) *A History of the Guyanese Working People, 1891–1905*. Johns Hopkins University Press, Baltimore.
- Santos J.O.S., Potter P.E., Reis N.J., Hartman L.A., Fletcher I.R., McNaughton N.J. (2003) Age, source and regional stratigraphy of the Roraima Supergroup and Roraima-like outliers in northern South America based on U–Pb geochronology. *Geological Society of America Bulletin*, Vol. 115, No. 3, pp. 331–348, [http://dx.doi.org/10.1130/0016-7606\(2003\)115%3C0331:ASARSO%3E2.0.CO;2](http://dx.doi.org/10.1130/0016-7606(2003)115%3C0331:ASARSO%3E2.0.CO;2)
- Schulze D.J., Canil D.M., Channer D.M.D., Kaminsky F.V. (2006) Layered mantle structure beneath the western Guyana Shield, Venezuela: Evidence from diamonds and xenocrysts in Guaniamo kimberlites. *Geochimica et Cosmochimica Acta*, Vol. 70, No. 1, pp. 192–205, <http://dx.doi.org/10.1016/j.gca.2005.08.025>
- Shigley J.E., Breeding C.M. (2013) Optical defects in diamond: A quick reference chart. *G&G*, Vol. 49, No. 2, pp. 107–111, <http://dx.doi.org/10.5741/GEMS.49.2.107>
- Smith B.M., Walter J.W., Bulanova G.P., Mikhail S., Burnham A.D., Gobbo L., Kohn S.C. (2016) Diamonds from Dachine, French Guiana: A unique record of early Proterozoic subduction. *Lithos*, Vol. 265, pp. 82–95, <http://dx.doi.org/10.1016/j.lithos.2016.09.026>
- Spencer S. (2007) *A Dream Deferred: Guyana, Identities Under the Colonial Shadow*. Hansib Publications, London.
- Tappert R., Stachel T., Harris J.W., Muehlenbachs K., Brey G.P. (2006) Placer diamonds from Brazil: Indicators of the composition of the Earth’s mantle and the distance to their kimberlitic sources. *Economic Geology*, Vol. 101, No. 2, pp. 453–470, <http://dx.doi.org/10.2113/gsecongeo.101.2.453>
- Tassinari C.C.G. (1997) The Amazonian Craton. In M.J. De Wit and M.J. Ashwal, Eds., *Greenstone Belts*. Clarendon Press, Oxford, pp. 558–566.
- Taylor R. (1999) Gem News: A visit to Venezuelan diamond mines. *G&G*, Vol. 35, No. 4, pp. 209–210.

For online access to all issues of GEMS & GEMOLOGY from 1934 to the present, visit:

[gia.edu/gems-gemology](http://gia.edu/gems-gemology)



# THE SHAPE OF EKANITE

Lutz Nasdala, K.A. Geeth Sameera, G.W.A. Rohan Fernando, Manfred Wildner, Chutimun Chanmuang N., Gerlinde Habler, Annalena Erlacher, and Radek Škoda

Despite its high thorium content, and consequent radioactivity, ekanite is still commonly traded in the Sri Lankan gem market. Gem-quality ekanite is derived from several gravel deposits in the country. However, rough specimens do not show rounded shapes that would be expected for stones transported by water; rather, they have remarkably uneven surfaces with multitudes of hollows, bumps, and cavities. Only after the recent discovery of ekanite in its host calc-silicate rock near Ampegama, Southern Province, can the striking shapes be understood. Fluid-driven alteration of ekanite, still inside the host rock, results in the formation of banded nodules with heterogeneous disintegration rims of an earthy consistency. These rims are readily removed by weathering, whereas the interior remnant consisting of chemically and physically resistant, unaltered ekanite persists.

In secondary gem deposits in Sri Lanka, ekanite is a rare mineral, but when found, it frequently occurs with gem characteristics. Rough pebbles have remarkable outer shapes that show concave dents and hollows (figure 1). Apart from its shape, the gemological properties of ekanite resemble those of the borosilicate kornerupine. The most highly valued stones from Sri Lankan deposits are clear, transparent, and show a vivid yellowish green that is reminiscent of the tender leaves of banana plants (figure 2). Most ekanite specimens are rich in inclusions and show a turbid aspect and in some cases four-rayed asterism (Gübelin, 1961). Ekanite (ideally  $\text{Ca}_2\text{ThSi}_8\text{O}_{20}$ ) is a phyllosilicate whose thorium content of about 24 wt.%, along with minor uranium, causes harmful radioactivity (Tennakone, 2011) that makes stones unsuitable for setting in daily-worn jewelry, though different assessments seem to exist. Ashbaugh (1988) found that gem ekanite is tens of times more radioactive than “low zircon” stones of comparable weight. Gübelin (1961) came to the conclusion that ekanites could be worn in jewelry without any greater harm, whereas De Silva (2008) mentioned “three reported deaths due to keeping ekanites at close proximity to three gem dealers.” High-quality faceted ekanites are nevertheless highly sought-after collector items, even though prospective buyers should exercise safe handling.

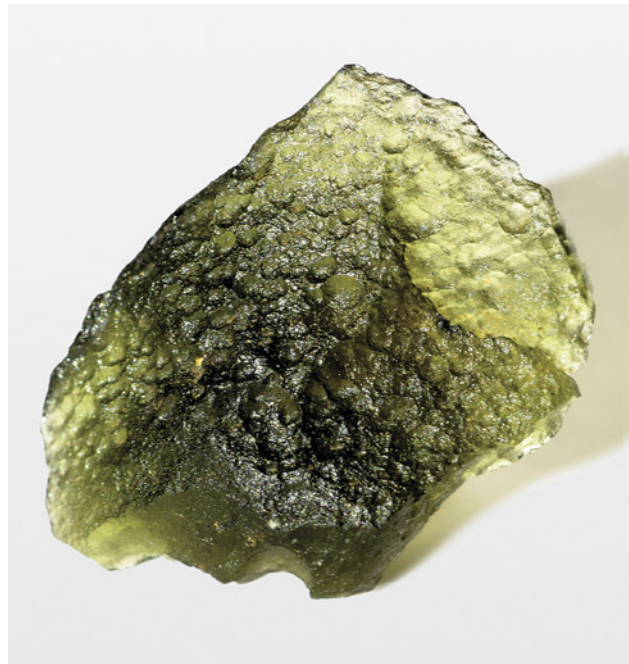


Figure 1. This specimen (2.95 g, 22 mm in longest dimension) from Ellawala, Sabaragamuwa Province, shows the typical surface texture of rough ekanite found in Sri Lankan placers. Photo by Manfred Wildner.

Ekanite is named after its discoverer, Francis Leo Danvil Ekanayake (1898–1971), a Colombo-based customs officer and Fellow of the Gemmological Association of Great Britain. Ekanayake’s contemporaries considered him a capable and painstaking gemologist with a flair for the unusual (Mitchell,

See end of article for About the Authors and Acknowledgments.

GEMS & GEMOLOGY, Vol. 58, No. 2, pp. 156–167,

<http://dx.doi.org/10.5741/GEMS.58.2.156>

© 2022 Gemological Institute of America

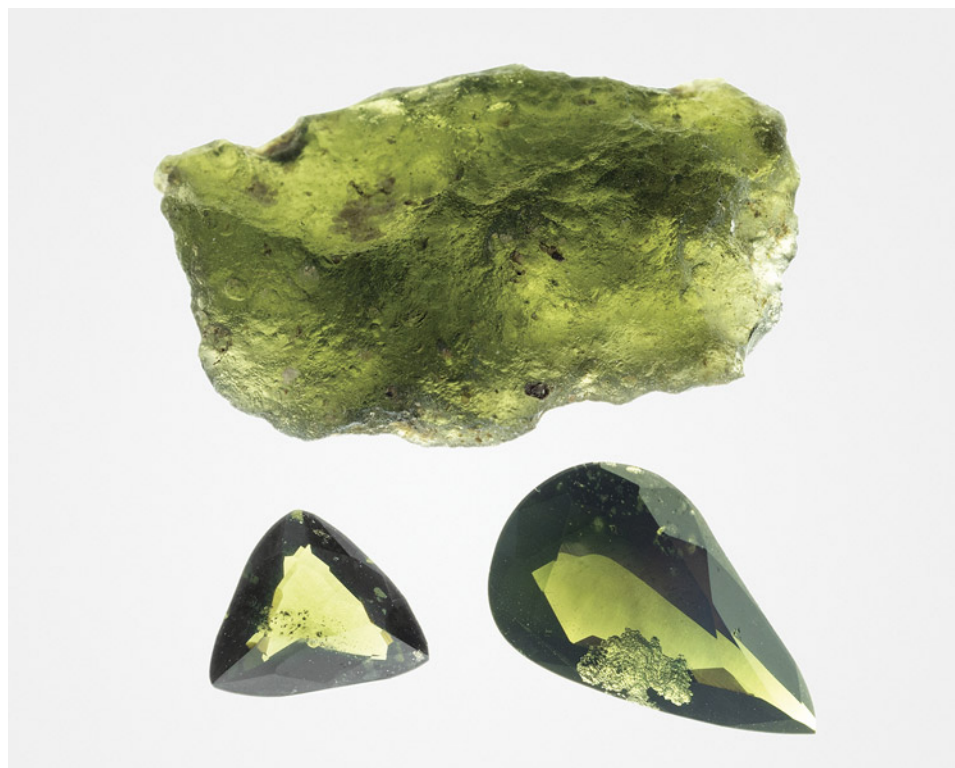


Figure 2. In transmitted light, many ekanite specimens show an attractive yellowish green color. The rough stone (2.90 g) measures 20 mm in longest dimension and the cut stones are 0.65 ct and 2.73 ct. All the specimens originate from placers near Okkampitiya, Uva Province. Photo by Manfred Wildner.

1961), in addition to being well-versed in rare gem minerals (Gübelin, 1961). In 1953, Ekanayake came across two unusual glassy cabochons in the local Colombo gem market that originated from a riverbed gem pit near Ellawala. Immediately he was convinced he had found a new gem species, whereas others considered the material to be devitrified natural or antique glass (Mitchell, 1954). Ekanayake's conviction was supported by the observation that the material, despite being a glass, contained numerous acicular inclusions having crystallographic orientation (Mitchell, 1961). Investigations continued for more than seven years, until a note describing the new mineral was published (Anderson et al., 1961).

The original ekanite was characterized as metamict by Anderson et al. (1961). The notion of metamict goes back to Brøgger (1893), who used *metamikte* to describe a class of minerals that show well-shaped crystal forms despite being amorphous. Today, the term is applied irrespective of the outer form to delineate minerals that were initially crystalline but transformed to a glassy state due to internally or externally sourced irradiation over time (Hamberg, 1914; Ewing et al., 1987; Ewing, 1994). It took more than two decades after the initial description until a non-metamict ekanite (tetragonal space group *I422*) was found in the Tombstone Mountains of Canada's Yukon Territory (Szymański et al., 1982).

Over the intervening years, ekanite has been discovered in several other localities in Sri Lanka (Disanayake and Rupasinghe, 1993; Mathavan et al., 2000; Nasdala et al., 2017; Sameera et al., 2020a,b; see figure 3) and other countries (e.g., Demartin et al., 1982; Walstrom and Dunning, 2003; Russo et al.,

### In Brief

- Despite being found in gravel deposits, Sri Lankan gem ekanites do not show rounded but remarkably uneven shapes.
- Only recently, ekanite was found in its calc-silicate host rock.
- Here, ekanites show features of fluid-driven alteration progressing inward, and botryoidal growth of alteration products leads to convex surface shapes of the product-phase aggregates.
- After weathering of the alteration products, chemically durable ekanite remnants having concave surface features are left.

2013). One remarkable feature of Sri Lankan ekanite is that most specimens, unlike other gems in placer deposits, are not water-worn crystals or rounded pebbles. Rather, the rough material typically shows



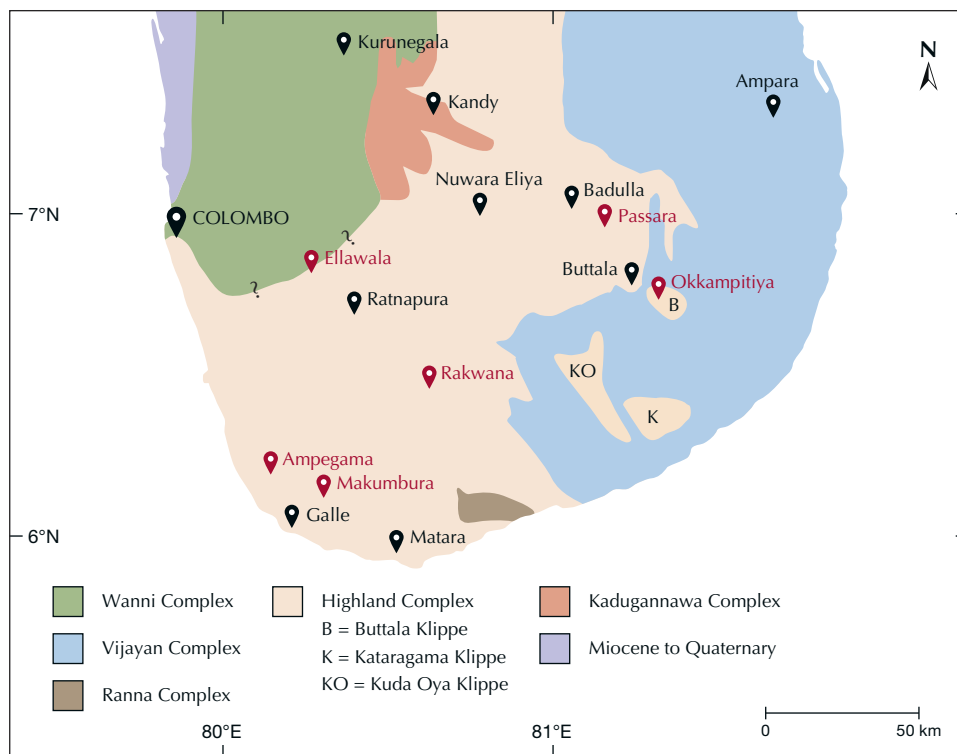


Figure 3. Simplified geological map of southern Sri Lanka (modified from Mathavan and Fernando, 2001; Kröner et al., 2013). Locations of ekanite occurrences are highlighted in red (major cities are in black). Question marks between Highland Complex and Wannai Complex were adopted from the original references; they indicate that the boundary is uncertain and merely inferred based on field evidence.

shapes that—along with the green color—bear a strong resemblance to moldavite-type tektite (see again figure 1; compare to Bouška, 1994; Hyršl, 2015). The underlying causes of the rough surface textures in ekanite are discussed in the present paper, along with an explanation of why attempts by local gem dealers to enhance ekanite by heat treatment invariably fail.

### SAMPLES AND EXPERIMENTAL METHODS

The authors have studied ekanite fragments and ekanite-containing specimens of calc-silicate rock we collected in a quarry near Ampegama (for a brief petrological description, see Sameera et al., 2020a), located about 20 km north-northwest of the city of Galle in Southern Province (see again figure 3). Ekanite specimens from Ellawala in Sabaragamuwa Province and Okkampitiya in Uva Province were photographed to illustrate the typical shapes of this mineral in Sri Lankan gem placers. These are the lead author's samples, purchased from local miners.

Four Ampegama rock samples containing ekanite were impregnated with Araldite epoxy and cut using a diamond saw blade. A polished section and an exposed 25 mm thin section attached to a glass slide were produced from each rock sample. Thin sections were carbon-coated for back-scattered electron (BSE) imaging and electron probe micro-analysis (EPMA), as described below. In addition, double-side polished

plane-parallel sections (250 and 1020  $\mu\text{m}$  thickness) were prepared from a separated ekanite fragment. After measuring the refractive index and obtaining optical absorption spectra, the slabs were heat-treated in air (the 250  $\mu\text{m}$  slab at 1400°C and the 1020  $\mu\text{m}$  slab at 750°C) for 48 h. After gentle repolishing, even the (now dull) 250  $\mu\text{m}$  slab was found to be still too thick for optical absorption spectroscopy and therefore thinned to 110  $\mu\text{m}$  thickness. After we obtained another optical absorption spectrum, this slab was embedded in epoxy and subjected to chemo-mechanical repolishing with an alkaline colloidal silica suspension on a polyurethane plate, for the removal of potential near-surface strain. After being coated with carbon, it was subjected to forward-scattered electron (FSE) imaging, as described below.

Specific gravity was determined by weighing three ekanite chips in distilled water and in air. A drop of liquid detergent was added to the distilled water to decrease surface tension. Refraction of the polished slab was measured using a Krüss ER601-LED refractometer equipped with a diode lamp emitting 589 nm light. Both measurements were repeated five times.

Macroscopic luminescence images were taken using a long-wave UV lamp or 385 nm LED illumination. Photomicrographs of thin sections (including optical images in plane-polarized transmitted-light mode and luminescence images in reflected-light mode)

were obtained by means of a modified Olympus BX-series microscope equipped with a USH-103OL mercury burner and DP 70 digital camera, using a UV-transmissive XL Fluor 4×/340 objective (numerical aperture 0.28). Here, luminescence images were obtained with a beam splitter and filters in the optical pathway that allowed us to illuminate the sample with UV light (<370 nm wavelength) and to photograph only the sample's visible emissions (>400 nm wavelength). BSE and FSE images were obtained in an FEI Quanta 3D FEG dual-beam field-emission gun scanning electron microscope (FEG-SEM) operated at 15 kV and 4 nA. The sample tilt was 70°, and the FSE detector position was adjusted to yield predominant orientation contrast. For the basic principles of FSE orientation-contrast imaging, see Prior et al. (1996).

Major-element analyses were done using wavelength-dispersive X-ray spectrometry on a Cameca SX 100 EPMA system operated at 15 kV. The beam current was set to 20 nA for analyzing unaltered (or "fresh") ekanite and 10 nA for alteration products. The focal-spot diameter of the electron beam was 8–10 µm. The following minerals and synthetic materials were used for calibration (lines analyzed and peak counting times are quoted in parentheses): andalusite (Al-Kα, 20 s), wollastonite (Si-Kα, 20 s; Ca-Kα, 20 s), almandine (Fe-Kα, 20 s), vanadinite (Pb-Mα, 120 s), CaTh(PO<sub>4</sub>)<sub>2</sub> (Th-Mα, 20 s) and UO<sub>2</sub> (U-Mβ, 80 s). Background counting times were half of the respective peak counting times. Cameca's Peaksight software, which is based on the method of Ziebold (1967), was used to calculate detection limits. Matrix correction and data reduction were done using the modified φ(ρz) routine of Merlet (1994). Additional EPMA experimental details are described elsewhere (Breiter et al., 2009; Škoda et al., 2015).

Room-temperature optical absorption spectra were obtained using a Bruker IFS66v/S spectrometer equipped with a mirror-optics IR-scope II microscope and quartz beam splitter. The following combinations of light sources and detectors were used: W lamp and Ge detector (for the spectral range 7500–10000 cm<sup>-1</sup>), W lamp and Si detector (10000–20000 cm<sup>-1</sup>), and Xe lamp and GaP detector (20000–26000 cm<sup>-1</sup>). All optical absorption spectra therefore consist of a combination of three sub-spectra, which were aligned to match in absorbance if necessary. Circular areas 200 µm in diameter were analyzed in transmission geometry.

Room-temperature Raman spectra of inclusions in ekanite were obtained from chips and polished sections, and photoluminescence (PL) spectra of the alteration rims were obtained from thin sections.

Analyses were done using a Horiba LabRAM HR Evolution spectrometer. This dispersive system was equipped with an Olympus BX-series optical microscope and a Peltier-cooled, Si-based charge-coupled device detector. Raman spectra of the inclusions in ekanite were excited using a 473 nm diode laser (11 mW at the sample), Raman measurements of the alteration rims were conducted with a 633 nm He-Ne (10 mW) and a 785 nm diode laser (24 mW), and PL was excited using an external, air-cooled 407 nm diode laser (500 mW; unfocused laser beam). The emitted PL and Raman scattered light, respectively, were collected using a 50× objective (numerical aperture 0.50; free working distance 10.6 mm) and dispersed using a diffraction grating with 1800 grooves per millimeter. The spectral resolution was about 1 cm<sup>-1</sup>. More experimental details are described elsewhere (Zeug et al., 2018).

## RESULTS AND DISCUSSION

**General Characterization.** Near Ampegama, ekanite is found as a rare constituent of a calc-silicate metamorphic rock composed primarily of diopside, wollastonite, K-feldspar, and scapolite, occasionally together with minor fluorite and graphite (Sameera et al., 2020a). Ekanite mostly occurs as xenomorphic nodules up to 3 cm in size. Many but not all of them are surrounded by orange to pale brownish alteration rims with an earthy consistency. In fresh conditions, the mineral is vivid olive green to yellowish green. Close to the alteration rims, it may in some cases show discoloration and appear greenish blue (figure 4A). The material is transparent and exhibits conchoidal to uneven fracture. Unaltered ekanite has a vitreous luster and is isotropic. As ekanite is in fact tetragonal, the observed isotropy indicates that the material is present in a metamict (i.e., glassy) state. Its RI was 1.59 ± 0.01, and the SG was determined as 3.27 ± 0.01. Ekanite is apparently non-luminescent under both long-wave and short-wave UV light.

The results of EPMA chemical analyses are summarized in table 1. Ekanite from Ampegama, if unaltered, has a relatively uniform chemical composition that corresponds to the formula Ca<sub>2</sub>Th<sub>0.9</sub>U<sub>0.1</sub>Si<sub>8</sub>O<sub>20</sub> (calculated on the basis of 20 oxygen atoms per formula unit). The composition is fairly similar to that of ekanite from Ellawala (Anderson et al., 1961) and Okkampitiya (Nasdala et al., 2017). To the best of our knowledge, no analysis of ekanite from Rakwana in Sabaragamuwa Province, Passara in Uva Province (both were quoted by Dissanayake and Rupasinghe,

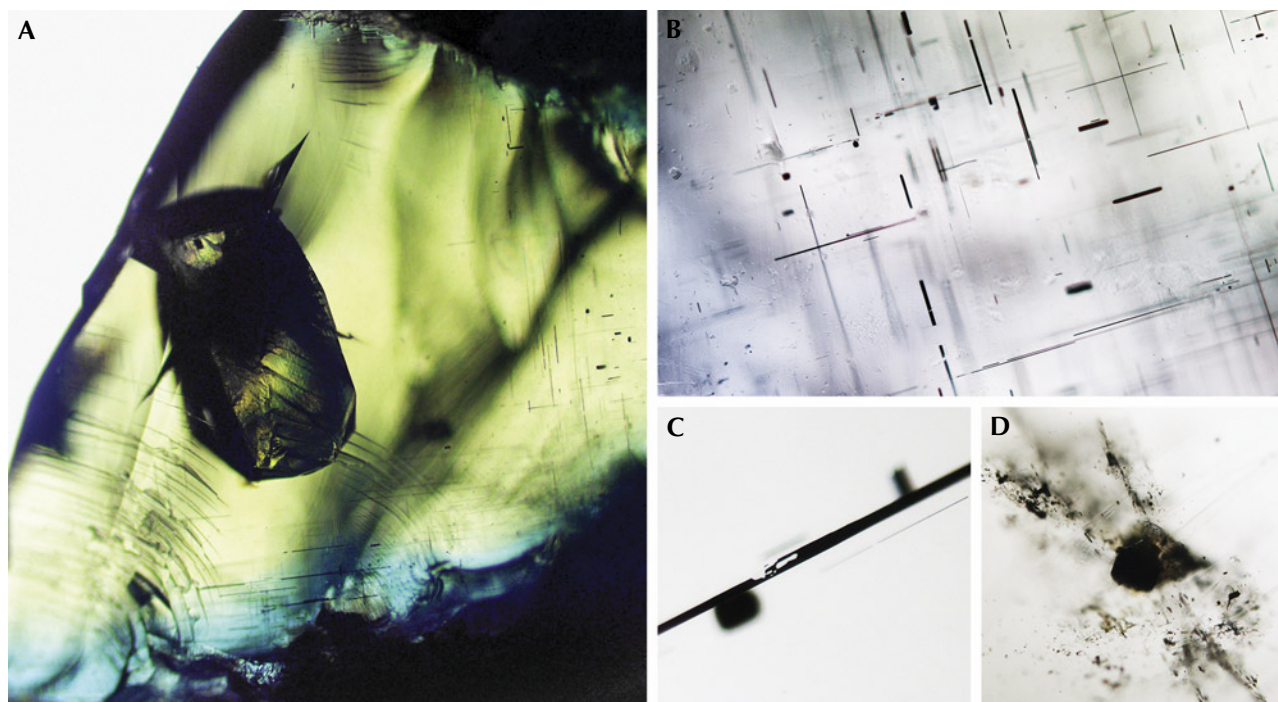


Figure 4. A: Transmitted-light photo of a rough ekanite (field of view 6 mm) from Ampegama with alteration-induced discoloration and characteristic conchoidal fracture. It contains a large K-feldspar and numerous acicular inclusions. B: Needles in the glassy host have a crystallographically controlled orientation conforming to the host's previously tetragonal symmetry (field of view 1.6 mm). C: Partially filled hollow needle (field of view 120  $\mu\text{m}$ ). D: Xenomorphic thorite inclusion associated with silica glass, wollastonite, and apatite (field of view 630  $\mu\text{m}$ ). Photomicrographs by Chutimun Chanmuang N.

1993), or Makumbura in Southern Province (Sameera et al., 2020b) has been undertaken thus far.

Concordant  $^{206}\text{Pb}/^{238}\text{U}$  and  $^{207}\text{Pb}/^{235}\text{U}$  ratios of ekanite from Okkampitiya (Nasdala et al., 2017) indicate

**TABLE 1.** Mean chemical composition (in wt.%) of Ampegama ekanite and its alteration products, obtained by EPMA analysis.

Major oxides <sup>a</sup>	Unaltered ekanite (n = 13)	Alteration rim (colorless) (n = 6)	Alteration rim (brownish) (n = 7)	Detection limit
Al <sub>2</sub> O <sub>3</sub>	0.13 ± 0.01 <sup>ab</sup>	0.30 ± 0.33	0.14 ± 0.04	0.03
SiO <sub>2</sub>	56.2 ± 0.3	43.3 ± 1.4	51.8 ± 7.6	0.03
CaO	13.26 ± 0.11	9.82 ± 0.33	8.13 ± 4.26	0.05
FeO	0.23 ± 0.03	0.33 ± 0.03	0.18 ± 0.11	0.07
PbO	0.81 ± 0.05	0.83 ± 0.23	0.52 ± 0.17	0.10
ThO <sub>2</sub>	27.5 ± 0.5	35.0 ± 0.4	27.5 ± 2.8	0.13
UO <sub>2</sub>	2.61 ± 0.63	3.61 ± 0.32	2.76 ± 1.93	0.19
Total	100.7 ± 0.6	93.3 ± 1.3	91.1 ± 3.4	

<sup>a</sup>The elements F, Na, Mg, P, Sc, Ti (all 0.05), Mn (0.07), Sr (0.15), Y (0.08), Zr (0.11), La (0.15), Ce (0.16), Pr (0.24), Nd (0.23), and Sm (0.12) were also sought for, but mean concentrations were below the EPMA detection limits (values in brackets, in wt.%).

<sup>b</sup>All errors are quoted at the 2 $\sigma$  level.

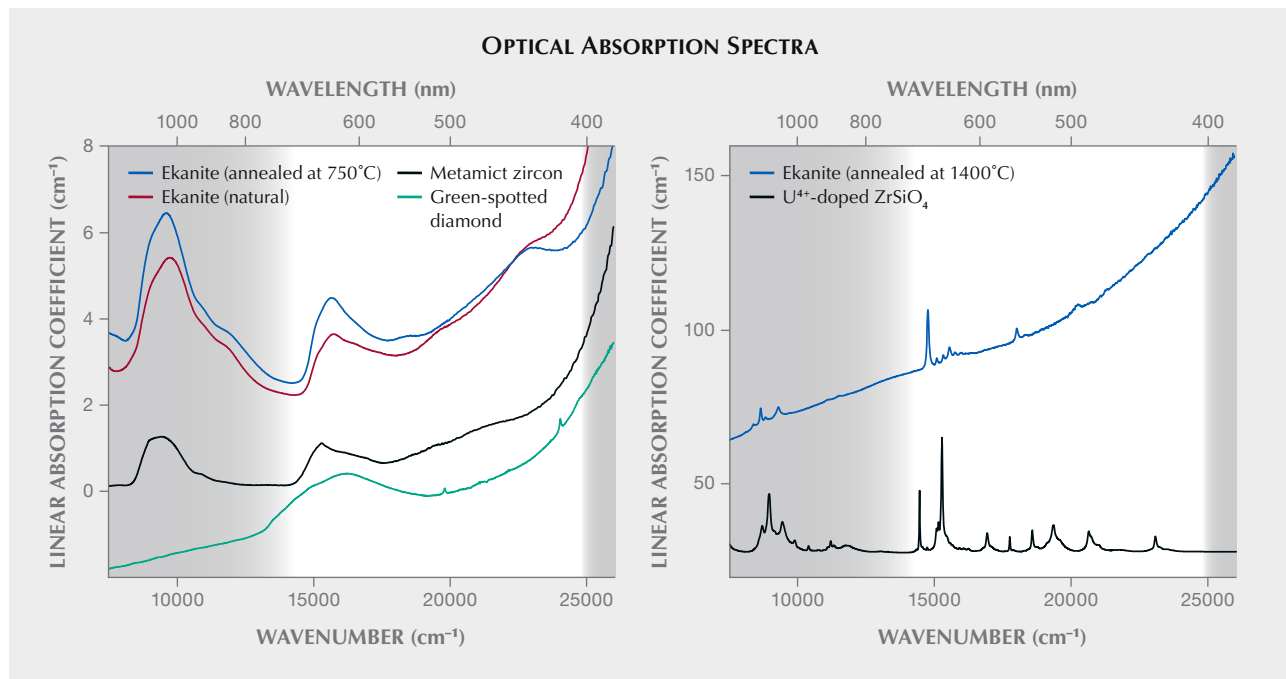
that lead is mainly radiogenic and hence was widely excluded during the primary growth of this mineral. Assuming the same is true for the Ampegama ekanite, the measured mean concentrations of thorium (24.2 wt. %), uranium (2.30 wt. %), and lead (0.75 wt. %; converted from the respective oxide concentrations quoted in table 1) are converted to a “chemical age” (Montel et al., 1996; Suzuki and Kato, 2008) of roughly 525 Ma. From this age and present thorium and uranium concentrations, and using the equation of Murakami et al. (1991), a time-integrated self-irradiation dose of  $14.0 \times 10^{19}$  alpha events per gram of material is calculated. This value exceeds the threshold of Sri Lankan zircon to alpha-event amorphization (Zhang et al., 2000; Nasdala et al., 2002) by about one order of magnitude. It explains the present glassy state of ekanite as resulting from extensive radioactive self-irradiation of initially tetragonal ekanite over long time periods.

This assignment is also supported by microscopic observations. Similar to ekanite from Ellawala (Mitchell, 1961; Gübelin, 1961), the Ampegama ekanite contains numerous acicular fluid and two-

phase inclusions that show a crystallographically controlled orientation of needles with the long axes at 90° angles to each other (figure 4, A and B). This is explained by the primary formation of tetragonal ekanite with crystallographically oriented inclusions within the host crystal, followed by irradiation-induced vitrification of ekanite that did not affect the orientations of the inclusions. Some of the needles are filled incompletely (figure 4C). Solid inclusions of irregular shape (figure 4D), determined by Raman spectroscopy, include thorite, quartz and silica glass, K-feldspar, apatite, wollastonite, and calcite.

**Optical Absorption and Heat Treatment.** Optical absorption spectra obtained from a natural ekanite slab and its heat-treated analogues are presented in figure 5. The green color of natural (metamict) ekanite is due to two main spectral features. First, there is an absorption continuum, tentatively assigned to defect-related “color centers” (see, for instance, Greenidge, 2018), that gradually increases toward the blue-violet-UV range of the electromagnetic spectrum. Second, there

Figure 5. Optical absorption spectra of green metamict ekanite, its analogue annealed at 750°C (left; sample thicknesses 1.02 mm), and a brownish green chip that was annealed at 1400°C (right; sample thickness 110 µm). The reference spectrum of a green “low zircon” was obtained from sample N-17 (described in detail by Nasdala et al., 2002). The reference spectrum of irradiation-spotted diamond is from Nasdala et al. (2013) and that of U<sup>4+</sup>-doped ZrSiO<sub>4</sub> from Zeug et al. (2018). Reference spectra are presented on an arbitrary absorbance scale. Spectral ranges that are invisible to the human eye have gray background shade. Note the vast increase of the linear absorption coefficient after high-temperature treatment of ekanite.



is a pronounced absorption band in the red to orange range whose maximum lies near  $15700\text{ cm}^{-1}$  (637 nm wavelength). This band could be assigned to  $\text{Fe}^{2+}$  or  $\text{Fe}^{2+}\text{--Fe}^{3+}$  charge transfer (Smith, 1978; compare to Tenakone, 2011), which appears rather unlikely, however, because of the low iron concentration of 0.18 wt.% (converted from the FeO content of 0.23 wt.% quoted in table 1). Note that Okkampitiya ekanite (see again figure 2) is vivid yellowish green in spite of its even lower iron content of only 0.11 wt.% (Nasdala et al., 2017). Alternative assignments of the red-orange band include the—strongly broadened—analogue of the main  $\text{U}^{4+}$  absorption band in zircon (Kempe et al., 2016), or an analogue of defect absorption in diamond (GR1 = neutral carbon vacancy; Clark and Walker, 1973; Nasdala et al., 2013) or zircon (electron-hole defect; Kempe et al., 2016). In the case of the latter, it appears likely that the red-orange absorption band of metamict ekanite is assigned to an oxygen-site vacancy. Clarification of the issue might require synthetic ekanite to be subjected to ion-irradiation experiments.

The green color is explained by the joint effect of a short-wavelength absorption continuum and a red-orange band that bracket a “reduced absorption window” in the green to yellow range, at around  $17850\text{ cm}^{-1}$  (560 nm). The fact that ekanite also transmits well in the long-wavelength range below  $15000\text{ cm}^{-1}$  (above 665 nm) does not significantly affect the coloration, because of the relatively poor sensitivity of the human eye in this spectral range.

Although Sri Lankan ekanite typically has green hues that are quite attractive for gem purposes, local dealers have undertaken several—always ineffective—attempts to enhance its color by heating. Published results on how metamict ekanite responds to heating are decidedly contradictory. According to Anderson et al. (1961), recrystallization of the metamict material to a tetragonal phase with a body-centered unit cell occurs in the range  $650\text{--}1000^\circ\text{C}$ . This unit cell was later assigned to “true crystalline ekanite” by Szymański et al. (1982). At temperatures above  $1000^\circ\text{C}$ , Anderson et al. (1961) observed remelting and formation of huttonite ( $\text{ThSiO}_4$ ). In contrast, Zeug et al. (2015) found that ekanite remains glassy and transparent up to  $900^\circ\text{C}$ , while the yellowish green color becomes slightly more bluish (see also figure 5, left). Zeug et al. (2015) detected initial nucleation of several poorly ordered phases only at around  $1000^\circ\text{C}$ . Between  $1100$  and  $1450^\circ\text{C}$ , crystalline ekanite formed, without any sign of melting. The  $1450^\circ\text{C}$  annealing product was identified as ekanite using X-

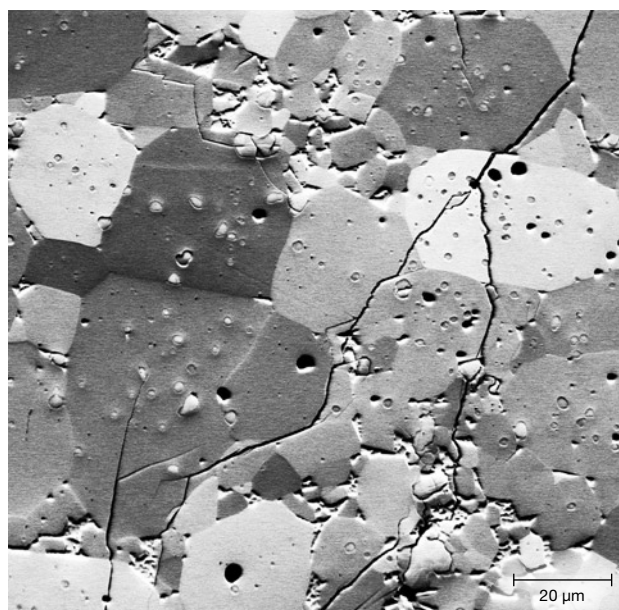


Figure 6. Forward-scattered electron (FSE) image of ekanite annealed at  $1400^\circ\text{C}$  showing predominantly crystal-orientation contrast. The majority of the flawed material ( $>98\text{ vol.}\%$ ) consists of polycrystalline ekanite whose individual polygonal crystals have diverse orientations, indicated by different levels of gray. Image by Gerlinde Habler.

ray powder diffraction and Raman spectroscopy (Nasdala et al., 2017). In agreement with this latter result, heating of Ampegama ekanite to  $750^\circ\text{C}$  in the present study did not affect the metamict state, and heating to  $1400^\circ\text{C}$  yielded polycrystalline, tetragonal ekanite.

Recrystallized ekanite has an unattractive appearance, as it is brownish green to pale brownish and non-transparent. Mitchell (1961) described it as “putty-colored.” Compared to the transparent metamict starting material, the increase of the absorption continuum toward low wavelengths is depleted, and the total absorbance is about 30–40 times higher (figure 5, right). There are a number of narrow lines we assign to tetravalent uranium, based on their similarity to the absorption of  $\text{U}^{4+}$  in zircon (compare to Richman et al., 1967; Mackey et al., 1975). The huge increase in total absorbance, visually recognizable from the loss of transparency, is assigned to the transformation of a glass to a polycrystalline compound. The texture of the annealing product is visualized through FSE imaging (figure 6): The material consists mainly of numerous polygonal, variably oriented ekanite crystals up to 50 nm in size. Minor phases ( $\text{USiO}_4$ , silica,  $\text{Ca}_3\text{Si}_3\text{O}_9$ , and others) occur as inclusions inside the ekanite crystals or along grain boundaries. Note that in initial recrystallization stages in a glassy phase, nucleation of other

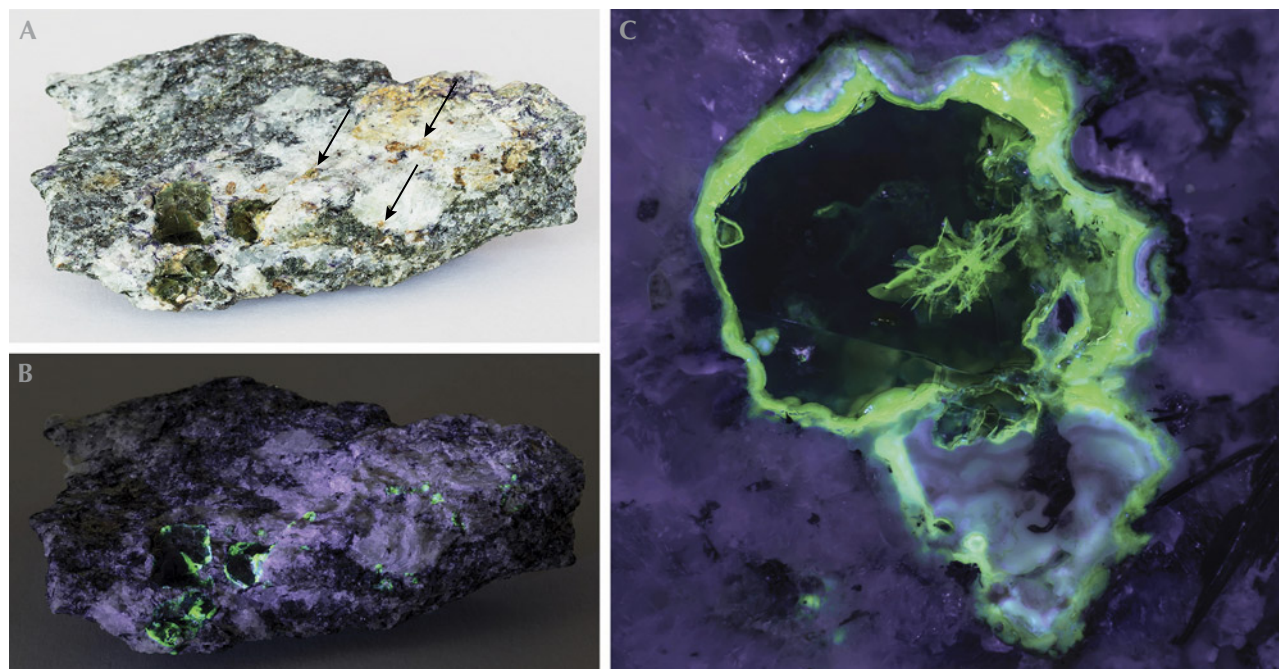
phases may be energetically favored (Capitani et al., 2000). Also, high-temperature heating typically causes loss of the radiogenic lead, which in turn disturbs the initial equilibrium of Th+U+Pb with Ca and Si. Slight deviation of the total composition from that of ekanite necessarily leads to minor formation of other phases (for analogous effects in the annealing of zircon, see Nasdala et al., 2002). Both the presence of nanocrystals of these additional phases and the high number of grain boundaries of fine-grained ekanite aggregates cause loss of transparency and increased absorption. In summary, heating of metamict ekanite below the temperature of spontaneous nucleation (about 1000°C) has minor effects, whereas high-temperature annealing of the material leads to the formation of a dull, polycrystalline compound. The latter is therefore ill-advised in attempting enhancement.

**Study of Alteration Products.** In the host rock, green ekanite is typically surrounded (or even completely replaced) by yellowish gray to ochre assemblages of secondary phases (figure 7A). These phases are interpreted as products of fluid-driven alteration processes,

which is supported by their strongly deficient EPMA totals (table 1). Deficient analytical totals of alteration products may be caused by the presence of light elements that are not analyzed in the EPMA, and they may also be due to their common sub-micrometer porosity (Pointer et al., 1988; Nasdala et al., 2009).

In plane-polarized transmitted light (figure 8), the alteration rims appear heterogeneous, often with a banded texture, and consist of colorless and brownish domains and zones. Compared to unaltered ekanite, the colorless alteration phase is strongly depleted in silicon and calcium, whereas thorium is notably enriched (table 1). The brownish domains show pronounced heterogeneity. Some yield lower and others higher BSE intensity, compared to the neighboring unaltered ekanite (figure 8, far left images). Correspondingly the chemical composition of the brownish domains is decidedly heterogeneous, indicated by large standard deviations from the mean values (table 1). In cross-polarized transmitted light (figure 8), the colorless alteration material does not show any interference color, indicating that it has a glassy structure. The majority of brown regions, in contrast, show low

Figure 7. A: Hand-specimen (width 10.5 cm) of calc-silicate rock from Ampegama, containing several clear, dark bottle-green ekanite nodules surrounded by yellow-to-ochre alteration products. Some smaller nodules are altered completely (three are marked by arrows). B: Only the alteration products show intense greenish luminescence under the long-wave UV lamp. C: PL image of a polished rock specimen (field of view 14 mm) obtained under 385 nm LED illumination. Alteration of the central metamict ekanite has started from the outer rim and internal fractures. Photos by Manfred Wildner.



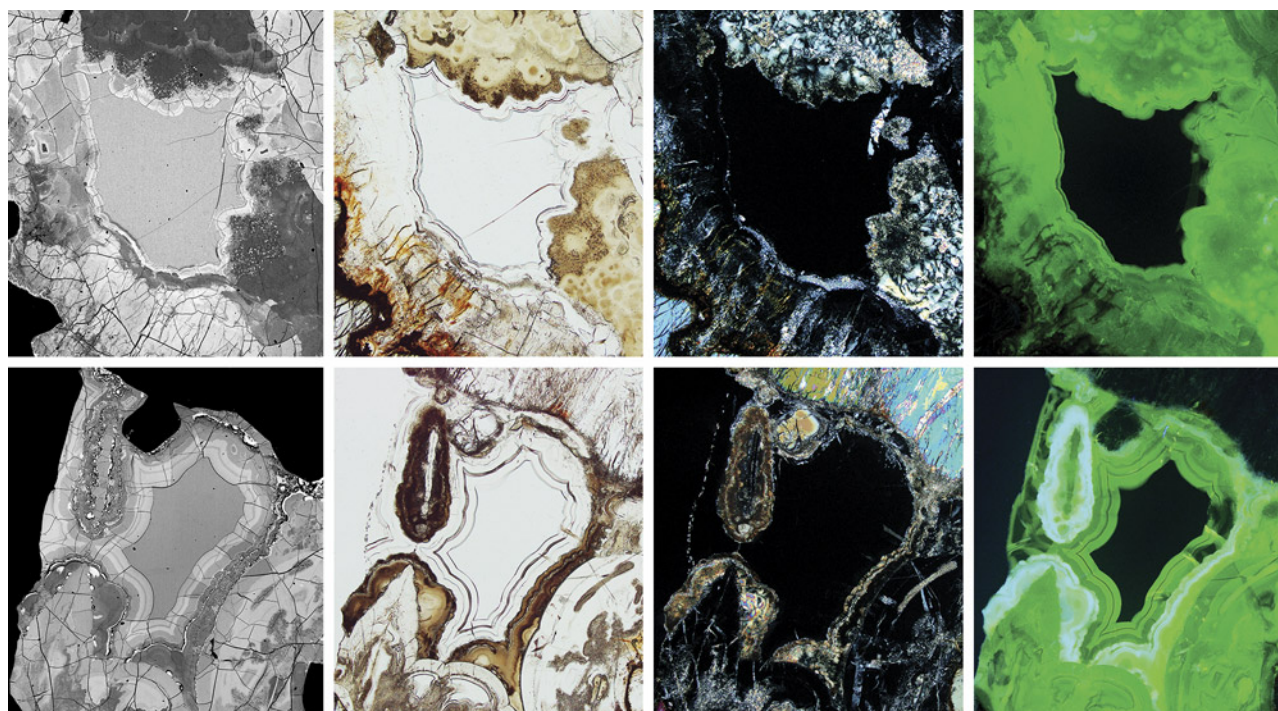


Figure 8. Two series of BSE, plane-polarized transmitted-light, cross-polarized transmitted light, and PL images (from left to right) showing heterogeneous alteration rims surrounding fresh metamict ekanite in the center. The alteration rims emit intense green, uranyl-related photoluminescence. 30  $\mu\text{m}$  thin section; field of view 1.72 mm. BSE images by Chutimun Chanmuang N., all others by Lutz Nasdala.

birefringence. In some of the dark brown regions (figure 8, bottom row), aragonite was detected, whereas the identification of all other alteration material using Raman spectroscopy failed, as no evaluable band patterns were obtained. Interestingly, there is no significant lead loss in the alteration products, compared to fresh ekanite. The virtually unvaried presence of lead in the alteration products may indicate either that these phases did not exclude lead upon formation or that alteration occurred soon after ekanite formation, with subsequent transformation of thorium and uranium to lead in the alteration products themselves. Further investigations will be needed to address this issue.

Most of the alteration products show distinct greenish luminescence under UV or violet-blue excitation, while the fresh ekanite appears inert (figures 7 and 8). A representative PL spectrum is presented in figure 9. We assign the broad-band green emission to hexavalent uranium ions that are present in the form of  $(\text{UO}_2)^{2+}$  (i.e., uranyl) groups. The observation of green, uranyl-related emission is consistent with significant concentrations of uranium and relatively low concentrations of iron in the alteration products (table 1; compare to Gaillou et al., 2008). Only aragonite-containing zones yield even more intense PL

(figure 8, far bottom right image); here the green uranyl-related band is overlain by a broad band in the orange-red range whose cause remains unknown.

The PL spectra of many, but not all, uranyl-containing crystalline minerals show a pattern consisting of energetically equidistant bands (Gorobets and Sidorenko, 1974; deNeufville et al., 1981; Wang et al., 2008). Such patterns are also observed from natural opal (Fritsch et al., 2015; Othmane et al., 2016), synthetic glasses (Mahurin et al., 2003), and even uranyl ions and complexes in solutions (McGlynn and Smith, 1961; Moulin et al., 1995). For comparison, we collected the PL spectra of the uranyl-containing species metatobernite, hyalite, and a uranyl glass under the same conditions (figure 9). Thus, the presence or absence of a pattern of equidistant bands does not depend on the host's crystallinity. Such patterns are assigned to the coupling of electronic transitions with oscillations of the linear  $\text{O}=\text{U}=\text{O}$  groups. Energetic differences among neighboring bands depend on the frequencies of uranyl stretching vibrations and hence allow the calculation of  $\text{U}=\text{O}$  bond distances (Jones, 1959). The observation that the studied alteration rims yield non-structured emission is ascribed to an overlay of many vibrational modes, due to extensive irregularity of  $\text{U}=\text{O}$  bonds caused by exten-

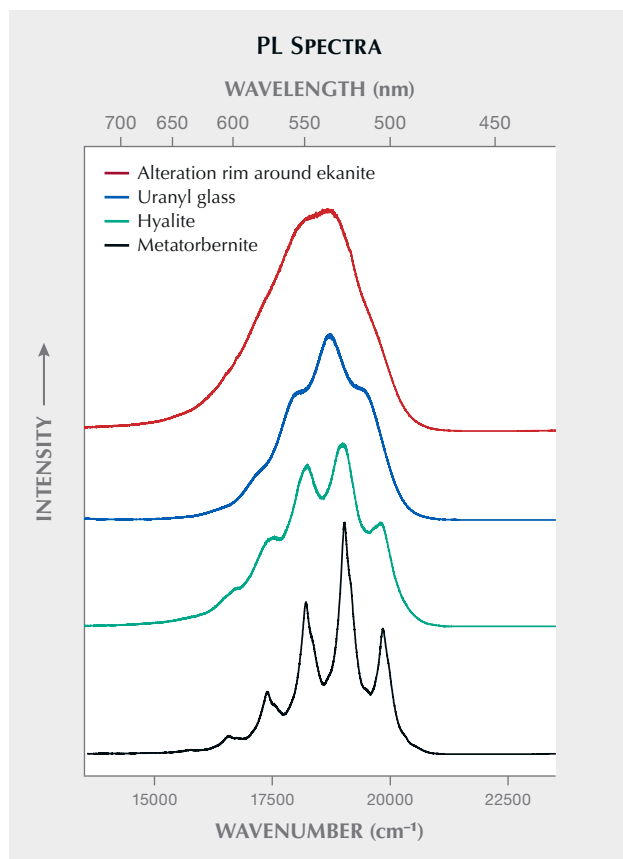


Figure 9. PL spectrum (407 nm excitation) of the green-luminescing alteration rim surrounding ekanite, compared with the spectra of three other uranyl-bearing substances.

sively irregular arrangements of nearest neighbor atoms in the glassy structure.

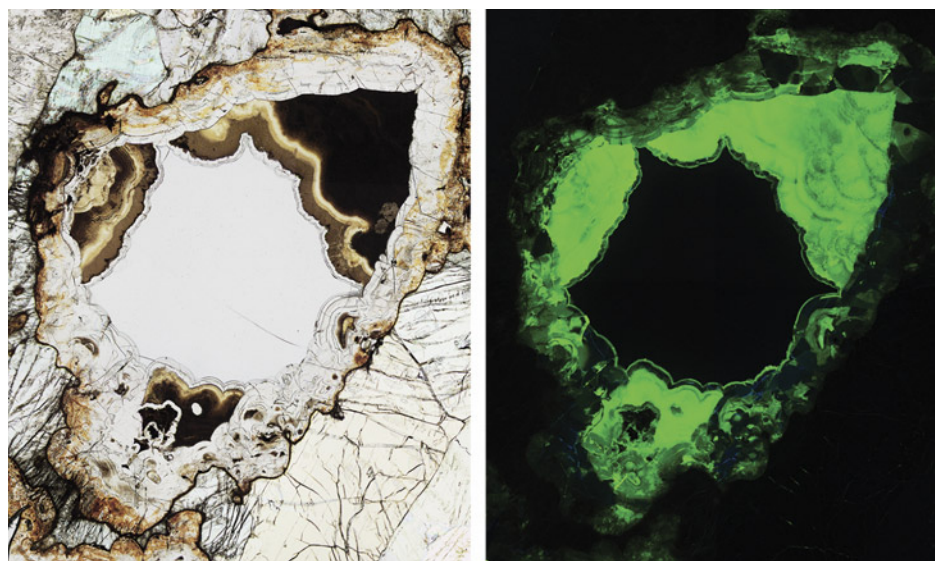


Figure 10. Pair of plane-polarized transmitted-light (left) and photoluminescence (right) photomicrographs of a strongly altered ekanite nodule in its host calc-silicate rock (30  $\mu\text{m}$  thin section). The central, well-preserved remnant of metamict ekanite is colorless and non-luminescent; its irregular shape corresponds to that of rough specimens found in placers. Photomicrographs by Lutz Nasdala; field of view 5.1 mm.

In optical microscopy, the practical benefit of the intense uranyl luminescence of the alteration products is that the shape of the central remnant of fresh ekanite, which does not luminesce, is easily recognized (figure 10). The latter exhibits concave surface features analogous to that of rough ekanite specimens (compare to figure 1). The formation of concave surfaces is therefore explained by the alteration of ekanite in its host rock, whose identity for all secondary deposits remains unknown. Fluid-driven alteration presumably has progressed inward, resulting in concentrically grown reaction rims of secondary phases, at the expense of primary ekanite.

## CONCLUSIONS

The physical properties, chemical composition, and general appearance of Ampegama ekanite are broadly similar to ekanite from other Sri Lankan locations, except that the material is not found in a secondary deposit but *in situ*. In the calc-silicate host rock, fluid-driven chemical alteration decomposes primary ekanite, and the botryoidal growth of alteration products leads to convex surface shapes of the product-phase aggregates, which in turn result in the concave shapes of the ekanite remnant. It is a simple conclusion by analogy that the same may have happened in the (still unknown) host rocks of ekanite found near Ellawala and Okkampitiya. After weathering of the host rock, the soft and earthy alteration products are effectively removed, leaving behind rough ekanite with their dimpled surface patterns. As rough ekanite specimens found near Ellawala and Okkampitiya gen-



erally show high degrees of preservation of such surface features, in most cases virtually without abrasion signs, transport pathways from the point of weather-

ing of the host rock to the place of deposition must be short. Consequently, it appears likely that the ekanite is rather eluvial or colluvial.

#### ABOUT THE AUTHORS

Professor Dr. Nasdala is chairholder for Mineralogy and Spectroscopy, Prof. Dr. Wildner and Dr. Chanmuang N. are researchers, and Ms. Erlacher is a student, at the Institut für Mineralogie und Kristallographie, University of Vienna. Mr. Sameera is a geologist working at the Geological Survey and Mines Bureau in Sri Jayawardenepura Kotte, and student at the Postgraduate Institute of Science, University of Peradeniya. Prof. Dr. Fernando is chairholder for Geology at the Department of Physics, Faculty of Natural Sciences, The Open University of Sri Lanka in Nugegoda. Dr. Habler is a researcher at the Department für Lithosphärenforschung, Vienna University. Dr. Škoda is a researcher at the Department of Geological Sciences, Faculty of Science, Masaryk University in Brno.

#### ACKNOWLEDGMENTS

Most of the samples studied herein were obtained during a February 2020 field trip co-organized by E. Gamini Zoysa. Export permission for rock samples was kindly granted by the Geological Survey and Mines Bureau. Sample preparation was done by Andreas Wagner, Gerald Giester, Christoph A. Hauzenberger, Friedrich Koller, and Robert F. Martin are thanked for helpful discussions. Constructive comments and suggestions of three anonymous peers are gratefully acknowledged. Authors LN and AE acknowledge travel support from the Faculty of Geosciences, Geography and Astronomy, University of Vienna.

#### REFERENCES

- Anderson B.W., Claringbull G.F., Davis R.J., Hill D.K. (1961) Ekanite, a new metamict mineral from Ceylon. *Nature*, Vol. 190, No. 4780, p. 997, <http://dx.doi.org/10.1038/190997a0>
- Ashbaugh C.E. III (1988) Gemstone irradiation and radioactivity. *G&G*, Vol. 24, No. 4, pp. 196–213, <http://dx.doi.org/10.5741/GEMS.24.4.196>
- Bouška V. (1994) *Moldavites: The Czech Tektites*. Stylizace, Prague, 69 pp.
- Breiter K., Copjaková R., Škoda R. (2009) The involvement of F, CO<sub>2</sub>, and As in the alteration of Zr-Th-REE-bearing accessory minerals in the Hora Svaté Kateriny A-type granite, Czech Republic. *The Canadian Mineralogist*, Vol. 47, No. 6, pp. 1375–1398, <http://dx.doi.org/10.3749/canmin.47.6.1375>
- Brøgger W.C.A. (1893) Amorf. In C. Blangstrup et al., Eds., *Salmonsens Store Illustrerede Konversationsleksikon 1*. Brøndene Salmonsens, Copenhagen, pp. 742–743.
- Capitani G.C., Leroux H., Doukhan J.C., Ríos S., Zhang M., Salje E.K.H. (2000) A TEM investigation of natural metamict zircons: Structure and recovery of amorphous domains. *Physics and Chemistry of Minerals*, Vol. 27, No. 8, pp. 545–556, <http://dx.doi.org/10.1007/s002690000100>
- Clark C.D., Walker J. (1973) The neutral vacancy in diamond. *Proceedings of the Royal Society of London A: Mathematical, Physical and Engineering Sciences*, Vol. 334, No. 1597, pp. 241–257, <http://dx.doi.org/10.1098/rspa.1973.0090>
- De Silva N. (2008) Ekanite – discovery of a new rare gemstone by Mr FDL Ekanayake. <http://jewelry-blog.internetstones.com/ekanite-discovery-of-a-new-rare-gemstone-by-mr-fdl-ekanayake/> (accessed April 19, 2022).
- Demartin F., Gramaccioli C.M., Liborio G., Tumaini C. (1982) Ekanite nei proietti vulcanici di Pitigliano (Grosseto). *Rendiconti della Società Italiana di Mineralogia e Petrologia*, Vol. 38, No. 3, pp. 1401–1406.
- deNeufville J.P., Kasdan A., Chimenti R.J.L. (1981) Selective detection of uranium by laser-induced fluorescence: a potential remote-sensing technique. 1: Optical characteristics of uranyl geologic targets. *Applied Optics*, Vol. 20, No. 8, pp. 1279–1296, <http://dx.doi.org/10.1364/AO.20.001279>
- Dissanayake C.B., Rupasinghe M.S. (1993) A prospectors' guide map to the gem deposits of Sri Lanka. *G&G*, Vol. 29, No. 3, pp. 173–181, <http://dx.doi.org/10.5741/GEMS.29.3.173>
- Ewing R.C. (1994) The metamict state: 1993—The centennial. *Nuclear Instruments and Methods in Physics Research Section B: Beam Interactions with Materials and Atoms*, Vol. 91, No. 1–4, pp. 22–29, [http://dx.doi.org/10.1016/0168-583X\(94\)96186-7](http://dx.doi.org/10.1016/0168-583X(94)96186-7)
- Ewing R.C., Chakoumakos B.C., Lumpkin G.R., Murakami T. (1987) The metamict state. *MRS Bulletin*, Vol. 12, No. 4, pp. 58–66, <http://dx.doi.org/10.1557/S0883769400067865>
- Fritsch E., Megaw P.K.M., Spano T.L., Chauviré B., Rondeau B., Gray M., Hainschwang T., Renfro N. (2015) Green-luminescing hyalite opal from Zacatecas, Mexico. *Journal of Gemmology*, Vol. 34, No. 6, pp. 490–508.
- Gaillou E., Delaunay A., Rondeau B., Bouhnik-le-Coz M., Fritsch E., Cornen G., Monnier C. (2008) The geochemistry of gem opals as evidence of their origin. *Ore Geology Reviews*, Vol. 34, No. 1–2, pp. 113–126, <http://dx.doi.org/10.1016/j.oregeorev.2007.07.004>
- Gorbets B.S., Sidorenko G.A. (1974) Luminescence of secondary uranium minerals at low temperatures. *Soviet Atomic Energy*, Vol. 36, No. 1, pp. 5–12, <http://dx.doi.org/10.1007/BF01123095>
- Greenidge D. (2018) Investigations of color center phenomena in topaz and quartz through electron spin resonance with reference to optical absorption and nuclear magnetic resonance: Implications for extended mineral applications. *Malaysian Journal of Fundamental and Applied Sciences*, Vol. 14, pp. 142–149, <http://dx.doi.org/10.11113/mjfas.v14n1-2.958>
- Gübelin E.J. (1961) Ekanite – another new metamict gem from Ceylon. *G&G*, Vol. 10, No. 6, pp. 163–179, 191.
- Hamberg A. (1914) Die radioaktiven Substanzen und die geologische Forschung. *Geologiska Föreningen i Stockholm Förhandlingar*, Vol. 36, No. 1, pp. 31–96, <http://dx.doi.org/10.1080/11035891309449550>
- Hyršl J. (2015) Gem News International: Moldavites: natural or fake? *G&G*, Vol. 51, No. 1, pp. 103–105.
- Jones L.H. (1959) Determination of U-O bond distance in uranyl complexes from their infrared spectra. *Spectrochimica Acta*, Vol. 15, No. 6, pp. 409–411, [http://dx.doi.org/10.1016/S0371-1951\(59\)80333-7](http://dx.doi.org/10.1016/S0371-1951(59)80333-7)
- Kempe U., Trinkler M., Pöppl A., Himcinschi C. (2016) Coloration of natural zircon. *The Canadian Mineralogist*, Vol. 54, No. 3, pp. 635–660, <http://dx.doi.org/10.3749/canmin.1500093>
- Kröner A., Rojas-Agramonte Y., Kehelpannala K.V.W., Zack T., Hegner E., Geng H.Y., Wong J., Barth M. (2013) Age, Nd-Hf isotopes, and geochemistry of the Vijayan Complex of eastern and southern Sri Lanka: A Grenville-age magmatic arc of unknown derivation. *Precambrian Research*, Vol. 234, pp. 288–321,

- <http://dx.doi.org/10.1016/j.precamres.2012.11.001>
- Mackey D.J., Runciman W.A., Vance E.R. (1975) Crystal-field calculations for energy levels of  $U^{4+}$  in  $ZrSiO_4$ . *Physical Review B*, Vol. 11, pp. 211–218, <https://dx.doi.org/10.1103/PhysRevB.11.211>
- Mahurin S.M., Dai S., Schumacher R.F. (2003) Spectroscopic determination of heterogeneities in uranyl-doped glasses. *Journal of Non-Crystalline Solids*, Vol. 325, No. 1-3, pp. 70–75, [http://dx.doi.org/10.1016/S0022-3093\(03\)00364-8](http://dx.doi.org/10.1016/S0022-3093(03)00364-8)
- Mathavan V., Fernando G.W.A.R. (2001) Reactions and textures in grossular-wollastonite-scapolite calc-silicate granulites from Maligawila, Sri Lanka: Evidence for high-temperature isobaric cooling in the meta-sediments of the Highland Complex. *Lithos*, Vol. 59, No. 4, pp. 217–232, [http://dx.doi.org/10.1016/S0024-4937\(01\)00057-3](http://dx.doi.org/10.1016/S0024-4937(01)00057-3)
- Mathavan V., Kalubandara S.T., Fernando, G.W.A.R. (2000) Occurrences of two new types of gem deposits in the Okkampitya gem field, Sri Lanka. *Journal of Gemmology*, Vol. 27, No. 2, pp. 65–72.
- Merlet C. (1994) An accurate computer correction program for quantitative electron probe microanalysis. *Microchimica Acta*, Vol. 114/115, pp. 363–376, <http://dx.doi.org/10.1007/BF01244563>
- McGlynn S.P., Smith J.K. (1961) The electronic structure, spectra, and magnetic properties of actinyl ions. Part I. The uranyl ion. *Journal of Molecular Spectroscopy*, Vol. 6, No. 1, pp. 164–187, [https://dx.doi.org/10.1016/0022-2852\(61\)90237-5](https://dx.doi.org/10.1016/0022-2852(61)90237-5)
- Mitchell R.K. (1954) Some notes on unusual gems. *Journal of Gemmology*, Vol. 4, No. 5, pp. 210–211.
- (1961) Ekanite – Ceylon gemmologist discovers new mineral. *Journal of Gemmology*, Vol. 8, No. 3, pp. 96–98.
- Montel J.-M., Foret S., Veschambre M., Nicollet C., Provost A. (1996) Electron microprobe dating of monazite. *Chemical Geology*, Vol. 131, No. 1-4, pp. 37–53, [http://dx.doi.org/10.1016/0009-2541\(96\)00024-1](http://dx.doi.org/10.1016/0009-2541(96)00024-1)
- Moulin C., Decambox P., Moulin V., Decaillon J.G. (1995) Uranium speciation in solution by time-resolved laser-induced fluorescence. *Analytical Chemistry*, Vol. 67, No. 2, pp. 348–353, <http://dx.doi.org/10.1021/ac00098a019>
- Murakami T., Chakoumakos B.C., Ewing R.C., Lumpkin G.R., Weber W.J. (1991) Alpha-decay event damage in zircon. *American Mineralogist*, Vol. 76, No. 9-10, pp. 1510–1532.
- Nasdala L., Lengauer C.L., Hancher J.M., Kronz A., Wirth R., Blanc P., Kennedy A.K., Seydoux-Guillaume A.-M. (2002) Annealing radiation damage and the recovery of cathodoluminescence. *Chemical Geology*, Vol. 191, No. 1-3, pp. 121–140, [http://dx.doi.org/10.1016/S0009-2541\(02\)00152-3](http://dx.doi.org/10.1016/S0009-2541(02)00152-3)
- Nasdala L., Kronz A., Wirth R., Váci T., Pérez-Soba C., Willner A., Kennedy A.K. (2009) The phenomenon of deficient electron microprobe totals in radiation-damaged and altered zircon. *Geochimica et Cosmochimica Acta*, Vol. 73, No. 6, pp. 1637–1650, <http://dx.doi.org/10.1016/j.gca.2008.12.010>
- Nasdala L., Grambole D., Wildner M., Gigler A.M., Hainschwang T., Zaitsev A.M., Harris J.W., Milledge J., Schulze D.J., Hofmeister W., Balmer W.A. (2013) Radio-colouration of diamond: A spectroscopic study. *Contributions to Mineralogy and Petrology*, Vol. 165, No. 5, pp. 843–861, <http://dx.doi.org/10.1007/s00410-012-0838-1>
- Nasdala L., Corfu F., Blaimauer D., Chanmuang C., Ruschel K., Škoda R., Wildner M., Wirth R., Zeug M., Zoysa E.G. (2017) Neoproterozoic amorphous “ekinite” ( $Ca_2Th_{0.9}U_{0.1}Si_8O_{20}$ ) from Okkampitya, Sri Lanka: A metamict gemstone with excellent lead-retention performance. *Geology*, Vol. 45, No. 10, pp. 919–922, <http://dx.doi.org/10.1130/G39334.1>
- Othmane G., Allard T., Vercouter T., Morin G., Fayek M., Calas G. (2016) Luminescence of uranium-bearing opals: Origin and use as a pH record. *Chemical Geology*, Vol. 423, pp. 1–6, <http://dx.doi.org/10.1016/j.chemgeo.2015.12.010>
- Pointer C.M., Ashworth J.R., Ixer R.A. (1988) The zircon-thorite mineral group in metasomatized granite, Ririwai, Nigeria 2. Zoning, alteration and exsolution in zircon. *Mineralogy and Petrology*, Vol. 39, No. 1, pp. 21–37, <http://dx.doi.org/10.1007/BF01226260>
- Prior D.J., Trimby P.W., Weber U.D., Dingley D.J. (1996) Orientation contrast imaging of microstructures in rocks using forescatter detectors in the scanning electron microscope. *Mineralogical Magazine*, Vol. 60, No. 403, pp. 859–869, <http://dx.doi.org/10.1180/minmag.1996.060.403.01>
- Richman I., Kisliuk P., Wong E.Y. (1967) Absorption spectrum of  $U^{4+}$  in zircon ( $ZrSiO_4$ ). *Physical Review*, Vol. 155, No. 2, pp. 262–267, <https://dx.doi.org/10.1103/PhysRev.155.262>
- Russo M., Campostrini I., Demartin F. (2013) Nuove specie minerali al Monte Somma: V. L'ekinite. *Micro*, Vol. 11, pp. 142–144.
- Sameera K.A.G., Fernando G.W.A.R., Dharmapriya P.L. (2020a) First report on in-situ occurrences of ekanite from Galle, southwestern Highland Complex, Sri Lanka. In N.H. Koralegedara and A. Ratnayake, Eds., *Proceedings of the 36th Annual Technical Sessions “Global Challenges and the Role of Geologists.”* Geological Society of Sri Lanka, p. 3.
- Sameera K.A.G., Wickramasinghe W.A.G.K., Harankahawa S.B., Welikanna C.R., de Silva K.T.U.S. (2020b) Radiometric surveying for Th and U mineralization in southwestern, Sri Lanka: Radiological, mineralogical and geochemical characteristics of the radioactive anomalies. *Journal of the Geological Society of Sri Lanka*, Vol. 21, No. 2, pp. 57–80, <http://dx.doi.org/10.4038/jgssl.v21i2.49>
- Škoda R., Pláčil J., Jonsson E., Copjaková R., Langhof J., Vašinová Galiová M. (2015) Redefinition of thalénite-(Y) and discreditation of fluorthalénite-(Y): A re-investigation of type material from the Österby pegmatite, Dalarna, Sweden, and from additional localities. *Mineralogical Magazine*, Vol. 79, No. 4, pp. 965–983, <http://dx.doi.org/10.1180/minmag.2015.079.4.07>
- Smith G. (1978) Evidence for absorption by exchange-coupled  $Fe^{2+}$ – $Fe^{3+}$  pairs in the near infra-red spectra of minerals. *Physics and Chemistry of Minerals*, Vol. 3, No. 4, pp. 375–383, <http://dx.doi.org/10.1007/BF00311848>
- Suzuki K., Kato T. (2008) CHIME dating of monazite, xenotime, zircon and polycrase: Protocol, pitfalls and chemical criterion of possibly discordant age data. *Gondwana Research*, Vol. 14, No. 4, pp. 569–586, <http://dx.doi.org/10.1016/j.gr.2008.01.005>
- Szymański J.T., Owens D.R., Roberts A.C., Ansell H.G., Chao G.Y. (1982) A mineralogical study and crystal-structure determination of nonmetamict ekanite,  $ThCa_2Si_8O_{20}$ . *The Canadian Mineralogist*, Vol. 20, No. 1, pp. 65–75.
- Tennakone K. (2011) Thorium minerals in Sri Lanka, history of radioactivity and thorium as a future energy source: A compendium to commemorate the International Year of Chemistry 2011. *Journal of the National Science Foundation of Sri Lanka*, Vol. 39, No. 2, pp. 97–111, <http://dx.doi.org/10.4038/jnsfsr.v39i2.3170>
- Walstrom R.E., Dunning G.E. (2003) The Baumann Prospect, Chickencoop Canyon, Tulare County, California. *Mineralogical Record*, Vol. 34, pp. 159–166.
- Wang Z., Zachara J.M., Liu C., Gassman P.L., Felmy A.R., Clark S.B. (2008) A cryogenic fluorescence spectroscopic study of uranyl carbonate, phosphate and oxyhydroxide minerals. *Radiochimica Acta*, Vol. 96, No. 9-11, pp. 591–598, <http://dx.doi.org/10.1524/ract.2008.1541>
- Zeug M., Ruschel K., Blaimauer D., Lengauer C.L., Nasdala L. (2015) Effects of radiation damage on the  $Nd^{3+}$  luminescence of ekanite,  $ThCa_2Si_8O_{20}$ . In G.B. Andreozzi and F. Bosi, Eds., *Proceedings of the 8th European Conference on Mineralogy and Spectroscopy*, Rome, Italy, September 9–11, 2015. *Periodico di Mineralogia*, Vol. 84, pp. 197–198.
- Zeug M., Nasdala L., Wanthanachaisaeng B., Balmer W.A., Corfu F., Wildner M. (2018) Blue zircon from Ratanakiri, Cambodia. *Journal of Gemmology*, Vol. 36, No. 2, pp. 112–132.
- Zhang M., Salje E.K.H., Farnan I., Graeme-Barber A., Daniel P., Ewing R.C., Clark A.M., Leroux H. (2000) Metamictization of zircon: Raman spectroscopic study. *Journal of Physics: Condensed Matter*, Vol. 12, No. 8, pp. 1915–1925, <http://dx.doi.org/10.1088/0953-8984/12/8/333>
- Ziebold T.O. (1967) Precision and sensitivity in electron microprobe analysis. *Analytical Chemistry*, Vol. 39, No. 8, pp. 858–861, <http://dx.doi.org/10.1021/ac60252a028>

# A GEMOLOGICAL AND SPECTROSCOPIC STUDY WITH MOBILE INSTRUMENTS OF “EMERALDS” FROM THE CORONATION CROWN OF NAPOLEON III

Stefanos Karamelas, Eloïse Gaillou, Annabelle Herreweghe, Farida Maouche, Ugo Hennebois, Sophie Leblan, Bérengère Meslin Sainte Beuve, Michel Lechartier, Didier Nectoux, and Aurélien Delaunay

Forty-five “emeralds,” formerly set in the coronation crown of Napoleon III, were studied using nondestructive mobile spectroscopic and gemological means. Adorned with emeralds, diamonds, and gold, the crown was created in 1855 by royal jeweler Alexandre Gabriel Lemonnier but dismantled in 1887 for the auctioning of the French crown jewels. Some of the emeralds were donated to the École des Mines (Paris School of Mines, now known as Mines Paris - PSL) in 1887, prior to the auction. Our examination revealed that 41 out of 45 gems were indeed natural emeralds, presenting no evidence of clarity enhancement. Their gemological characteristics and age suggest a Colombian provenance. The other four samples were determined to be artificial glass containing iron and/or copper and possibly other chromophores. These glass imitations could have been set when the crown was created or shortly thereafter. This study is part of an effort to examine gemstones of historical meaning and significance worldwide.

The collection of the French crown jewels was established on June 15, 1530, by Francis I and enriched by later kings and emperors, such as Henry II, Henry IV, Louis XIV, Napoleon I, Louis XVIII, and Napoleon III. This important collection of loose gemstones and high-end jewelry included many significant gems: the Regent, Grand Sancy, and French Blue (later Hope) diamonds; the Grand Sapphire; and the Côte de Bretagne red spinel (see Bapst, 1889 and Morel, 1988 for details on the collection and its history). It is worth mentioning that most of the jewels were kept as individual stones and used in custom settings designed for each new sovereign, and then dismantled again when a successor came to power.

After the end of the French Empire, the crown jewels were exhibited twice in Paris, in 1878 at the Exposition Universelle (World’s Fair) and in 1884 in the State Room at the Louvre. Both exhibitions

were heavily guarded and attracted large crowds of admirers. However, the popularity of the two events did not prevent the unprecedented sale of this national treasure.

## In Brief

- Forty-five “emeralds” formerly set in the coronation crown of Napoleon III were studied with nondestructive mobile gemological and spectroscopic means.
- Of these, 41 samples were found to be natural emeralds from Colombia without clarity enhancement.
- Four samples were found to be artificial glass containing iron and/or copper and possibly other chromophores; no evidence of recently fabricated glass was found.

During the French Third Republic, most of the crown jewels were dismantled and sold at an auction at the Louvre, held May 12–23, 1887. The auction was intended to get rid of these symbols of royalty and empire. Some unset gems, however, were put

See end of article for About the Authors and Acknowledgments.

GEMS & GEMOLOGY, Vol. 58, No. 2, pp. 168–183,

<http://dx.doi.org/10.5741/GEMS.58.2.168>

© 2022 Gemological Institute of America





Figure 2. Left: A reproduction of the crown of Napoleon III, displayed at the Abeler collection of crowns and regalia in Wuppertal, Germany. Modified from Wikimedia Commons. Right: The royal jeweler Lemonnier also produced a very similar crown for Empress Eugénie in 1855. Photo by Stéphane Maréchalle; courtesy of RMN-Grand Palais (Louvre Museum).

1990; Fritsch et al., 2007; Gaillou and Post, 2007; Gaillou et al., 2010, 2012, 2022; Galopim de Carvalho, 2014; Post and Farges, 2014; Farges et al., 2015). These gems from the crown were kept in the vault of the museum of the École des Mines in Paris until 2016, when the museum opened an exhibition of gems from the French crown jewels. The present paper is part of an ongoing project on the study of the gems previously adorning historic jewels, led by the French Gemmological Laboratory (LFG) and the Museum of Mineralogy, Mines Paris - PSL, which owns the gems.

The crown (figure 2, left) was created in 1855 by royal jeweler Alexandre-Gabriel Lemonnier and presented at the “Exposition Universelle” in Paris the same year. Lemonnier’s very similar crown for Empress Eugénie is shown in figure 2 (right). Napoleon III’s crown was adorned at the bottom part with eight large emeralds ranging from 14.5 to 23.7 ct (with a total weight of more than 150 carats) as well as eight large diamonds weighing 17.00 to 26.33 ct that were previously mounted in another royal crown. These diamonds included the 19.07 ct Grand Mazarin, the 19.22 ct De Guise, and the 25.53 ct Fleur-de-Pêcher. Fifty smaller “emeralds” were also incorporated: 34

rectangular step-cut stones forming an equator around the globe atop the crown (and topped with a diamond cross) with a total weight of 10.03 carats, and 16 round and oval brilliant-cut stones circling the midsection, with a total weight of 17.26 carats. Morel (1988, p. 338) notes that shortly after the crown’s creation, the eight large diamonds were removed and later used in other jewels of Empress Eugénie, replaced by “strass” (artificial glass, possibly containing lead) imitations. Morel also noted that the emeralds were left set in the crown.

Five years after the fall of the empire, the eight large emeralds were restituted to Empress Eugénie on October 5, 1875. In 1887, Napoleon III’s crown was melted down and the stones were separated into different suites. During the auction of the French crown jewels in May 1887, the eight large diamonds were sold to the highest bidder (the diamond cross was sold to the jeweler Boucheron earlier that year). The 50 smaller “emeralds” were part of the donation to the École des Mines. Today, 33 of the 34 gems from the upper part of the crown as well as 12 of the 16 gems from the midsection are cataloged in the Museum’s collection, and these are presented below.

## MATERIALS AND METHODS

Examined here are the 45 green stones, reportedly emeralds, that were donated during the Third Republic's historical deposit of 1887 into the collection of the *École des Mines* (formally the *École Normale Supérieure des Mines de Paris*, or ENSMP), now called Mines Paris - PSL. The catalog numbers of the school's mineral, gem, meteorite, and rock collection still bear the initials "ENSMP," all entered under a single catalog number: all entered under a single old catalog number: M. 4849.

This study investigates some of the 96 emeralds that were part of this original donation; the 46 emerald beads are excluded. We only focus on the gems mentioned as "16 emeralds of 16.79 carats" and "34 emeralds of 10.03 carats" in total weight (see again figure 1), as these can be traced back to the coronation crown of Napoleon III. Among the 50 emeralds donated in 1887, 45 of them are still in the museum's collection, the curators having no record of the remaining five.

As the ENSMP collection has evolved over the 135 years since the gems from the crown jewels arrived, the donation that was deposited under a single reference number was dispatched into several catalog numbers. The 50 emeralds from Napoleon III's crown were divided into three series. The first series consists of the previously mentioned 34 emeralds from the top part of the crown, under the name ENSMP 69880, 33 of which are still in the collection (figure 3 and table 1; note that sample ENSMP 69880\_5 is missing). The second series of 16 emeralds from the midsection of the crown was split into at least two catalog numbers—four stones under ENSMP 69881 and eight under ENSMP 69866 (figure 4 and table 1)—while the last four remain missing. The reason for splitting this second series is not clear, but as we will see later, series ENSMP 69881 has characteristics unlike the others.

As the set of 45 samples is considered a national treasure, the project had to be conducted on-site at the Museum of Mineralogy, Mines Paris - PSL. Be-

*Figure 3. The 33 emeralds of suite ENSMP 69880, originally set in the crown of Napoleon III, ranging from 0.180 to 0.408 ct. Photo by Eloïse Gaillou; © Museum of Mineralogy, Mines Paris - PSL.*



**TABLE 1.** Properties of samples from the crown of Napoleon III.

Reference number	Weight (ct)	Dimensions (mm)	Shape/Cutting Style
ENSMP 69866_1	1.156	7.12–7.19 × 3.48	Round/Brilliant
ENSMP 69866_2	1.071	7.11–7.22 × 3.42	Round/Brilliant
ENSMP 69866_3	0.955	6.90 × 6.23 × 3.67	Oval/Brilliant
ENSMP 69866_4	1.339	7.06–7.18 × 4.11	Round/Brilliant
ENSMP 69866_5	1.036	7.10–7.21 × 3.23	Round/Brilliant
ENSMP 69866_6	0.929	6.92–7.13 × 3.10	Round/Brilliant
ENSMP 69866_7	1.091	6.95–7.19 × 3.40	Round/Brilliant
ENSMP 69866_8	0.854	6.93–7.07 × 3.07	Round/Brilliant
ENSMP 69880_1	0.366	4.67 × 3.73 × 3.05	Rectangular/Step
ENSMP 69880_2	0.299	4.43 × 3.78 × 2.45	Rectangular/Step
ENSMP 69880_3	0.408	4.77 × 3.81 × 3.23	Rectangular/Step
ENSMP 69880_4	0.293	4.44 × 3.59 × 2.65	Rectangular/Step
ENSMP 69880_6	0.305	4.60 × 3.69 × 2.52	Rectangular/Step
ENSMP 69880_7	0.317	4.48 × 3.72 × 2.71	Rectangular/Step
ENSMP 69880_8	0.310	4.14 × 3.85 × 3.03	Rectangular/Step
ENSMP 69880_9	0.342	4.38 × 3.71 × 2.91	Rectangular/Step
ENSMP 69880_10	0.358	4.65 × 3.73 × 2.90	Rectangular/Step
ENSMP 69880_11	0.214	3.86 × 3.42 × 2.47	Rectangular/Step
ENSMP 69880_12	0.364	4.54 × 3.72 × 3.03	Rectangular/Step
ENSMP 69880_13	0.361	4.62 × 3.70 × 3.10	Rectangular/Step
ENSMP 69880_14	0.303	4.67 × 3.67 × 2.66	Rectangular/Step
ENSMP 69880_15	0.343	4.44 × 3.68 × 2.91	Rectangular/Step
ENSMP 69880_16	0.344	4.61 × 3.70 × 2.80	Rectangular/Step
ENSMP 69880_17	0.315	4.60 × 3.64 × 2.48	Rectangular/Step
ENSMP 69880_18	0.371	4.63 × 3.74 × 3.06	Rectangular/Step
ENSMP 69880_19	0.331	4.54 × 3.66 × 2.84	Rectangular/Step
ENSMP 69880_20	0.236	3.88 × 3.45 × 2.44	Rectangular/Step
ENSMP 69880_21	0.317	4.47 × 3.69 × 2.81	Rectangular/Step
ENSMP 69880_22	0.381	4.70 × 3.71 × 3.18	Rectangular/Step

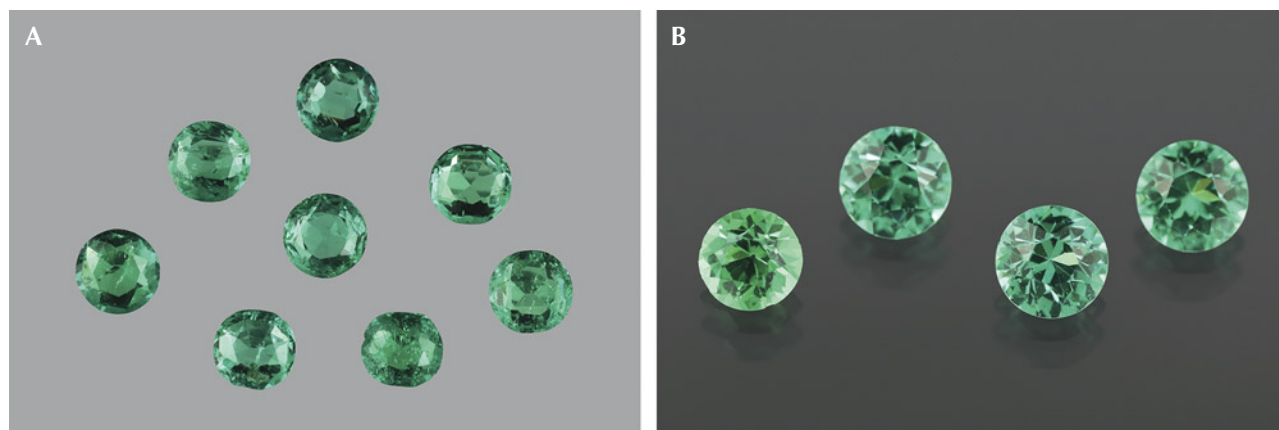
**TABLE 1 (continued).** Properties of samples from the crown of Napoleon III.

Reference number	Weight (ct)	Dimensions (mm)	Shape/Cutting Style
ENSMP 69880_23	0.318	4.54 × 3.61 × 2.64	Rectangular/Step
ENSMP 69880_24	0.297	4.61 × 3.64 × 2.54	Rectangular/Step
ENSMP 69880_25	0.240	3.87 × 3.47 × 2.68	Rectangular/Step
ENSMP 69880_26	0.327	4.55 × 3.69 × 2.75	Rectangular/Step
ENSMP 69880_27	0.245	3.91 × 3.65 × 2.57	Rectangular/Step
ENSMP 69880_28	0.229	3.90 × 3.40 × 2.56	Rectangular/Step
ENSMP 69880_29	0.217	3.93 × 3.81 × 2.09	Rectangular/Step
ENSMP 69880_30	0.287	3.97 × 3.50 × 3.02	Rectangular/Step
ENSMP 69880_31	0.233	4.34 × 3.88 × 2.08	Rectangular/Step
ENSMP 69880_32	0.247	3.91 × 3.62 × 2.42	Rectangular/Step
ENSMP 69880_33	0.221	3.91 × 3.61 × 2.27	Rectangular/Step
ENSMP 69880_34	0.180	3.83 × 3.67 × 1.88	Rectangular/Step
ENSMP 69881_1	0.939	5.86–5.87 × 4.04	Round/Brilliant
ENSMP 69881_2	0.703	5.28–5.39 × 3.83	Round/Brilliant
ENSMP 69881_3	0.929	5.84–5.87 × 3.98	Round/Brilliant
ENSMP 69881_4	0.919	5.80–5.83 × 3.92	Round/Brilliant

cause of this constraint, the samples were studied using LFG's mobile spectrometers as well as classical

gemological tools. The samples and their dimensions are listed in table 1. All samples were examined with

Figure 4. A: The eight emeralds from suite ENSMP 69866, ranging from 0.854 to 1.339 ct. B: The four stones from suite ENSMP 69881, weighing from 0.703 to 0.939 ct. Photos by Eloïse Gaillou; © Museum of Mineralogy, Mines Paris - PSL.





classic gemological tools. Observation was performed using a Zeiss Stemi 508 binocular microscope (magnification up to 80×) equipped with a fiber-optic light source and an incorporated camera to acquire photos all mounted on an Eickhorst Gemmaster base. Luminescence was examined using a 6-watt ultraviolet lamp (Vilber Lourmat VL-6.LC) with long-wave UV (365 nm) and short-wave UV (254 nm) light, equipped with a CN-6 darkroom (10 cm distance between the sample and the lamp). Refractive indexes were taken with a refractometer and mass and density with a hydrostatic balance.

Raman and photoluminescence (PL) spectra were obtained using a mobile Raman spectrometer (Magilabs GemmoRaman-532SG) with a 532 nm laser excitation and spectral resolution of 11  $\text{cm}^{-1}$ , ranging for Raman spectra from 200 to 2000  $\text{cm}^{-1}$  (with 1 second exposure time and 4 accumulations) and for PL spectra from 540 to 760 nm (0.3 to 0.4 second exposure time and 30 accumulations). All spectra were acquired with the laser pointing at the table, the flattest part of the stone. Calibration of the Raman spectrometer was made with a diamond, using its 1331.8  $\text{cm}^{-1}$  Raman line. Due to this study requiring the use of a mobile instrument, the spectral resolution was over 10  $\text{cm}^{-1}$ . This precluded us from reaching a conclusion regarding the alkali content, which would have required the use of the exact position and full width at half maximum of the band at 1070  $\text{cm}^{-1}$  to differentiate emeralds containing either low or high concentrations of alkali elements (Huong et al., 2014; Bersani et al., 2014; Jehlička et al., 2017; Karampelas et al., 2019). Indeed, in order to obtain the real shape of this band, relatively high spectral resolution (<2  $\text{cm}^{-1}$ ) must be used in the acquisition of the Raman spectra. Moreover, the spectral resolution of the instrument could also affect the exact position of the PL bands. For example, if the spectral resolution is not optimal, the real shape of the band is not obtained and it appears broader and in slightly shifted positions. The suggestion that the exact position of the  $\text{Cr}^{3+}$   $R_1$  line can give information regarding an emerald's country of origin (Moroz et al., 2000; Thomson et al., 2014) should be considered with caution. Visible/near-infrared (Vis-NIR) spectra were acquired from 365 to 1000 nm using a mobile instrument (0.05 to 0.10 seconds acquisition time and 50 accumulations) with an integrating sphere (Magilabs Gemmosphere). Fourier-transform infrared (FTIR) spectra were obtained with a mobile instrument (Bruker Alpha II) in the 400 to 8000  $\text{cm}^{-1}$  range (4  $\text{cm}^{-1}$  spectral resolution and 100 scans) using a DRIFT accessory as a beam condenser (Hainschwang et al., 2006).

## RESULTS AND DISCUSSION

**Gemological Properties and Appearance.** Dimensions, weights, and shapes and cutting styles of the 45 examined samples are presented in table 1. The first suite of 33 gems (ENSMP 69880) consists of rectangular step cuts, weighing from 0.180 to 0.408 ct (figure 3). The total weight of the 33 samples from series ENSMP 69880 is 9.919 carats instead of the 10.030 carats mentioned in the archives, registering all 34 original samples. The second suite (ENSMP 69866) is composed of eight roundish brilliants (one with a more oval shape), weighing from 0.854 to 1.339 ct, for a total weight of 8.431 carats (figure 4A). The last suite (ENSMP 69881) is composed of four round brilliants weighing from 0.703 to 0.939 ct (figure 4B), for a total weight of 3.49 carats.

All 33 rectangular gems of suite ENSMP 69880 (figure 3) and all eight roundish gems of suite ENSMP 69866 (figure 4A) presented a vivid green color. The four round-shaped stones from suite ENSMP 69881 displayed instead an intense green with a slightly yellowish tint (figure 4B). The refractive index of samples from series ENSMP 69866 and ENSMP 69880 varied from 1.570 to 1.588, and their specific gravity values from 2.60 to 2.75, consistent with beryl. The color observed for those samples was consistent with the emerald variety of beryl. All samples were inert under UV lamp excitation, except for one (ENSMP 69866\_3) that exhibited a weak red fluorescence to long-wave UV only. This difference in fluorescence behavior could be explained by a slightly larger ratio of chromium to iron in this emerald; fluorescence is present when the ratio is significant and becomes less intense with a decrease in chromium to iron ratio (Bosshart, 1991b).

Samples from series ENSMP 69881 presented completely different characteristics: a refractive index of about 1.64, a specific gravity between 3.56 and 3.78 (depending on the stone), and a chalky yellowish fluorescence that was weaker to long-wave UV than to short-wave UV. The RI, SG, and UV reaction are similar to those observed in artificial glass containing lead (Nassau, 1980; Webster and Anderson, 1983).

**Macroscopic and Microscopic Observations.** Standard macroscopic observation revealed surface-reaching cracks in some samples (figure 5). This could be attributed to multiple uses of gems in different jewelry pieces over time. This practice of reusing gemstones from the French crown jewels, sometimes

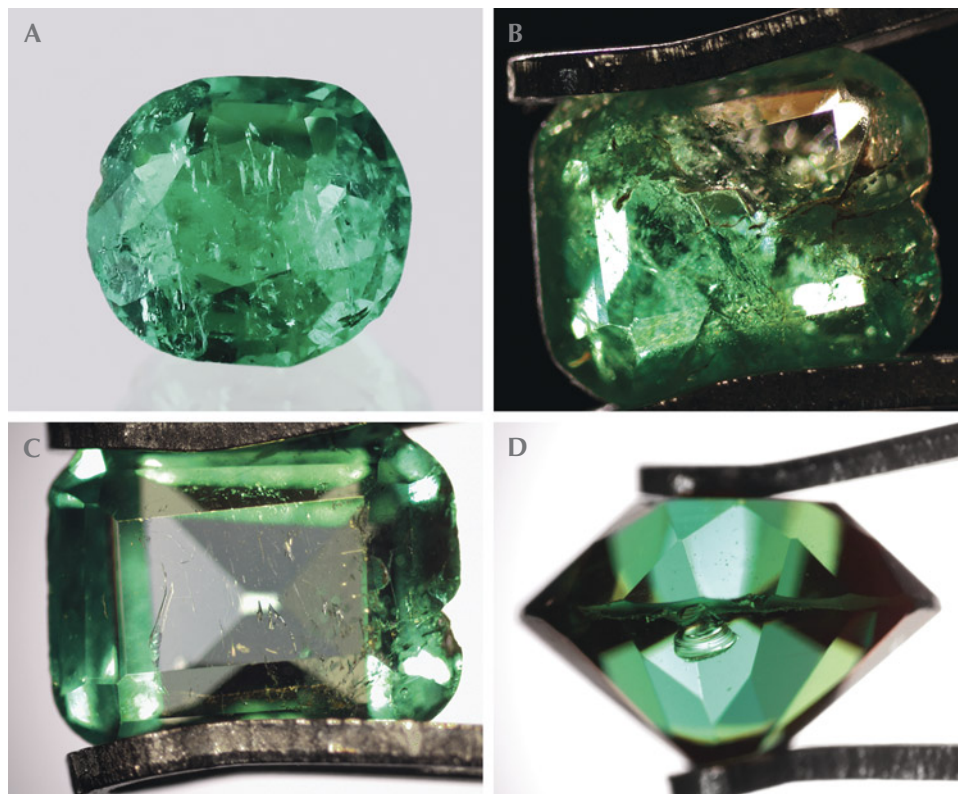


Figure 5. Photos of specimens from this study presenting visible cracks and fractures, possibly due to multiple uses in jewelry. A: ENSMP 69866\_3 (0.955 ct). B: ENSMP 69880\_2 (0.299 ct). C: ENSMP 69880\_6 (0.305 ct). D: ENSMP 69881\_3 (0.929 ct). Photos by B.M.S. Beuve/LFG (A) and U. Hennebois/LFG (B-D); © Museum of Mineralogy, Mines Paris - PSL.

even recutting them, is well known (e.g., Bapst, 1889; Morel, 1988). The purpose was to create contemporary pieces of jewelry in style with the era, which then could be used by the new ruler. Interestingly, sample ENSMP 69881\_3 shows a conchoidal fracture (figure 5D).

Under the microscope, samples from suites ENSMP 69866 and ENSMP 69880 (41 of the 45 studied samples) presented natural features such as multi-phase inclusions with jagged outlines, color zoning, transparent crystals (possibly carbonates), and *gota de aceite* (Spanish for “drop of oil”) patterns (figures 6

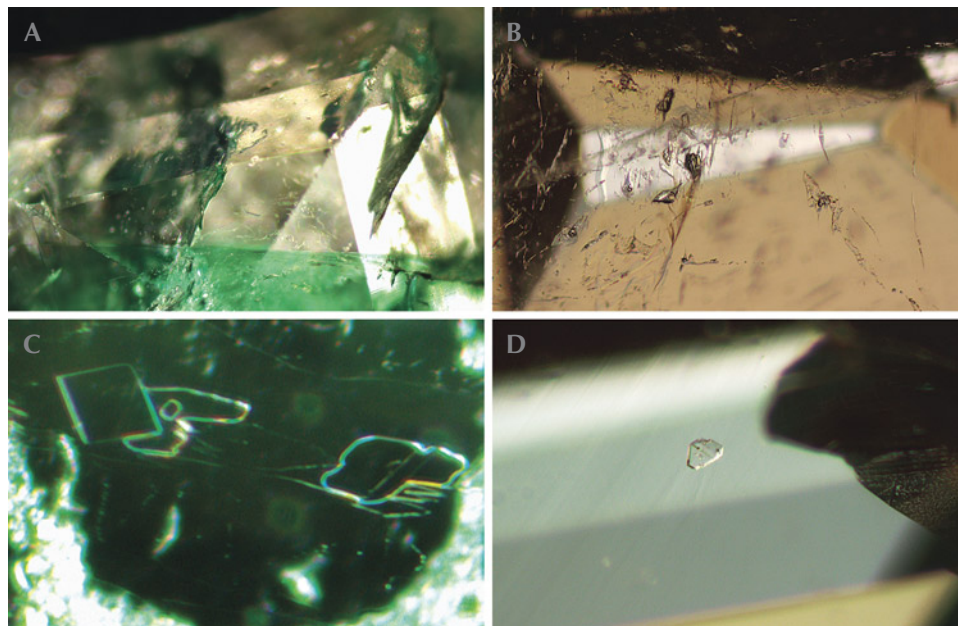


Figure 6. A: Color zoning observed in ENSMP 69880\_9, field of view 2 mm. B and C: Multi-phase inclusions with jagged outlines observed in ENSMP 69880\_23 and in ENSMP 69866\_4; fields of view 1.2 and 0.5 mm, respectively. D: A transparent crystal (possibly a carbonate) observed in ENSMP 69880\_22; field of view 1 mm. Photomicrographs by Ugo Hennebois/LFG; © Museum of Mineralogy, Mines Paris - PSL.

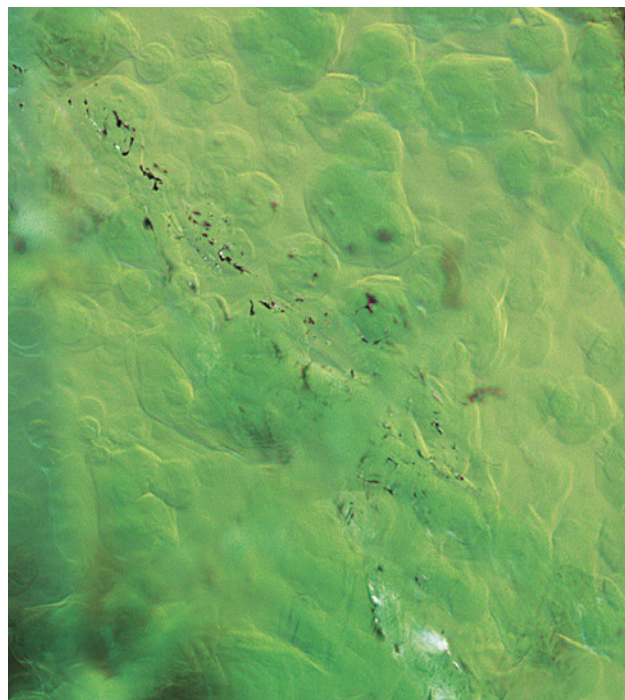


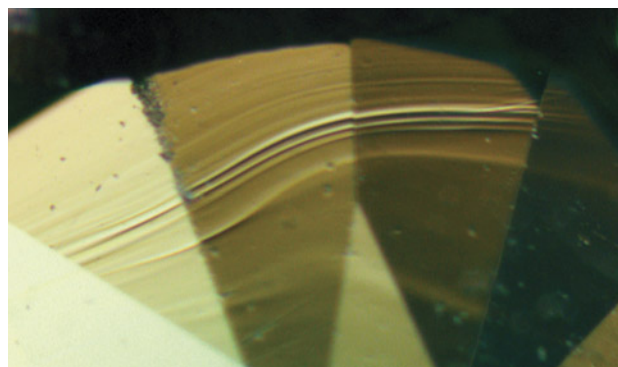
Figure 7. Gota de aceite structures observed in ENSMP 69866\_2; field of view 1.5 mm. Photomicrograph by Ugo Hennebois/LFG; © Museum of Mineralogy, Mines Paris - PSL.

and 7). Inclusions with jagged outlines are observed in natural emeralds from Colombia and occasionally from Afghanistan, China, and a small occurrence in Zambia (specifically from Musakashi and not the more productive Kafubu deposits), as well as mines of more academic interest (Bosshart, 1991b; Saeseaw et al., 2014, 2019; Schmetzer, 2014; Krzemnicki et al., 2021). The *gota de aceite* appearance such as that observed in ENSMP 69866\_2 (figure 7) is documented in emeralds from Colombia but seldom observed in emeralds from other origins (Ringsrud, 2008; Hain-schwang, 2010; Fritsch et al., 2017). These structures display octagonal color zoning due to fibrous growth at a fast growth rate, followed by a later growth episode, possibly slower, which filled the space between the fibers. The *gota de aceite* appearance is most likely due to light scattering at the irregular interface between the two growth episodes (Fritsch et al., 2017). No indications of treatment, such as the clarity enhancement applied to emerald since well before the fourteenth century (Johnson et al., 1999; Kiefert et al., 1999), were observed microscopically in any of these samples. The four samples from suite ENSMP 69881 presented no mineral inclusions. Only

one displayed “flow patterns” (figure 8), along with bubbles characteristic of glass (Webster and Anderson, 1983; Gübelin and Koivula, 1986).

**Raman Spectroscopy.** Raman spectra of three representative samples, from suites ENSMP 69866 and ENSMP 69880, are presented in figure 9A. Spectra showed bands typical of beryl. The vibration at around  $685\text{ cm}^{-1}$  is linked to Be-O stretching; at around  $1070\text{ cm}^{-1}$ , the vibration is related to Si-O and/or Be-O stretching, along with a less intense band at around  $1010\text{ cm}^{-1}$  due to Si-O stretching. The weaker bands between  $200$  and  $600\text{ cm}^{-1}$  are linked to  $\text{Si}_6\text{O}_{18}$  ring vibrations (Adams and Gardner, 1974; Hagemann et al., 1990; Kim et al., 1995; Moroz et al., 2000; Bersani et al., 2014; Jehlička et al., 2017). The spectra presented some differences in the relative intensities of the Raman bands (see again figure 9A). These result from the different crystallographic orientations in which the gems are cut and the spectra acquired. The band at around  $685\text{ cm}^{-1}$  is the most intense, with the bands at around  $1010$  and  $1070\text{ cm}^{-1}$  having a similar intensity (e.g., sample ENSMP 69880\_3, red line in figure 9A) when the spectrum is acquired with the laser beam parallel to the *c*-axis of the crystal. When spectra are acquired with the laser perpendicular to the *c*-axis of the crystal (e.g., sample ENSMP 69866\_1, black line in figure 9A), the band at  $1070\text{ cm}^{-1}$  is slightly more intense than that at  $685\text{ cm}^{-1}$ , while the band at around  $1010\text{ cm}^{-1}$  is significantly less intense (Moroz et al., 2000; Bersani et al., 2014; Jehlička et al., 2017; Karampelas et al., 2019). All samples from suites ENSMP 69866 and ENSMP 69880 (representing 41 of the 45 samples) showed the

Figure 8. These “flow patterns” were observed in ENSMP 69881\_3; field of view 2 mm. Photomicrograph by Ugo Hennebois/LFG; © Museum of Mineralogy, Mines Paris - PSL.



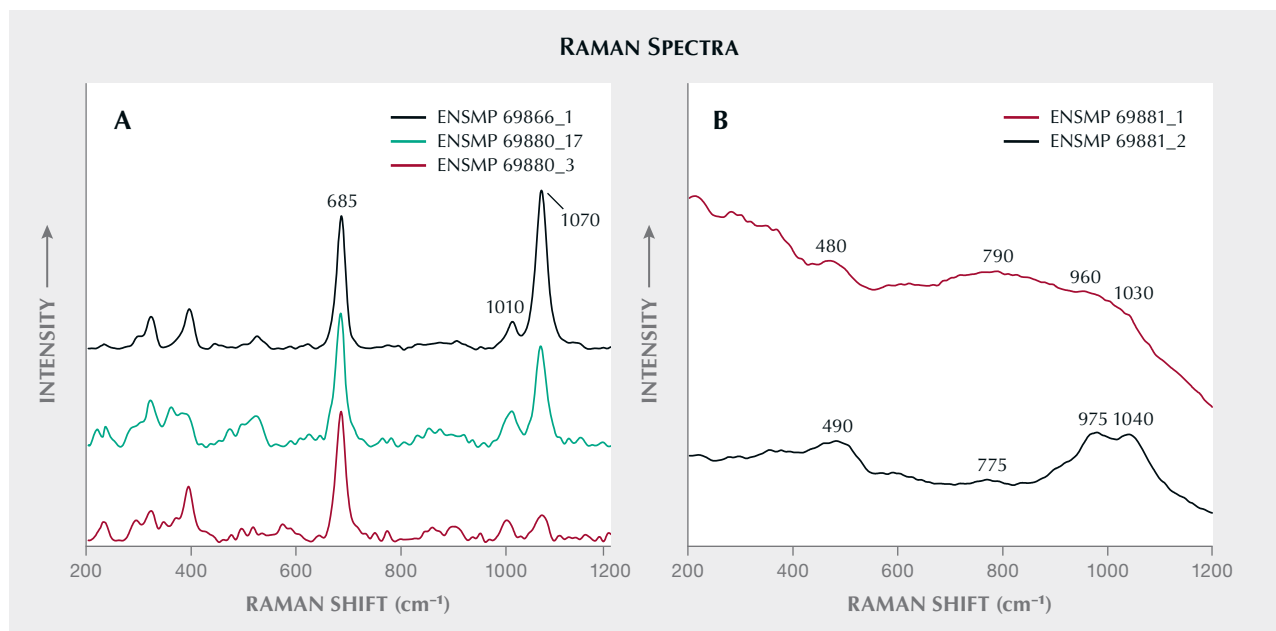


Figure 9. Raman spectra obtained using a mobile instrument with 532 nm laser excitation, in the range of 200 to 1200  $\text{cm}^{-1}$ , of some typical samples (all spectra are shifted for clarity). A: Typical spectra for the ENSMP 69866 and 69880 suites, showing vibrations characteristic of beryl. The differences from spectrum to spectrum are due to different crystallographic orientations of the gems; the spectrum of 69866\_1 is obtained nearly perpendicular to the c-axis, and the spectrum of 69880\_3 is obtained nearly parallel to the c-axis. B: Typical spectra for the ENSMP 69881 suite, showing large bands sometimes detected in glass, centered at slightly different positions.

beryl-related Raman bands, which only differ in relative intensity.

Raman spectra of all samples from suites ENSMP 69866 and ENSMP 69880 presented strong luminescence phenomena above 2000  $\text{cm}^{-1}$  (i.e., from the yellow to the red part of the electromagnetic spectrum). For that reason, it was impossible using this instrument to study the type I water (lacking a nearby alkali ion) and type II water (with alkali ions nearby) vibrations appearing at around 3609 and 3598  $\text{cm}^{-1}$ , respectively (Huong et al., 2010; Bersani et al., 2014; Jehlička et al., 2017; Karampelas et al., 2019).

Raman spectra of two of the four samples from suite ENSMP 69881 are presented in figure 9B. The spectra showed broad bands at slightly different positions, similar to those observed in glassy silicates, with Si-O stretching and bending and corresponding Raman bands at around 1000  $\text{cm}^{-1}$  and 500  $\text{cm}^{-1}$ , respectively (Colomban et al., 2006). Glasses are relatively poor Raman scatterers, and the signal-to-noise ratio of the mobile Raman instrument did not allow us to draw clear conclusions; however, the spectra are similar to those observed in lead glass (Colomban et al., 2006; Robinet et al., 2006; Ben Kacem et al., 2017). This kind of glass (e.g., “flint glass,” which may display a relatively high refractive index—up to

2.00, depending on lead content—and dispersion) is known to have been manufactured for several centuries (Ben Kacem et al., 2017).

**Photoluminescence Spectroscopy.** PL spectra of all ENSMP 69866 and ENSMP 69880 samples presented a sharp band at around 680 nm and another more intense sharp band at around 684 nm. These emission bands are linked to  $\text{Cr}^{3+}$   $R_2$  and  $R_1$  lines, respectively, in the beryl structure. They are accompanied by a broad band in the red part of the visible range, centered around 710 nm (see two examples in figure 10A), possibly also linked to chromium (Wood, 1965; Moroz et al., 2000; Thomson et al., 2014). Positions and relative intensities of the  $R$  lines presented some orientation effects (see again figure 10A). In the studied samples, the  $R_1$  line ranged from 683.7 to 683.9 nm, similar to some emeralds from Colombia as well as some from Russia and Afghanistan (Thomson et al., 2014; Karampelas et al., 2019).

The four ENSMP 69881 samples presented a broad PL band at 560 nm with a shoulder at around 580 nm, less intense for sample ENSMP 69881\_2 (figure 10B, black line), along with a broader band centered at around 700 to 710 nm, with different relative intensities for the two samples (see again figure 10B).

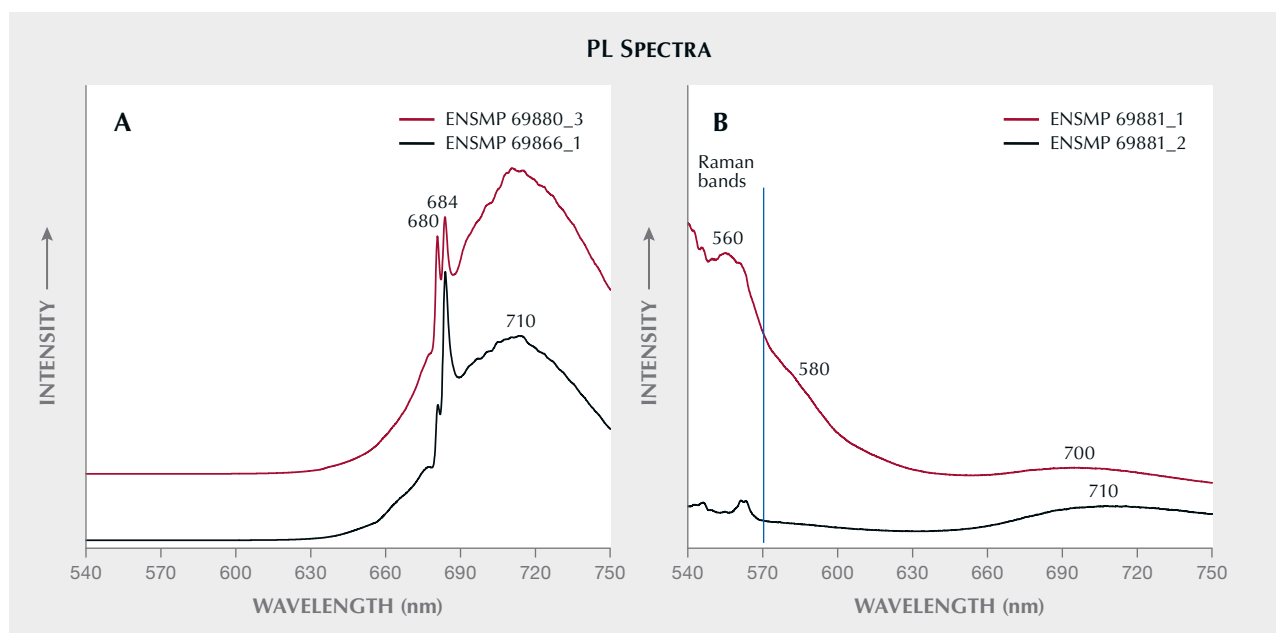


Figure 10. Typical PL spectra of the samples studied, in the range of 540 to 750 nm (spectra are shifted for clarity). A: In the ENSMP 69866 and 69880 suites, PL bands related to chromium in the beryl structure in the red part of the electromagnetic spectrum are observed in all spectra. B: In the ENSMP 69881 suite, large bands possibly due to oxygen-related centers in glass are observed. Both spectra show the Raman bands below 570 nm.

The bands in the green part are possibly due to oxygen deficiency-related centers (Skuja, 1998). In the red part of the spectra, the observed bands might be due to non-bridging oxygen-hole centers in glass (Sakurai et al., 1999). Green luminescence under UV light can be found in glass imitations of gems (Webster and Anderson, 1983).

**Visible/Near-Infrared (Vis-NIR) Spectroscopy.** Two typical Vis-NIR spectra of samples from suites ENSMP 69866 and ENSMP 69880 are shown in figure 11A. All 41 stones from these suites presented similar spectra. The broad absorptions at around 430 and 610 nm are both linked to  $\text{Cr}^{3+}$  and  $\text{V}^{3+}$  in beryl. The two sharp bands of weak intensity at around 680 nm are due to  $\text{Cr}^{3+}$   $R_1$  and  $R_2$  lines. No absorptions linked to iron are observed in the near-infrared part of the electromagnetic spectrum (Wood and Nassau, 1968; Bosshart, 1991b; Saeseaw et al., 2014, 2019; Schmetzer, 2014). Most natural emeralds from Colombia, as well as some from Afghanistan and a small occurrence recently discovered in Zambia, present spectra without any absorption linked to iron, or with low-to medium-intensity bands linked to iron in the NIR region (Bosshart, 1991b; Saeseaw et al., 2014, 2019; Giuliani et al., 2019; Giuliani and Groat, 2019; Karampelas et al., 2019; Krzemnicki et al., 2021). The

slight differences in position and relative intensity of the absorption bands are also due to crystallographic orientation effects. The small sharp band at around 960 nm is due to the presence of water in beryl.

Figure 11B presents two Vis-NIR spectra of the suite of four ENSMP 69881 specimens, all four spectra being similar in shape. A large absorption band centered at around 800 nm due to  $\text{Fe}^{2+}$  and/or  $\text{Cu}^{2+}$  is observed, along with a total absorption (cut off) from 380 to 400 nm due to  $\text{Fe}^{3+}$  (or  $\text{Fe}^{3+}\text{-S}^{2-}$ ) and a transmission window in the green part of the visible range at around 510 nm (Schreurs and Brill, 1984; Carl et al., 2007; Meulebroeck et al., 2010, 2011). Using this mobile Vis-NIR instrument, a clear image of the absorption in the NIR (above 1000 nm) and in the UV (below 365 nm) cannot be obtained to better characterize the exact cause of the color. However, we observed no absorption bands due to elements used for recent glass coloration. For example, the use of chromium began after the second half of the nineteenth century, and it was not observed in any of the studied glasses (Meulebroeck et al., 2016).

**Infrared (IR) Absorption Spectroscopy.** Figure 12A presents a typical FTIR spectrum of a sample from series ENSMP 69866 (black line). At around  $3500\text{ cm}^{-1}$ , a total absorption is observed, which is due to

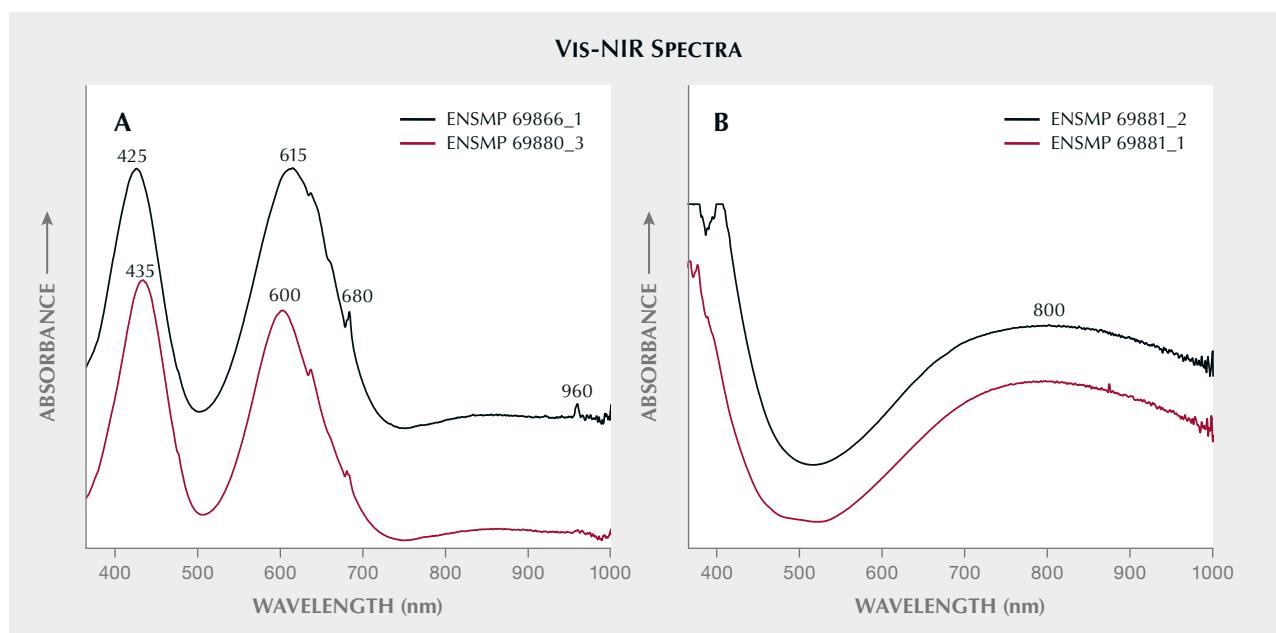


Figure 11. Visible/near-infrared (Vis-NIR) spectra from 365 to 1000 nm of representative samples of the different suites. All spectra are shifted for clarity. A: Representative spectra of suites ENSMP 69866 and 69880. Bands related to both chromium and vanadium in the beryl structure are observed at around 430 and 610 nm. Crystallographic orientation can affect the exact position and relative intensity of these bands. B: Representative spectra of suite ENSMP 69881. These show a large band centered at around 800 nm, possibly due to ferrous iron (and/or copper), and a cutoff from 380 to 400 nm, possibly due to ferric iron (possibly with the participation of sulfur).

vibrations linked to the stretching of water molecules in the beryl structure. The combination water bands are situated in the range of 4500 to 8000  $\text{cm}^{-1}$ . For example, a series of bands at around 5270  $\text{cm}^{-1}$  due to type I water (without an alkali ion nearby) and type II water (with alkali ions nearby) can be observed (Wood and Nassau, 1967, 1968). In the NIR region at about 1400 nm (7142  $\text{cm}^{-1}$ ), the absorption is due to type I water; at around 1408 nm (7102  $\text{cm}^{-1}$ ), the band is due to type II water (figure 12, A and B). Using the mobile FTIR instrument, the signal-to-noise ratio in the NIR (i.e., above 6500  $\text{cm}^{-1}$ ) was sometimes low and the bands were not always well resolved (see again figure 12A). However, in all spectra of samples from suites ENSMP 69866 and ENSMP 69880, the bands due to type I water were of equal or greater intensity than those due to type II water. This characteristic was also observed for emeralds with low alkali element concentration, such as those from Colombia (Saeseaw et al., 2014; Karampelas et al., 2019). From 2200 to 2850  $\text{cm}^{-1}$ , some weak bands linked to  $\text{H}_2\text{O}$ ,  $\text{D}_2\text{O}$ ,  $\text{CO}_2$ , and chlorine were observed (de Donato et al., 2004; Rondeau et al., 2008). Notably, beryl's FTIR spectra also presented strong crystallographic orientation phenomena: The relative intensity of these bands

varied when spectra were acquired under different crystallographic orientations. No bands linked to clarity enhancement of emerald, which are commonly observed at around 3000  $\text{cm}^{-1}$  (Johnson et al., 1999; Kiefert et al., 1999), were identified in any of these samples.

In figure 12A, a typical spectrum of a sample from the ENSMP 69881 suite is also presented in red. It is similar to the FTIR spectrum produced by other artificial glasses (Stephan, 2020; Cooper et al., 2020). Below 3200  $\text{cm}^{-1}$ , large bands due to combination modes and overtones of silicate glasses are observed. The bands at around 3500  $\text{cm}^{-1}$  are possibly due to symmetric stretching of water molecules and/or stretching vibrations of the Si-OH group. The weaker bands at around 4500  $\text{cm}^{-1}$  are due to combination Si-OH modes (Efimov and Pogareva, 2006).

**Summary of Results.** Of the 45 samples, 41 were confirmed to be emerald (suites ENSMP 69866 and 69880). As these stones are of gem quality and were set in the crown of Napoleon III in 1855, we can exclude any “young” emerald provenances, such as mines in Zambia and Zimbabwe, or even historic deposits with emeralds of lesser gem quality, such as those in Egypt and Austria (Giuliani et al., 2000, 2019).

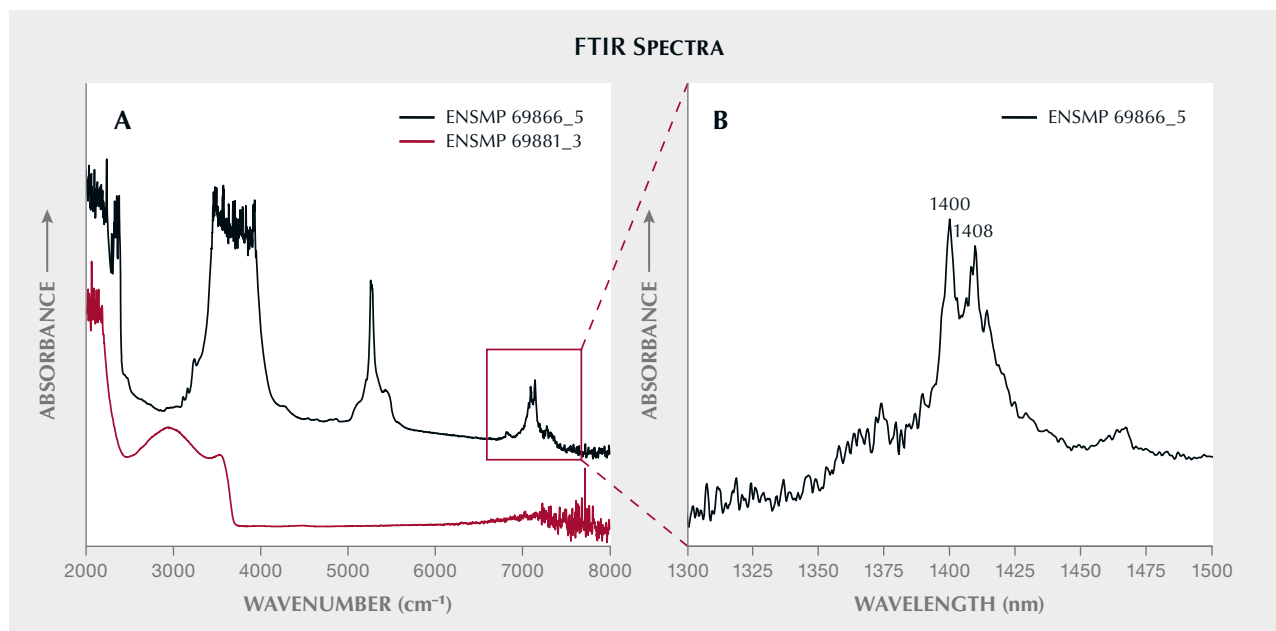


Figure 12. FTIR spectra of representative samples in this study. All spectra are shifted for clarity. A: FTIR spectra in the range of 2000 to 8000 cm<sup>-1</sup> for samples ENSMP 69866\_5 and ENSMP 69881\_3. Bands characteristic of vibrations in the beryl structure are observed in the black spectrum, and large bands linked to glass are observed in the red spectrum. B: FTIR spectrum in the range of 1300 to 1500 nm (about 7692–6666 cm<sup>-1</sup>) of sample ENSMP 69866\_5. The intensity of the band at about 1400 nm (due to type I water) is stronger than the intensity of the band at about 1408 nm (due to type II water).

From the sixteenth century until the early twentieth century, the vast majority of gem-quality emeralds originated from Colombia (Keller, 1981; Bosshart, 1991a, Giuliani et al., 2000; Schmetzer et al., 2020).

The existence of the specific inclusion scene (e.g., three-phase inclusions with jagged outlines and *gota de aceite*), the fact that the NIR band related to type I water in beryl is of equal or greater intensity than the band related to type II water (signifying the presence of relatively low concentrations of alkali metals), and the absence of iron-related absorption bands in the Vis-NIR spectra all suggest that the samples came from Colombian mines. None of the samples presented microscopic or spectroscopic evidence of clarity enhancement. Emeralds with similar characteristics are found in other jewels from the same period (Keller, 1981; Karampelas and Wörle, 2022).

The microscopic and spectroscopic data of the four samples from suite ENSMP 69881 were found to be consistent with artificial glass. This was first accounted for in the museum's internal gem identification report by one of the authors (FM), who made the determination using classic gemological tools in the 2010s. Their relatively high refractive index and specific gravity values point toward artificial glass con-

taining lead. The spectroscopic characteristics of the artificial glasses from Napoleon III's crown do not present any evidence of a recently fabricated glass. It is therefore possible that these imitations were part of the 1887 donation and not substituted at a later stage at the museum. Still, the cut and shape differ significantly from the identified emeralds, suggesting they were not set at the same time as the original crown's creation in 1855. Instead, they could have been replacements shortly thereafter, when the eight large main diamonds were removed for use in other jewels created for Empress Eugénie (Morel, 1988).

Additional nondestructive measurements of the trace elements with a well-calibrated energy-dispersive X-ray fluorescence (EDXRF) spectrometer might help to further study the fabrication of the green glasses and also support the Colombian origin of the emeralds. Moreover, the use of a Raman spectrometer with more than one laser excitation wavelength and better spectral resolution, combined with the use of spectrometers covering the UV region down to 250 nm and the NIR up to 1500 nm, would provide further assistance in identifying the fabrication of the green glasses and further confirming the emeralds' Colombian origin.

## CONCLUSIONS AND PERSPECTIVES

In all, 41 out of 45 samples from ENSMP 69866 and ENSMP 69880 showed natural inclusions along with standard gemological observations characteristic of emerald. The Vis-NIR spectra presented absorption bands characteristic of  $\text{Cr}^{3+}$  and  $\text{V}^{3+}$ , while iron-related bands were not observed in any of the spectra. In the NIR region, as analyzed by FTIR spectroscopy, the bands due to type I water were of equal or greater intensity than those due to type II water. A combination of spectroscopic and classic gemological methods points to Colombia as the most likely source of these 41 natural emeralds, given the crown's age.

The four samples from suite ENSMP 69881 presented different characteristics. Classic gemological testing methods identified them as artificial glasses containing lead. Their Vis-NIR spectra revealed  $\text{Fe}^{2+}$  and/or  $\text{Cu}^{2+}$  as well as  $\text{Fe}^{3+}$  (or  $\text{Fe}^{3+}\text{-S}^{2-}$ ) as the main causes of their coloration. We uncovered no evidence of the glass having been recently fabricated. Consequently, it is possible that these four artificial glass stones were set in the crown prior to their donation to the École des Mines. Morel (1988, p. 338) reports that the eight large diamonds were removed from the crown not long after its creation and replaced by “strass” (glass imitations, possibly containing lead). The substitution of these green glass stones for the original emeralds could have occurred at the same time.

As part of an ongoing collaboration between the LFG and the Mineralogy Museum of the École des Mines, the authors will continue investigating other gems that once belonged to the French crown jewels. It is only logical that in addition to exhibiting these gems, the Museum seeks to understand the science behind them, as educational and outreach tools. As this set of gems is considered a priceless national treasure, such studies can only be conducted within the Museum, using classical nondestructive gemo-

logical tools and mobile spectrometers. In the last two decades, several instruments useful for characterizing gems *in situ* have been developed in mobile versions, drawing the interest of researchers from various disciplines (Reiche et al., 2004; Petrová et al., 2012; Barone et al., 2016; Panczer et al., 2021; Karampelas and Wörle, 2022).

Only a few gemstones that once belonged to crown jewels or regalia have been scientifically examined—some still belong to royalty (Spain and the United Kingdom, for example), while others have been studied for their historical or artistic merit but not their gemological value. However, there has been a stronger desire over the last few decades to overcome these biases, and some museums are putting national treasures under their microscopes and spectrometers, publishing and sharing their results. We can acknowledge George Bosshart for conducting one of the first gemological studies of the Dresden Green, a 41 ct diamond from one of the oldest museums in the world, the Green Vaults (1723) in Dresden, Germany (Bosshart, 1989). As the French crown jewels were dispersed in 1887, a few pieces eventually landed in museums equipped with instruments and researchers willing to study great and historical gem treasures, such as the Hope diamond and the Napoleon diamond necklace at the Smithsonian Institution (Gaillou and Post, 2007; Gaillou et al., 2010, 2012, 2022; Post and Farges, 2014) and the Grand Sapphire of Louis XIV at the National Museum of Natural History in Paris (Farges et al., 2015). These gemstones are all remarkable not only for their history and consummate lapidary and jewelry skills, but also for the overall quality of the stones themselves and our understanding of their geologic and geographic origin. We can only hope that more museums will allow *in situ* nondestructive studies of their gemstones, whether set in jewels or not, in order to tell the full story and offer these treasures the appreciation they deserve.

### ABOUT THE AUTHORS

Dr. Karampelas (s.karampelas@ifg.paris) is chief gemologist, Mrs. Herreweghe, Mr. Hennebois, Mrs. Leblan, and Mrs. Meslin Sainte Beuve are gemologists, and Mr. Delaunay is director, at the Laboratoire Français de Gemmologie (LFG) in Paris. Dr. Gaillou (eloise.gaillou@minesparis.psl.eu) is curatrix, Mrs. Maouche is exhibit specialist, Mr. Lechartier is technician, and Dr. Nectoux is curator and director, of the Museum of Mineralogy, Mines Paris - PSL.

### ACKNOWLEDGMENTS

Sophie Guermann from University of Neuchâtel, Switzerland, is thanked for some of the information on the history of the crown. Constructive comments and suggestions of three anonymous reviewers are gratefully acknowledged.



## REFERENCES

- Adams D.M., Gardner I.R. (1974) Single-crystal vibrational spectra of beryl and diopside. *Journal of the Chemical Society, Dalton Transactions*, Vol. 14, pp. 1502–1505, <http://dx.doi.org/10.1039/dt9740001502>
- Balfour I. (1987) *Famous Diamonds*. Collins, London, 224 pp.
- Bapst G. (1889) *Histoire des Joyaux de la Couronne de France*, Hachette, Paris, 749 pp.
- Barone G., Mazzoleni P., Raneri S., Jehlička J., Vandenabeele P., Lottici P.P., Lamagna G., Manenti A.M., Bersani D. (2016) Raman investigation of precious jewelry collections preserved in Paolo Orsi regional museum (Siracusa, Sicily) using portable equipment. *Applied Spectroscopy*, Vol. 70, No. 9, pp. 1420–1431, <http://dx.doi.org/10.1177/0003702816662592>
- Ben Kacem I., Gautron L., Coillot D., Neuville D.R. (2017) Structure and properties of lead silicate glasses and melts. *Chemical Geology*, Vol. 461, pp. 104–114, <http://dx.doi.org/10.1016/j.chemgeo.2017.03.030>
- Bersani D., Azzi G., Lambruschi E., Barone G., Mazzoleni P., Raneri S., Longobardo U., Lottici P.P. (2014) Characterization of emeralds by micro-Raman spectroscopy. *Journal of Raman Spectroscopy*, Vol. 45, No. 11–12, pp. 1293–1300, <http://dx.doi.org/10.1002/jrs.4524>
- Bosshart G. (1989) The Dresden Green. *Journal of Gemmology*, Vol. 21, No. 6, pp. 351–362.
- (1991a) Emeralds from Colombia (Part 1). *Journal of Gemmology*, Vol. 22, No. 6, pp. 355–361.
- (1991b) Emeralds from Colombia (Part 2). *Journal of Gemmology*, Vol. 22, No. 7, pp. 409–425.
- Carl R., Gerlach S., Rüssel C. (2007) The effect of composition on UV-Vis-NIR spectra of iron doped glasses in the systems  $\text{Na}_2\text{O}/\text{MgO}/\text{SiO}_2$  and  $\text{Na}_2\text{O}/\text{MgO}/\text{Al}_2\text{O}_3/\text{SiO}_2$ . *Journal of Non-Crystalline Solids*, Vol. 353, No. 3, pp. 244–249, <http://dx.doi.org/10.1016/j.jnoncrysol.2006.11.010>
- Colomban P., Tournie A., Bellot-Gurlet L. (2006) Raman identification of glassy silicates used in ceramics, glass and jewellery: A tentative differentiation guide. *Journal of Raman Spectroscopy*, Vol. 37, No. 8, pp. 841–852, <http://dx.doi.org/10.1002/jrs.1515>
- Cooper A., Price J., Breitzmann H. (2020) Lab Notes: Artificial glass imitating a Paraíba tourmaline. *G&G*, Vol. 56, No. 4, pp. 518–520.
- de Donato P., Cheilletz A., Barres O., Yvon J. (2004) Infrared spectroscopy of OD vibrators in minerals at natural dilution: Hydroxyl groups in talc and kaolinite, and structural water in beryl and emerald. *Applied Spectroscopy*, Vol. 58, No. 5, pp. 521–527, <http://dx.doi.org/10.1366/000370204774103336>
- Efimov A.M., Pogareva V.G. (2006) IR absorption spectra of vitreous silica and silicate glasses: The nature of bands in the 1300 to 5000  $\text{cm}^{-1}$  region. *Chemical Geology*, Vol. 229, No. 1–3, pp. 198–217, <http://dx.doi.org/10.1016/j.chemgeo.2006.01.022>
- Farges F., Panczer G., Benbalagh N., Riondet G. (2015) The Grand Sapphire of Louis XIV and the Ruspoli sapphire. *G&G*, Vol. 51, No. 4, pp. 392–409, <http://dx.doi.org/10.5741/GEMS.51.4.392>
- Fritsch E., Rondeau B., Hainschwang T., Quellier M.-H. (2007) A contribution to the understanding of pink color in diamond: The unique, historical «Grand Condé». *Diamond and Related Materials*, Vol. 16, No. 8, pp. 1471–1474, <http://dx.doi.org/10.1016/j.diamond.2006.12.006>
- Fritsch E., Rondeau B., Devouard B., Pinsault L., Latouche C. (2017) Why are some crystals gem quality? Crystal growth considerations on the “gem factor.” *The Canadian Mineralogist*, Vol. 55, No. 4, pp. 521–533, <http://dx.doi.org/10.3749/canmin.1700013>
- Gaillou E., Post J.E. (2007) An examination of the Napoleon Diamond Necklace. *G&G*, Vol. 43, No. 4, pp. 352–357, <http://dx.doi.org/10.5741/GEMS.43.4.352>
- Gaillou E., Wang W., Post J.E., King J.M., Butler J.E., Collins A.T., Moses T.M. (2010) The Wittelsbach-Graff and Hope diamonds: Not cut from the same rough. *G&G*, Vol. 46, No. 2, pp. 80–88, <http://dx.doi.org/10.5741/GEMS.46.2.80>
- Gaillou E., Post J.E., Rost D., Butler J.E. (2012) Boron in natural type IIb blue diamonds: Chemical and spectroscopic measurements. *American Mineralogist*, Vol. 97, No. 1, pp. 1–18, <http://dx.doi.org/10.2138/am.2012.3925>
- Gaillou E., Maouche F., Barthe A., Nectoux D., Lechartier M. (2022) Émeraudes historiques de la collection de l'École Nationale Supérieure des Mines de Paris. *Le Règne Minéral*, in press.
- Galopim de Carvalho R. (2014) Evolution of diamond cuts in Portuguese jewellery and sacred objects during the 16th–18th centuries: A brief review. *Journal of Gemmology*, Vol. 34, No. 2, pp. 114–128.
- Giuliani G., Groat L.A. (2019) Geology of corundum and emerald gem deposits. *G&G*, Vol. 55, No. 4, pp. 464–489, <http://dx.doi.org/10.5741/GEMS.55.4.464>
- Giuliani G., Chaussidon M., Schubnel H.-J., Piat D.H., Rollion-Bard C., France-Lanord C., Giard D., de Narvaez D., Rondeau B. (2000) Oxygen isotopes and emerald trade routes since antiquity. *Science*, Vol. 287, No. 5453, pp. 631–633, <http://dx.doi.org/10.1126/science.287.5453.631>
- Giuliani G., Groat L.A., Marshall D., Fallick A.E., Branquet Y. (2019) Emerald deposits: A review and enhanced classification. *Minerals*, Vol. 9, No. 2, 63 pp., <http://dx.doi.org/10.3390/min9020105>
- Gübelin E.J., Koivula J.I. (1986) *Photoatlas of Inclusions in Gemstones, Volume 1*. Opinio Publishers, Basel, Switzerland, 532 pp.
- Hagemann H., Lucken A., Bill H., Gysler-Sanz J., Stalder H.A. (1990) Polarized Raman spectra of beryl and bazzite. *Physics and Chemistry of Minerals*, Vol. 17, No. 5, pp. 395–401, <http://dx.doi.org/10.1007/BF00212207>
- Hainschwang T. (2010) Une description de quelques émeraudes extraordinaires, les émeraudes gota de acete et les émeraudes étoilées. *Revue de l'Association Française de Gemmologie*, Vol. 171, pp. 7–9.
- Hainschwang T., Notari F., Fritsch E., Massi L. (2006) Natural, untreated diamonds showing the A, B and C infrared absorptions (“ABC diamonds”), and the H2 absorption. *Diamond and Related Materials*, Vol. 15, No. 10, pp. 1555–1564, <http://dx.doi.org/10.1016/j.diamond.2005.12.029>
- Huong L.T.-T., Häger T., Hofmeister W. (2010) Confocal micro-Raman spectroscopy: A powerful tool to identify natural and synthetic emeralds. *G&G*, Vol. 46, No. 1, pp. 36–41, <http://dx.doi.org/10.5741/GEMS.46.1.36>
- Huong L.T.-T., Hofmeister W., Häger T., Karamelas S., Kien N.D.-T. (2014) A preliminary study on the separation of natural and synthetic emeralds using vibrational spectroscopy. *G&G*, Vol. 50, No. 4, pp. 287–292, <http://dx.doi.org/10.5741/GEMS.50.4.287>
- Jehlička J., Culka A., Bersani D., Vandenabeele P. (2017) Comparison of seven portable Raman spectrometers: Beryl as a case study. *Journal of Raman Spectroscopy*, Vol. 48, No. 10, pp. 1289–1299, <http://dx.doi.org/10.1002/jrs.5214>
- Johnson M.L., Elen S., Muhlmeister S. (1999) On the identification of various emerald filling substances. *G&G*, Vol. 35, No. 2, pp. 82–107, <http://dx.doi.org/10.5741/GEMS.35.2.82>
- Kane R.E., McClure S.R., Menzhausen J. (1990) The legendary Dresden Green diamond. *G&G*, Vol. 26, No. 4, pp. 248–266, <http://dx.doi.org/10.5741/GEMS.26.4.248>
- Karamelas S., Wörle M. (2022) Spectroscopic study of the coloured gems in a 19th century pendant from Einsiedeln Abbey. *Journal of Raman Spectroscopy*, Vol. 53, No. 3, pp. 563–569, <http://dx.doi.org/10.1002/jrs.6194>
- Karamelas S., Al-Shaybani B., Mohamed F., Sangsawong S., Al-Alawi A. (2019) Emeralds from the most important occurrences: Chemical and spectroscopic data. *Minerals*, Vol. 9, No. 9, p. 561 (29 pp.), <http://dx.doi.org/10.3390/min9090561>
- Keller P.C. (1981) Emeralds of Colombia. *G&G*, Vol. 17, No. 2, pp. 80–92, <http://dx.doi.org/10.5741/GEMS.17.2.80>

- Kiefert L., Hänni H.A., Chalain J.-P., Weber W. (1999) Identification of filler substances in emeralds by infrared and Raman spectroscopy. *Journal of Gemmology*, Vol. 26, No. 8, pp. 501–520.
- Kim C.C., Bell M.I., McKeown D.A. (1995) Vibrational analysis of beryl ( $\text{Be}_3\text{Al}_2\text{Si}_6\text{O}_{18}$ ) and its constituent ring ( $\text{Si}_6\text{O}_{18}$ ). *Physica B: Condensed Matter*, Vol. 205, No. 2, pp. 193–208, [http://dx.doi.org/10.1016/0921-4526\(94\)00290-C](http://dx.doi.org/10.1016/0921-4526(94)00290-C)
- Krzemnicki M.S., Wang H.A.O., Büche S. (2021) A new type of emerald from Afghanistan's Panjshir Valley. *Journal of Gemmology*, Vol. 37, No. 5, pp. 474–495.
- Meulebroeck W., Baert K., Wouters H., Cosyns P., Ceglia A., Cagno S., Janssens K., Nys K., Terryn H., Thienpont H. (2010) The identification of chromophores in ancient glass by the use of UV-Vis-NIR spectroscopy. *Conference Proceedings SPIE Photonics Europe - Optical Sensing and Detection*, p. 77260D, <http://dx.doi.org/10.1117/12.853666>
- Meulebroeck W., Cosyns P., Baert K., Wouters H., Cagno S., Janssens K., Terryn H., Nys K., Thienpont H. (2011) Optical spectroscopy as a rapid and low-cost tool for the first-line analysis of glass artefacts: A step-by-step plan for Roman green glass. *Journal of Archaeological Science*, Vol. 38, No. 9, pp. 2387–2398, <http://dx.doi.org/10.1016/j.jas.2011.04.023>
- Meulebroeck W., Wouters H., Nys K., Thienpont H. (2016) Authenticity screening of stained glass windows using optical spectroscopy. *Scientific Reports*, Vol. 6, article no. 37726, 10 pp., <http://dx.doi.org/10.1038/srep37726>
- Morel B. (1988) *The French Crown Jewels*. Fonds Mercator, Antwerp, 417 pp.
- Moroz I., Roth M., Boudeulle M., Panczer G. (2000) Raman microspectroscopy and fluorescence of emeralds from various deposits. *Journal of Raman Spectroscopy*, Vol. 31, No. 6, pp. 485–490, [http://dx.doi.org/10.1002/1097-4555\(200006\)31:6%3C485::AID-JRS561%3E3.0.CO;2-M](http://dx.doi.org/10.1002/1097-4555(200006)31:6%3C485::AID-JRS561%3E3.0.CO;2-M)
- Nassau K. (1980) *Gems Made by Man*. Chilton Book Company, Radnor, Pennsylvania, 364 pp.
- Panczer G., Romeo E., Riondet G. (2021) The book of hours of King Francis I of France: History and gemmological analysis. *Journal of Gemmology*, Vol. 37, No. 6, pp. 580–595.
- Patch S.S. (1976) *Blue Mystery: The Story of the Hope Diamond*. Smithsonian Institution Press, Washington, DC.
- Petrová Z., Jehlička J., Čapoun T., Hanus R., Trojek T., Goliáš V. (2012) Gemstones and noble metals adorning the sceptre of the Faculty of Sciences of Charles University in Prague: Integrated analysis by Raman and XRF handheld instruments. *Journal of Raman Spectroscopy*, Vol. 43, No. 9, pp. 1275–1280, <http://dx.doi.org/10.1002/jrs.4043>
- Post J.E., Farges F. (2014) The Hope diamond: Rare gem, historic jewel. *Rocks & Minerals*, Vol. 89, No. 1, pp. 16–26, <http://dx.doi.org/10.1080/00357529.2014.842831>
- Reiche I., Pages-Camagna S., Lambacher L. (2004) *In situ* Raman spectroscopic investigations of the adorning gemstones on the reliquary *Heinrich's Cross* from the treasury of Basel Cathedral. *Journal of Raman Spectroscopy*, Vol. 35, No. 8-9, pp. 719–725, <http://dx.doi.org/10.1002/jrs.1197>
- Ringsrud R. (2008) *Gota de aceite*: Nomenclature for the finest Colombian emeralds. *G&G*, Vol. 44, No. 3, pp. 242–245, <http://dx.doi.org/10.5741/GEMS.44.3.242>
- Robinet L., Couptry C., Eremin K., Hall C. (2006) The use of Raman spectrometry to predict the stability of historic glasses. *Journal of Raman Spectroscopy*, Vol. 37, No. 7, pp. 789–797, <http://dx.doi.org/10.1002/jrs.1540>
- Rondeau B., Fritsch E., Peucat J.-J., Nordrum F.S., Groat L.A. (2008) Characterization of emeralds from a historical deposit: Byrud (Eidsvoll), Norway. *G&G*, Vol. 44, No. 2, pp. 108–122, <http://dx.doi.org/10.5741/GEMS.44.2.108>
- Saeseaw S., Pardieu V., Sangsawong S. (2014) Three-phase inclusions in emerald and their impact on origin determination. *G&G*, Vol. 50, No. 2, pp. 114–132, <http://dx.doi.org/10.5741/GEMS.50.2.114>
- Saeseaw S., Renfro N.D., Palke A.C., Sun Z., McClure S.F. (2019) Geographic origin determination of emerald. *G&G*, Vol. 55, No. 4, pp. 614–646, <http://dx.doi.org/10.5741/GEMS.55.4.614>
- Sakurai Y., Nagasawa K., Nishikawa H., Ohki Y. (1999) Characteristic red photoluminescence band in oxygen-deficient silica glass. *Journal of Applied Physics*, Vol. 86, No. 1, pp. 370–373, <http://dx.doi.org/10.1063/1.370740>
- Schmetzer K. (2014) Letters: Analysis of three-phase inclusions in emerald. *G&G*, Vol. 50, No. 4, pp. 316–319.
- Schmetzer K., Martayan G., Ortiz J.G. (2020) History of the Chivor emerald mine, part I (1880–1925): From rediscovery to early production. *G&G*, Vol. 56, No. 1, pp. 66–109, <http://dx.doi.org/10.5741/GEMS.56.1.66>
- Schreurs J.W.H., Brill R.H. (1984) Iron and sulfur related colors in ancient glasses. *Archaeometry*, Vol. 26, No. 2, pp. 199–209, <http://dx.doi.org/10.1111/j.1475-4754.1984.tb00334.x>
- Skujala L. (1998) Optically active oxygen-deficiency-related centers in amorphous silicon dioxide. *Journal of Non-Crystalline Solids*, Vol. 239, No. 1-3, pp. 16–48, [http://dx.doi.org/10.1016/S0022-3093\(98\)00720-0](http://dx.doi.org/10.1016/S0022-3093(98)00720-0)
- Stephan M. (2020) Lab Notes: Clarity-enhanced glass imitating emerald. *G&G*, Vol. 56, No. 1, p. 133.
- Thomson D.B., Kidd J.D., Aström M., Scarani A., Smith C.P. (2014) A comparison of R-line photoluminescence of emeralds from different origins. *Journal of Gemmology*, Vol. 34, No. 4, pp. 334–343.
- Webster R., Anderson B.W. (1983) *Gems: Their Sources, Descriptions and Identification*, 4th ed. Butterworth-Heinemann, Oxford, UK, 1044 pp.
- Wood D.L. (1965) Absorption, fluorescence, and Zeeman effect in emerald. *The Journal of Chemical Physics*, Vol. 42, No. 10, pp. 3404–3410, <http://dx.doi.org/10.1063/1.1695742>
- Wood D.L., Nassau K. (1967) Infrared spectra of foreign molecules in beryl. *The Journal of Chemical Physics*, Vol. 47, No. 7, pp. 2220–2228, <http://dx.doi.org/10.1063/1.1703295>
- (1968) Characterization of beryl and emerald by visible and infrared absorption spectroscopy. *American Mineralogist*, Vol. 53, No. 5-6, pp. 777–800.

# CHARACTERISTICS OF NEWLY DISCOVERED AMBER FROM PHU QUOC, VIETNAM

Le Ngoc Nang, Pham Trung Hieu, Lam Vinh Phat, Pham Minh Tien, Ho Nguyen Tri Man, and Ha Thuy Hang

The authors examine the gemological properties and commercial potential of a new source of amber, discovered in 2020 on the Vietnamese island of Phu Quoc. It is the only known amber locality in Vietnam so far. The Phu Quoc amber possesses reddish orange to orangy yellow hues and is transparent, with sizes up to 10 cm. The samples exhibited strong blue fluorescence under ultraviolet light (both long-wave and short-wave). Internally, they displayed disk-like inclusions and gas bubbles, but few botanical inclusions were found. Their characteristic FTIR peaks can be distinguished from those of amber found in other sources worldwide. Although amber from Phu Quoc is a recent discovery and has only been investigated in two small areas, its commercial potential is promising based on the samples' quality and the wide distribution of the host rock on the island.

Amber, an organic gemstone fossilized from tree resin (Ross, 1999), comes from several sources globally, most notably the Baltic region, Myanmar, the Dominican Republic, and Indonesia. Amber from each locality shows distinctive characteristics. In 2020, a sandstone miner working on the Vietnamese island of Phu Quoc came across an orange-yellow material buried inside the sandstone layers. He collected loose and bedrock-hosted samples, the largest up to 10 cm (figure 1), and submitted them to Liu Gemological

*Figure 1. Amber from Phu Quoc: matrix measuring approximately 6 × 10 cm and a 1.69 ct, 11.93–9.41 × 4.98 mm cabochon of transparent, orangy red amber set in a 14K gold ring. Photo by Le Ngoc Nang.*



Research and Application Center (LIULAB) in Ho Chi Minh City, where they were identified as amber. With the miner's help, the authors visited the site to collect amber samples. During our field trip, we found a second deposit, also in a sandstone mine, located about a kilometer from the first amber outcrop (figure 2).

## In Brief

- Vietnamese amber was first discovered on the island of Phu Quoc in 2020.
- The amber is characterized by strong blue fluorescence under UV lighting and weak green fluorescence under daylight-equivalent illumination.
- Amber nodules were found in sandstone, accompanied by veins of black jet. The wide coverage of sandstone on the island suggests the possibility of additional discoveries.
- Phu Quoc amber's gemological properties are relatively similar to those from other global sources, but it can be differentiated by FTIR spectroscopy.

In the present study, Phu Quoc amber was characterized with standard gemological methods and Fourier-transform infrared spectroscopy (FTIR). Our results, combined with other published data from Baltic, Burmese, and Dominican amber (Wolfe et al.,

See end of article for About the Authors and Acknowledgments.

GEMS & GEMOLOGY, Vol. 58, No. 2, pp. 184–194,

<http://dx.doi.org/10.5741/GEMS.58.2.184>

© 2022 Gemological Institute of America

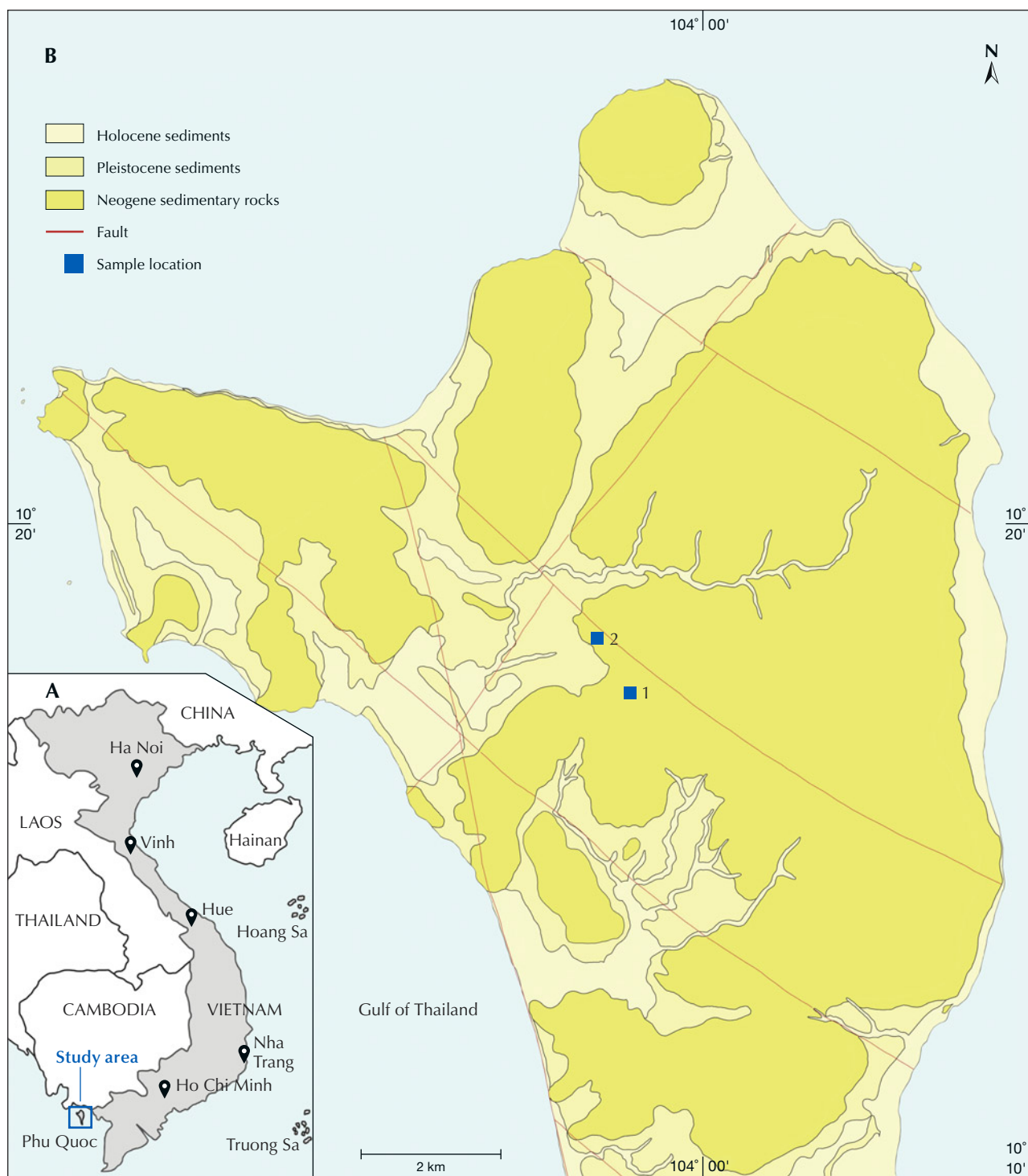


Figure 2. Geological map of northern Phu Quoc, from Duong et al. (1998) and modified by Le Ngoc Nang (2021). The two study areas (1 and 2) were visited in November 2020.

2009; Leelawatanasuk et al., 2013; Sun et al., 2015; Zhang et al., 2020), allowed us to compare the Phu Quoc samples with amber from commercially important sources.

### GEOLOGICAL SETTING

The island of Phu Quoc lies in the Gulf of Thailand, about 45 km off the southwestern coast of Vietnam. The island has an area of 574 km<sup>2</sup>. The terrain con-



Figure 3. A: Sandstone mine (site 1). B and C: Nodules of amber found in sandstone boulders, recovered from a depth of 15–20 m at site 1. Photos by Lam Vinh Phat.

sists mainly of low mountains, with the highest peak standing at 607 m (Duong et al., 1998). The amber sites found so far are in an area that is easily accessible by vehicle.

The geological formations in Phu Quoc are mostly sandstone and siltstone from the Miocene to the Holocene. The Phu Quoc amber source lies in the northern center of the island (figure 2), mainly containing Neogene sedimentary rocks, and is divided into two parts. The lower part is interbedded conglomerate, sandstone, and gray and green silt-

stone, distributed on the eastern margin of the island; the upper part is jet- and amber-bearing quartz sandstone with cross-bedding structure, distributed throughout most of northern Phu Quoc (My and Linh, 2005). The upper part is unconformably overlain by Holocene sediments.

The Phu Quoc amber is hosted in gray to whitish gray and fine- to medium-grained sandstone (My and Linh, 2005; Fyhn et al., 2010) (figure 3). Found in sandstone as nodules, samples are nearly round or distorted oval in shape, varying in size from a few

centimeters to 10 centimeters. The boundary between amber and sandstone is clear but uneven and difficult to detach (figures 1 and 3). Surrounding amber in sandstone is black jet in the form of plates, with veins in matrix ranging in size from a few centimeters to several tens of centimeters. Part of the amber boundary is in contact with the sandstone, and the rest is attached to the jet. The sedimentary rocks containing amber are situated at a depth of about 15–20 m and are about 30 m thick, accompanied by lamellar-like jet. The amber-bearing sedimentary rock is quartz sandstone with massive structure. Rock-forming minerals are >90% quartz and <10% cement (sericitized clay minerals), as seen under a petrographic microscope (figure 4).

### MATERIALS AND METHODS

A total of 38 amber samples (31 loose samples and 7 samples in matrix) were collected from two locations (sites 1 and 2) on November 17 and 18, 2020. These consisted of 26 samples (22 loose and 4 in matrix) from site 1 and 12 samples (nine loose and three in matrix) from site 2. In addition, we received three samples (two loose and one in matrix) from the sandstone mine worker from site 1. Twelve of the Phu Quoc samples were used for research analysis: two loose samples (nos. 1 and 2) from the mine

worker, and ten samples (nos. 3–12: eight loose and two in matrix) from the authors' set of 38 samples from both sites (figure 2). The samples were chosen based on size and quality. Five samples were cut into cabochons by one of the authors (PMT), and seven were kept rough (figure 5). For refractive index and FTIR measurements, the authors selected rough samples that had at least one flat-polished surface, were free of pores, and weighed more than 5 ct. The amber-bearing sandstones consisted mainly of amber and jet.

We used three additional samples from Myanmar (A-3), the Baltic Sea (Poland, A-2), and the Dominican Republic (A-1) to compare with the Phu Quoc amber by conducting gemological testing and FTIR advanced analysis at LIULAB (figure 5). Those three samples belong to the collection of minerals and gems of the Faculty of Geology, University of Science, Ho Chi Minh City.

Standard gemological methods were used to confirm the identity of the studied samples as amber. The amber's color was observed under a 60 W GLS LED daylight bulb (5000–6000K). Specific gravity values for samples 1–6 and 9–12 were measured using a hydrostatic scale, and their refractive indexes were recorded with a standard gemological refractometer. A polariscope was used to observe optical features on the

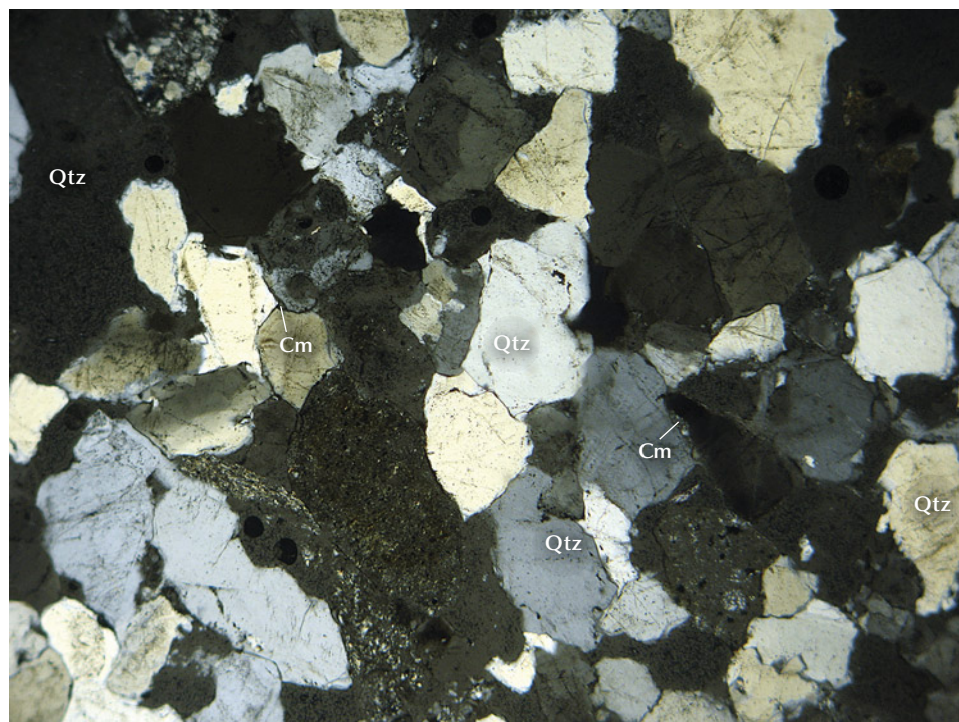


Figure 4. An amber-bearing sandstone thin section containing quartz (Qtz) and a small amount of cement (Cm; mainly sericitized clay minerals) surrounding the quartz grains. Photomicrograph by Ha Thuy Hang; field of view 0.6 mm.



Figure 5. The amber samples used in this study were in bedrock, rough, or cut into cabochons. Samples 1–12 are from Phu Quoc, A-1 from the Dominican Republic, A-2 from the Baltic region, and A-3 from Myanmar. Photos by Le Ngoc Nang.

same samples. Fluorescence reaction was tested on all the samples under ultraviolet light, both long-wave (365 nm) and short-wave (254 nm). Internal features were observed under a Carton SPZV50 gemological

microscope with 7× to 50× magnification. A 3 μm thin section of amber-bearing sandstone was examined under an Olympus CH-2 petrographic microscope at magnifications of 100×, 200×, and 400×.

For all samples, a hot needle test was applied to check for the characteristic scent of natural resin. We also checked the reaction to acetone as a means of separating amber from copal. Amber does not react with acetone, while copal reacts with acetone after 20 seconds (Ross, 1999).

Twelve amber samples—nine from Phu Quoc and one each from the Baltic Sea, Myanmar, and the Dominican Republic—were analyzed using an Agilent Cary 630 FTIR spectrometer. Data were acquired with a spectral range of 4000–650  $\text{cm}^{-1}$ , a resolution of 8  $\text{cm}^{-1}$ , and a scan time of 32 s.

## RESULTS AND DISCUSSION

Under daylight-equivalent illumination, the amber samples from Phu Quoc were predominantly reddish orange or orangy yellow. Black patches and spots in some samples (6 and 10) were preserved flora (tree bark). The samples exhibited predominantly subvit-

reous to resinous luster, and many samples displayed good transparency (figure 5). The samples also exhibited a white streak.

**Gemological Characteristics.** The specific gravity values of the 10 tested samples ranged from 1.03 to 1.04, corresponding to the SG of amber (Ross, 1999; Sun et al., 2015). These same 10 samples were singly refractive and had refractive index values ranging from 1.540 to 1.543, also consistent with amber (Ross, 1999; Sun et al., 2015) (table 1). Under long-wave and short-wave UV light, all Phu Quoc amber samples displayed strong to very strong light blue fluorescence (figure 6, top). They emitted green fluorescence on the surface under daylight-equivalent illumination (figure 6, bottom right) or against a dark background. The fluorescence phenomenon of the Phu Quoc amber is similar to that of Dominican and Indonesian amber (Poinar, 2010; Leelawatanasuk et al., 2013; Liu et al., 2014;

*Figure 6. Luminescence of Phu Quoc amber. All of the samples emitted strong to very strong light blue fluorescence in both long-wave (top left) and short-wave (top right) UV light. The bodycolor of Phu Quoc amber sample 3 is reddish orange (bottom left) and emitted weak green fluorescence under daylight-equivalent illumination (bottom right). Photos by Le Ngoc Nang.*

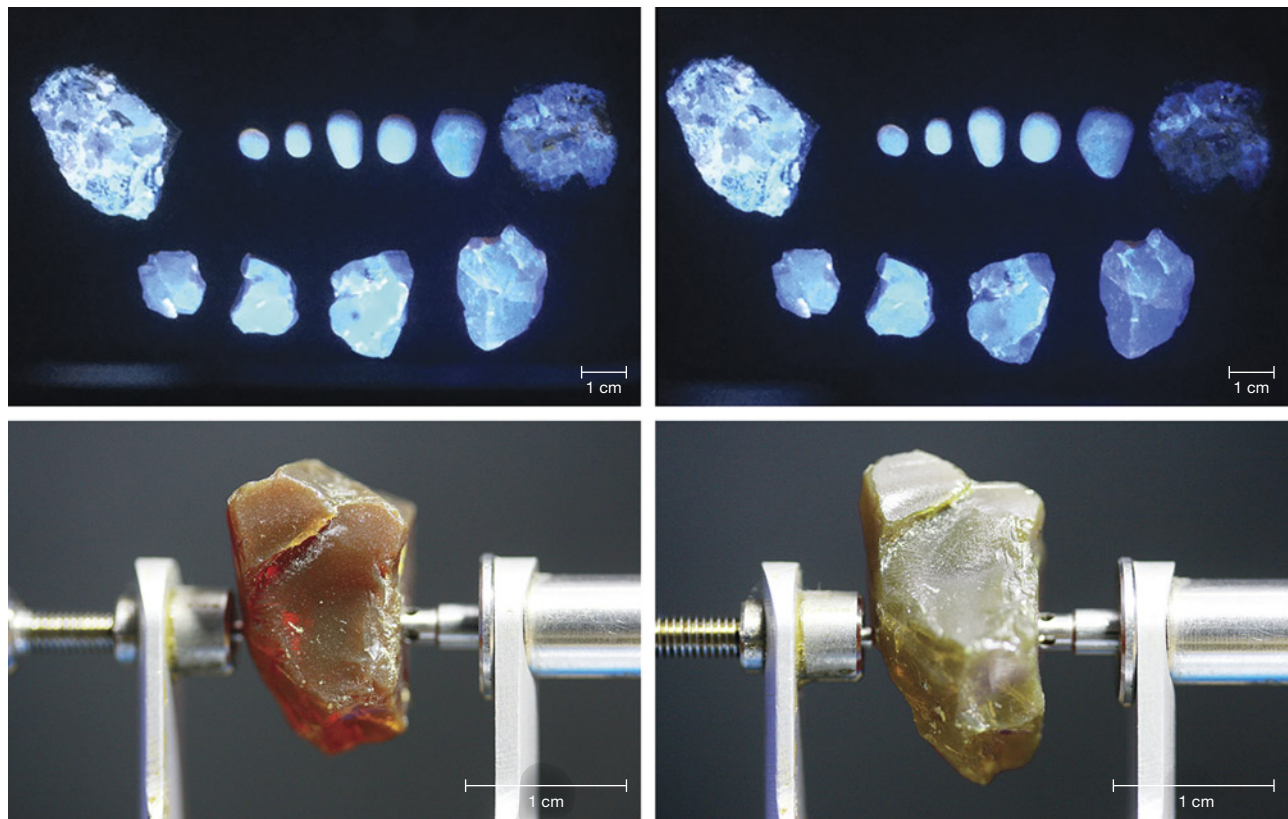




**TABLE 1.** Gemological properties of amber from Phu Quoc, Vietnam.

Sample no.	Weight (ct)	Color	Shape	SG	RI	Inclusions
1	17.92	Yellowish orange	Irregular	1.04	1.540	Spangle, gas bubble
2	22.11	Intense reddish orange	Irregular	1.06	1.541	Spangle, gas bubble, flora
3	7.22	Reddish orange	Irregular	NA	NA	Gas bubble, flora
4	10.03	Intense reddish orange	Irregular	1.04	1.542	Gas bubble, flora
5	5.18	Orangy red	Irregular	1.05	1.540	Gas bubble, flora
6	5.10	Brownish yellowish orange	Pear	1.05	1.541	NA
7	122.77 <sup>a</sup>	Yellow	Roundish nodule	NA	NA	NA
8	76.40 <sup>a</sup>	Reddish orange	In matrix	NA	NA	Gas bubble, flora
9	1.69	Reddish orange	Oval	1.05	1.541	Spangle, gas bubble
10	1.99	Intense bluish reddish orange	Drop	1.04	1.543	Gas bubble
11	0.82	Reddish orange	Oval	1.04	1.542	Spangle, gas bubble
12	1.05	Orangy yellow	Oval	1.03	1.542	Spangle, gas bubble
A-1	4.68	Yellow	Near-round	1.04	NA	None
A-2	7.16	Orangy yellow	Near-round	1.07	1.542	Spangle, gas bubble
A-3	11.94	Yellow-orange	Drop	1.03	1.540	Gas bubble, insect

<sup>a</sup>Total weight of sample, including host rock, in grams. NA: not available

Kocsis et al., 2020; Zhang et al., 2020). However, the Phu Quoc amber showed weaker fluorescence under daylight than Dominican or Indonesian amber.

Hot needle testing on all 12 amber samples released the natural scent of resin, distinguishing it from the burning scent of synthetic polymer (Ross, 1999). None of the Phu Quoc samples reacted to acetone, proving they were amber and not copal (Ross, 1999).

**Optical Characteristics.** Under the polariscope, the Phu Quoc amber presented the phenomenon of alternately blinking light and dark when rotated every

45°. Although there are no detailed studies to explain the phenomenon, this optical characteristic known as anomalous double refraction (ADR) is commonly seen under a polariscope. Accordingly, internal stress helps to explain the degree of anomalous extinction in amber (Kratochvíl, 2009).

**Internal Characteristics.** The Phu Quoc samples contained four types of internal characteristics: gas bubbles, disk-like inclusions (spangle) with a colorless core inside, round-film inclusions, and flora inclusions (figure 7 and table 1). Gas bubble inclusions indicating

the origin as tree resin (viscous and cool) are found in amber from most sources worldwide. In Phu Quoc samples, the gas bubble inclusions were accompanied by a typical flow structure. The disk-like inclusions contained air bubbles at the center, suggesting the condition of Phu Quoc amber, which were influenced by geothermal heat due to sedimentary depth (depth of burial) (Ross, 1999). Round-film inclusions are quite commonly seen, and they are also the spangles that reflect light to create interference colors. The flora inclusions were remnants of reddish brown wood fibers. Significantly, insects were not found in any of the amber samples inspected, unlike amber from most other sources (Penney, 2016).

**FTIR Analysis.** The FTIR spectra of the Phu Quoc samples shown in figure 8A include peaks at 2923, 2861, 2100, 1695, 1455, 1379, 1261, 1156, 970, and 815  $\text{cm}^{-1}$ . The FTIR results of Baltic, Burmese, and

Dominican amber are shown in figure 8, B–D. The results were consistent with previously published FTIR spectra of Burmese amber (Jiang et al., 2020), Baltic amber (Guiliano et al., 2007; Wolfe et al., 2009), and Dominican amber (Xin et al., 2021).

Phu Quoc amber exhibited an absorption band at around 2900  $\text{cm}^{-1}$  with two peaks at 2923 and 2861  $\text{cm}^{-1}$ , representing the stretching vibration of the  $\text{sp}^3$  hybridized C-H bond of the methyl and methylene groups (Guiliano et al., 2007). These are the typical absorption bands of amber and plastic or materials containing the C-H bond.

In the range of 2800–1800  $\text{cm}^{-1}$ , Phu Quoc amber displayed a weak band at 2100  $\text{cm}^{-1}$  caused by alkyne  $\text{C}\equiv\text{C}$  stretching, which was similar to that of Dominican samples. Meanwhile, Burmese and Baltic amber did not show any significant bands in this region.

The spectral range between 1800 and 1200  $\text{cm}^{-1}$  for Phu Quoc amber included a peak at 1455  $\text{cm}^{-1}$  for

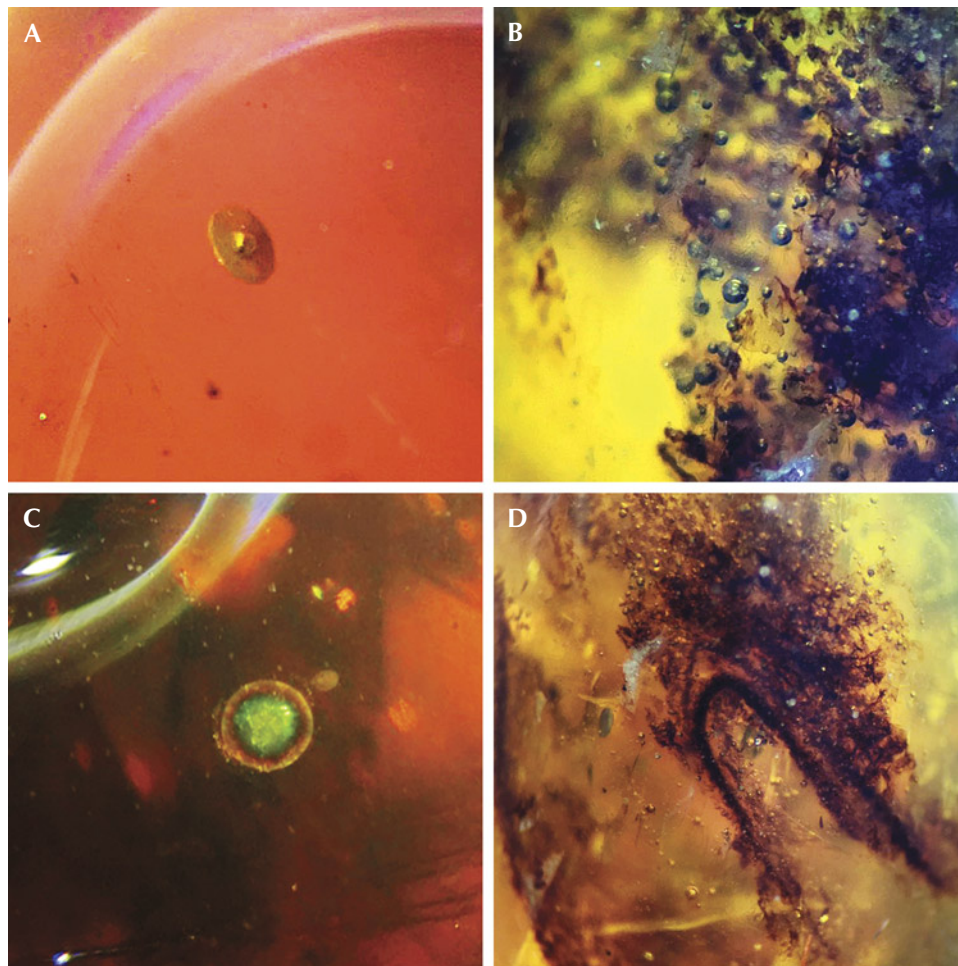


*Figure 7. Inclusions in Phu Quoc amber. A: A spangle with an inclusion at the center. B: Gas bubbles assembled with botanical remnants. C: A spangle with interference colors. D: Tree bark remnants. Photomicrographs by Le Ngoc Nang; fields of view 4.5 mm (A and C) and 5.5 mm (B and D).*

methylene ( $\text{CH}_2$ ) bending and another at  $1379\text{ cm}^{-1}$  for methyl ( $\text{CH}_3$ ) bending (Pavia et al., 2014). The strong absorption bands at  $1695$  and  $1261\text{ cm}^{-1}$  are related to  $\text{C}=\text{O}$  stretching and  $\text{C}-\text{O}$  carbonyl bonds, respectively (possibly ester and acid). The simultaneous presence of the peaks shows that there are many types of carbonates in this amber's composition (Sun et al., 2015). In the  $1800\text{--}1200\text{ cm}^{-1}$  range, the spectral absorption bands were similar to those of the Dominican samples. Meanwhile, the absence of a  $1261\text{ cm}^{-1}$  peak in Burmese and Baltic amber differentiated them from Phu Quoc amber.

Between  $1200$  and  $800\text{ cm}^{-1}$ , the Phu Quoc amber displayed weak absorption peaks at  $1156$ ,  $970$ , and  $815\text{ cm}^{-1}$ , while Burmese, Baltic, and Dominican amber displayed medium absorption peaks at  $1149$ ,  $1031$ ,  $975$ , and  $813\text{ cm}^{-1}$ . The weak  $1156\text{ cm}^{-1}$  peak is

assigned to  $\text{C}-\text{O}$  stretching of tertiary alcohol (Pavia et al., 2014). Additionally, the Baltic amber presented a spectral peak at  $888\text{ cm}^{-1}$ . For Phu Quoc amber, no peaks were detected at  $3048$ ,  $1642$ , and  $887\text{ cm}^{-1}$ , proving it was genuine amber rather than copal (Sun et al., 2015).

The FTIR spectra of Phu Quoc samples exhibited characteristics similar to those of Baltic, Burmese, and Dominican amber. However, the spectra of Phu Quoc amber displayed some characteristics unique to the deposit. The existence of  $1261$  and  $1156\text{ cm}^{-1}$  bands and the absence of  $3450$  and  $1149\text{ cm}^{-1}$  peaks revealed distinguishing features in both composition and polymer structures. These differences play an important role in defining the geographic origin of amber from global sources (including Phu Quoc amber).

Figure 8. FTIR spectra of amber from Phu Quoc (A) and other sources (B–D).

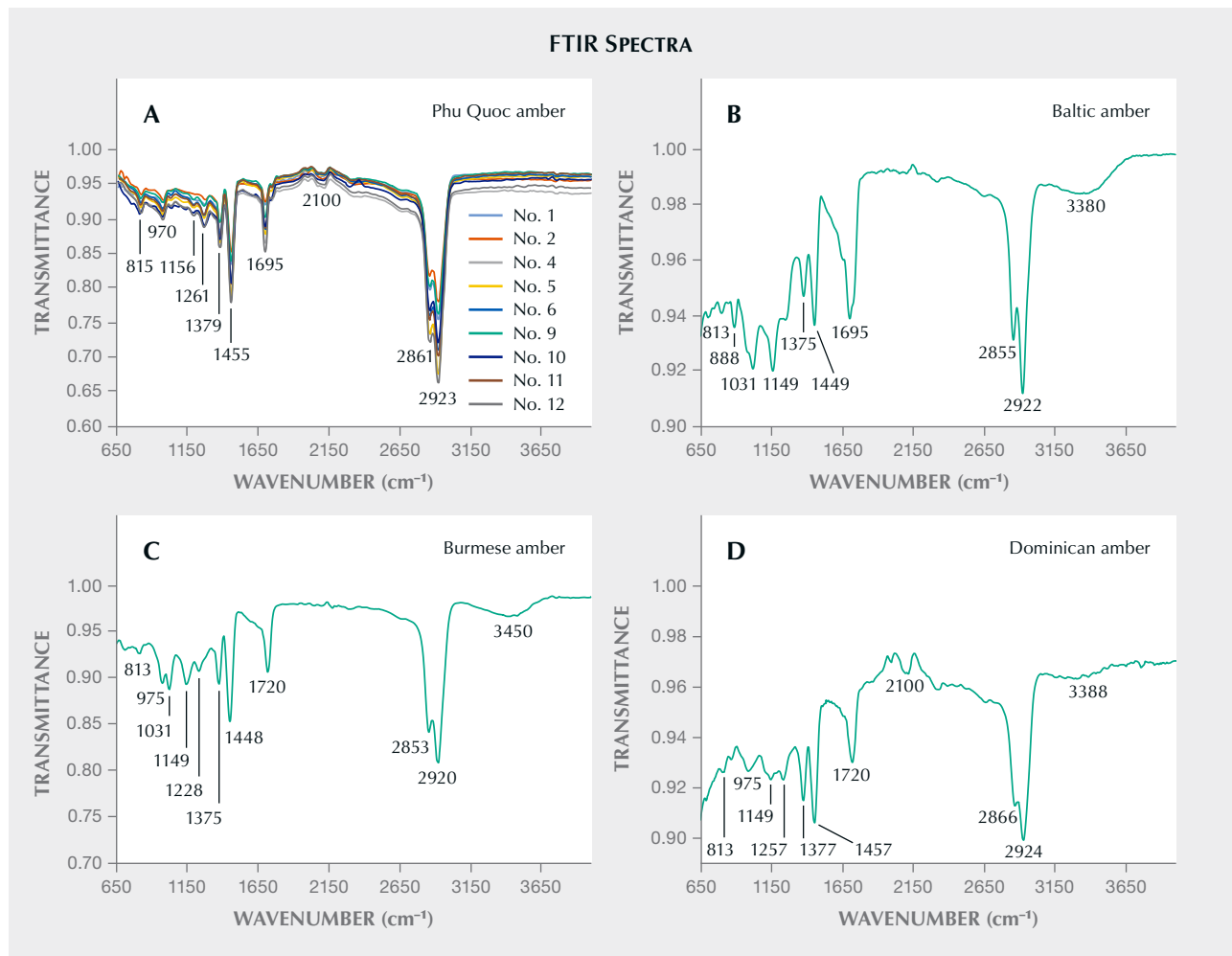




Figure 9. Gem-quality amber from Phu Quoc: an 11.16 ct rough and cabochons weighing 1.02–1.40 ct. Photo by Le Ngoc Nang.

## COMMERCIAL POTENTIAL

Based on our initial evaluation, Phu Quoc amber is of high enough quality to be suitable for jewelry manufacturing (figures 1 and 9). The color ranges from highly valued yellowish orange to orangy red, similar to that of Baltic and Burmese amber. Most are transparent, especially the samples smaller than 1 cm. The Phu Quoc amber is suitable for cabochons and carvings. Although we carried out our research within a small area, the sandstone formation (amber host rock) covers almost the entire island (My and Linh, 2005), suggesting the possibility of finding amber over a wide area. While these factors signal

the commercial potential of Phu Quoc amber, further assessment is needed.

## CONCLUSIONS

Standard gemological properties, FTIR spectroscopy, and other tests confirmed that the samples represent the first Vietnamese source of amber. The material's attractive color, transparency, and size make it suitable for jewelry. In addition, the wide distribution of the Neogene sandstone host rock on this island indicates strong commercial potential. With the discovery of amber on Phu Quoc, Vietnam could become an important supplier of this organic gem.

### ABOUT THE AUTHORS

Le Ngoc Nang is a postgraduate in the Faculty of Geology at the University of Science (<https://en.hcmus.edu.vn>), Vietnam National University Ho Chi Minh City, and CEO of Liu Gemological Research and Application Center. Dr. Pham Trung Hieu is associate professor in the Faculty of Geology at the University of Science, Vietnam National University Ho Chi Minh City. Lam Vinh Phat is manager of gemstone identification, and Pham Minh Tien is a technical specialist, at Liu Gemological Research and Application Center. Ho Nguyen Tri Man is a lecturer in the Faculty of Geology and Petroleum Engineering at the University of Technology, Viet-

nam National University. Ha Thuy Hang is a lecturer in the Faculty of Geology at the University of Science, Vietnam National University Ho Chi Minh City.

### ACKNOWLEDGMENTS

The authors sincerely thank Mr. Nguyen Thanh Nha from the Institute of Chemical Technology for his support in utilizing advanced analysis methods. We also express gratitude to our clients for the use of their samples to carry out this research. This research was funded by Vietnam National University Ho Chi Minh City (VNU-HCM) under grant number C2022-18-31.

## REFERENCES

- Duong C.T. et al. (1998) Report on the result of geological mapping and mineral exploration. Ha Tien – Phu Quoc map series, scale 1:50,000, South Vietnam Geological Mapping Division, General Department of Geology and Minerals of Vietnam (in Vietnamese).
- Fyhn M.B., Petersen H.I., Mathiesen A., Nielsen L.H., Pedersen S.A., Lindström S., Bojesen-Koefoed J.A., Abatzis I., Boldreel L.O. (2010) Vietnamese sedimentary basins: Geological evolution and petroleum potential. *GEUS Bulletin*, Vol. 20, pp. 91–94, <http://dx.doi.org/10.34194/geusb.v20.4990>
- Guiliano M., Asia L., Onoratini G., Mille G. (2007) Applications of diamond crystal ATR FTIR spectroscopy to the characterization of ambers. *Spectrochimica Acta Part A: Molecular Biomolecular Spectroscopy*, Vol. 67, No. 5, pp. 1407–1411, <http://dx.doi.org/10.1016/j.saa.2006.10.033>
- Jiang X., Zhang Z., Wang Y., Kong F. (2020) Gemmological and spectroscopic characteristics of different varieties of amber from the Hukawng Valley, Myanmar. *Journal of Gemmology*, Vol. 37, No. 2, pp. 144–162.
- Kocsis L., Usman A., Jourdan A.-L., Hassan S.H., Jumat N., Daud D., Briguglio A., Slik F., Rinyu L., Futó I. (2020) The Bruneian record of “Borneo amber”: A regional review of fossil tree resins in the Indo-Australian Archipelago. *Earth-Science Reviews*, Vol. 201, article no. 103005, <http://dx.doi.org/10.1016/j.earscirev.2019.103005>
- Kratochvíl P. (2009) Structure and properties of polymers. *Materials Science and Engineering*, Vol. 1, pp. 135–156. In R.D. Rawlings, Ed., *Encyclopedia of Life Support Systems*, EOLSS Publishers, Oxford, UK.
- Leelawatanasuk T., Wathanakul P., Paramita S., Sutthirat C., Sriprasert B., Bupparennoo P. (2013) The characteristics of amber from Indonesia. *The Australian Gemmologist*, Vol. 25, No. 4, pp. 142–145.
- Liu Y., Shi G., Wang S. (2014) Color phenomena of blue amber. *G&G*, Vol. 50, No. 2, pp. 134–140, <http://dx.doi.org/10.5741/GEMS.50.2.134>
- My B.P., Linh T.H. (2005) On the stratigraphy and age of continental sediments in the Phu Quoc Island, Tho Chu and An Thoi archipelagoes, Kien Giang Province. *Journal of Geology*, pp. A/291.
- Pavia D.L., Lampman G.M., Kriz G.S., Vyvyan J.A. (2014) *Introduction to Spectroscopy*, 5th ed. Cengage Learning, Stamford, Connecticut.
- Penney D. (2016) *Amber Palaeobiology: Research Trends and Perspectives for the 21st Century*. Siri Scientific Press.
- Poinar G. (2010) Palaeoecological perspectives in Dominican amber. In *Proceedings Annales de la Société entomologique de France*, Vol. 46, Taylor & Francis, pp. 23–52.
- Ross A. (1999) *Amber*. Harvard University Press, Cambridge, Massachusetts, 112 pp.
- Sun T.T., Kleišmantas A., Nyunt T.T., Minrui Z., Krishnaswamy M., Ying L.H. (2015) Burmese amber from Hti Lin. *Journal of Gemmology*, Vol. 34, No. 7, pp. 606–615.
- Wolfe A.P., Tappert R., Muehlenbachs K., Boudreau M., McKellar R.C., Basinger J.F., Garrett A. (2009) A new proposal concerning the botanical origin of Baltic amber. *Proceedings of the Royal Society B*, Vol. 276, No. 1672, pp. 3403–3412, <http://dx.doi.org/10.1098/rspb.2009.0806>
- Xin C., Li Y., Wang Y., Shi G. (2021) Characterisation of patchy blue and green colouration in Dominican blue amber. *Journal of Gemmology*, Vol. 37, No. 7, pp. 702–715.
- Zhang Z., Jiang X., Wang Y., Kong F., Shen A.H. (2020) Fluorescence characteristics of blue amber from the Dominican Republic, Mexico, and Myanmar. *G&G*, Vol. 56, No. 4, pp. 484–496, <http://dx.doi.org/10.5741/GEMS.56.4.484>

For online access to all issues of GEMS & GEMOLOGY from 1934 to the present, visit:

[gia.edu/gems-gemology](http://gia.edu/gems-gemology)



# Learn from the Experts

Explore our self-paced eLearning  
courses on diamonds, colored stones,  
pearls and jewelry.



Scan to learn  
more and try a  
complimentary lesson



GIA®



# NATURAL RADIOACTIVITY IN SELECT SERPENTINITE-RELATED NEPHRITE SAMPLES: A COMPARISON WITH DOLOMITE-RELATED NEPHRITE

Dariusz Malczewski, Michał Sachanbiński, and Maria Dziurawicz

The published literature offers only a few records of direct measurement of the natural radioactivity in nephrite. The present study used high-purity germanium (HPGe) low-background gamma-ray spectrometry to measure activity concentrations of primordial radionuclides in 11 serpentinite-related nephrite (ortho-nephrite) samples from deposits in Poland, Russia, Canada, and New Zealand, along with three samples of rodingite and serpentinite from a nephrite deposit in Naślawice, Poland. All nephrite samples exhibited very low  $^{40}\text{K}$ ,  $^{232}\text{Th}$ , and  $^{238}\text{U}$  activity concentrations that fell within the range of published values for ultrabasic and basic rocks. The nephrite samples from Jordanów (Poland) gave the highest uranium and thorium activity concentration values. Two samples of plagiogranitic rodingite showed significantly higher  $^{238}\text{U}$  and  $^{232}\text{Th}$  activity concentrations than the values measured for nephrite. Nephrite thorium and uranium concentrations correlated strongly ( $r = 0.98$ ), and the corresponding Th/U ratios appear unique according to geographical location. The mean estimated potassium, thorium, and uranium concentrations from ortho-nephrite analyzed here were compared with corresponding mean values previously reported for dolomite-related nephrite (para-nephrite). The comparison indicates that the ortho-nephrites studied have similar uranium concentrations but lower mean potassium concentrations and higher mean thorium concentrations than those reported for para-nephrite in the literature.

Nephrite jade is an almost monomineral rock made of full-grained (felted), cryptocrystalline amphiboles (actinolite and tremolite) (Łoboś et al., 2008; Adamo and Bocchio, 2013; Gil et al., 2020; Gao et al., 2020). Nephrite usually appears green with varying degrees of saturation but may also exhibit white, gray, black, yellow, brown, and red coloration (Luo et al., 2015; Gil et al., 2020). In most cases, the color of nephrite is influenced by  $\text{Cr}^{3+}$ ,  $\text{Fe}^{2+}$ , and  $\text{Fe}^{3+}$  ions that produce a wide range of light to dark green hues (Suturin et al., 1980; Hobbs, 1982). The intensity of the green coloration is mainly a function of the total iron content (Wilkins et al., 2003; Grapes and Yun, 2010). This sometimes creates mottled, striped, or veined varieties with marbled patterns.

Nephrite's internal structure typically appears fibrous, with an intricately woven microstructure of thin tremolite filaments and microtubules that form kidney-like shapes. The name "nephrite" thus derives from the Greek word for kidney (Łoboś et al., 2008). It is characterized by a high degree of compactness and coherence as well as extreme compressive strength. One nephrite from British Columbia, Canada, exhibited a fracture strength of about 200  $\text{MN m}^{-2}$  (Makepeace and Simandl, 2001). By contrast, nephrite has a hardness of approximately 6.5 on the Mohs scale. The specific gravity of nephrite usually ranges between 2.90 and 3.06 (Żaba, 2006). The main global economic deposits of nephrite jade occur in Canada, Russia, China, the United States, South Korea, New Zealand, Australia, Poland, Italy, and Switzerland. These are usually classified as:

1. Endogenic deposits formed as a result of geological processes of internal origin. The origin of these deposits relates to serpentinites

See end of article for About the Authors and Acknowledgments.

GEMS & GEMOLOGY, Vol. 58, No. 2, pp. 196–213,

<http://dx.doi.org/10.5741/GEMS.58.2.196>

© 2022 Gemological Institute of America

(ortho-nephrite, serpentinite-related nephrite) and dolomites (para-nephrite, dolomite-related nephrite).

2. Exogenic deposits representing secondary placer deposits of nephrite blocks associated with river and stream sediments, for instance, in East Sayan (Russia), New Zealand, and British Columbia (Canada).

This study measured the radioactivity concentration of  $^{40}\text{K}$ ,  $^{232}\text{Th}$ , and  $^{238}\text{U}$  in ortho-nephrite samples from five known nephrite deposits using gamma-ray spectrometry. A major goal of this research was to ascertain whether, as valued decorative stones and gemstones, nephrite may pose a radiological risk to those who handle them, such as artisans or collectors. The authors also sought to compare Th/U ratios of ortho- and para-nephrite. As a secondary goal, the research sought evidence that Th/U concentration ratios vary with the geographic origin of nephrite. The results were compared with limited data available from previous studies on samples from the same localities. Previously published data consist primarily of potassium concentrations but also include thorium and uranium concentrations reported for para-nephrite and obtained by other analytical methods (Leaming, 1978; Łoboś et al., 2008; Grapes and Yun, 2010; Burtseva et al., 2015; Gil et al., 2015).

Dolomite-related nephrite forms at the contact between dolomite marble and a granitic intrusion or siliceous metasediments (Nichol, 2000; Yui and Kwon, 2002; Gil et al., 2015). Different formation processes cause ortho-nephrite and para-nephrite to vary in terms of their concentrations of transition metals and trace elements. Due primarily to lower iron and chromium concentrations, para-nephrite displays lighter colors ranging from white to light green (Luo et al., 2015). Ratios of iron to magnesium and concentrations of chromium, nickel, cobalt, and manganese distinguish para-nephrite from ortho-nephrite. Along with trace element concentrations, hydrogen and oxygen stable isotopic ratios have been used to determine the geographic origin of select dolomite-related nephrite deposits (Gao et al., 2020). As many concentrations of minor elements overlap for both types of nephrite, expanding the range of trace element determinations and overall geochemical datasets could refine models and criteria for distinguishing dolomite-related and serpentinite-related nephrite. Expanded geochemical datasets also offer greater accuracy and precision to studies of nephrite provenance.

Consensus holds that ortho-nephrite forms due to initial rodingitization and subsequent serpentinite transformation under the influence of gabbroic or acid magma injection (Gil et al., 2015). Genetic relations between these phases and associated rock types thus warranted investigation of both serpentinite and rodingite that co-occur at the Naślawice locality.

## In Brief

- Gamma-ray measurements indicate very low  $^{40}\text{K}$ ,  $^{232}\text{Th}$ , and  $^{238}\text{U}$  activity concentrations in 11 serpentinite-related (ortho-nephrite) samples.
- Two samples of plagiogranitic rodingite from a nephrite deposit in Naślawice (Poland) showed significantly higher  $^{238}\text{U}$  and  $^{232}\text{Th}$  activity concentrations than those measured for nephrite samples.
- Thorium and uranium concentrations correlate positively and linearly in the ortho-nephrites analyzed.
- Nephrite, a valued decorative stone and gemstone, does not pose a radiological risk to artisans or collectors.

## MATERIALS AND METHODS

This study analyzed samples of gem-quality ortho-nephrite originating from Poland (Naślawice, Jordanów), Russia (Siberia, East Sayan), Canada (British Columbia), and New Zealand (South Island). Polished nephrite samples referred to as NS1, NS2, and NS3 (table 1 and figure 1, A–C) were collected by M. Sachanbiński from an active serpentinite and nephrite quarry in Naślawice (Łoboś et al., 2008).

Raw jade samples referred to as JR1, JR2, and JR3 (table 1 and figure 1, D–F) belong to the collection of M. Sachanbiński and come from the historic jade quarry in Jordanów (Prichystal, 2013). Nephrite in Naślawice and nearby Jordanów occurs in serpentinite of the Gogołów-Jordanów Massif (GJM), which forms part of the Ślęza Ophiolite, itself part of the Mid-Sudetic Ophiolite (Gil, 2013; Gil et al., 2020). These nephrites occur as irregular bodies within the so-called black wall, a chlorite body within a contact zone of rodingite dikes and serpentinite. The serpentinites in Jordanów and Naślawice host completely transformed gabbro and plagiogranites as well as partially rodingitized leucogranites. Nephrite from Jordanów and Naślawice is considered of high gemological quality and usually appears green but without uniform coloration. Varied shades of green create unique patterns on the material's surface.



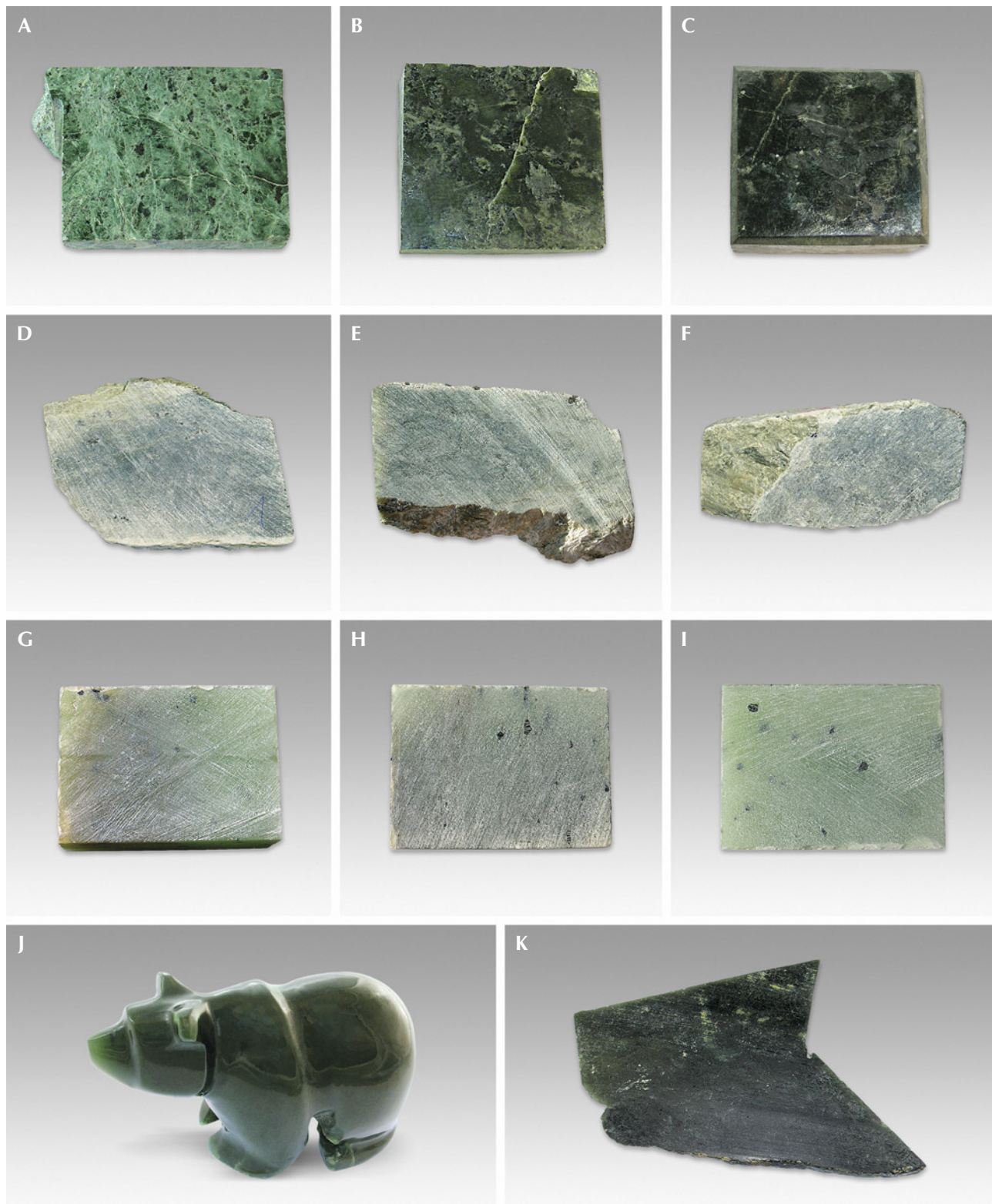


Figure 1. Photographs of ortho-nephrite samples analyzed. A: From Nasławice (NS1), 7 cm in length. B: From Nasławice (NS2), 7 cm in length. C: From Nasławice (NS3), 3 cm in length. D: From Jordanów (JR1), 4 cm in length. E: From Jordanów (JR2), 4 cm in length. F: From Jordanów (JR3), 4 cm in length. G: From Siberia (SB1), 3 cm in length. H: From Siberia (SB2), 3 cm in length. I: From Siberia (SB3), 3 cm in length. J: Bear carving from British Columbia (CN1), 7 cm in length. K: From New Zealand (NZ1), ~7 cm across. All photos by D. Malczewski.

Actinolite represents the main mineral comprising nephrite, and secondary minerals include chlorite, antigorite, grossular, chromite, and iron oxides.

Russian nephrite samples SB1, SB2, and SB3 (table 1 and figure 1, G–I) belong to the collection of M. Sachanbiński. These were donated by a Russian geologist during the International Mineralogical Association conference in Novosibirsk, Russia, in September 1978. The samples come from the Ospa deposit located in the East Sayan nephrite-bearing area (southern folded periphery of the Siberian craton). This deposit represents an apo-ultrabasic nephrite (Burtseva et al., 2015). Nephrite from the deposit appears greenish blue in color and exhibits different degrees of saturation (Suturin et al., 1980). Mineral compositions consist primarily of actinolite and tremolite fibers, pyroxene, diopside, serpentine, talc, chromite, graphite, and fuchsite. Accessory mineral content ranges from 0.5 to 1.5%. All of the above-mentioned nephrite samples from Naślawice and Jordanów (Poland) and Siberia (Russia) will be donated to the Mineralogical Museum of the University of Wrocław (Poland).

Canadian sample CN1 is a dark green nephrite carved in the form of a small bear (table 1 and figure 1J). This carving also belongs to the collection of M. Sachanbiński and was purchased during the 17th General Meeting of the IMA in Toronto in August 1998. It was made by a First Nations artisan using material from British Columbia, where more than 50 nephrite occurrences have been reported. These consist of individual blocks, talus blocks, boulder fields, and *in situ* bodies that occur primarily at contacts between serpentinite and cherts, or other metasedimentary and igneous rocks formed in submarine environments. Secondary minerals in the nephrite include spinel, diopside, uvarovite, titanite, chlorite, and talc (Leaming, 1978; Makepeace and Simandl, 2001).

Nephrite sample NZ1 from the South Island of New Zealand exhibits a waxy luster and blackish green color (table 1, figure 1K). This sample was donated to the Mineralogical Museum at the Institute of Earth Sciences, University of Silesia by L. Sajkowski, a Polish geologist living and working in New Zealand. Grapes and Yun (2010) describe this nephrite from northern Westland as occurring as rare pebbles and boulders weighing up to several tons, found in glacial outwash gravels and till. They also appear in streams and rivers that drain the nephrite source area of the *pounamu* ultramafic rocks located in the northern part of the Southern Alps (Ireland et al., 1984; Cooper, 1995).

Samples RN1, RN2, and RN3 represent rodingite (table 1). Rodingite is a rare type of metasomatic rock consisting of grossular, diallage, and accessory magnetite, apatite, and serpentinized olivine. It can be enriched in epidote, prehnite, and vesuvianite (Bell et al., 1911; O'Brien and Rodgers, 1973; Hatzipanagiotou and Tsikouras, 2001; Kobayashi and Kaneda, 2010; Heflik et al., 2014). The samples and rock type are considered to have high ornamental value. The analyzed samples belong to the collection of S. Madej from the University of Wrocław and come from an active serpentinite and jade quarry in Naślawice. Dubińska et al. (2004) distinguish two types of rodingite. The first type, boninite rodingite, contains relict clinopyroxene and vesuvianite, garnet, and diopside. The second type, plagiogranite rodingite, contains relics of checkerboard albite and hydrogrossular, clinozoisite, zoisite, and late diopside. Macroscopically, samples RN1 and RN2 (plagiogranite rodingites; figure 2, A and B) exhibit alternating, fine-grained, light and pink-colored laminae and medium-grained, dark gray laminae. In their study of the phase compositions of this type of rodingite, Szełęg (2006) reported quartz (approx. 63%), zoisite (approx. 25%), carbonate-hydroxyl apatite, hydrogrossular, albite, and smaller amounts of apatite, titanite, chromite, uraninite, and thorianite. Sample RN3 (boninite rodingite) (figure 2C) exhibits dull to light green color and varied mineral composition.

Sample SRN (table 1, figure 2D) belongs to the collection of M. Sachanbiński and represents a typical serpentinite from the deposit in Naślawice. Serpentinites occurring there formed as a result of complex, long-term transformation of harzburgite and lherzolite (Dubińska and Gunia, 1997). These belong to the Gogołów-Jordanów Serpentinite Massif of the Śleża Ophiolite and probably formed at around 400 Ma (million years ago) (Gil et al., 2015). The serpentinite from Naślawice appears dark green in color and consists primarily of antigorite and sometimes contains olivine, bronzite, diallage, diopside, and hornblende. They sometimes resemble nephrite or are nephritized to varying degrees. Subordinate minerals include magnesite, braunite, chromite, apatite, garnet, and others. Macroscopically, these minerals are prized for their decorative value. The use of serpentinite as tools or decorative objects dates back to the Neolithic (around 3000 BCE) in Lower Silesia. The stone was originally used in tools and weapons (e.g., axes, knives, and hoes) and is used today in ornamental objects (see box A).

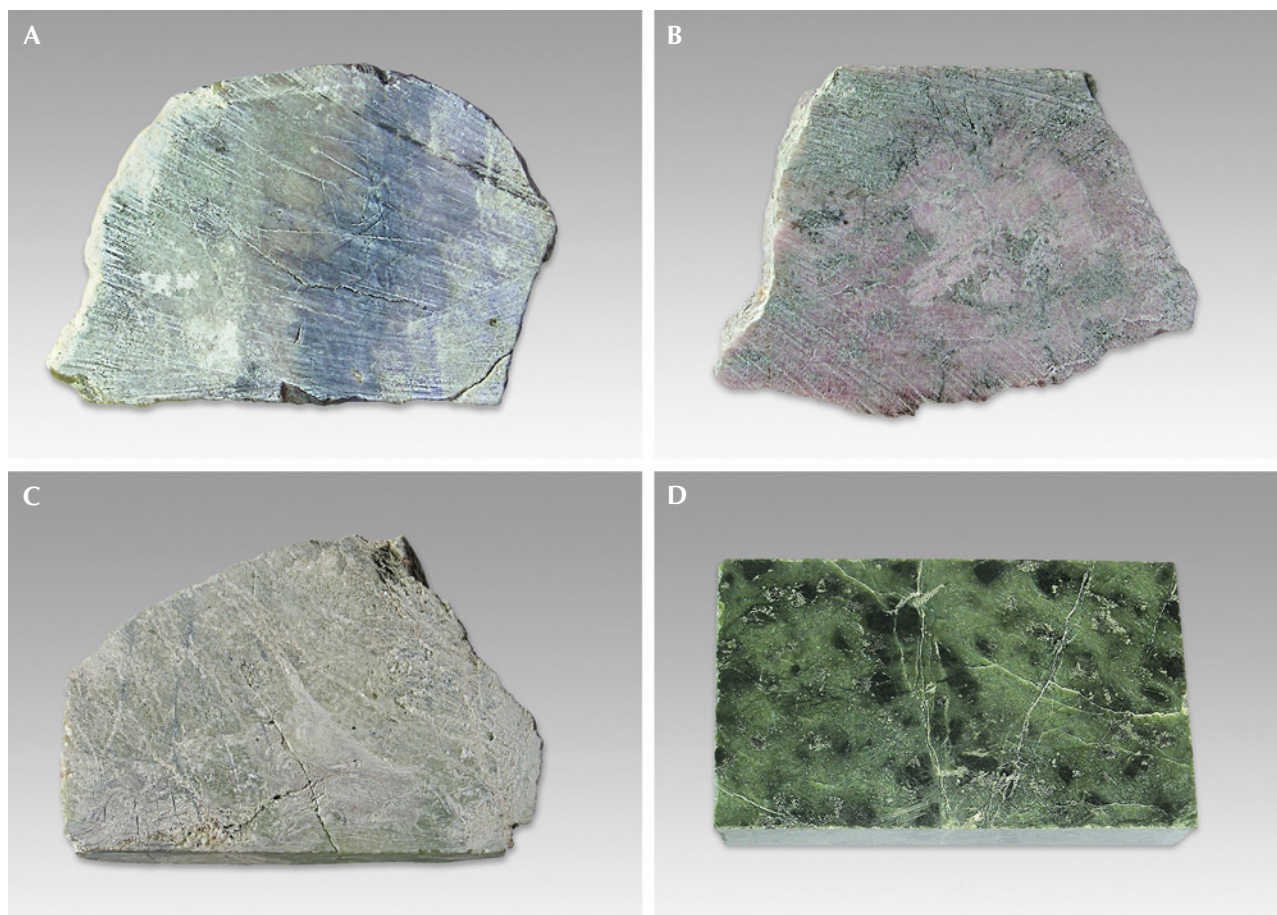


Figure 2. Samples of rodingite and serpentinite from Naślawice. A: Plagiogranitic rodingite (RN1), 4 cm in length. B: Plagiogranitic rodingite (RN2), 6 cm in length. C: Boninitic rodingite (RN3), 6.5 cm in length. D: Serpentinite (SRN), 6 cm in length. All photos by D. Malczewski.

The activity concentrations (in  $\text{Bq kg}^{-1}$ ) of the naturally occurring radionuclides in nephrite, rodingite,

and serpentinite samples, shown in table 1, were measured using a GX4018 gamma-ray spectrometry

## BOX A: USE OF NEPHRITE JADE

The practical and ornamental use of nephrite jade by humans dates back to at least the early Neolithic. Because its fracture yields sharp, durable edges, nephrite was initially used to make axes, knives, scrapers, and other simple cutting tools. A pile deposit discovered along the shores of Lake Constance, Switzerland, contained 30,000 jade axes weighing a total of 6000 kg (Hobbs, 1982; Prichystal, 2013). A younger Stone Age site near Jordanów (Jordansmuhl) in Lower Silesia, Poland, is interpreted as a serpentinite and nephrite mining and processing center (Prichystal, 2013). A block of jade weighing over two tons excavated from the Jordanów site in 1889 was on display in the New York Metropolitan Museum of Art (Gil, 2013).

Jade continues to be used for ornamental and decorative objects such as jewelry and art. Some of the highest-quality nephrite, referred to as *pounamu* in the Maori language, is mined in New Zealand (Hobbs, 1982; Prichystal, 2013). The Maori utilized jade for ornaments, art, and tools—in the latter case until the introduction of metal in the nineteenth century. Chinese culture and artwork have featured jade since its earliest inception, and jade carving is particularly well developed in East Asia (Douglas, 2005; Wang, 2011). Nephrite jade has been considered a symbol of wealth and power, and thus many jade artifacts have survived intact into modern times. From antiquity to the present day, nephrite jade has been considered a store of value and items made from it have been prized as gifts.

**TABLE 1.** Measured radionuclide activity concentrations and calculated weight concentrations of  $^{40}\text{K}$ ,  $^{232}\text{Th}$ , and  $^{238}\text{U}$  from ortho-nephrite, rodingite, and serpentinite samples.<sup>a</sup>

Rock/Sample	$^{40}\text{K}$		$^{232}\text{Th}$		$^{238}\text{U}$	
	Bq kg <sup>-1</sup>	Total K wt.% <sup>b</sup>	Bq kg <sup>-1</sup>	ppm	Bq kg <sup>-1</sup>	ppm
<b>Nephrite</b>						
NS1	1.5	0.005	0.5	0.12	1.6	0.13
NS2	1.2	0.004	0.6	0.15	1.8	0.15
NS3	5.5	0.018	2.0	0.49	4.5	0.36
JR1	17	0.055	4.4	1.08	19	1.34
JR2	13	0.042	4.7	1.16	20	1.62
JR3	14	0.045	4.3	1.06	17	1.38
SB1	5.1	0.016	1.9	0.47	6.2	0.50
SB2	6.8	0.022	2.0	0.49	5.9	0.48
SB3	5.1	0.016	1.9	0.47	6.6	0.53
CN1	27	0.087	0.8	0.20	1.2	0.10
NZ1	4.2	0.014	1.5	0.37	1.3	0.11
<b>Rodingite</b>						
RN1	14	0.045	130	32.0	292	23.6
RN2	28	0.091	18	4.43	172	13.9
RN3	2.7	0.009	4.6	1.13	10	0.81
<b>Serpentinite</b>						
SRN	1	0.003	0.7	0.17	1.1	0.09

<sup>a</sup>Measurement uncertainties are plotted with this data in figures 4–7.

<sup>b</sup>The following conversion factors were used: K (wt.%) =  $^{40}\text{K}$  (Bq kg<sup>-1</sup>)/309.11; Th (ppm) =  $^{232}\text{Th}$  (Bq kg<sup>-1</sup>)/4.06; and U (ppm) =  $^{238}\text{U}$  (Bq kg<sup>-1</sup>)/12.35 (International Atomic Energy Agency, 2003). Uncertainties fell within 5–10% of measured values for activity concentrations below 2 Bq kg<sup>-1</sup>.

system at the Laboratory of Natural Radioactivity, Institute of Earth Sciences, University of Silesia (Malczewski et al., 2018a, 2018b; see also box B). The system uses a high-purity germanium (HPGe) detec-

tor (45.2% efficiency) in a lead and copper shield (10.2 cm) with a multichannel-buffer Lynx instrument. The energy resolutions of the detector were 0.8 keV at 122 keV and 1.7 keV at 1330 keV. Each sample was

analyzed for 96 h. The activity concentrations of  $^{232}\text{Th}$  and  $^{238}\text{U}$  were determined based on the gamma-ray activity concentrations of  $^{208}\text{Tl}$ ,  $^{212}\text{Pb}$ , and  $^{228}\text{Ac}$  for thorium, and  $^{214}\text{Pb}$  and  $^{214}\text{Bi}$  for uranium. Radionuclide activity concentrations were calculated from the following gamma-ray transitions (energy in keV):  $^{40}\text{K}$  (1460.8);  $^{208}\text{Tl}$  (583.1, 860.5, 2614.5);  $^{212}\text{Pb}$  (238.6, 300.1);  $^{214}\text{Pb}$  (242, 295.2, 351.9);  $^{214}\text{Bi}$  (609.3, 1120.3, 1764.5); and  $^{228}\text{Ac}$  (338.32, 911.6, 964.6, 969.1). Laboratory Sourceless Calibration Software (LabSOCS) and Genie 2000 v.3.4 software packages were both used to analyze spectra, calibrate efficiency, and determine radionuclides.

Consistency of the activity concentrations calculated for gamma-ray transitions for a given multiline radionuclide (e.g.,  $^{208}\text{Tl}$ ,  $^{214}\text{Bi}$ ,  $^{214}\text{Pb}$ , and  $^{228}\text{Ac}$ ) were checked using line activity consistency evaluator (LACE) analysis. For all measurements, the multiline radionuclides gave activity concentration ratios approaching unity. The average minimum detectable

activity concentration (MDA) for measured radionuclides was  $0.1 \text{ Bq kg}^{-1}$ . Figure 3 shows examples of gamma-ray spectra for nephrite samples NS1 and JR1 and rodingite sample RN1.

## RESULTS AND DISCUSSION

Table 1 lists measured activity concentrations for  $^{40}\text{K}$ ,  $^{232}\text{Th}$ , and  $^{238}\text{U}$  in  $\text{Bq kg}^{-1}$  and calculated potassium (wt. %), thorium (ppm), and uranium (ppm) concentrations for nephrite, rodingite, and serpentinite samples.

$^{40}\text{K}$ . As seen in figure 4 and table 1, the  $^{40}\text{K}$  activity concentrations recorded for nephrite samples analyzed ranged from  $1.2 \text{ Bq kg}^{-1}$  for NS2 to  $27 \text{ Bq kg}^{-1}$  for CN1. Nephrite from Naślawice, Jordanów, and Siberia gave average values of 2.7, 15, and  $5.7 \text{ Bq kg}^{-1}$ , respectively. The New Zealand nephrite (NZ1) had an intermediate value of  $4.2 \text{ Bq kg}^{-1}$ . The average value for all samples was  $9.1 \text{ Bq kg}^{-1}$  (figure 4). These values exceed  $^{40}\text{K}$  ac-

## BOX B: NATURAL RADIOACTIVITY

Natural radioactivity results from the spontaneous decay of naturally occurring radioisotopes. All elements having an atomic number greater than 83 consist only of radioactive isotopes. The three natural types of radioactive nuclei decay include alpha ( $\alpha$ , emission of helium nuclei), beta ( $\beta$ , emission of electrons or positrons), and gamma ( $\gamma$ , emission of the shortest electromagnetic waves) decay. The SI unit of radioactivity is the becquerel (Bq), equal to one decay per second. The becquerel replaced the curie (Ci), the unit equal to  $3.7 \times 10^{10}$  disintegrations per second or the radioactivity of 1 g of  $^{226}\text{Ra}$  ( $1 \text{ Bq} = 0.27 \times 10^{-10} \text{ Ci}$ ). The main source of radioactivity in minerals, rocks, and soils derives from the  $^{232}\text{Th}$ ,  $^{235}\text{U}$ ,  $^{238}\text{U}$  decay series, and  $^{40}\text{K}$  (non-series). The  $^{232}\text{Th}$ ,  $^{235}\text{U}$ , and  $^{238}\text{U}$  series consist of 6  $\alpha$  and 4  $\beta$ , 7  $\alpha$  and 4  $\beta$ , and 8  $\alpha$  and 6  $\beta$  decays, respectively. Many of the  $\alpha$  and  $\beta$  decays are accompanied by gamma-ray radiation. The major gamma transitions from potassium, thorium, and uranium are commonly used in estimating weight concentrations based on measured activity concentrations. Due to the low natural abundance of  $^{235}\text{U}$  (0.72% of natural uranium), the activity concentration of this isotope is usually negligible compared to that of  $^{238}\text{U}$ . Its activity concentration is thus not taken into account.

Typical soils and carbonate rocks give average  $^{40}\text{K}$ ,  $^{232}\text{Th}$ , and  $^{238}\text{U}$  activity concentrations of 400, 30, and  $35 \text{ Bq kg}^{-1}$  and 80, 7, and  $27 \text{ Bq kg}^{-1}$ , respectively (Van Schmus, 1995; UNSCEAR, 2000). Among the most common rock types, acidic igneous rocks such as granite and rhyolite give the highest radioactivity values. These typ-

ically range from 900–1400, 50–200, and 37–72  $\text{Bq kg}^{-1}$  for  $^{40}\text{K}$ ,  $^{232}\text{Th}$ , and  $^{238}\text{U}$ , respectively.

The activity concentration index assesses radiological hazards to human health posed by building materials, including rock surfaces used in paneling or countertops. The European Union standard index  $I$ , as defined by the European Atomic Energy Community (2013), represents the sum of three isotopic fractions expressed as:

$$I = \frac{A_{\text{Ra}}}{300 \text{ Bq kg}^{-1}} + \frac{A_{\text{Th}}}{200 \text{ Bq kg}^{-1}} + \frac{A_{\text{K}}}{3000 \text{ Bq kg}^{-1}}$$

where  $A_{\text{Ra}}$ ,  $A_{\text{Th}}$ , and  $A_{\text{K}}$  represent  $^{226}\text{Ra}$  ( $^{238}\text{U}$ ),  $^{232}\text{Th}$ , and  $^{40}\text{K}$  ( $\text{Bq kg}^{-1}$ ) activity concentrations in surroundings or material. The value of index  $I$  should not exceed unity, which corresponds to the indoor dose rate of  $1 \text{ mSv y}^{-1}$ . The sievert (Sv) is the SI unit of equivalent dose and effective dose equal to  $1 \text{ J kg}^{-1}$ . The external hazard index  $H_{\text{ex}}$  is also commonly used to evaluate the radiological risk of building materials. It is calculated as follows:

$$H_{\text{ex}} = \frac{A_{\text{Ra}}}{370 \text{ Bq kg}^{-1}} + \frac{A_{\text{Th}}}{259 \text{ Bq kg}^{-1}} + \frac{A_{\text{K}}}{4810 \text{ Bq kg}^{-1}}$$

An  $H_{\text{ex}}$  index equal to unity corresponds to an external gamma-ray dose of  $1.5 \text{ mSv y}^{-1}$  from a material. With a few exceptions, the overwhelming majority of rock building materials are characterized by  $I$  and  $H_{\text{ex}}$  values less than one. All ortho-nephrites measured in this study have extremely low average  $I$  and  $H_{\text{ex}}$  values of 0.04 and 0.03, respectively.

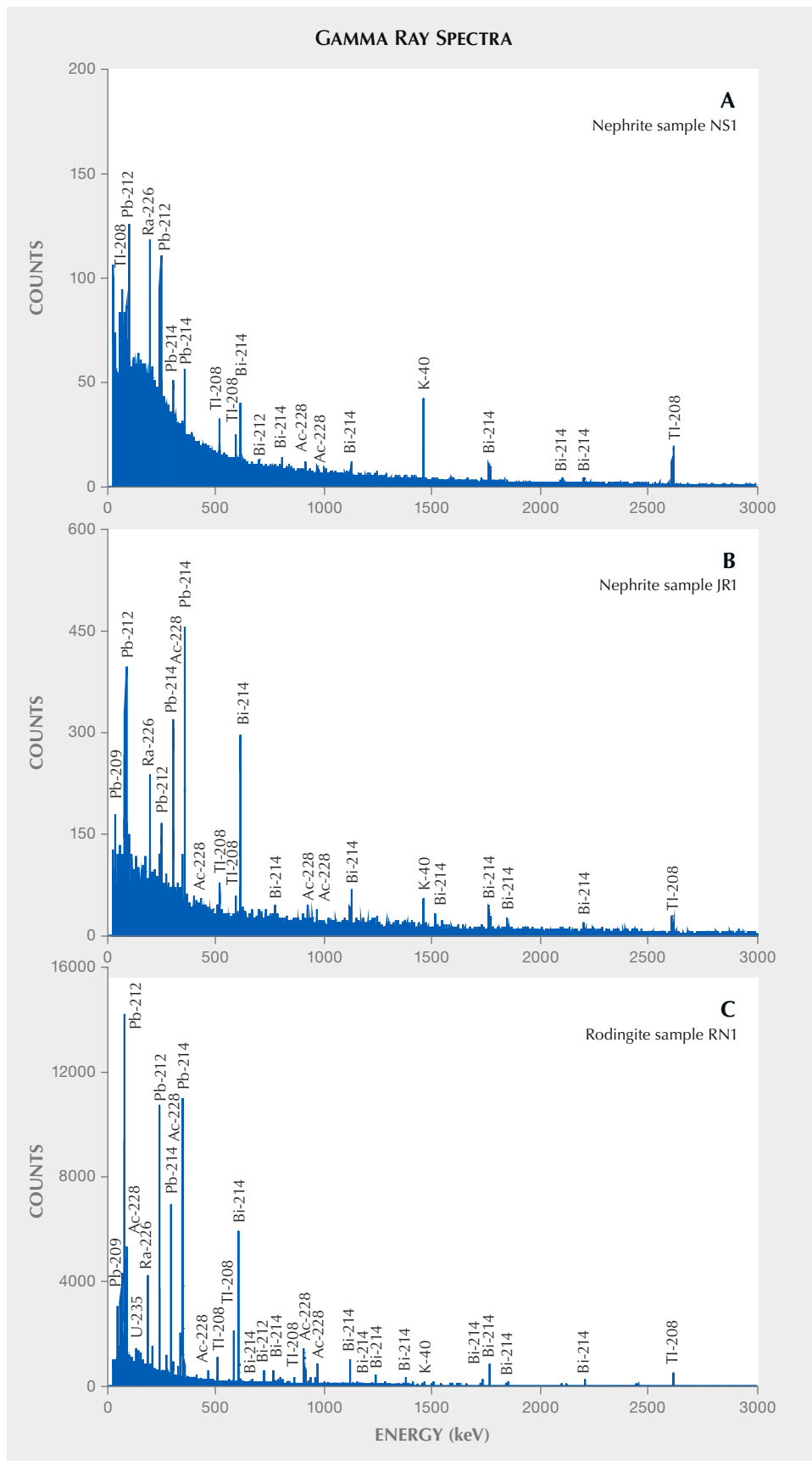


Figure 3. Gamma-ray spectra from nephrite sample NS1 (A), nephrite sample JR1 (B), and rodingite sample RN1 (C). Characteristic gamma-ray emitters are marked above the corresponding peaks. Note the different y-axis count scales for the three samples.

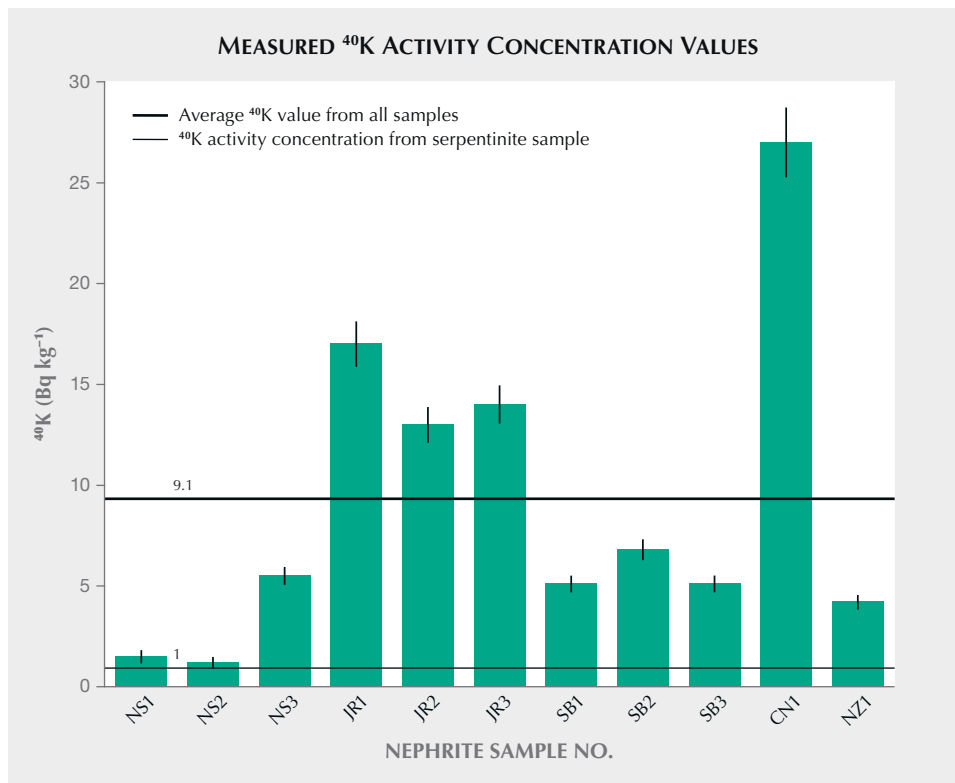


Figure 4. Measured <sup>40</sup>K activity concentration values. The thick horizontal line represents the average <sup>40</sup>K value measured from all samples in this study. The thin horizontal line represents the <sup>40</sup>K activity concentration for the serpentine sample (SRN). The thin vertical lines are error bars.

tivity concentration values estimated from ultramafic rocks (~ 0.3 Bq kg<sup>-1</sup>; Van Schmus, 1995) and serpenti-

nite (1 Bq kg<sup>-1</sup>) but fell below average values measured in gabbros from Lower Silesia (73 Bq kg<sup>-1</sup>; Plewa and

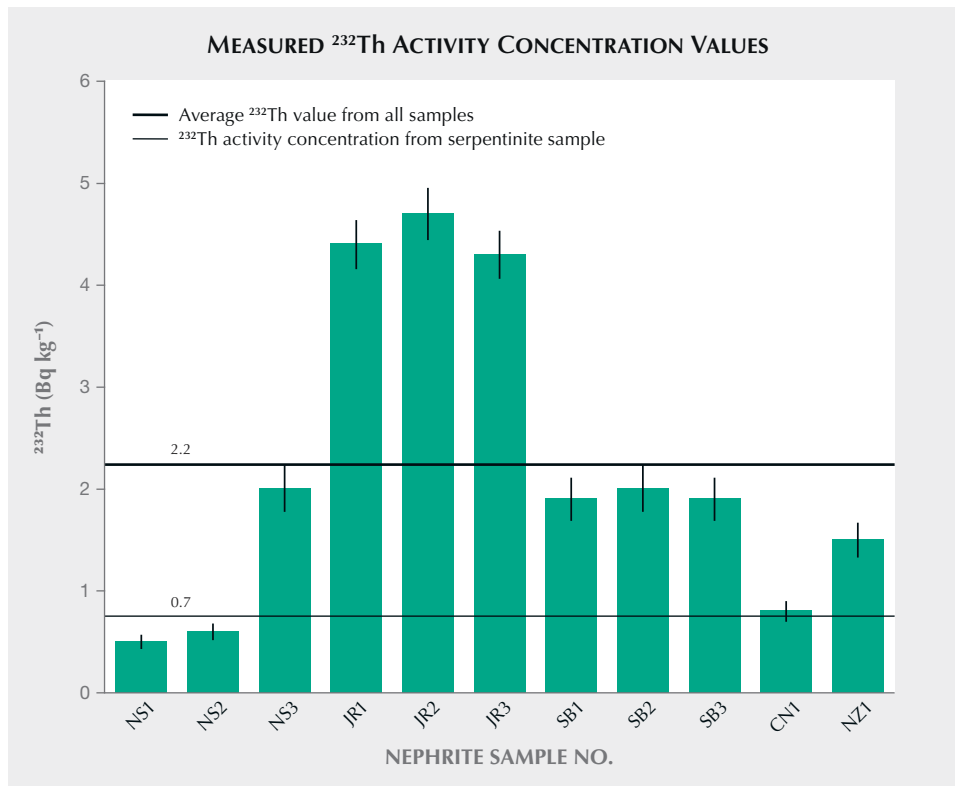


Figure 5. Measured <sup>232</sup>Th activity concentration values. The thick horizontal line represents the average <sup>232</sup>Th values from all samples. The thin horizontal line represents the <sup>232</sup>Th activity concentration for the serpentine sample (SRN). The thin vertical lines are error bars.

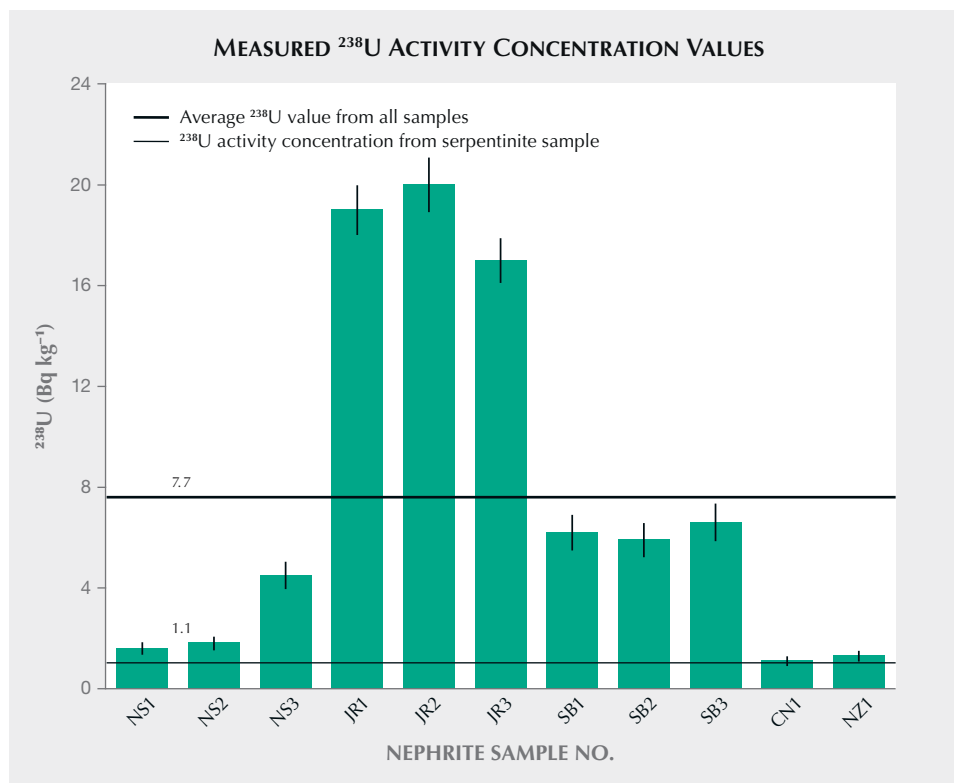


Figure 6. Measured  $^{238}\text{U}$  activity concentration values. The thick horizontal line represents the average  $^{238}\text{U}$  value from all samples in this study. The thin horizontal line represents the  $^{238}\text{U}$  activity concentration for the serpentinite sample (SRN). The thin vertical lines are error bars.

Plewa, 1992). Typical granites give values ranging from 900–1400 Bq kg $^{-1}$ .

**$^{232}\text{Th}$ .** As seen in table 1 and figure 5, the nephrite from Jordanów had the highest activity concentration values associated with  $^{232}\text{Th}$  series isotopes. Values of 4.3, 4.4, and 4.7 Bq kg $^{-1}$  yielded an average  $^{232}\text{Th}$  activity concentration of 4.5 Bq kg $^{-1}$ . The samples from Siberia and Naślawice (NS3) showed the second-highest values at about 2 Bq kg $^{-1}$ . Sample NZ1 had a similar value of 1.5 Bq kg $^{-1}$ . The samples from Naślawice (NS1 and NS2) gave the lowest  $^{232}\text{Th}$  activity concentrations of 0.5–0.6 Bq kg $^{-1}$ . Sample CN1 also had a low value of 0.8 Bq kg $^{-1}$ . All samples combined gave an average  $^{232}\text{Th}$  activity concentration of 2.2 Bq kg $^{-1}$  (figure 5). All measured activity concentrations exceeded values reported for ultrabasic rocks of an order of 10 $^{-2}$  Bq kg $^{-1}$  (Van Schmus, 1995). The  $^{232}\text{Th}$  activity concentration for all samples except NS1 and NS2 exceeded that measured from SRN (0.7 Bq kg $^{-1}$ ). Activity concentrations for nephrite samples analyzed fell below the average estimated for gabbros from Lower Silesia (6.4 Bq kg $^{-1}$ ) and well below that previously estimated for granites, which give  $^{232}\text{Th}$  activity concentrations ranging from 50–200 Bq kg $^{-1}$  with an average of 70 Bq kg $^{-1}$  (Eisenbud and Gesell, 1997).

**$^{238}\text{U}$ .** Table 1 and figure 6 show that the nephrite samples from Jordanów had the highest average activity concentration associated with  $^{238}\text{U}$  series isotopes (19 Bq kg $^{-1}$ ). Samples from Siberia gave the second-highest average value at 6.3 Bq kg $^{-1}$ . Samples CN1 and NZ1 showed the lowest  $^{238}\text{U}$  activity concentrations of 1.2 and 1.3 Bq kg $^{-1}$ , respectively. As with their  $^{40}\text{K}$  and  $^{232}\text{Th}$  values, the NS1 and NS2 nephrites from Naślawice gave lower  $^{238}\text{U}$  activity concentration values (1.6 and 1.8 Bq kg $^{-1}$ ) relative to sample NS3 (4.5 Bq kg $^{-1}$ ). All samples had higher  $^{238}\text{U}$  activity concentration values than those measured from ultrabasic rocks (~0.1 Bq kg $^{-1}$ ; Van Schmus, 1995) and from the serpentinite sample SRN (1.1 Bq kg $^{-1}$ ). As shown in figure 6, the  $^{238}\text{U}$  activity concentration average of 7.7 Bq kg $^{-1}$  measured for all nephrite samples exceeded the average of 4.1 Bq kg $^{-1}$  measured from gabbros (Plewa and Plewa, 1992). This relatively high value arises from the significantly higher  $^{232}\text{Th}$  activity concentration measured in the nephrite samples from Jordanów. The calculated mean for the orthonephrites analyzed fell below the previously reported average values for granite of 40 Bq kg $^{-1}$  (Eisenbud and Gesell, 1997).

This study also compared  $^{40}\text{K}$ ,  $^{232}\text{Th}$ , and  $^{238}\text{U}$  activity concentrations from orthonephrite with those previously measured from marbles using the same



technique. Calcite marbles from the Sławniowice quarry (Lower Silesia, Poland) and Alpine marbles from the vicinity of Aussois (France) gave average  $^{232}\text{Th}$  activity concentration values of  $2.4 \text{ Bq kg}^{-1}$  (Malczewski and Żaba, 2012; Moska, 2019). This approximated average value for  $^{232}\text{Th}$  ( $2.2 \text{ Bq kg}^{-1}$ ) was measured from the ortho-nephrites analyzed. The  $^{238}\text{U}$  activity concentrations in calcite marbles ranged from  $16\text{--}23 \text{ Bq kg}^{-1}$ . Nephrite  $^{238}\text{U}$  activity concentrations ranged from 2 to  $20 \text{ Bq kg}^{-1}$  with an average value of  $\sim 8 \text{ Bq kg}^{-1}$ . The measured  $^{40}\text{K}$  activity concentrations for calcite marbles ranged from  $12\text{--}80 \text{ Bq kg}^{-1}$ , while that for nephrite ranged from  $1.2\text{--}27 \text{ Bq kg}^{-1}$  with an average of  $9 \text{ Bq kg}^{-1}$ . The dolomite marbles collected from the Sławniowice mine gave  $^{40}\text{K}$  activity concentrations of  $122 \text{ Bq kg}^{-1}$  and  $^{232}\text{Th}$  activity concentrations of  $5 \text{ Bq kg}^{-1}$ . These exceeded values measured from calcite marbles, but the two rock types exhibited similar  $^{238}\text{U}$  concentrations of  $\sim 13 \text{ Bq kg}^{-1}$ . The ortho-nephrites analyzed gave comparable  $^{232}\text{Th}$  and  $^{238}\text{U}$  activity concentration values but lower  $^{40}\text{K}$  activity concentration values relative to those of calcite and dolomite marbles. Based on their analyses using an HPGe detector, Fares et al. (2011) reported a

higher average  $^{238}\text{U}$  activity concentration of  $57 \text{ Bq kg}^{-1}$  for commercial marbles from Egypt.

**Rodingite.** As noted earlier, the rodingite samples associated with the Naślawice and Jordanów nephrite deposits classify as boninite (RN3) and plagiogranite rodingite (RN1 and RN2). As shown in table 1 and figure 7, sample RN1 gave the highest  $^{238}\text{U}$  and  $^{232}\text{Th}$  activity concentrations of 292 and  $130 \text{ Bq kg}^{-1}$ , respectively. These values significantly exceed the activity concentrations of all examined nephrites and activity concentrations of typical granites of 40 and  $70 \text{ Bq kg}^{-1}$  for  $^{238}\text{U}$  and  $^{232}\text{Th}$ , respectively (Eisenbud and Gesell, 1997). Sample RN2 also exhibited high uranium activity concentration but lower thorium-related activity concentration relative to sample RN1. The high  $^{238}\text{U}$  and  $^{232}\text{Th}$  activity concentration values in RN1 and RN2 rodingite samples likely reflect the presence of accessory zircon, thorianite, and uraninite (Szełęg, 2006). As expected, sample RN3, which was collected from a body in direct contact with the nephrite-bearing zone, exhibited significantly lower  $^{238}\text{U}$  and  $^{232}\text{Th}$  activity concentrations than samples RN1 and RN2. Activity concentrations

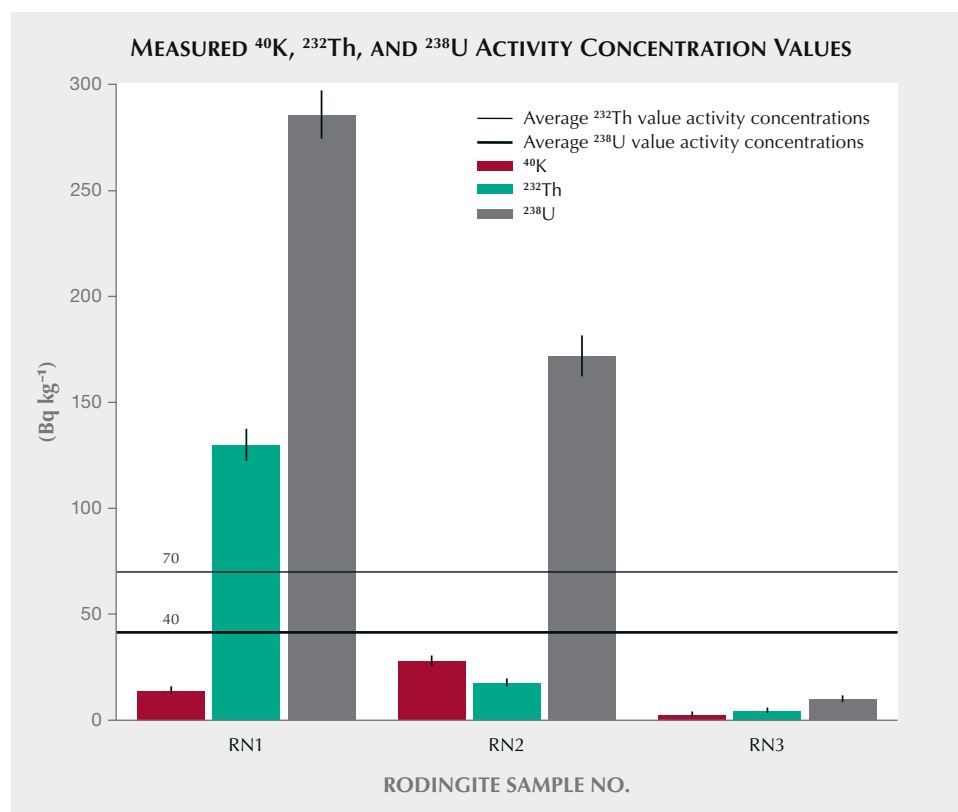


Figure 7. Measured  $^{40}\text{K}$ ,  $^{232}\text{Th}$ , and  $^{238}\text{U}$  activity concentration values for rodingite. The thin and thick horizontal lines respectively show the average  $^{232}\text{Th}$  and  $^{238}\text{U}$  activity concentrations in typical granites (Eisenbud and Gesell, 1997). The thin vertical lines are error bars.

measured from RN3 for  $^{238}\text{U}$  (10 Bq kg $^{-1}$ ) and  $^{232}\text{Th}$  (5 Bq kg $^{-1}$ ) exceeded those observed in ortho-nephrite samples from Nasławice, Siberia, British Columbia, and South Island but resembled those measured from the Jordanów samples. The rodingite samples exhibited relatively low  $^{40}\text{K}$  activity concentrations with a mean value of 15 Bq kg $^{-1}$ , which exceeded the mean value of 9.1 Bq kg $^{-1}$  measured from the nephrite samples. As with  $^{238}\text{U}$  and  $^{232}\text{Th}$  activity concentrations, sample RN3 gave the lowest  $^{40}\text{K}$  activity concentration of 3 Bq kg $^{-1}$ . Samples RN1 and RN2 gave higher activity concentrations of 14 and 28 Bq kg $^{-1}$ . These resembled values measured from the Jordanów nephrite samples and from CN1.

**Comparison of K, Th, and U Concentrations with Previous Data.** Concentrations estimated for potassium (wt.%), thorium (ppm), and uranium (ppm) showed similar trends among the samples as those observed for the  $^{40}\text{K}$ ,  $^{232}\text{Th}$ , and  $^{238}\text{U}$  activity concentration values. Nephrite potassium concentrations varied from 0.004 wt.% for sample NS2 to 0.087 wt.% for sample CN1, and the samples overall gave a mean value of 0.03%. Concentrations estimated for potassium, thorium, and uranium generally resembled the few previously obtained results for ortho-nephrite from the same locations. The nephrite samples from Nasławice in particular showed similar potassium concentrations. Łoboś et al. (2008) report average potassium concentrations of 0.004, 0.008, and 0.016 wt.% for three types of nephrite based on electron microscope analysis. These values correspond to  $^{40}\text{K}$  activity concentrations of approximately 1.2, 2.5, and 5.0 Bq kg $^{-1}$  and thus agree very well with activity concentrations measured from samples NS1, NS2, and NS3 by gamma-ray spectrometry (table 1). Prompt gamma neutron activation energy analysis (PGAA) indicated a bulk-rock potassium concentration of about 0.016 wt.% for the Jordanów nephrite sample. This value corresponds to a  $^{40}\text{K}$  activity concentration of less than 5 Bq kg $^{-1}$  (Gil et al., 2015). The concentration value and associated  $^{40}\text{K}$  activity concentration fell below values obtained by this study for the three samples from Jordanów, which gave an average potassium concentration of 0.050 wt.% and an average  $^{40}\text{K}$  activity concentration of 15 Bq kg $^{-1}$  (table 1). Extensive studies by Leaming (1978) and Nichol (2000) report an average potassium concentration of 0.038 wt.% and a corresponding  $^{40}\text{K}$  activity concentration of 12 Bq kg $^{-1}$  for Canadian nephrite from British Columbia. Gamma-ray measurements (table 1) of sample CN1 indicate a higher but comparable

$^{40}\text{K}$  activity concentration value of 27 Bq kg $^{-1}$  (0.087 wt.%). Grapes and Yun (2010) report average potassium concentrations for South Island nephrite of 0.012 wt.% based on electron microprobe analysis. These correspond to a  $^{40}\text{K}$  activity concentration of 3.8 Bq kg $^{-1}$  and fall within the measurement uncertainty of potassium values obtained for sample NZ1 (4.2 Bq kg $^{-1}$  and 0.014 wt.%). The above-mentioned literature sources provide no data on thorium and uranium concentrations.

Ortho-nephrite samples from the East Sayan area exhibit relatively large differences in potassium, thorium, and uranium concentrations. Inductively coupled plasma-mass spectrometry (ICP-MS) analysis gave average potassium concentrations of 0.05 wt.% (16 Bq kg $^{-1}$  of  $^{40}\text{K}$ ) for samples from the area (Burtseva et al., 2015). This value exceeds the average value of 0.016 wt.% (6 Bq kg $^{-1}$  of  $^{40}\text{K}$ ) obtained for samples SB1, SB2, and SB3. Burtseva et al. (2015) reported average thorium and uranium concentrations for nine samples of 0.06 ppm (~0.3 Bq kg $^{-1}$  for thorium) and 0.05 ppm (~0.6 Bq kg $^{-1}$  for uranium). The present study obtained mean thorium and uranium activity concentrations of 1.9 and 6.2 Bq kg $^{-1}$ , corresponding to concentrations of 0.48 and 0.51 ppm from East Sayan nephrite (table 1).

**Comparison of K, Th, and U Concentrations Measured from Para-Nephrite.** Luo et al. (2015) present detailed laser ablation-inductively coupled-mass spectrometry (LA-ICP-MS) trace element data for 138 samples collected directly from eight major dolomite-related nephrite deposits in East Asia. Figure 8 compares mean potassium, thorium, and uranium concentrations reported in Luo et al. (2015) with results from ortho-nephrite samples reported in this study. As seen in figure 8A, the ortho-nephrites exhibit an average potassium concentration of 0.03 wt.%, whereas the para-nephrites from East Asia exhibit an average potassium concentration of 0.07 wt.% (22 Bq kg $^{-1}$ ) with standard deviations of 0.02 and 0.04%, respectively. Nichol (2000) reports a mean potassium concentration of  $0.1 \pm 0.02$  wt.% for para-nephrite samples from southern Australia. This corresponds to a  $^{40}\text{K}$  activity concentration of approximately 30 Bq kg $^{-1}$ , a value that resembles that measured for sample CN1, which gave the highest  $^{40}\text{K}$  activity concentration among the ortho-nephrite samples (table 1). Similarly, dolomite-related nephrite from Val Malenco (Italy) had a mean potassium concentration of  $0.04 \pm 0.004$  wt.%, which slightly exceeded the average values

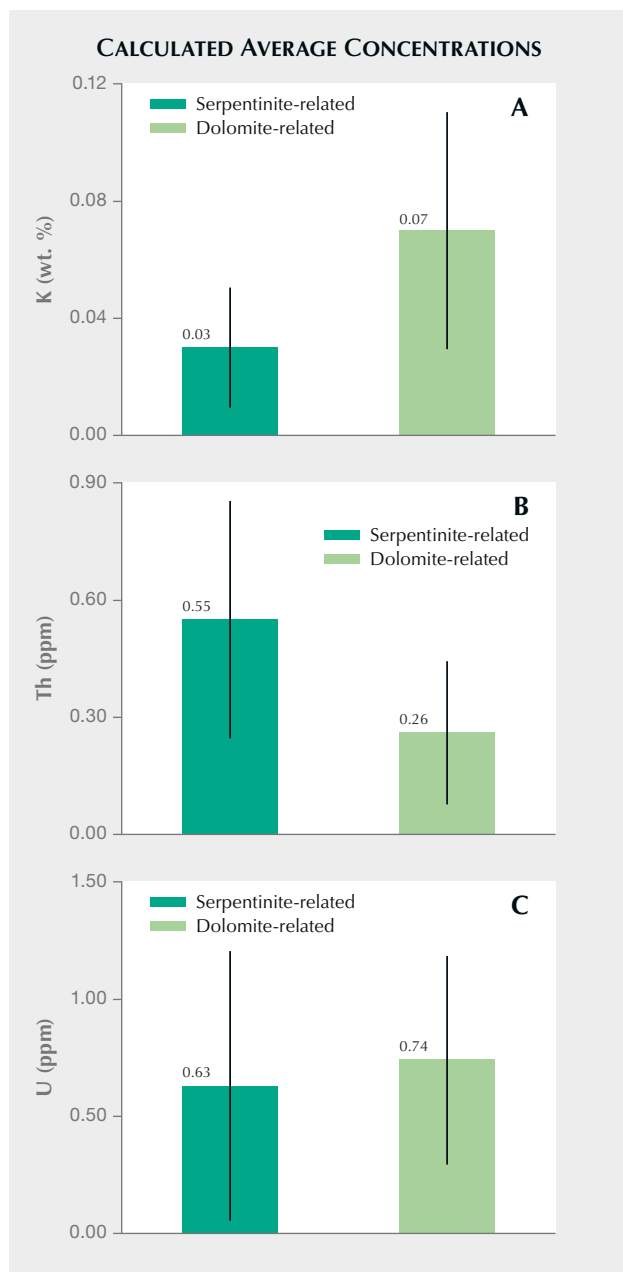


Figure 8. Comparison of calculated average concentrations of potassium (wt. %), thorium (ppm), and uranium (ppm) in ortho-nephrites (serpentine-related, darker green bar) analyzed in this study and from para-nephrite (dolomite-related, lighter green bar) data reported by Luo et al. (2015). The thin vertical lines are error bars.

obtained for ortho-nephrites reported here. A concentration of 0.04 wt. % potassium corresponds to a  $^{40}\text{K}$  activity concentration of about  $12 \text{ Bq kg}^{-1}$ . This estimate resembles values measured for the Jordanów nephrites (table 1). Results also show that the

mean potassium concentration calculated from ortho-nephrite  $^{40}\text{K}$  activity concentration generally falls below that measured for para-nephrite (figure 8A). However, potassium concentrations often overlap for both types of nephrite. Serpentine-related nephrites gave an estimated average thorium concentration of  $0.55 \pm 0.30 \text{ ppm}$ , which exceeds that estimated for para-nephrite ( $0.26 \pm 0.18 \text{ ppm}$  or  $1.1 \pm 0.7 \text{ Bq kg}^{-1}$ ) by a factor of two (figure 8B). The relatively large dispersion of thorium concentrations for both types of nephrite means that value ranges partially overlap. Excluding the Jordanów samples with the highest thorium concentrations gives a calculated mean of 0.35 for the remaining serpentine-related nephrites. This value still exceeds the values estimated for dolomite-related nephrite. As shown in figure 8C, serpentine-related nephrites gave an average U concentration of  $0.63 \pm 0.57 \text{ ppm}$ , while dolomite-related nephrites had an average uranium concentration of  $0.74 \pm 0.44 \text{ ppm}$  ( $9.1 \pm 5.4 \text{ Bq kg}^{-1}$ ). Ortho-nephrite and para-nephrite showed very similar average uranium concentrations, but samples from different nephrite deposit locations give relatively variegated values. In summary, the relatively large standard deviations associated with calculated mean potassium, thorium, and uranium concentrations suggest that these parameters alone would not be enough to clearly distinguish ortho-nephrite from para-nephrite but may serve as approximate indicators of host rock type, especially in terms of their potassium and thorium parameters.

**Correlations Between Th and U Concentrations.** As seen in figure 9,  $^{232}\text{Th}$  and  $^{238}\text{U}$  concentrations correlate strongly in ortho-nephrites analyzed and give a correlation coefficient of 0.98. A fitted line shows samples NS1 and NZ1 deviate slightly from this trend. Figure 9 shows that Jordanów samples (JR1–JR3) form a distinct data cluster with uranium concentrations ranging from 1.3 to 1.7 ppm and thorium concentrations from 1.0 to 1.2 ppm. All other ortho-nephrite samples range from about 0.1 to 0.6 ppm in terms of both uranium and thorium concentrations. A gap of 0.7 to 1.3 ppm for uranium and 0.6 to 1.0 for thorium thus exists between the Jordanów samples and others. Excluding the CN1 sample, other samples also show strong K-Th and K-U correlations (table 1).

The dolomite-related nephrites from deposits in East Asia studied by Luo et al. (2015) showed weaker correlations between average thorium and uranium concentrations. These gave average thorium concen-

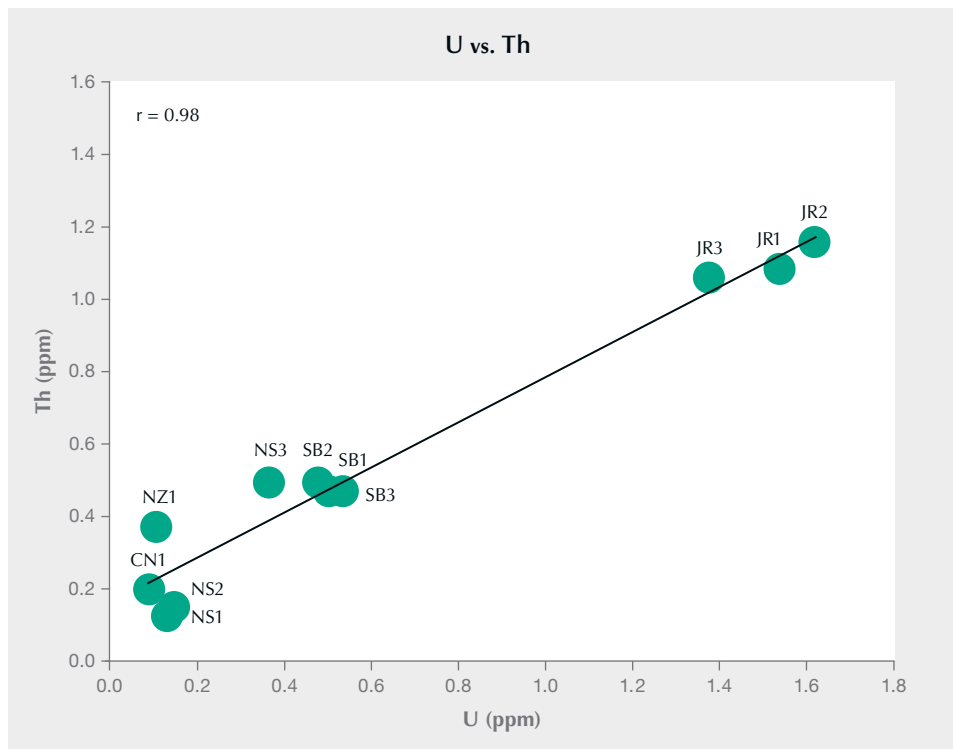


Figure 9. Correlation between thorium (ppm) and uranium (ppm) for ortho-nephrites analyzed in this study. The solid line represents the linear fit of  $\text{Th (ppm)} = 0.16 + 0.62 \times \text{U (ppm)}$ , with a correlation coefficient of  $r = 0.98$ .

trations of 0.07 to 0.70 ppm and uranium concentrations from 0.2 to 1.4 ppm. Data from these para-nephrites show a high degree of visible scatter, and linear regression gives a correlation coefficient of 0.42

(figure 10). The weaker correlation between thorium and uranium concentrations for para-nephrite (figure 10) compared to that observed for ortho-nephrite (figure 9) most likely arises from greater differentiation of

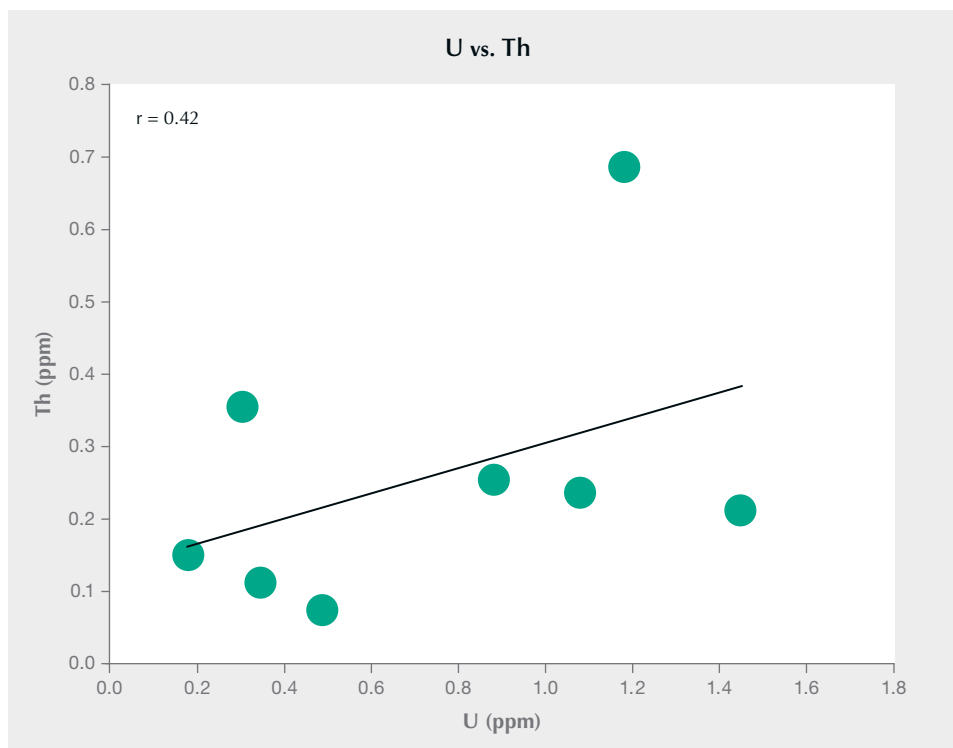


Figure 10. Correlation between thorium (ppm) and uranium (ppm) for para-nephrites based on data reported in table 2 of Luo et al. (2015). The solid line represents a linear fit of  $\text{Th (ppm)} = 0.13 + 0.17 \times \text{U (ppm)}$ , with a correlation coefficient of  $r = 0.42$ .

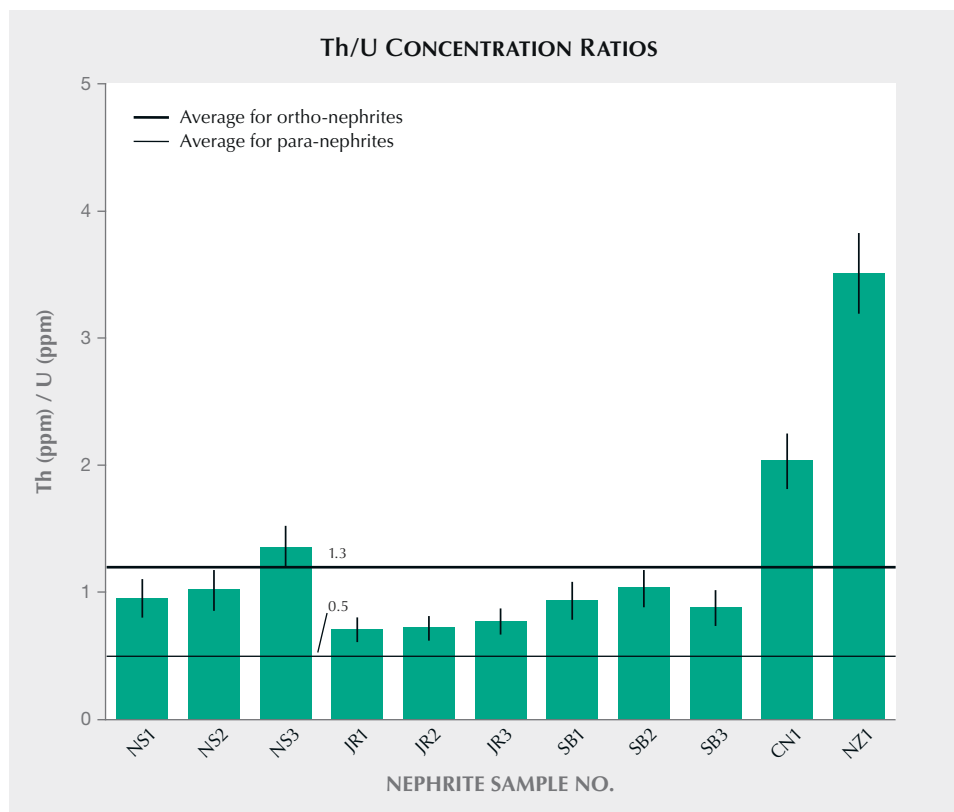


Figure 11. Concentration ratios of Th/U. The thick horizontal line shows the average for ortho-nephrites in the present study. The thin horizontal line shows the average for para-nephrites based on data reported by Luo et al. (2015). The thin vertical lines are error bars.

thorium and uranium concentrations in dolomites (and carbonates in general), which are the host rocks for para-nephrite.

**Th/U Concentration Ratios.** As shown in figure 11, Th/U ratios for the serpentinite-related nephrites vary from 0.70 to 3.51 with an average value of 1.30. The average Th/U concentration ratios were  $1.11 \pm 0.12$ ,  $0.73 \pm 0.02$ , and  $0.95 \pm 0.05$  for nephrite from Naślawice, Jordanów, and Siberia, respectively. Nephrite from these locations can be differentiated within standard deviations based on their Th/U ratio (figure 11). Despite its higher thorium and uranium concentrations, sample NS3 gave a Th/U ratio similar to that of samples NS1 and NS2. Samples CN1 and NZ1 gave relatively higher Th/U ratios of  $2.03 \pm 0.14$  and  $3.51 \pm 0.25$ , respectively.

The data presented by Luo et al. (2015) indicates a calculated mean Th/U value of 0.5 for dolomite-related nephrite. This value falls below the value of 1.3 estimated for serpentinite-related nephrite by the present study (figure 11). The calculated values of 1.3 and 0.5 for serpentinite- and dolomite-related nephrite (respectively) resemble Th/U concentration ratios in the host rocks. Serpentinites and their peridotite protoliths both exhibit a Th/U ratio of approx-

imately 2 (Van Schmus, 1995; Pasquale et al., 2001). As listed in table 1, the serpentinite from Naślawice (SN1) gave a ratio of 1.9, which approaches the mean value estimated for ortho-nephrite. Previous studies of dolomite and dolomite marble using gamma-ray spectrometry show that the average Th/U ratio for these rocks is about 0.5 (Chiozzi et al., 2002; Malczewski et al., 2005; Malczewski and Żaba, 2012; Moska, 2019). Generally, carbonate rocks have a mean Th/U value of 0.8 (Van Schmus, 1995). Again, the average value of the Th/U ratio calculated for the para-nephrites based on the results obtained by Luo et al. (2015) agrees well with those reported for carbonate rocks and especially dolomites.

## CONCLUSIONS

This study reports gamma-ray spectrometric analysis of serpentinite-related nephrite samples from several well-known global localities. Measurements indicate very low  $^{40}\text{K}$ ,  $^{232}\text{Th}$ , and  $^{238}\text{U}$  activity concentrations that pose no radiological risk. Measured activity concentrations fell below values reported in the literature for acid igneous rocks. By contrast, the mean  $^{40}\text{K}$ ,  $^{232}\text{Th}$ , and  $^{238}\text{U}$  activity concentration values exceeded average values reported in literature sources for ultrabasic rocks and, to a lesser ex-



*Figure 12. This 90 × 20 mm nephrite carving is from the Kutcho Jade mine in northwest British Columbia, Canada. Photo by Robert Weldon; courtesy of Jade West Group.*

tent, for serpentinites. Compared to gabbroic rocks from Lower Silesia (Poland), the ortho-nephrites ex-

hibited lower  $^{40}\text{K}$  and  $^{232}\text{Th}$  activity concentrations and slightly higher  $^{238}\text{U}$  activity concentrations. The

measured serpentinite-related nephrites were characterized by extremely low average values of radiological hazard indices  $I$  and  $H_{ex}$  of 0.04 and 0.03, with the upper levels of both indices equal to unity. Calculated thorium (ppm) and uranium (ppm) concentrations strongly correlate. Nephrite from Nasławice, Jordanów, and Siberia show distinct

Th/U ratios, indicating that this parameter may distinguish material from these respective localities. Our results suggest that relative to para-nephrite, ortho-nephrite (figure 12) exhibits lower potassium concentration values and higher thorium concentrations. Both types of nephrite jade exhibit similar uranium concentrations.

#### ABOUT THE AUTHORS

*Dr. Malczewski is a nuclear physicist and assistant professor at the Institute of Earth Sciences of the University of Silesia (Poland), specializing in the field of natural and anthropogenic radioactivity in the geosphere and researching metamict minerals as natural analogues for understanding the storage of high-level nuclear waste. Professor Sachanbiński, who specializes in the physics of minerals, gemology, and mineralogy, is an emeritus professor at the University of Wrocław and teaches at the College of Arts and Management in Wrocław. Dr. Dziurawicz is a geologist, geophysicist, and assistant professor at the Institute of Earth Sciences of the University of Silesia, specializing in natural and anthropogenic environmental radioactivity.*

#### ACKNOWLEDGMENTS

*This work was partially supported by the National Science Centre of Poland through grant no. 2018/29/B/ST10/01495 and the research program at the Institute of Earth Sciences, University of Silesia, ZB-14-2020. We thank the Mineralogical Museum at the Institute of Earth Sciences, University of Silesia, and Stanisław Madej for the New Zealand jade sample and rodingite samples used in this research. The authors would like to thank Sandra Malczewska for the digital processing of photos according to publication requirements.*

#### REFERENCES

- Adamo I., Bocchio R. (2013) Nephrite jade from Val Malenco, Italy: Review and update. *G&G*, Vol. 49, No. 2, pp. 98–106, <http://dx.doi.org/10.5741/GEMS.49.2.98>
- Bell J.M., de Coursey Clarke E., Marshall P. (1911) Geology of the Dun Mountain Subdivision. *New Zealand Geological Survey, Bulletin No. 12*, pp. 31–35.
- Burtseva M.V., Ripp G.S., Posokhov V.F., Murzintseva A.E. (2015) Nephrites of East Siberia: Geochemical feature and problems of genesis. *Russian Geology and Geophysics*, Vol. 56, No. 3, pp. 402–410, <http://dx.doi.org/10.1016/j.rgg.2015.02.003>
- Chiozzi P., Pasquale V., Verdoya M. (2002) Naturally occurring radioactivity at the Alps-Apennines transition. *Radiation Measurements*, Vol. 35, No. 2, pp. 147–154, [http://dx.doi.org/10.1016/S1350-4487\(01\)00288-8](http://dx.doi.org/10.1016/S1350-4487(01)00288-8)
- Cooper A.F. (1995) Nephrite and metagabbro in the Haast Schist at Muddy Creek, northwest Otago, New Zealand. *New Zealand Journal of Geology and Geophysics*, Vol. 38, No. 3, pp. 325–332, <http://dx.doi.org/10.1080/00288306.1995.9514660>
- Douglas J.G. (2005) A review of some recent research on early Chinese jades. In *Scientific Examination of Art: Modern Techniques in Conservation and Analysis*. National Academies Press, Washington, DC, pp. 206–214.
- Dubińska E., Gunia P. (1997) The Sudetic ophiolite: Current view on its geodynamic model. *Geological Quarterly*, Vol. 41, No. 1, pp. 1–20.
- Dubińska E., Bylina P., Kozłowski A., Dörr W., Nejbert K., Schastok J., Kulicki C. (2004) U-Pb dating of serpentinization: Hydrothermal zircon from a metasomatic rodingite shell (Sudetic ophiolite, SW Poland). *Chemical Geology*, Vol. 203, No. 3–4, pp. 183–203, <http://dx.doi.org/10.1016/j.chemgeo.2003.10.005>
- Eisenbud M., Gesell T. (1997) *Environmental Radioactivity Concentration from Natural, Industrial and Military Sources*. Academic Press, San Diego.
- European Atomic Energy Community (2013) Council Directive EU 2013/59/Euratom. Laying down basic safety standards for protection against the dangers arising from exposure to ionising radiation.
- Fares S., Yassene A.A.M., Ashour A., Abu-Assy M.K., Abd El-Rahman M. (2011) Natural radioactivity and the resulting radiation doses in some kinds of commercially marble collected from different quarries and factories in Egypt. *Natural Science*, Vol. 3, No. 10, pp. 895–905, <http://dx.doi.org/10.4236/ns.2011.310115>
- Gao K., Fang T., Lu T., Lan Y., Zhang Y., Wang Y., Chang Y. (2020) Hydrogen and oxygen stable isotope ratios of dolomite-related nephrite: Relevance for its geographic origin and geological significance. *G&G*, Vol. 56, No. 2, pp. 266–280, <http://dx.doi.org/10.5741/GEMS.56.2.266>
- Gil G. (2013) Petrographic and microprobe study of nephrites from Lower Silesia (SW Poland). *Geological Quarterly*, Vol. 57, No. 3, pp. 395–404, <http://dx.doi.org/10.7306/gq.1101>
- Gil G., Barnes J.D., Boschi C., Gunia P., Szakmány G., Bendő Z., Raczyński P., Péterdi B. (2015) Origin of serpentinite-related nephrite from Jordanów and adjacent areas (SW Poland) and its comparison with selected nephrite occurrences. *Geological Quarterly*, Vol. 59, No. 3, pp. 457–472, <http://dx.doi.org/10.7306/gq.1228>
- Gil G., Bagiński B., Gunia P., Madej S., Sachanbiński M., Jokubauskas P., Belka Z. (2020) Comparative Fe and Sr isotope study of nephrite deposits hosted in dolomitic marbles and serpentinites from the Sudetes, SW Poland: Implications for Fe-Au-bearing skarn formation and post-obduction evolution of the oceanic lithosphere. *Ore Geology Reviews*, Vol. 118, article no. 103335, <http://dx.doi.org/10.1016/j.oregeorev.2020.103335>
- Grapes R.H., Yun S.T. (2010) Geochemistry of a New Zealand nephrite weathering rind. *New Zealand Journal of Geology and Geophysics*, Vol. 53, No. 4, pp. 413–426, <http://dx.doi.org/10.1080/00288306.2010.514929>
- Hatzipanagiotou K., Tsikouras B. (2001) Rodingite formation from

- diorite in the Samothraki ophiolite, NE Aegean, Greece. *Geological Journal*, Vol. 36, No. 2, pp. 93–109, <http://dx.doi.org/10.1002/gj.887>
- Heflik W., Natkaniec-Nowak L., Dumańska-Słowik A. (2014) Rodingite from Naślawice and the other occurrences of these rocks in Lower Silesia (SW Poland). *Geological Quarterly*, Vol. 58, No. 1, pp. 31–40.
- Hobbs J.M. (1982) The jade enigma. *G&G*, Vol. 18, No. 1, pp. 3–19, <http://dx.doi.org/10.5741/GEMS.18.1.3>
- International Atomic Energy Agency (2003) IAEA-TECDOC-1363: Guidelines for radioelement mapping using gamma ray spectrometry data. Vienna.
- Ireland T.R., Reay A., Cooper A.F. (1984) The Pounamu ultramafic belt in the Dietrich Range, Westland, New Zealand. *New Zealand Journal of Geology and Geophysics*, Vol. 27, No. 3, pp. 247–256.
- Kobayashi S., Kaneda H. (2010) Rodingite with Ti- and Cr-rich vesuvianite from the Sartuohai chromium deposit, Xinjiang, China. *Journal of Mineralogical and Petrological Sciences*, Vol. 105, No. 3, pp. 112–122, <http://dx.doi.org/10.2465/jmps.081224>
- Leaming S.F. (1978) *Jade in Canada*. Geological Survey of Canada, Paper 78-19. Energy, Mines & Resources, Canada, 59 pp.
- Łoboś K., Sachanbiński M., Pawlik T. (2008) Nephrite from Naślawice in Lower Silesia (SW Poland). *Przełąd Geologiczny*, Vol. 56, No. 11, pp. 991–999 (in Polish with English abstract).
- Luo Z., Yang M., Shen A.H. (2015) Origin determination of dolomite-related white nephrite through iterative-binary linear discriminant analysis. *G&G*, Vol. 51, No. 3, pp. 300–311, <http://dx.doi.org/10.5741/GEMS.51.3.300>
- Makepeace K., Simandl G.J. (2001) Jade (nephrite) in British Columbia, Canada. *Program and Extended Abstracts for 37th Forum on the Geology of Industrial Minerals 37*, pp. 209–210.
- Malczewski D., Żaba J. (2012) Natural radioactivity in rocks of the Modane-Aussois region (SE France). *Journal of Radioanalytical and Nuclear Chemistry*, Vol. 292, No. 1, pp. 123–130, <http://dx.doi.org/10.1007/s10967-011-1428-9>
- Malczewski D., Teper L., Lizurek G., Dorda J. (2005) In situ gamma-ray spectroscopy in common rock raw materials mined in Kraków vicinity, Poland. In *Naturally Occurring Radioactive Materials (NORM IV): Proceedings of an International Conference Held in Szczyrk, Poland, 17–21 May 2004*. IAEA-TECDOC-1472. International Atomic Energy Agency, Lanham, Maryland, pp. 368–376.
- Malczewski D., Dziurowicz M., Krzykowski T., Grabias A. (2018a) Spectroscopic characterization and thermal recrystallization study of an unknown metamict phase from Tuften Quarry, Southern Norway. *The Canadian Mineralogist*, Vol. 56, No. 4, pp. 365–373, <http://dx.doi.org/10.3749/canmin.1800015>
- Malczewski D., Dziurowicz M., Krzykowski T., Stryjewski A. (2018b)  $^{222}\text{Rn}$  and  $^{220}\text{Rn}$  emanations from zircon crystals as a function of absorbed alpha-doses. *The Canadian Mineralogist*, Vol. 56, No. 4, pp. 451–462, <http://dx.doi.org/10.3749/canmin.1700089>
- Moska A. (2019) Natural and anthropogenic radioactivity of the Opawa Mountains and their western foreland. PhD thesis. University of Silesia, Katowice, Poland (in Polish with English abstract).
- Nichol D. (2000) Two contrasting nephrite jade types. *Journal of Gemmology*, Vol. 27, No. 4, pp. 193–200.
- O'Brien J.P., Rodgers K.A. (1973) Xonitlite and rodingites from Wairere, New Zealand. *Mineralogical Magazine*, Vol. 39, No. 302, pp. 233–240.
- Pasquale V., Verdoya M., Chiozzi P. (2001) Radioactive heat generation and its thermal effects in the Alps-Apennines boundary zone. *Tectonophysics*, Vol. 331, No. 3, pp. 269–283, [http://dx.doi.org/10.1016/S0040-1951\(00\)00294-8](http://dx.doi.org/10.1016/S0040-1951(00)00294-8)
- Plewa M., Plewa S. (1992) *Petrophysics*. Geological Publishing House, Warsaw, 326 pp. (in Polish).
- Prichystal A. (2013) *Lithic Raw Materials in Prehistoric Times of Eastern Central Europe*. Masaryk University, Brno, Czech Republic.
- Suturin A.N., Zamaletdinov R.S., Letnikov F.A., Sekerin A.P., Burmakina G.V., Suturina T.A., Platonov A.N., Belitchenko V.P., Vokhmentser A.Y. (1980) Mineralogy and genesis of nephrites in the USSR. In Sidorenko, Eds., *Gem Minerals: Proceeding of the XI General Meeting of IMA*, Novosibirsk, September 4–10, 1978 (in Russian).
- Szeleg E. (2006) Crystalline chemistry of titanite from Lower Silesian. PhD thesis. University of Silesia, Katowice, Poland (in Polish).
- UNSCEAR (2000) Sources and Effects of Ionizing Radiation: Vol I. United Nations Scientific Committee on the Effects of Atomic Radiation. UNSCEAR 2000 Report to the General Assembly, with Scientific Annexes. United Nations, New York.
- Van Schmus W.R. (1995) Natural radioactivity of the crust and the mantle. In T.J. Ahrens, Ed., *Global Earth Physics: A Handbook of Physical Constants*. AGU Reference Shelf I, American Geophysical Union, Washington, DC, pp. 283–291.
- Wang R. (2011) Progress review of the scientific study of Chinese ancient jade. *Archaeometry*, Vol. 53, No. 4, pp. 674–692, <http://dx.doi.org/10.1111/j.1475-4754.2010.00564.x>
- Wilkins C.J., Tennant W.C., Williamson B.E., McCammon C.A. (2003) Spectroscopic and related evidence on the coloring and constitution of New Zealand jade. *American Mineralogist*, Vol. 88, No. 8-9, pp. 1336–1344, <http://dx.doi.org/10.2138/am-2003-8-917>
- Yui T.F., Kwon S.T. (2002) Origin of a dolomite-related jade deposit at Chumcheon, Korea. *Economic Geology*, Vol. 97, No. 3, pp. 593–601, <http://dx.doi.org/10.2113/gsecongeo.97.3.593>
- Żaba J. (2006) *Illustrated Dictionary of Rocks and Minerals*. Videograf II Ltd., Katowice, Poland (in Polish).

For online access to all issues of GEMS & GEMOLOGY from 1934 to the present, visit:

[gia.edu/gems-gemology](http://gia.edu/gems-gemology)

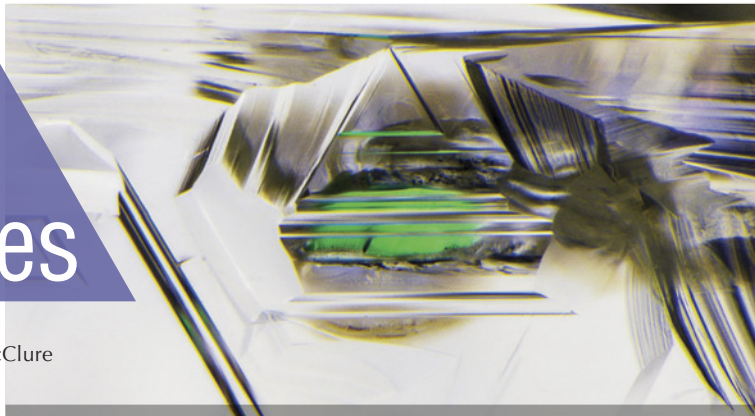




# Lab Notes

## Editors

Thomas M. Moses | Shane F. McClure



### Rare Orange BENITOITE

A bright orange benitoite (figure 1) weighing 2.29 ct was recently examined at the Carlsbad laboratory. Standard gemological testing revealed a refractive index of 1.756 to over the limit (OTL) and a specific gravity of 3.68. The fluorescence reaction was strong orange in long-wave ultraviolet light and medium blue in short-wave UV (figure 2). The benitoite was slightly color-zoned orange and blue; the blue portion's pleochroism was very light blue and darker blue, while the orange portion's pleochroism was orangy yellow and dark orange. Microscopic examination showed altered crystals with discoid fractures (figure 3) and strong doubling. The discoid fractures were consistent with heated benitoite.

Benitoite is a barium titanium silicate ( $\text{BaTiSi}_3\text{O}_9$ ) known as the California state gem, and it only occurs in gem quality in San Benito County, California. The New Idria District produces medium to medium-dark blue and lighter blue colors. According to a previous study published in *G&G*, pink and colorless examples are considered rare. In addition, heat treatment of lighter-color or colorless benitoite may result in an orange color. Since only a small portion of



Figure 1. The size and bright color of this 2.29 ct orange benitoite are exceptionally rare.

the treated material successfully changes color, orange benitoite is considered rare (B.M. Laurs et al., "Benitoite from the New Idria District, San Benito County, California," Fall 1997 *G&G*, pp. 166–187).

Figure 2. The orange benitoite's response to long-wave (left) and short-wave UV (right).

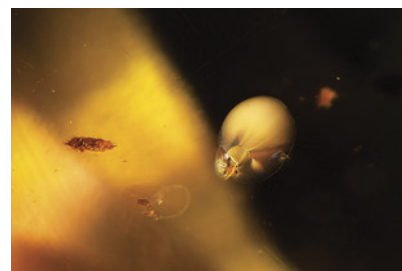
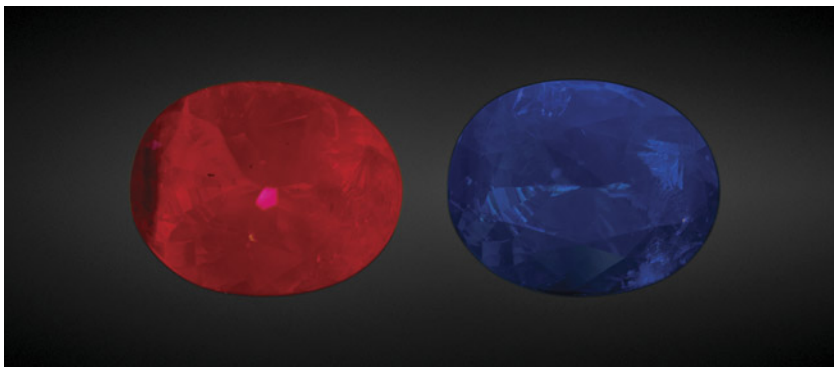


Figure 3. The orange benitoite contained several discoid fractures with healed fringes, consistent with heat-treated benitoite. Field of view 2.33 mm.

This benitoite was faceted by Bill Vance of Vance Gems, who stated that the rough was colorless prior to heat treatment. The bright orange color and large size make this an exceptional example of orange benitoite. Very few of these have been examined at GIA, and this 2.29 ct gemstone is the largest example we have observed.

Amy Cooper and Nathan Renfro

*Editors' note: All items were written by staff members of GIA laboratories.*

GEMS & GEMOLOGY, Vol. 58, No. 2, pp. 214–225.

© 2022 Gemological Institute of America



Figure 4. This set consists of a 48.63 ct piece of manmade glass (left), 9.17 and 6.21 ct laboratory-grown sapphires with resin imitation of matrix on the surface (center), and an 8.46 ct natural blue sapphire rough (right).

### Interesting Set of BLUE “ROUGH” GEMSTONES

The selling of simulants and synthetics mixed with parcels of natural stones is an old form of deception. It usually happens close to mines, where inexperienced buyers assume the gemstones come directly from the source—and where advanced testing is likely not available prior to the purchase.

The Carlsbad laboratory recently received a group of four blue rough

stones (figure 4) submitted as natural sapphire for identification and origin reports. The largest weighed 48.63 ct and measured approximately  $22.88 \times 19.67 \times 15.19$  mm. The material was partially fashioned, with evidence of polish lines on the surfaces. Careful microscopic examination revealed multiple gas bubbles, distinct flow marks associated with blue coloration, and conchoidal fractures. Weak snake pattern bands were observed under the polariscope. The hydrostatic specific

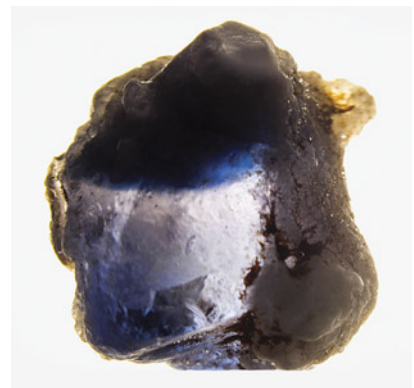
gravity was 2.48. These observations suggested a glass imitation, which was confirmed by comparing the infrared spectrum with that of manmade glass.

The next two were more convincing imitations of natural sapphire. They weighed 9.17 and 6.21 ct and measured approximately  $16.00 \times 10.06 \times 8.30$  mm and  $10.31 \times 9.38 \times 8.71$  mm, respectively. Resin that coated the surface (figure 5) resembled matrix composed of natural minerals commonly seen on natural corundum rough. The resin started to melt with the touch of a hot pointer. Brownish materials trapped in cavities resembled iron oxide stains one would expect to see in natural rough. Though difficult to see inside of the stones due to their rough surfaces, a few gas bubbles were observed through a small transparent area. Raman spectroscopy matched corundum, and immersion in water (figure 6) revealed curved blue banding. Laser ablation–inductively coupled plasma–mass spectrometry (LA-ICP-MS) detected no gallium and revealed trace elements of impurities consistent with synthetic corundum. Hydrostatic specific gravity values were 3.76 and 3.59, respectively. Both values were below the SG of corundum (3.9–4.05), a result of the lower SG of the resin on the surface. Both were reported as laboratory-grown sapphire with a comment stating, “Imitation matrix and resin is present on the surface.”

Figure 5. A resin imitation of matrix on the surface of a laboratory-grown sapphire. Field of view 7.19 mm.



Figure 6. Curved blue banding visible in the 6.21 ct laboratory-grown sapphire immersed in water.



The last piece of rough was a blue stone weighing 8.46 ct and measuring  $13.85 \times 9.89 \times 7.60$  mm. The frosted natural surface made it difficult to see inside the stone, but some natural-looking fingerprints and strong, straight inky blue banding were observed. The Raman spectrum matched with corundum, and a hydrostatic SG of 3.96 confirmed it. The stone was immersed in methylene iodide to confirm the zoning was straight and not curved. Medium chalky blue fluorescence to short-wave UV and a strong  $3309\text{ cm}^{-1}$  series in its Fourier-transform infrared (FTIR) spectrum proved that heat treatment had been applied to the stone. LA-ICP-MS revealed natural chemistry, including about 200 ppma iron and other trace elements such as gallium (~25 ppma), vanadium (~3.5 ppma), magnesium (~35 ppma), chromium (~1.5 ppma), and titanium (~80 ppma). Based on appearance, color zoning, and chemistry, this stone was reported as natural sapphire, heat treated, with Madagascar as the country of origin.

This was an interesting study of how synthetics and simulants can be mixed with their natural counterparts to misrepresent a parcel. However, careful examination and standard gemological testing are usually enough to identify them correctly.

*Najmeh Anjomani*

## DIAMONDS

### The Type IIb De Beers Cullinan Blue Diamond

Type IIb blue diamonds are extremely rare in nature. When people think of blue diamonds, the Hope diamond immediately springs to mind. The famed 45.52 ct Fancy Deep grayish blue cushion-cut treasure, now housed in the Smithsonian National Museum of Natural History in Washington, DC, has a long and fascinating history. First examined by GIA in 1960 and graded by GIA in 1988 (R. Crowningshield, "Grading the Hope diamond," Summer 1989 *G&G*, pp. 91–94), it



Figure 7. The 15.10 ct De Beers Cullinan Blue diamond.

shares many special gemological characteristics with other rare type IIb (boron-containing) diamonds such as the Wittelsbach-Graff, once assumed to be cut from the same rough crystal as the Hope. Here we report another special diamond of this group.

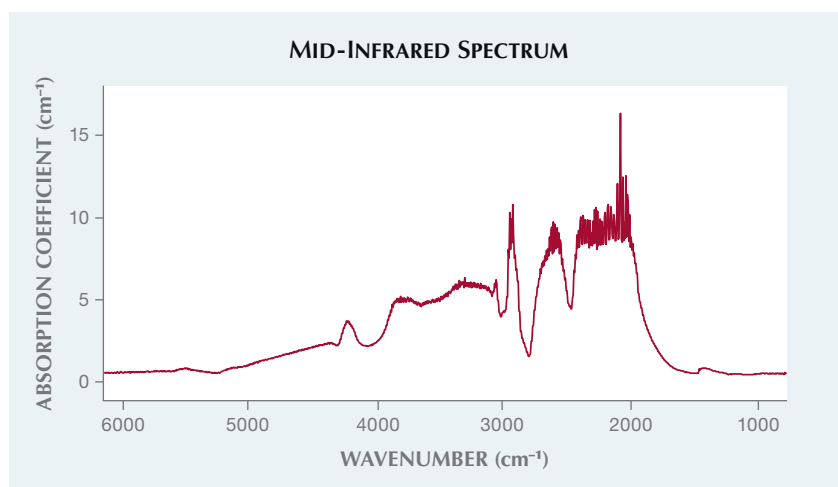
Recently graded by GIA and the recipient of a special monograph report was a 15.10 ct ( $17.47 \times 11.53 \times 7.94$  mm) Fancy Vivid blue cut-cornered rectangular step cut. Named the De Beers Cullinan Blue diamond (figure 7; see video at [www.gia.edu/gems-gemology/summer-2022-lab-notes-de-beers-cullinan-blue](http://www.gia.edu/gems-gemology/summer-2022-lab-notes-de-beers-cullinan-blue)), it was cut from a 39.34 ct rough type IIb diamond crystal mined by Petra from the Cullinan

(formerly Premier) mine in South Africa. Compared to the Hope and Wittelsbach-Graff, both of which were mined in the Golconda region of India, the De Beers Cullinan Blue has some important similarities in gemological and spectroscopic features but shows clear variations. Natural type IIb blue diamonds over 10 carats are exceedingly rare.

The blue color is distributed evenly throughout the stone. Visual observation under a gem microscope revealed a very clean stone. No inclusions or graining were observed. Accordingly, the diamond received a clarity grade of Internally Flawless. Under conventional long-wave and short-wave UV radiation, it showed no observable fluorescence or phosphorescence. This feature is dramatically different from that of the Hope and Wittelsbach-Graff, two large type IIb blue diamonds that exhibit strong and prolonged red phosphorescence to conventional short-wave UV radiation.

The absorption spectrum in the mid-infrared region showed typical absorption features related to boron in diamond, such as strong absorption at  $\sim 2800\text{ cm}^{-1}$  and a weak absorption peak in the range of  $1332\text{--}1200\text{ cm}^{-1}$  (figure 8). The intensities of these absorptions indicated a high

Figure 8. The mid-infrared spectrum of the type IIb De Beers Cullinan Blue diamond.



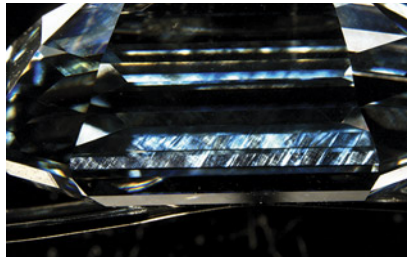
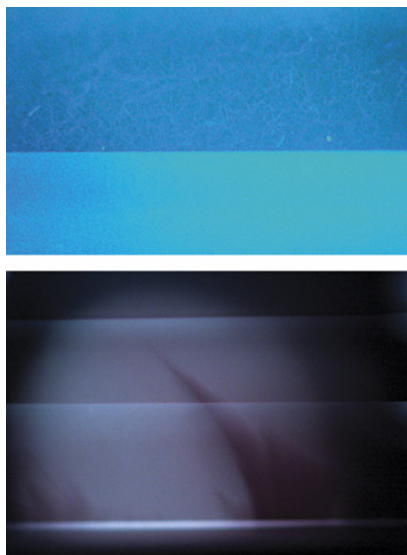


Figure 9. Observed with cross-polarized light was a strong tatami strain pattern with a dark gray color.

concentration of uncompensated boron of ~0.33 ppm. Natural type IIb diamonds typically contain 0.24–0.36 ppm (E. Gaillou et al., “Study of the Blue Moon diamond,” Winter 2014 *G&G*, pp. 280–286). The diamond’s boron concentration is close to that of the Hope (~0.36 ppm) and higher than that of the Wittelsbach-Graff (~0.19 ppm). Absorption from boron is the main contributor of color in natural type IIb diamonds.

Observation with a gemological

Figure 10. Under very strong short-wave UV, a weak aqua blue fluorescence with a subtle network of dislocations was observed (top). After exposure, a weak pinkish red phosphorescence was observed (bottom).



microscope equipped with crossed polarizers revealed a clear tatami pattern with a dark gray color (figure 9). Both the Wittelsbach-Graff and the Hope have different patterns and higher interference colors, a good indication that the De Beers Cullinan Blue has a much less distorted lattice structure. Under very strong short-wave UV, this diamond showed a weak aqua blue fluorescence with a subtle network of dislocations in the crystal structure, a pattern clearly different from the tight mosaic patterns observed in the Hope and the Wittelsbach-Graff (figure 10) (Gaillou et al., 2014).

These blue diamonds are among the rarest of gems. Recent research (E. Smith et al., “Blue boron-bearing diamonds from Earth’s lower mantle,” *Nature*, Vol. 560, No. 7716, 2018, pp. 84–87) has demonstrated that their boron derived from pieces of the earth’s crust sinking to the extremely deep depths of diamond formation. The gemological characteristics of the De Beers Cullinan Blue suggest it is one of these superdeep diamonds. Its combination of Fancy Vivid blue color grade in a step cut (a cut that does not enhance color, unlike other faceting

styles) (see video), 15.10 ct weight, and Internally Flawless clarity grade is exceptionally rare. It will remain one of the world’s most important diamonds.

*Paul Johnson, A’Dhi Lall, Madelyn Dragone, and Stephanie Persaud*

### The Grass Is Always Greener...

The Carlsbad laboratory recently examined a 0.97 ct Fancy grayish green diamond submitted for colored diamond grading service. Microscopic examination revealed a colorless diamond with green radiation stains scattered across the pavilion (figure 11).

These radiation stains were particularly unusual due to their linear appearance and resembled blades of grass in their morphology and color. These stains were prevalent along intentionally preserved rough natural diamond surfaces on the pavilion. Faceted surfaces along the pavilion were polished with particular effort to retain some of the green radiation stains. The resultant internal reflection of green light to the table created a uniform green bodycolor in this rare and beautiful diamond.

Figure 11. Blade-like green radiation stains. Also indicated is the boundary of the close-up view of the green stains in figure 12. Field of view 2.9 mm.



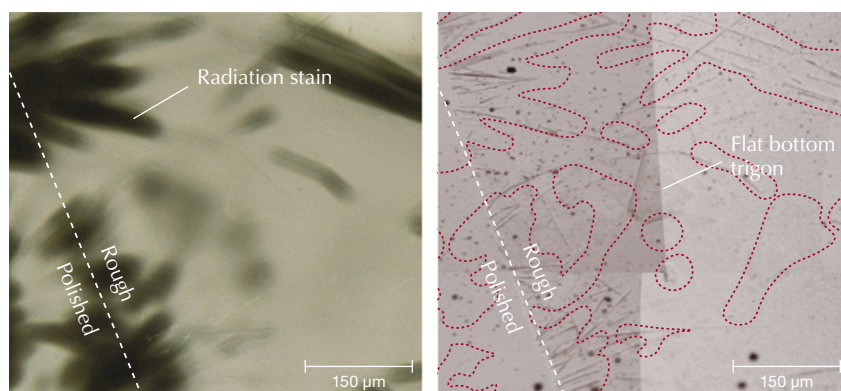


Figure 12. Radiation stains on the rough diamond's surface also penetrate to a polished side (left). Viewed with reflected light, the surface shows acicular indentations coincident with green stains (right).

Surface photomicrographs revealed long, linear, and acicular indentations concentrated near the center of the radiation stains (figure 12). Indentations crosscut flat-bottomed trigons, suggesting they post-dated diamond dissolution in the earth's mantle (e.g., R. Tappert and M. Tappert, *Diamonds in Nature: A Guide to Rough Diamonds*, Springer, Heidelberg, 2011). The green stains along the polished surface indicate that the radiation stains penetrated some depth into the diamond. These features have been observed previously at GIA (e.g., Spring 2021 *G&G Micro-World*, pp. 66–67; Spring

2022 *G&G Micro-World*, pp. 64–65) and may result from acicular to tabular radioactive minerals precipitating directly on the diamond surface in a paleoplacer to recent alluvial environment (e.g., R. Lauf, *Mineralogy of Uranium and Thorium*, Schiffer Publishing, Ltd., Atglen, Pennsylvania, 2016). Radiation damage created vacancies in the diamond lattice, which absorb red light and reflect green light, resulting in the green color of the radiation stains. Uncharged or neutral vacancies produce a photoluminescence response near the 741 nm zero phonon line called the GR1 defect (e.g., J.E. Shigley and C.M. Breeding,

"Optical defects in diamond: A quick reference chart," Summer 2013 *G&G*, pp. 107–111). The GR1 defect area from photoluminescence spectra can be measured and mapped to indicate the spatial distribution of this defect coincident with the radiation stains (figure 13).

It is unusual to see green radiation stains of this shape that correspond with indentations on a diamond surface. These features could be a commonly overlooked characteristic of green diamonds.

Michaela Stephan, Roy Bassoo, and Lo Combs

### 10 ct HPHT-Treated CVD LABORATORY-GROWN DIAMOND

Recent years have seen several size milestones for faceted diamonds grown by chemical vapor deposition (CVD). In all the published reports that commented on treatment, these record-size CVD diamonds were indicated to be as-grown and with no indications of post-growth treatment (Winter 2016 Lab Notes, pp. 414–416; "IGI Hong Kong certifies largest CVD grown diamond to date," 2020, <https://www.igi.org/gemblog/igi-hong-kong-certifies-largest-cvd-grown-diamond-to-date/>; Spring 2022 Lab Notes, pp. 54–56). For other recent milestone CVD diamonds reported within the trade, we could not confirm whether they were as-grown or treated. At the time of publication, the current benchmark is a 30.18 ct H-color diamond reportedly grown by Ethereal Green Diamond (Rapaport News, June 12, 2022).

Against this backdrop, a notable 10.04 ct CVD-grown diamond (figure 14) was recently submitted to the Carlsbad laboratory for a laboratory-grown diamond report. This emerald-cut stone with G color and VS<sub>2</sub> clarity had several growth remnants, including a cloud of dark non-diamond carbon. As with all laboratory-grown diamonds, it underwent extensive testing including spectroscopy to verify its CVD origin. IR absorption spectroscopy identified it as

Figure 13. Left: Map of the integrated area beneath the GR1 defect peak of the radiation stains on the diamond surface, derived from photoluminescence spectroscopy. Right: Reflected light image of the surface showing radiation stains (outlined in red) coincident with acicular indentations. The measurements were taken with a 532 nm laser at 1 mW power, 25 µm confocal spot size, 5 µm step size, and 100 Hz.

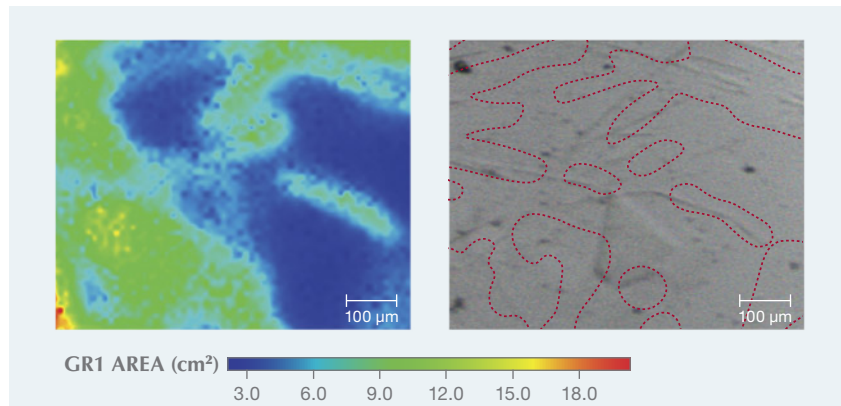
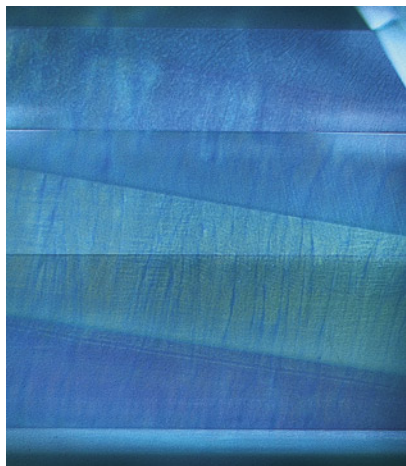




Figure 14. This 10.04 ct G-color CVD-grown diamond proved to have been HPHT treated.

type IIb with an uncompensated boron concentration of ~2 ppb. Spectral features such as the lack of a 468 nm peak in photoluminescence along with the coloration in the DiamondView fluorescence imaging (figure 15) confirmed it had undergone post-growth treatment (W. Wang et

Figure 15. The green and blue fluorescence colors in this DiamondView image confirm post-growth treatment of the 10.04 ct CVD-grown diamond.



al., "CVD synthetic diamonds from Gemesis Corp.," Summer 2012 *G&G*, pp. 80–97).

Many CVD-grown diamonds are subjected to high-pressure, high-temperature (HPHT) treatment after growth to remove a brownish appearance caused by extended defects (such as vacancy-related complexes). The brown color often correlates with a faster CVD growth rate, which the manufacturer uses knowing the color can be reduced by treatment afterward. It appears that when manufacturers create a CVD diamond of record-setting size, the growth is performed so slowly that subsequent HPHT treatment is not required for a colorless to near-colorless grade.

While some 80% of colorless to near-colorless CVD-grown diamonds have been subjected to post-growth treatment to reduce their brownish coloration (S. Eaton-Magaña et al., "Laboratory-grown diamond: A gemological laboratory perspective," *Jour-*

*nal of Gems & Gemmology*, Vol. 23, No. 6, 2021, pp. 25–39), this treatment is not often applied to larger stones. Therefore, evidence of HPHT treatment in a CVD-grown diamond larger than 10 carats is noteworthy. These products will likely become more commonplace in the future.

Sally Eaton-Magaña

## PEARLS

### A Reported Cassis Pearl from Key West, Florida

The Carlsbad laboratory recently examined an oval non-nacreous pearl weighing 29.78 ct and measuring 17.86 × 15.64 × 14.58 mm (figure 16). The pearl possessed a uniform pinkish orange bodycolor and a porcelaneous surface with flame structures. The flames were short and wide and tapered to a point. This fine, well-formed flame structure looked like a homogeneous spotted pattern throughout the pearl's

Figure 16. This oval pinkish orange porcelaneous pearl weighing 29.78 ct and measuring 17.86 × 15.64 × 14.58 mm was reportedly found in a queen helmet conch (*Cassis madagascariensis*), shown on the left with various *Cassis* species shells. Shells courtesy of Robin Willis.



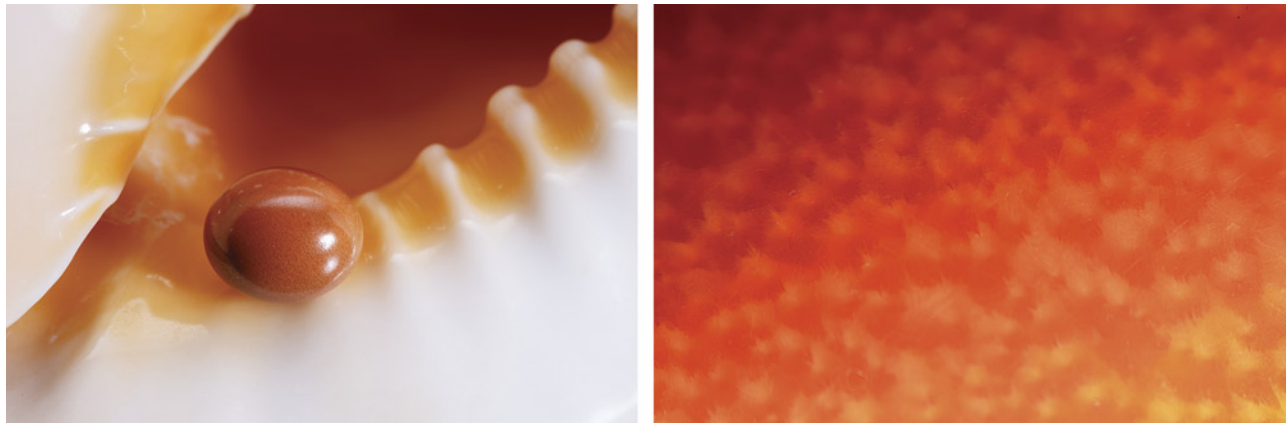


Figure 17. Left: This porcelainous pearl exhibited a fine, well-formed flame structure covering the entire surface, and a homogeneously spotted pattern was visible with the unaided eye. Right: Under magnification with fiberoptic illumination, the wide and spiky flame structure was evident. Field of view 2.90 mm.

surface (figure 17, left), yet the flame forms were evident at high magnification under the microscope (figure 17, right). Subsequently, Raman spectroscopic analysis with a 514 nm argon-ion laser verified the pearl was composed of aragonite, with peaks at 154, 181, 192, 207, 704, and 1085  $\text{cm}^{-1}$  (J. Urmos et al., "Characterization of some biogenic carbonates with Raman spectroscopy," *American Mineralogist*, Vol. 76, 1991, pp. 641–646); two strong polyene peaks at 1131 and 1523  $\text{cm}^{-1}$  were indicative of natural color (C. Hedegaard et al., "Molluscan shell pigments: An in situ resonance Raman

study," *Journal of Molluscan Studies*, Vol. 72, No. 2, 2006, pp. 157–162). Real-time microradiography (RTX) revealed a dark gray oval void-like feature in the center and a growth ring in the outer area of the pearl (figure 18). Such a void can be found in natural pearls from a number of porcelainous pearl-producing mollusks.

Orange porcelainous pearls are produced from various marine gastro-

pod species such as queen conch (*Lobatus gigas*), *Melo* species, *Cassia* species, and horse conch (*Fasciolarinae* subfamily). The flame characteristics and pinkish orange bodycolor of this pearl were unlike those of orange porcelainous pearls previously submitted to GIA. The client who submitted the pearl stated that it was found inside a queen helmet conch in the early 1960s by Bert Matcovich (fig-

Figure 18. RTX imaging revealed the growth structure of the pearl: an ovalish void-like feature of less radiopacity in the center and a growth ring in the outer area.

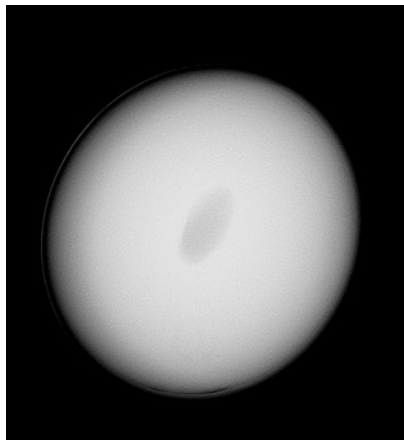


Figure 19. This photo shows the pearl and the queen helmet shell in which it was found. Photo courtesy of the Bert Matcovich family.



ure 19), who owned a shell shop in Key West, Florida. Born into a family of shellers with more than 60 years of experience, Matcovich fished the waters off Key West for conchs and visited local shrimp boats daily in the 1960s to purchase various types of shells. This pearl was a remarkable discovery.

Queen helmet, also known as emperor helmet, is the common name for a marine gastropod species called *Cassis madagascariensis*, which belongs to the Cassidae family. The species is generally distributed in the tropical western Atlantic, including the Caribbean Sea (J.H. Leal, "Gastropods," in K.E. Carpenter, *The Living Marine Resources of the Western Central Atlantic*, Vol. 1, Rome: Food and agriculture organization of the United Nations, 2002, pp. 99–127). Queen helmet shells have large, thick whorls with short spires, and three rows of knobs often appear on the body. They have a flat large parietal shield next to an aperture, and the color ranges from pale cream to deep salmon, often with a dark orangy brown color between the "teeth" (see again figure 19). Owing to their significant thickness, these colorful shells are widely used for cameo carving.

*Cassis* pearls typically have a fine and slender flame structure, often with intersecting flames. Their colors traditionally range from light orange to orangy brown, sometimes with patchy color. This pearl was unlike typical *Cassis* pearls examined by GIA, and its mollusk identity could not be confirmed with gemological testing. Nonetheless, this fine large natural non-nacreous pearl and its discovery story from six decades ago are noteworthy.

*Artitaya Homkrajae, Michaela Stephan, and Amiroh Steen*

### RFID Device Embedded in South Sea Bead Cultured Pearl Necklaces

New technologies are increasingly being applied to cultured pearls, and it is exciting to witness developments in pearl traceability. GIA's Bangkok laboratory recently received two

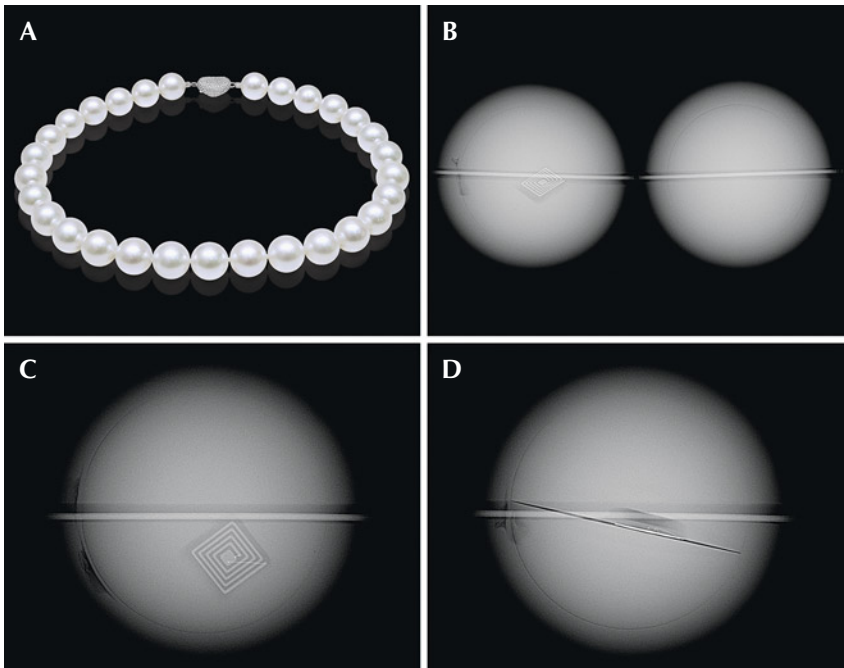


Figure 20. A: Necklace of South Sea bead cultured pearls, 14.80–15.90 mm in diameter. B and C: Real-time microradiography (RTX) revealed one bead cultured pearl in the necklace containing an RFID device showing an obvious demarcation of typical shell bead nuclei. The embedded electronic component is visible as a white opaque stepped square feature. D: When aligned at right angles to the previous direction, the electronic component is harder to see but can be observed within a long, sharp laminated plane separating the two parts of the shell bead nucleus.

South Sea bead cultured pearl necklaces, each consisting of 29 pearls ranging from 14.80 to 15.90 mm in diameter (strand A, figure 20A) and 14.40 × 14.20 mm to 16.20 mm in diameter (strand B, figure 21A). General observation under a binocular microscope revealed clear aragonite platelets characteristic of nacreous pearls, with no indications of treatment.

Real-time microradiography (RTX) revealed obvious demarcation features separating the shell bead nucleus from the overlying nacre layers. The nacre thickness range was consistent with bead cultured pearls produced by the *Pinctada maxima* mollusk (N. Sturman et al., "Bead cultured and non-bead cultured pearls from Lombok, Indonesia," Fall 2016 *G&G*, pp. 288–297). However, the most striking feature was the presence of some

electronic components within a few of the pearls. They were visible as opaque white squares with a stepped pattern in keeping with previously examined samples containing radio-frequency identification (RFID) devices (H.A. Hänni and L.E. Cartier, "Tracing cultured pearls from farm to consumer: A review of potential methods and solutions," *Journal of Gemmology*, Vol. 33, No. 7-8, 2013, pp. 239–246; Spring 2020 Lab Notes, pp. 134–136). Interestingly, only a single pearl in strand A (figure 20, B–D) and five pearls in strand B (figure 21, B–D) contained an RFID device. The device is usually positioned off the center of the bead to avoid being drilled.

GIA's Hong Kong lab has also begun seeing similar features in recent submissions (figure 22, A–B). The team compared the RTX data with



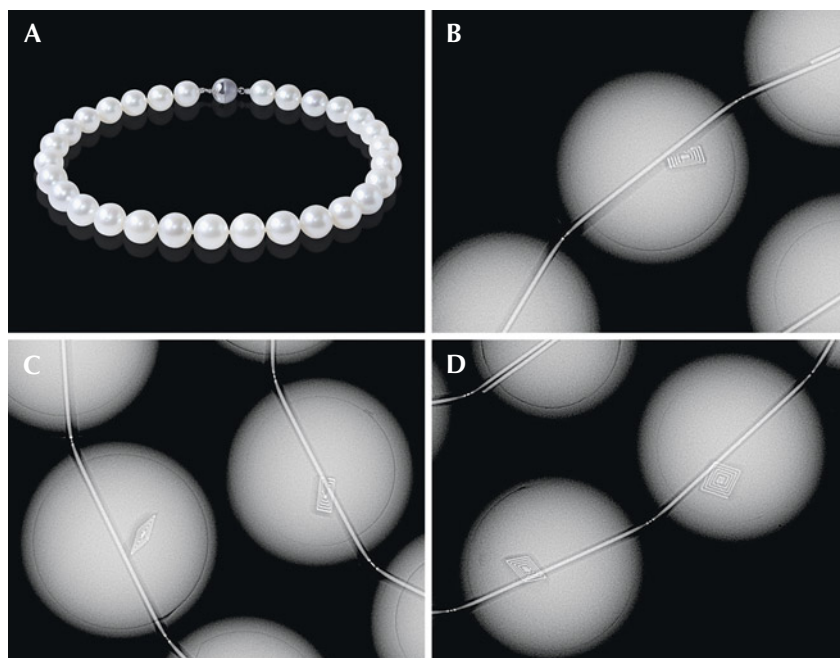
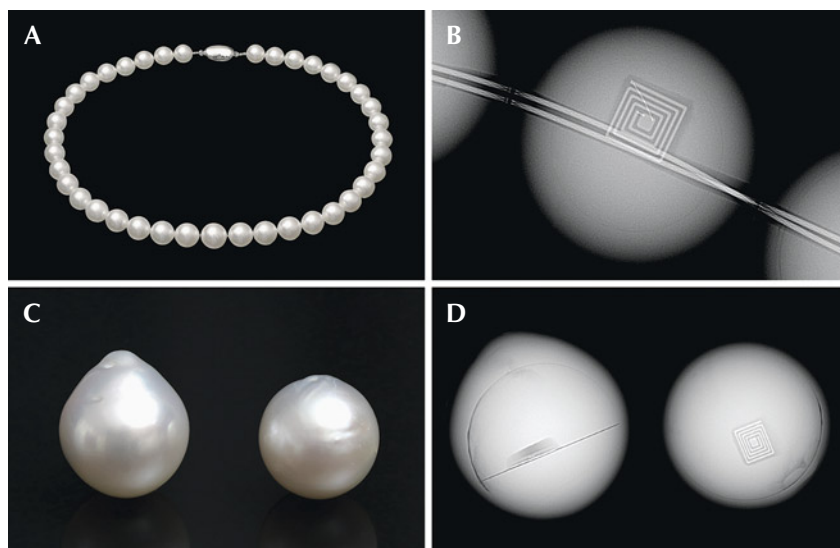


Figure 21. A: Necklace of South Sea bead cultured pearls, 14.40 × 14.20 mm to 16.20 mm in diameter. B–D: RTX analysis revealed five bead cultured pearls containing an off-center RFID device within the shell bead nucleus.

some known bead cultured pearls containing an RFID device (figure 22,

C–D) and confirmed that they were identical. The previous studies men-

Figure 22. A: Necklace of South Sea bead cultured pearls, 10.04–12.21 mm in diameter. B: RTX analysis of one of the pearls in the necklace revealed an RFID device. C: The internal structure was compared with two known bead cultured pearls containing RFID devices from GIA Hong Kong’s reference collection, and they proved to be identical. D: RTX clearly showed the outline of the square RFID device, as well as the sawn plane and small recess where the RFID device had been placed.



tioned earlier describing RFID devices in bead cultured pearls have shown that these nuclei are produced by a patented pearl technology invented by Fukui Shell Nucleus Factory, which also supplies laminated beads to certain pearl farms. This explains the link between the laminating technique and its application in the production of RFID shell beads.

The use of RFID shell beads is known to assist in the storage of certain data such as a pearl farm’s location, mollusk data, and harvest date. However, a specific RFID reader is required to retrieve the data, so we were unable to obtain the information stored within these particular devices. Since the RFID devices do not influence their external appearance, the pearls containing a shell bead nucleus with such components are still identified as bead cultured pearls. Because the RFID device could increase the weight and have a misleading effect if undetected, a special comment is routinely included on GIA pearl identification reports as a means of disclosure. While pearl tracing technology has not been extensively adopted by the cultured pearl industry, the increasing number of electronic devices in shell bead nuclei submitted to the laboratory is noteworthy. GIA will continue to monitor and provide updates to the pearl trade and consumers.

Nanthaporn Nilpetploy and  
Ying Wai Au

### Combination of Phenomena in Star and Cat’s-Eye Color-Change SAPPHIRE

The Tokyo lab recently examined a transparent 20.49 ct violet to purple color-change double cabochon sapphire, measuring 16.67 × 14.69 × 8.51 mm (figure 23) with a specific gravity of 3.99 and a spot refractive index of 1.77. Usually a star sapphire is only polished on one side, and the unpolished side does not show any phenomena. But this stone was polished on both sides, which resulted in a unique



Figure 23. This 20.49 ct star sapphire with a combination of phenomena exhibited a color change from violet (top) to purple (bottom). Side A is shown in these photos.

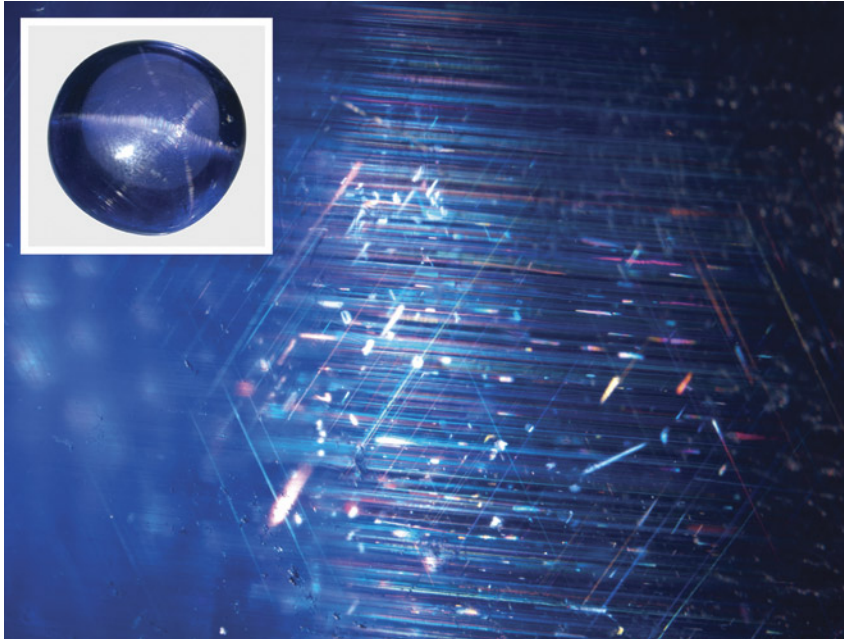
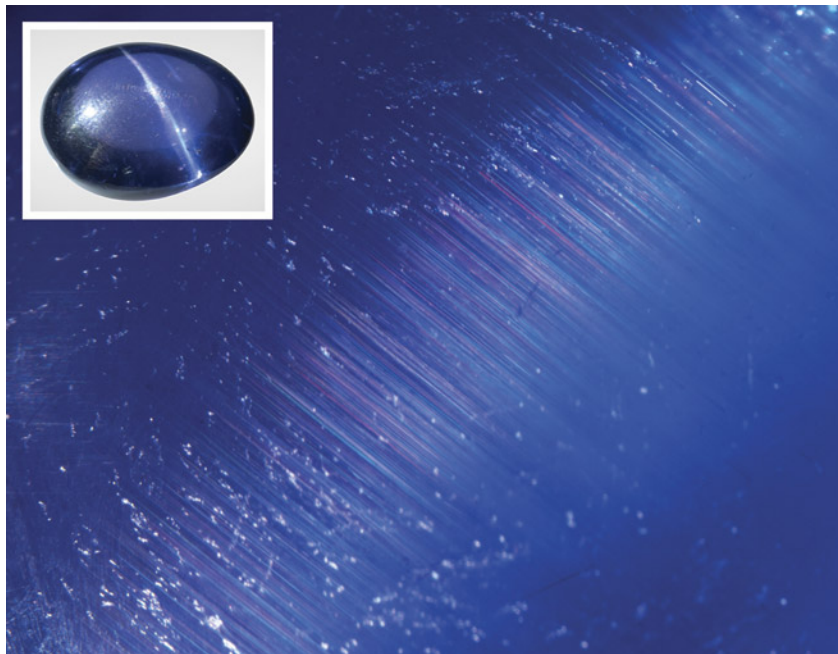


Figure 24. Side A: Intersecting sets of parallel needle inclusions producing six-rayed asterism. Field of view 5.8 mm. The photomicrograph is not aligned with the inset.

combination of phenomena. Side A displayed a six-rayed star. Side B also displayed a six-rayed star, but one line

containing two of the rays was much stronger, which made the phenomenon reminiscent of a cat's-eye.

Figure 25. Side B: Set of parallel needle inclusions producing chatoyancy. Field of view 5.8 mm. The photomicrograph is not aligned with the inset.



Chatoyancy is displayed when light reflects off a set of dense parallel elongated inclusions, such as needles; asterism occurs when such a set of inclusions is oriented in multiple directions. In the case of this stone, side A with the distinct six-rayed star had three sets of dense parallel needles and platelets close to the surface, intersecting at 60° angles (figure 24), which is common with six-rayed asterism. Side B also had three sets of these needles close to the surface, but the needles were more concentrated in one of the directions, producing a cat's-eye effect (figures 24 and 25). Interestingly, the chatoyancy in Side B and one line of asterism in Side A are contributed by the same group of needles.

Although color-change star sapphire is not particularly rare, color-change cat's-eye sapphire is far less common. Color-change sapphire with asterism on one side and chatoyancy on the other is without question a "phenomenal" gem.

Masumi Saito and  
Yusuke Katsurada

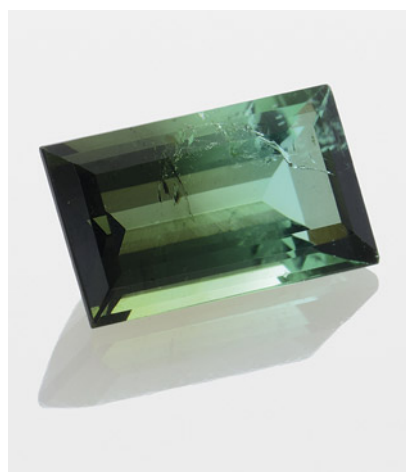


Figure 26. The 1.62 ct bicolor copper-bearing tourmaline.

**TABLE 1.** Mn, Fe, and Cu concentrations on each side of the bicolor tourmaline, measured by LA-ICP-MS (in ppmw, average of three spots).

	Mn	Fe	Cu
Bluish green	22826	566	7850
Dark yellowish green	17233	11287	4953
Detection limit (ppmw)	7.13	3.10	0.11

### Bicolor Cuprian TOURMALINE

A bicolor gem has two colors in one stone. Ametrine is a well-known bicolor gem, a purple and yellow quartz combining amethyst and citrine. In

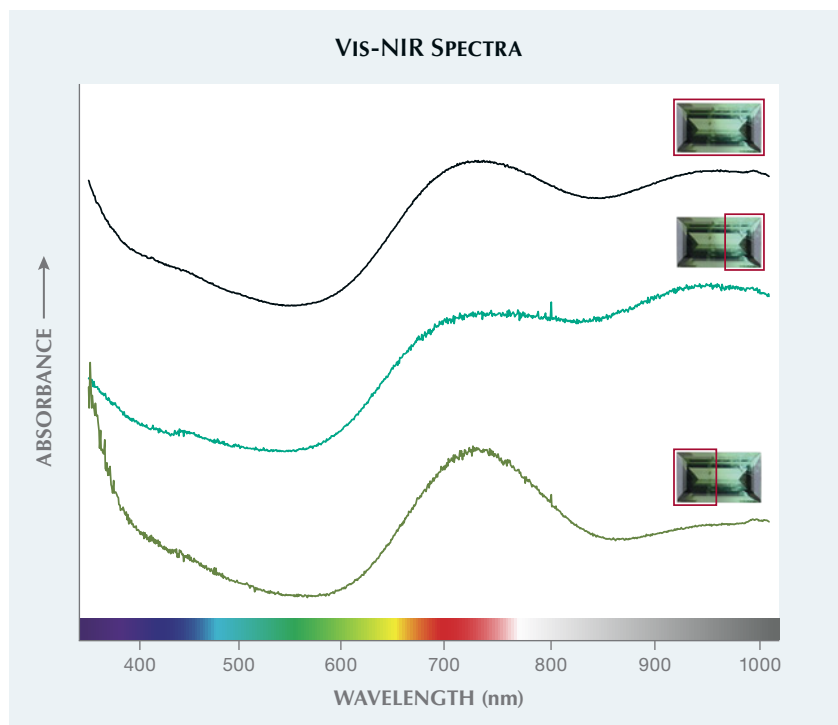
addition to the ametrine variety of quartz, other colored gemstones such as corundum and tourmaline can be naturally bicolor, although most of them do not have a specific variety

name. Most bicolor gem materials are cut to show different colors that are obvious when viewed in face-up orientation.

The Tokyo laboratory recently examined a bicolor rectangular step cut weighing 1.62 ct and measuring 9.14 × 5.47 × 3.71 mm (figure 26). The color was gradually distributed from bluish green to dark yellowish green along the length. This stone was doubly refractive with a refractive index of 1.620–1.640 and a specific gravity of 3.10. Microscopic observation revealed networked fluid inclusions and strong doubling. The stone was identified as tourmaline by these gemological features.

Paraíba tourmaline, a certain type of copper-bearing tourmaline, has been one of the most sought-after gemstones in the trade over the last three decades. In 2012, the Laboratory Manual Harmonisation Committee (LMHC) updated the definition of Paraíba tourmaline as “a blue (electric blue, neon blue, violet blue), bluish green to greenish blue, green (or yellowish green) tourmaline of medium-light to high saturation and tone (relative to this variety of tourmaline), mainly due to the presence of copper and manganese.” Visible/near-infrared (Vis-NIR) absorption was collected with GIA’s custom-made UV-Vis spectrometer to determine the chromophore. To be considered Paraíba tourmaline, the copper-related absorp-

Figure 27. Vis-NIR absorbance of the whole tourmaline (top), the bluish green portion (middle), and the dark yellowish green portion (bottom). Copper absorption is in the red (approximately 730 nm) and near-infrared regions (approximately 980 nm). Iron absorption is only in the red region (approximately 730 nm). Spectra are stacked for clarity.



tion needs to be dominant and the color appearance should be within the defined range.

Non-polarized absorption spectra of the whole stone showed two bands in the red and near-infrared regions (figure 27, black line). To measure the spectra of each color separately, one half of the gem was covered with opaque black cardboard to allow light to pass through only one color at a time. The results indicated that the dominant chromophore was different (figure 27; bluish green and dark green lines at the middle and bottom, respectively)—the bluish green part is colored by copper, whereas the dark yellowish green part is colored by iron (P.B. Merkel and C.M. Breeding, “Spectral differentiation between copper and iron colorants in gem tourmalines,” Summer 2009 *G&G*, pp. 112–119).

The trace element composition of each differently colored region was analyzed by laser ablation–inductively coupled plasma–mass spectrometry (LA-ICP-MS). As shown in table 1, the bluish green side shows lower iron (566 ppmw) and higher copper (7850 ppmw), and the dark yellowish green side shows higher iron (11287 ppmw) and lower copper (4953 ppmw). Comparing the different Vis-NIR absorption patterns of these portions (figure 27), the association of copper and iron for each color portion is in agreement with Merkel and Breeding (2009). By virtue of its color and its chromophore, only the bluish green portion is consistent with the definition of Paraíba tourmaline.

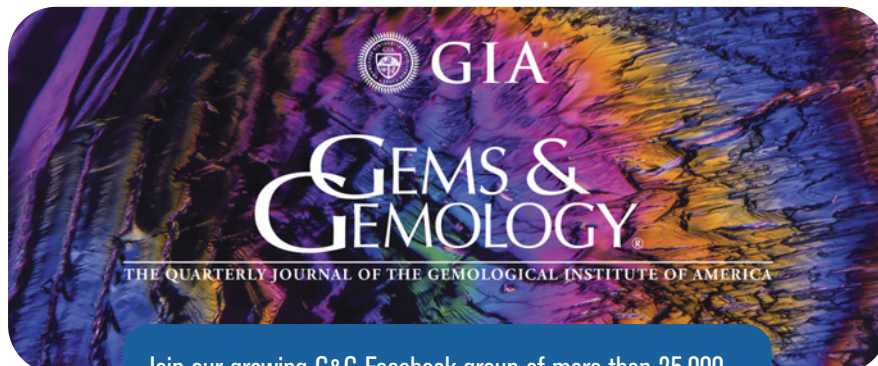
Sometimes we encounter cuprian tourmaline with chemical zoning, which has varying trace element concentrations within. A drastic differ-

ence, as in the case of this bicolor tourmaline with a non-Paraíba iron-colored portion, is not typical. The dark yellowish green part could have been polished off to make this a typical Paraíba tourmaline.

*Yusuke Katsurada*

#### PHOTO CREDITS

*Nathan Renfro—1–3; Annie Haynes—4, 14; Najmeh Anjomani—5, 6; Towfiq Ahmed—7; Madelyn Dragone—9; Stephanie Persaud—10; Michaela Stephan—11, 12; Roy Bassoo—12; Taryn Linzmeyer—15; Robert Weldon—16, 17 (left); Artitaya Homkrajae—17 (right); Amiroh Steen—18; Nuttapol Kitdee—20A, 21A; Tony Leung—22A; Shunsuke Nagai—23; 24 (inset), 25 (inset), 26; Yusuke Katsurada—24, 25*



**GIA**  
**GEMS & GEMOLOGY**  
THE QUARTERLY JOURNAL OF THE GEMOLOGICAL INSTITUTE OF AMERICA

Join our growing G&G Facebook group of more than 25,000 members, connecting gem enthusiasts from all over the world!





G&G

# Micro-World

Editor: Nathan Renfro

Contributing Editors: Elise A. Skalwold and John I. Kowula

## Apatite Cluster in Zambian Emerald

This author recently studied a 1.68 ct faceted emerald containing several inclusions, including blocky fluid inclusions, transparent brownish crystals, needles, and particle clouds. These inclusions as well as the trace element chemistry supported a Zambian geographic origin. The emerald also exhibited elongated transparent crystals that resembled amphibole. In this case, Raman spectroscopy confirmed the mineral as apatite. Interestingly, this apatite formed a distinct inclusion cluster consisting of a large hexagonal prismatic crystal (a morphology typical of the mineral) associated with a multitude of rod- and bamboo-shaped crystals in various directions (figure 1). Other solid crystals observed in Zambian emerald include mica, actinolite (amphibole), quartz, zircon, and chromite.

Apatite, a common phosphate mineral, has previously been reported in various forms and in many other types of gems such as corundum, spinel, feldspar, and garnet, and it is not surprising to find it in emerald. However, this is the first time the author has encountered this fantastic form of apatite in emerald.

*Ungkhana Atikarnsakul  
GIA, Bangkok*

*About the banner: The surface of this synthetic amethyst shows a multitude of rhombohedral crystal faces. Photomicrograph by Nathan Renfro; field of view 15.67 mm.*

GEMS & GEMOLOGY, VOL. 58, No. 2, pp. 226–233.

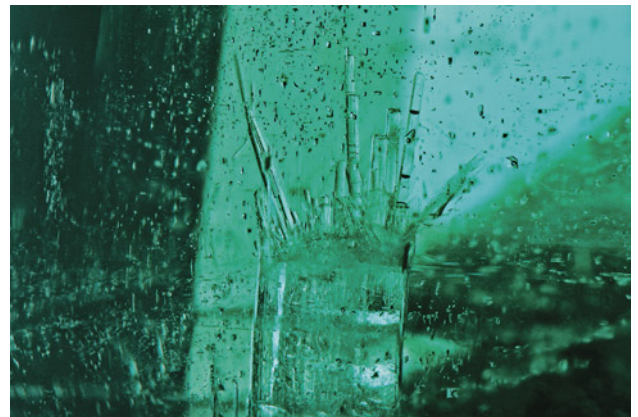
© 2022 Gemological Institute of America

## Blue Apatite in Tanzanian Garnet

In the micro-world, it can be challenging to identify inclusions based on sight alone, as many minerals can have a similar appearance. Occasionally, though, some inclusions have characteristic features that can aid in their identification.

Recently this author had the opportunity to observe a pyrope-spessartine garnet, reportedly from Lindi Province, Tanzania, that contained blue crystal inclusions ensconced among intersecting needles (figure 2). Analysis with micro-Raman spectroscopy identified the inclusions as apatite. Apatites are known for their bright blue hues, and these inclusions offered an attractive example.

*Figure 1. An inclusion cluster consisting of a hexagonal prismatic apatite crystal and many rod- and bamboo-shaped crystals of apatite in a Zambian emerald. Photomicrograph by Ungkhana Atikarnsakul; field of view 3.60 mm.*



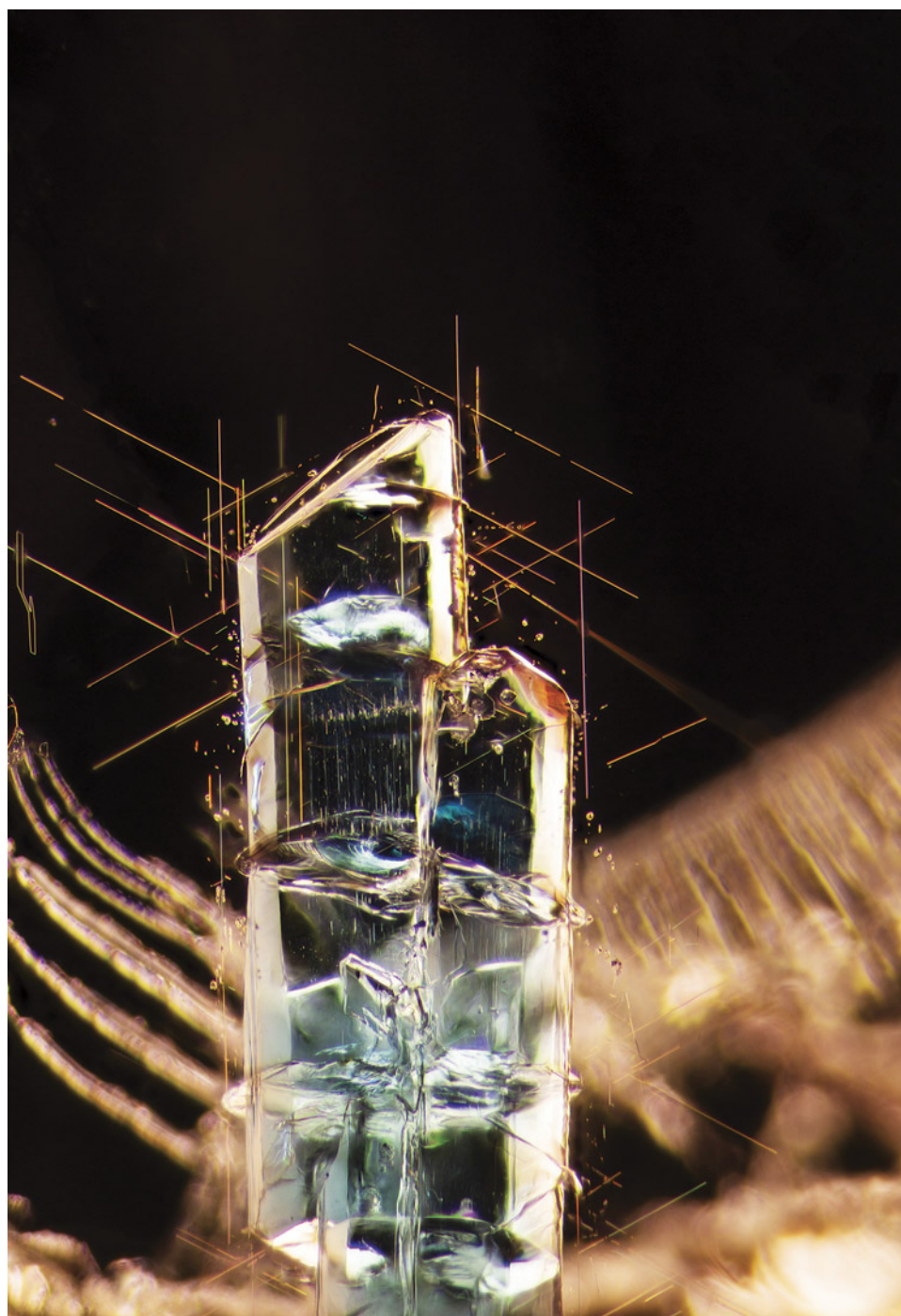


*Figure 2. Blue apatite crystals are beautifully framed by prominent rutile needles in a garnet from Tanzania. Photomicrograph by E. Billie Hughes; field of view 3.5 mm.*

While this sample hails from Tanzania, blue apatite has previously been reported as an inclusion in garnet from Madagascar (Winter 2020 *G&G Micro-World*, p. 526). These inclusions' distinctive appearance may help gemologists recognize the material in other samples, but further analysis should be performed to identify them definitively.

*E. Billie Hughes  
Lotus Gemology, Bangkok*

### **Large Diamond Inclusion in Diamond**

Recently, the authors examined a 2.01 ct Faint green round brilliant diamond with a fascinating diamond crystal inclusion that displayed a transparent, ghost-like appearance. Due to the large size of this nearly invisible crystal, the stone was given a clarity grade of SI<sub>2</sub>.

Photomicrography was used to document the features of this inclusion. Triangular etch features, also known as

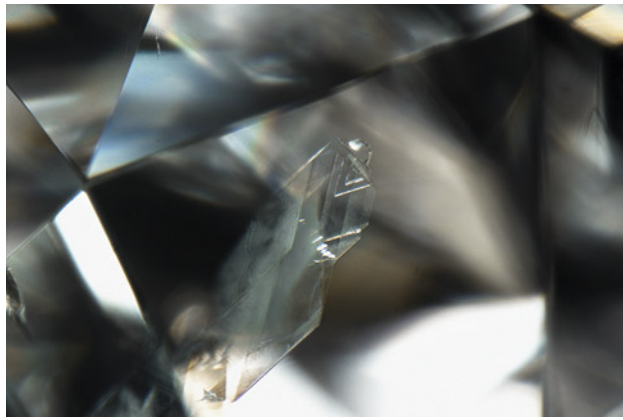


Figure 3. Trigons seen on a diamond crystal inclusion visible through the crown of a round brilliant diamond. Photomicrograph by A'Dhi Lall; field of view 2.11 mm.

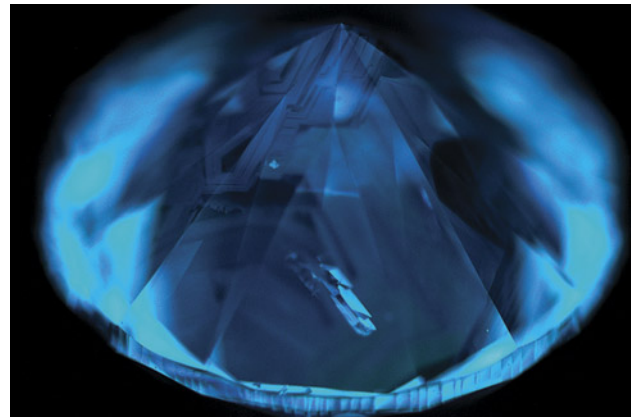


Figure 5. DiamondView image of the diamond inclusion in the diamond host. Image by Luthfia Syarbaini.

trigons, were seen on the inclusion (figure 3). These are typically natural growth markings of diamonds, confirming the inclusion as diamond. The diamond crystal inclusion appeared to have sharp and easily recognizable faces. Images with cross-polarized light show strain between the inclusion and the host diamond (figure 4). A DiamondView image also reveals the diamond crystal inclusion (figure 5).

Generally, the beauty and value of a diamond increase with the absence of inclusions. Yet the presence of a diamond inclusion gave this diamond a certain distinction, which in the authors' opinion added to its beauty and value.

*Luthfia Syarbaini, A'Dhi Lall, and Paul Johnson  
GIA, New York*

### Natural Diamond with Extensive Network of Etch Channels

The authors recently examined a 5.19 ct type IIa natural diamond (figure 6) displaying numerous etch channels (figure 7). Etch channels are open tubes whose formation is related to dissolution processes within the stone. They form due to the dissolution of dislocations inside the crystal during or after growth and can result in various patterns; most commonly, they form as trigons or rarely as channels that appear as parallel lines, zigzags, or "worm-like" structures (T. Lu et al., "Observation of etch channels in several natural diamonds," *Diamond and Related Materials*, Vol. 10, 2001, pp. 68–75, and references therein; Spring 2018 *G&G*

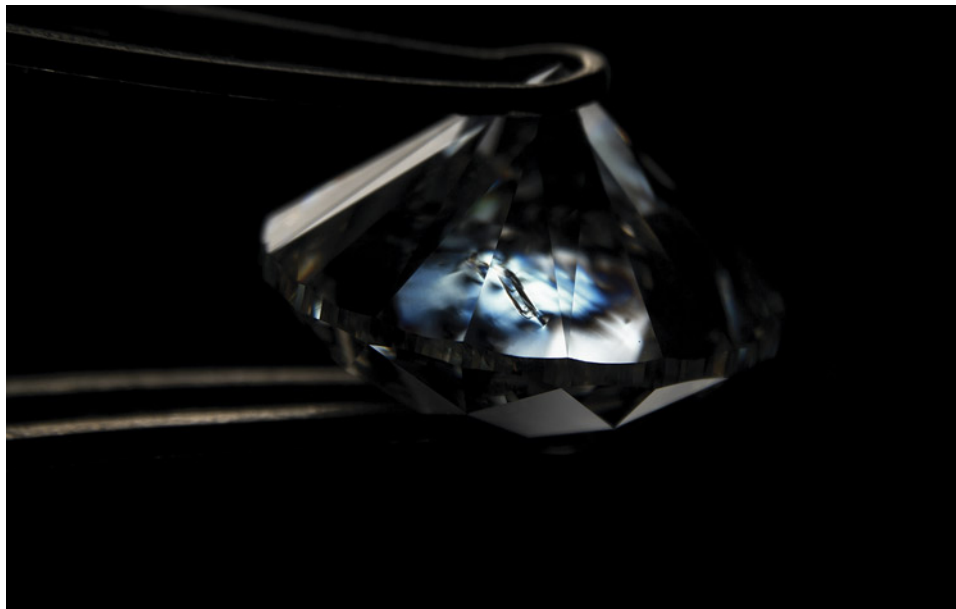


Figure 4. Strain between the host diamond and the diamond inclusion is revealed by the interference colors in cross-polarized light. Photomicrograph by A'Dhi Lall; field of view 13.55 mm.

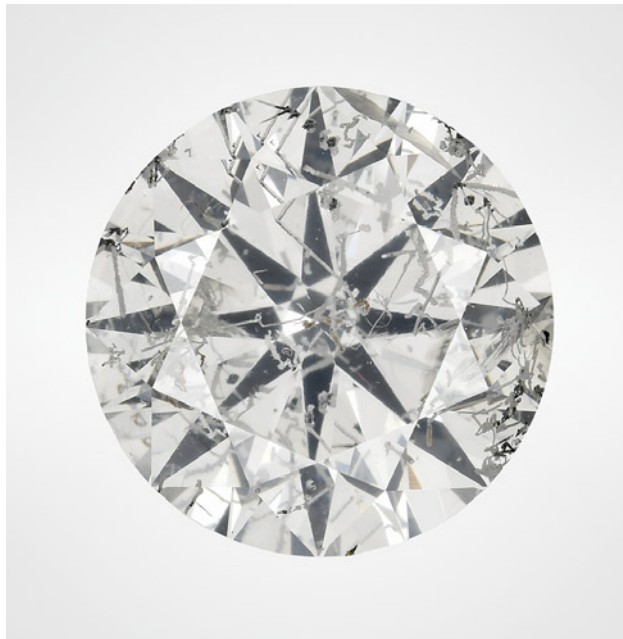


Figure 6. This 5.19 ct diamond with I color and I<sub>2</sub> clarity displays numerous etch channels visible to the eye. Photo by Annie Haynes.

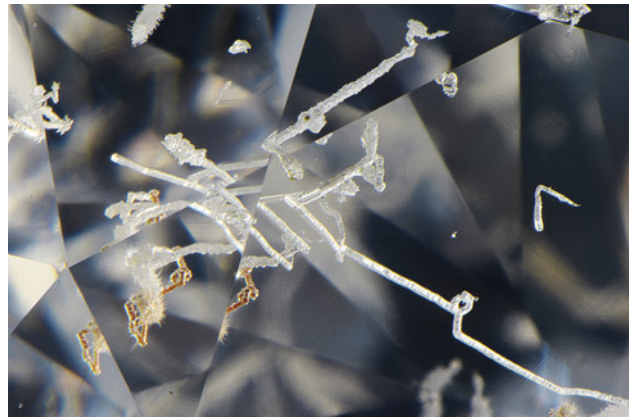


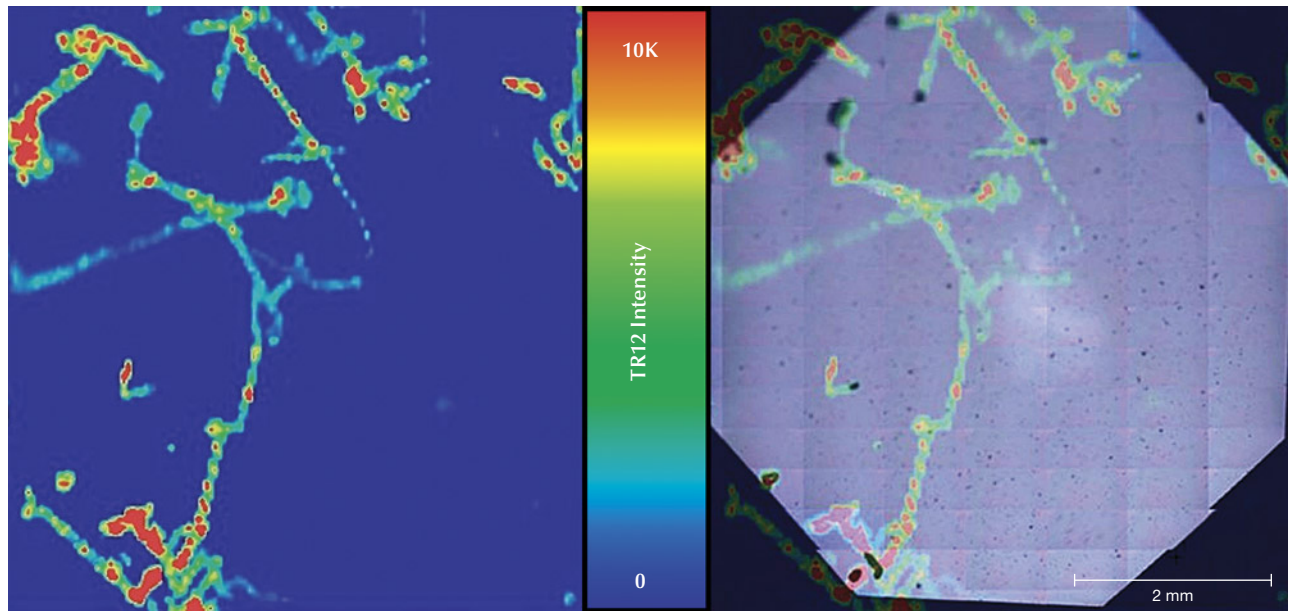
Figure 7. A network of natural etch channels gives this diamond a distinctive appearance. Most of the channels have a width of ~100–150 μm, while some (e.g., lower left) show evidence of brown radiation stains. Photomicrograph by Nathan Renfro; field of view 4.69 mm.

Micro-World, pp. 66–67). Etch channels terminate at typically rhombic openings visible at the surface of the stone (Spring 2018 *G&G* Micro-World, pp. 66–67). The extensive

network of etch channels in this diamond resulted in an I<sub>2</sub> clarity grade.

Photoluminescence (PL) mapping using 455 and 532 nm laser excitation (figures 8 and 9) revealed an increase in the GR1, 3H, and TR12 centers along the walls of the etch channels; all of these centers are defects associated with radiation exposure. The nitrogen vacancy centers NV<sup>0</sup> (zero-phonon line [ZPL] at 575 nm) and NV<sup>-</sup> (ZPL at 637

Figure 8. Left: False-color map showing the peak area intensity of the radiation-related TR12 center (ZPL at 469.9 nm); this 455 nm PL map was compiled from 18,768 spectra collected at 45 μm pixel size. Right: The false-color map overlain with a reflected light image of the table facet. Most of the etch channels seen in the false-color map correspond with an opening observed on the table.





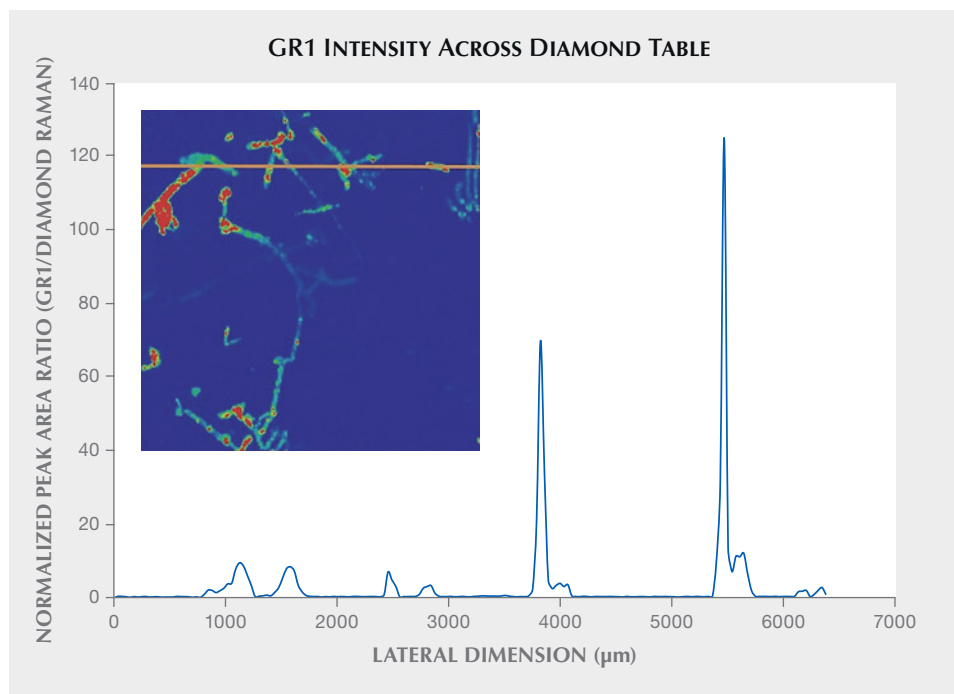


Figure 9. GR1/Raman peak area ratios calculated from the 532 nm PL map (inset) cutting across multiple channels along the orange line. Higher GR1/Raman areas are concentrated along the etch channels.

nm) were also concentrated along these channels. The concentration of these defects along the etch channels suggests that radioactive fluids once flowed through the tubes. The radioactive fluids had an impact on the areas in direct contact, creating elevated concentrations of radiation-related peaks. Other prominent PL peaks along the cavities were centered at 474, 598.75, and 461.5 nm. The radiation in these fluids would have been low enough to not create much observable staining, as patches of green to brown color associated with radiation staining were not observed in most of the etch channels. However, there were some isolated spots of green radiation stains and some channels with a brownish appearance (figure 7) and elevated concentrations of radiation-related features (figures 8 and 9). Additionally, the exposure to radioactive fluids must have occurred after the diamond was brought to the near-surface region following kimberlite eruption, as these radiation-related features would not withstand the high temperatures within the mantle.

Similar radiation features have previously been observed in another stone with cavities (Spring 2020 Lab Notes, pp. 126–127), but to a much lesser degree. The extensive network of etch channels within this diamond is one more example of the extraordinary possibilities within the natural world.

*Taryn Linzmeyer and Sally Eaton-Magaña  
GIA, Carlsbad*

### Eye Pattern in a Rock Fragment

Recently, the authors encountered a partially polished rock fragment measuring 14.50 × 9.43 × 2.43 mm and

weighing 3.45 ct that exhibited a very realistic eye pattern (figure 10). Various shades of yellow and green material formed the pupil and iris, while a distinctive white outline surrounded the iris as a sclera. Microscopic observation revealed different microcrystalline minerals. Raman spectroscopy identified pyroxene, feldspar, and quartz as the most abundant minerals. Energy-dispersive X-ray fluorescence (EDXRF) analysis revealed silicon as the dominant element, while traces of iron and potassium were also detected.

Naturally formed eye patterns in gems are rare but do exist, such as a “dragon’s eye” in a fire agate (Winter 2015 *G&G Micro-World*, p. 441) and a radial eye structure in a sapphire (Summer 2017 *G&G Micro-World*, pp. 244–245). While the textures in rocks are much more diverse than those in single-mineral gemstones, observing such a unique feature is always exciting.

*Ching Yin Sin  
GIA, Hong Kong*

*Piradee Siritheerakul  
GIA, Bangkok*

### Fracture-Filled Emerald with Mysterious Filler Patterns

Emeralds are known to have natural cracks or fractures. The filling of surface-reaching fractures with various oils and resins is the most common practice to minimize fractures to improve an emerald’s appearance. The author recently examined a 3.04 ct emerald that revealed a mysterious filler pattern along the fractures, resembling a

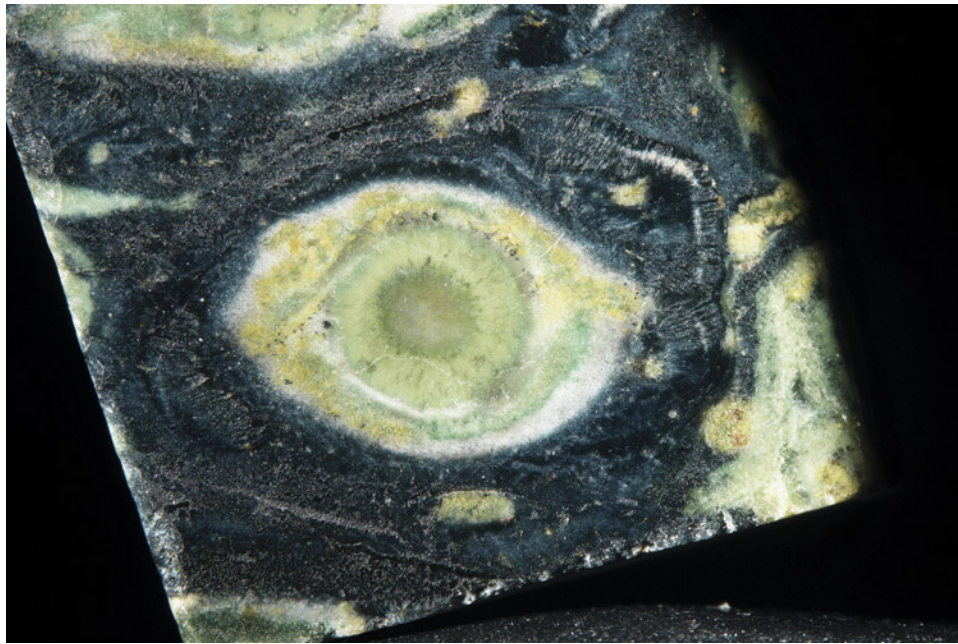


Figure 10. An eye pattern complete with pupil, iris, and sclera is clearly visible in this rock fragment. Photomicrograph by Polthep Sukpanish; field of view 12.5 mm.

labyrinth and convolution (figure 11). Fracture filling can be identified using various methods. In this case, it displayed a chalky fluorescence under long-wave ultraviolet flashlight and was also detected with simple microscopic observation and fiber-optic lighting. The internal graining, irregular two-phase inclusions, and long needles within this stone indicated a natural origin. This was a unique and visually interesting pattern in the fracture filling material of an emerald.

*Ungkhana Atikarnsakul  
GIA, Bangkok*

### Flux-Grown Synthetic Beryl Overgrowth

Most of the synthetic beryl currently on the market has been created by a hydrothermal process. Hydrothermally grown crystals have obviously different crystal forms compared to their natural counterparts. Hydrothermal synthetics are often easily identified by their typical zigzag- or chevron-patterned graining and color zoning. Flux-grown synthetics, though less common, are able to form more natural-looking crystals. However, despite having natural forms, flux synthetics contain many unusual inclusions that clearly distinguish them from their natural counter-

Figure 11. Emerald filler with labyrinth- and convolution-like pattern. Photomicrographs by Ungkhana Atikarnsakul; fields of view 2.0 mm (left) and 2.7 mm (right).

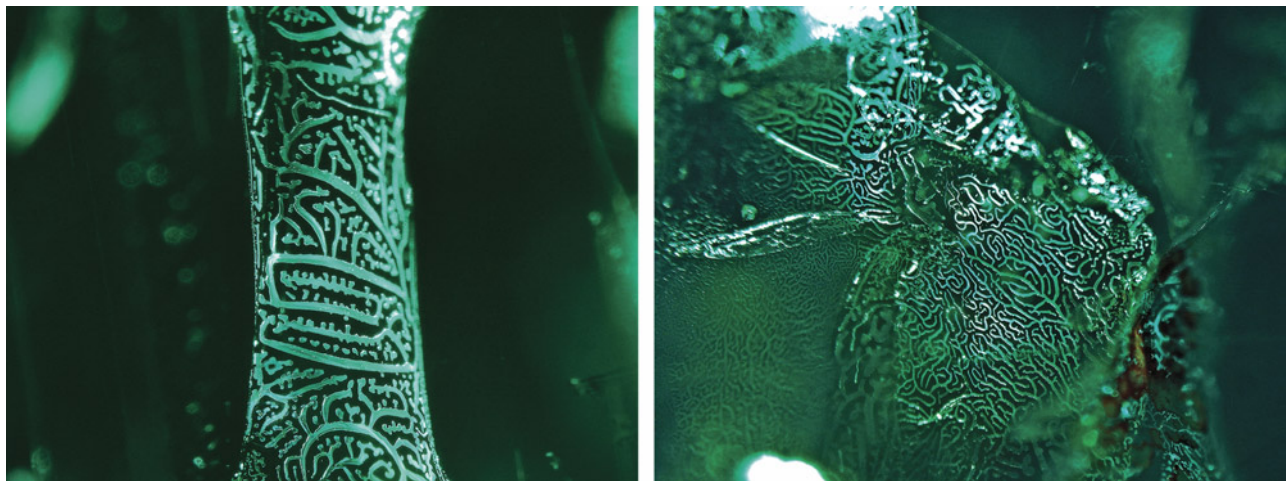




Figure 12. Doubly terminated flux synthetic beryl crystal, measuring 32.45 × 30.36 × 25.29 mm. Photo by Annie L. Haynes.

parts. Copper platelets that form within the crystal either from contamination or intentionally introducing metal in the growth material are obvious indications of synthetic origin. Flux fingerprints are another easily observed type of inclusion unique to flux synthetic crystals.

Weighing 211.78 ct, the hexagonal doubly terminated crystal in figure 12 looks like a natural beryl crystal at first glance. Eye-visible well-formed copper platelets and wispy flux fingerprints indicate that the stone did not form naturally. A closer look revealed reddish clouds of well-formed minute copper platelets and copper crystals. Euhedral red rod-like crystals of columbite were scattered throughout, similar to those in a natural sample. Partially healed tension cracks with white secondary flux particles were also present. A few areas throughout the crystal had unique thin angular and jagged films containing blue flux liquid and gas bubbles (figure 13). Areas with higher clarity reveal the boundary between the natural aquamarine seed crystal and the flux overgrowth. This stone is a product of synthetic flux beryl overgrowth on a natural aquamarine seed crystal produced in a Russian synthetic gem facility.

Jamie Price  
GIA, Carlsbad

### “Boomerang” Inclusion in a Rough Topaz

A 21.46 ct colorless rough topaz was recently submitted to Taiwan Union Lab of Gem Research (TULAB) for identification service. Microscopic observation showed a few prismatic brown inclusions with submetallic luster. One of the inclusions was a unique twinned crystal composed of two

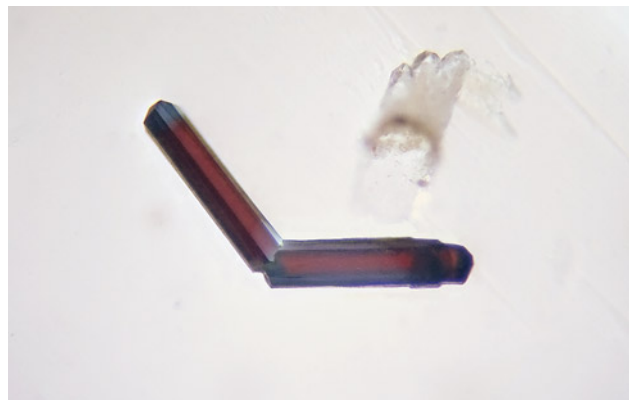


Figure 13. A suite of columbite rods, copper crystals, and a large air bubble seen within a film of blue flux liquid. Photomicrograph by Jamie Price; field of view 7.19 mm.

prismatic crystals forming a 120° intersection angle. With its shape and backdrop, the twinned crystal resembled a boomerang flying across the sky (figure 14). This inclusion was later confirmed to be tantalite-(Mn), based on Raman spectroscopy and comparison with the RRUFF database. Polarized light and reflected illumination were adopted to reduce doubling and obtain clearer photomicrographs, and the images were processed to extend depth of field.

Shu-Hong Lin  
Institute of Earth Sciences,  
National Taiwan Ocean University  
Taiwan Union Lab of Gem Research, Taipei  
Tsung-Ying Yang, Kai-Yun Huang, and Yu-Shan Chou  
Taiwan Union Lab of Gem Research, Taipei

Figure 14. The “boomerang” inclusion in this topaz was confirmed by Raman spectroscopy to be a twinned crystal of tantalite-(Mn). Photomicrograph by Shu-Hong Lin; field of view 0.71 mm.





*Figure 15. Several bright red to dark red well-formed trigonal crystals of cinnabar highlight the interior of the fluorite and calcite cluster from Spain. Photo by Diego Sanchez.*

### **Quarterly Crystal: Cinnabar in Fluorite**

This issue's Quarterly Crystal deals with a 362.09 ct crystal cluster of fluorite and calcite recently examined by the authors. The 55.79 × 42.80 × 38.63 mm specimen was colorless and transparent to translucent and played host to several small bright red to dark red well-formed trigonal crystals, visible in figure 15. These crystals were all situated on the same growth plane in the fluorite portion.

The fluorite and calcite specimen was obtained from Jordi Fabre of Fabre Minerals in Barcelona. It is from the Emilio

mine in the Caravia mining area in the Asturias region of northwestern Spain. The Emilio mine is known to produce fluorite crystals with inclusions of various sulfides, including cinnabar. Therefore, the pure red bodycolor of these inclusions, together with the trigonal symmetry shown in figure 16, strongly suggested they were cinnabar. Using Raman microspectrometry, we were able to identify the inclusions as cinnabar, thereby confirming our initial impression.

*John I. Koivula and Nathan Renfro  
GIA, Carlsbad*

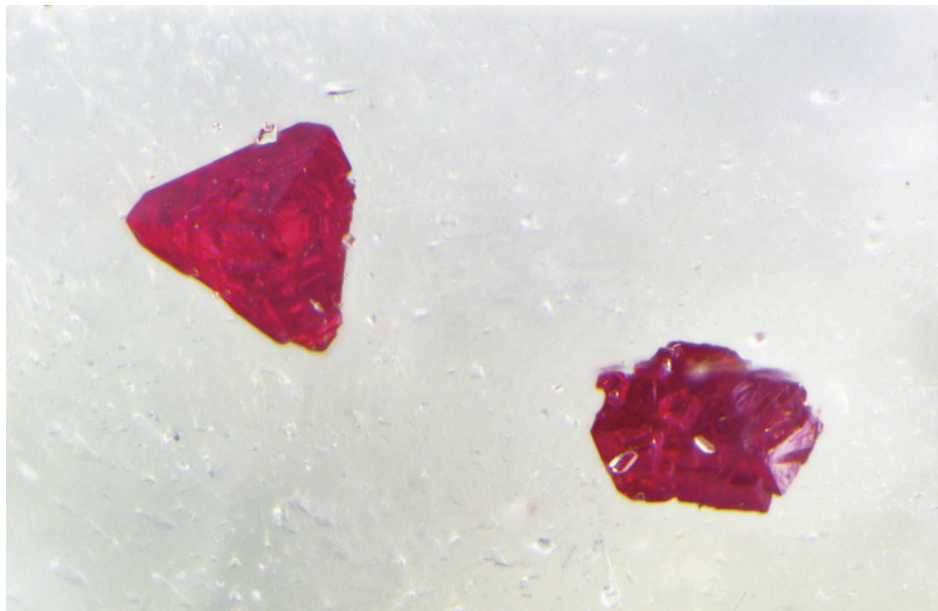
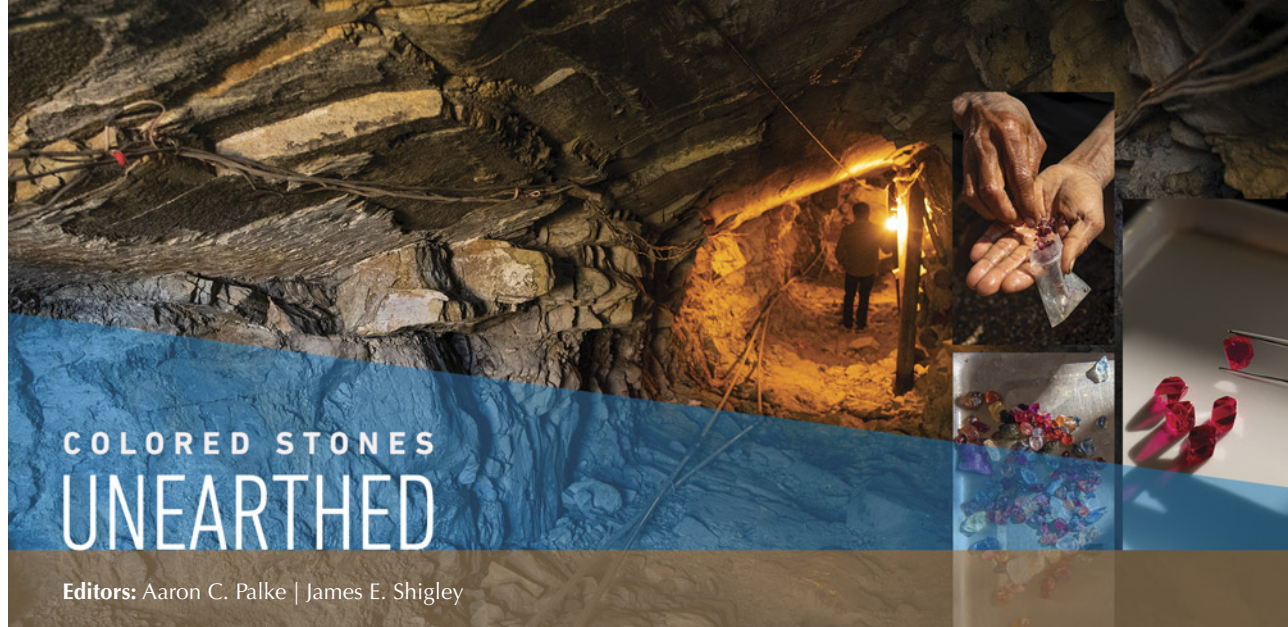


*Figure 16. A combination of optical microscopy and Raman analysis served to identify the trigonal inclusions as the mercury sulfide cinnabar. Photomicrograph by Nathan Renfro; field of view 2.35 mm.*



## Inclusions in Gemstones

James E. Shigley, Aaron C. Palke, John I. Koivula, and Nathan D. Renfro

Gem inclusions are mineral crystals or cavities filled with fluid and/or gas that occur in a host gemstone. Many gems contain microscopic inclusions (ranging in size from >1 mm down to submicroscopic nanoscale inclusions) that can reveal much about the host material. As a result, the use of the microscope (or loupe) to examine these inclusions offers one of the most important methods available for gem identification.

Inclusions are important for determining the natural, synthetic, or treated character of a gem, and for establishing the likely geographic origin of a valuable colored stone. In addition to their usefulness for identification, inclusions cause certain distinctive and desirable optical phenomena such as asterism and chatoyancy, as well as some of the features used in clarity grading. In this new installment of “Colored Stones Unearthed,” we will discuss inclusions in gems—how they form, how they are studied, and what they mean not only for gemologists but also for geoscientists.

### Brief History of Inclusion Studies

While the study of inclusions might seem to be a modern concept requiring the use of advanced microscopes with sophisticated optical lenses, early naturalists did have some basic knowledge of how inclusions could be used to understand the geological history of a gem. Consider

amber, for instance. By observing insects trapped in amber, Pliny the Elder was able to conclude that amber represents fossilized tree resin (Ball, 1950) (figure 1).

However, it was only much later that inclusions began to be classified and studied in a more systematic fashion. The pioneering scientist Robert Boyle was perhaps one of the first to describe inclusions in gems—“a specimen of quartz with a cavity containing a fluid with a moveable gas bubble, and reddish brown hair-like inclusions in amethyst” (Boyle, 1672). With the improvements in design and functionality of optical microscopes beginning in the late 1700s, scientists started to use them to examine tiny features in rocks and minerals (Kile, 2003, 2013). Déodat

*Figure 1. Inclusions of insects entombed in amber, such as these two wasps captured in an eternal embrace, offered ancient naturalists a clue to the geological origins of this gemstone. Photomicrograph by John I. Koivula.*



*Editors' note: Questions or topics of interest should be directed to Aaron Palke (apalke@gia.edu) or James Shigley (jshigley@gia.edu).*

GEMS & GEMOLOGY, VOL. 58, NO. 2, pp. 234–242.

© 2022 Gemological Institute of America

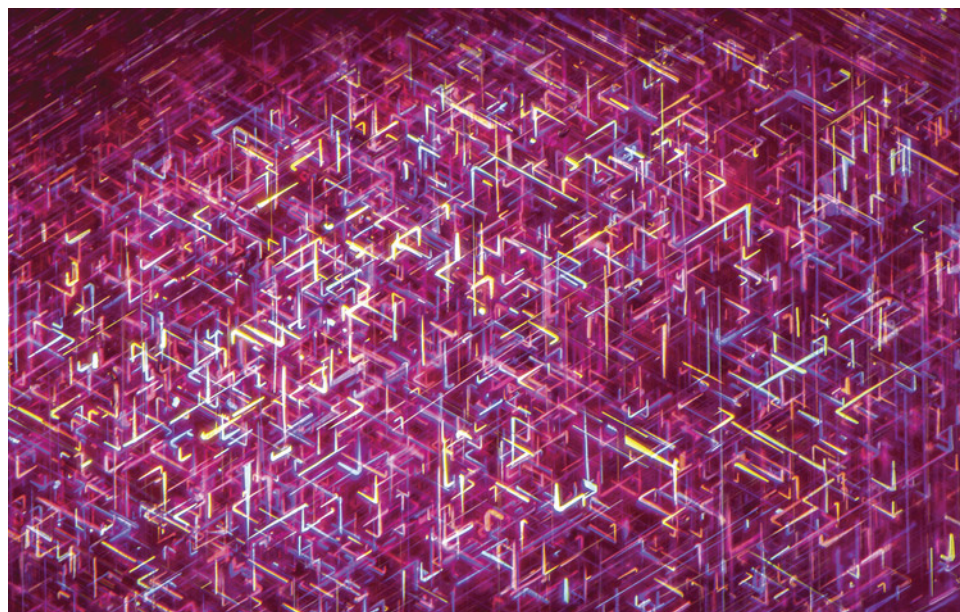


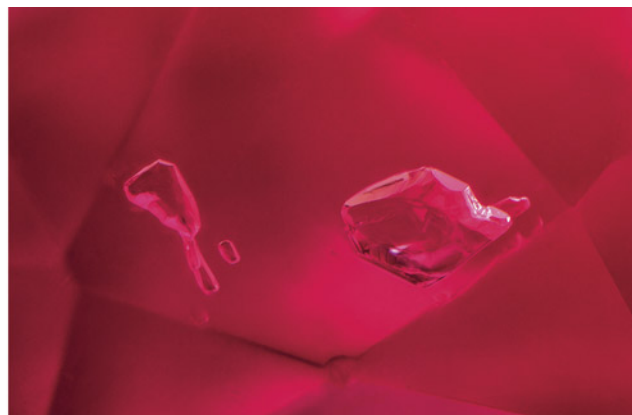
Figure 2. Oriented inclusions such as the rutile needles in this ruby were recognized as the cause of asterism early on in the study of inclusions. Photomicrograph by Nathan Renfro; field of view 1.80 mm.

de Dolomieu discussed the presence of a hydrocarbon fluid (petroleum oil) in quartz in 1792. In 1819, Chester Dewey detailed a quartz specimen from Massachusetts that displayed a cavity containing a liquid with a moveable bubble and several black or brown particles (1818, pp. 345–346). Noted scientists Humphry Davy (1822), David Brewster (1826, 1827, 1844, 1845a,b, 1863), and William Nicol (1828) each described minerals that contained inclusions consisting of one or more fluids and moveable gas bubbles. In 1854, Johann Reinhard Blum and his coauthors published a book discussing various mineral inclusions they had observed. By linking observations on mineral inclusions and host rock formation, Henry Clifton Sorby (1858) became one of the founders of the geological science of petrography with an article titled “On the microscopical structure of crystals, indicating the origin of minerals and rocks.” An

1862 article by Gustav Rose identified the presence of oriented, needle-like inclusions, such as those seen in the star ruby in figure 2, as the cause of asterism in minerals. The first descriptions of inclusions specifically in gem minerals were published in several articles by Henry Sorby in 1869 and by Isaac Lea between 1866 and 1876. Other reports on solid and fluid inclusions in various minerals followed (e.g., Hartley, 1876, 1877).

The use of inclusions to understand a gem’s geological growth environment can be understood with the examples shown in figures 3–6. Ruby derived from extremely pure calcite ( $\text{CaCO}_3$ ) marble, as in the deposits of Mogok, Myanmar, often contains calcite inclusions (figure 3), whereas magnesium-rich spinel from the same geological region in Mogok will likely contain magnesium-rich dolomite [ $\text{CaMg}(\text{CO}_3)_2$ ] (figure 4). Similarly, emeralds from mica-rich

Figure 3. The geological growth environment of marble-hosted rubies from Myanmar (left) is reflected in their internal features, such as calcite inclusions (right). Photos by Robert Weldon (left; courtesy of William F. Larson) and Nathan Renfro (right; field of view 1.44 mm).



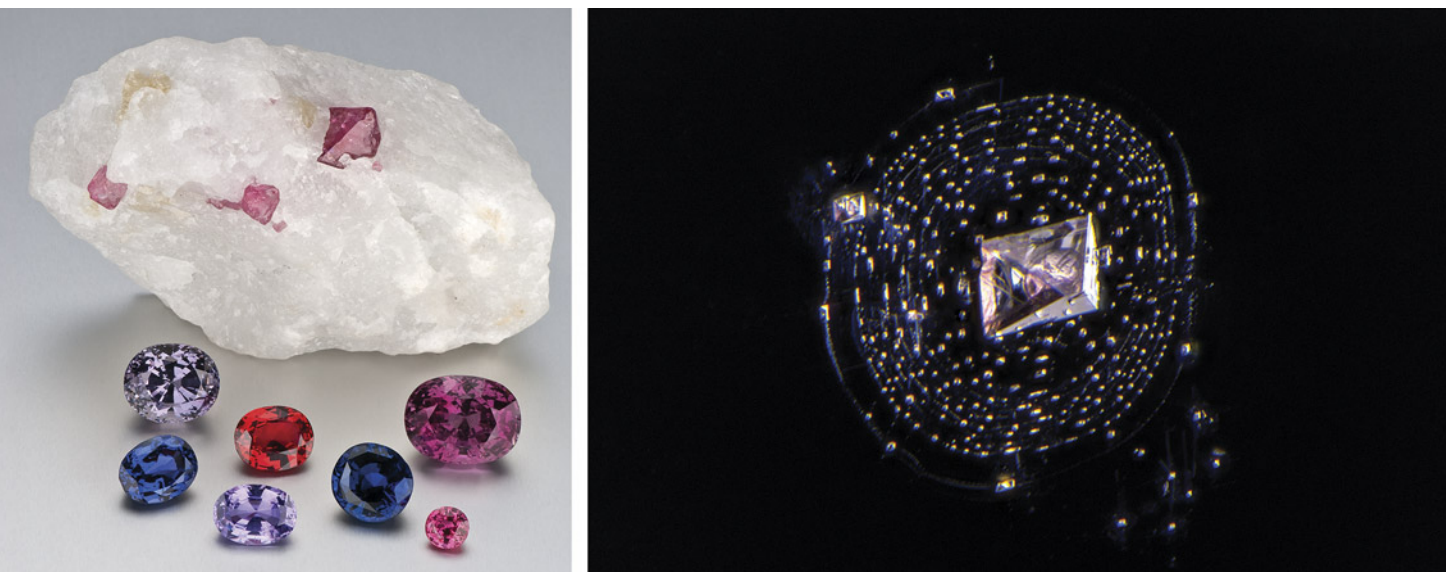


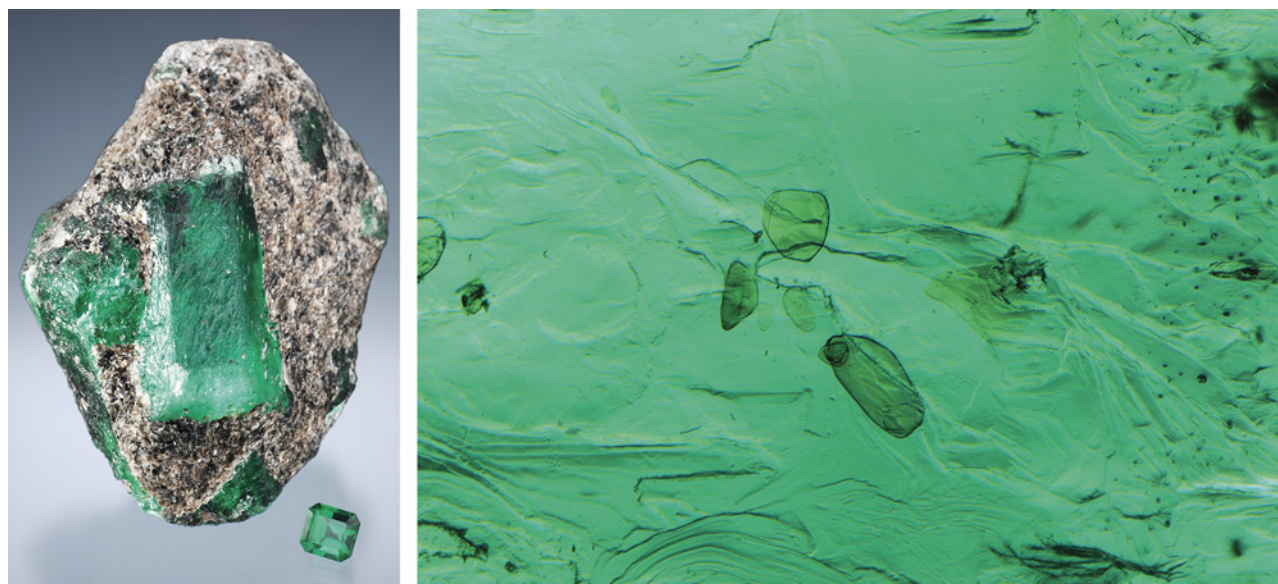
Figure 4. Left: Magnesium-rich spinel often forms in impure marbles where the magnesium-rich mineral dolomite is present. Right: These spinels contain inclusions where carbonate minerals are more likely to be dolomite than calcite, as seen in this dolomite-filled negative crystal. Photos by Robert Weldon (left) and Nathan Renfro (right; field of view 1.30 mm).

rocks called schists, such as Russian emeralds, often contain mica inclusions (figure 5). On the other hand, emeralds from the hydrothermal deposits in Colombia, where the gems occur in veins rich in carbonate, quartz, and pyrite, often contain inclusions of carbonate minerals. Figure 6 shows an exceptional example of a carbonate inclusion, which itself contains a pyrite inclusion that perfectly

matches the mineralogy seen in many emerald-bearing hand samples from Colombia.

Beginning in the 1940s, the well-known European gemologist Eduard Gübelin began publishing a series of important articles in *Gems & Gemology* and *Journal of Gemology* on inclusions and the evidence they could provide on the geologic and geographic origin of the host gemstone

Figure 5. Emeralds from mica-rich schists, such as Russian emeralds (left), display inclusions that give away their geological origins, such as fields of dark mica platelets (right). Photos by Robert Weldon (left; courtesy of R.T. Boyd Limited) and Nathan Renfro (right; field of view 2.04 mm).



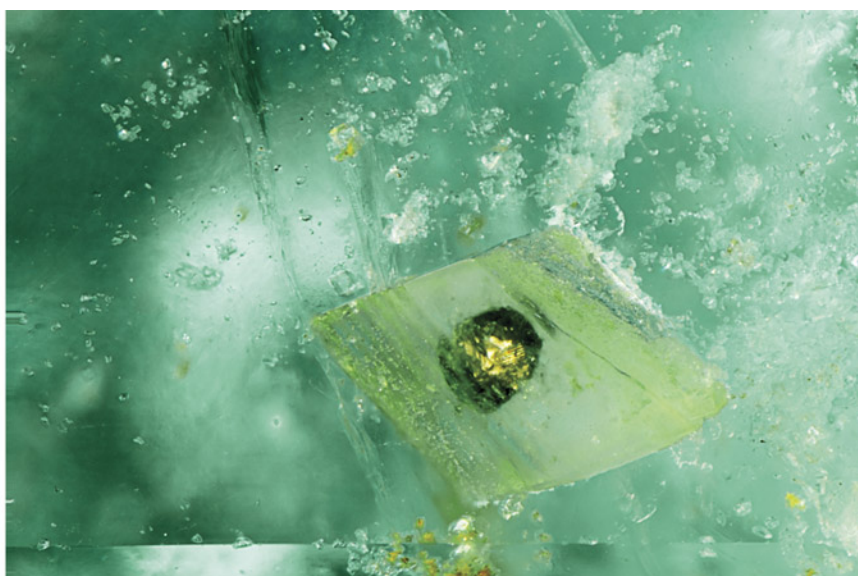


Figure 6. Left: Emerald from Chivor, Colombia, on carbonate and pyrite matrix. Right: Inclusions in Colombian emeralds provide evidence of their unique geological origins, such as this pyrite within a carbonate inclusion. Photos by Robert Weldon (left; courtesy of Cornerstone Minerals and Greg Turner) and Jonathan Muyal (right; vertical field of view 2.34 mm).

(e.g., Gübelin, 1944–1946, 1948, 1950, 1953, 1969, 1974). Dr. Gübelin's publications were followed by several important books on gem inclusions coauthored by John Koivula (1986, 2005, 2008) that have been widely used and appreciated by the gemological community. Hollister and Crawford (1981), Roedder (1984), Samson et al. (2003), and Chi et al. (2020) contributed technical summaries on fluid inclusion research.

### Inclusions in Minerals and Gems

Minerals frequently contain small inclusions of foreign materials (solids, liquids, and gases) that were trapped during mineral formation, and these can be seen with magnification. Crystals that formed during metamorphism by solid-state recrystallization, or almost entirely in the solid state without significant involvement of fluids, can display solid inclusions. Those that occur in igneous and sedimentary rocks were formed in the presence of a geological fluid and, as a result, can contain single or multiphase inclusions of that fluid (as well as solid or vapor inclusions). These geological fluids consist of high-density silicate or carbonatite melts, low-density water-rich fluids or vapors, and, in rare cases, organic hydrocarbons (oils). Following crystallization, the mineral crystals in all of these rock types can become cleaved or fractured one or more times, and these cleavages and fractures can later become healed in the presence of liquid or gaseous fluids. Tiny amounts of these fluids can remain as inclusions along the healed zone (figure 7). The crystal form of the host mineral typically determines the morphology of these fluid inclusions. Fluid inclusions usually have a geometric, angular shape that reflects the typical

crystal forms of the host. For this reason, these fluid inclusions are often referred to as “negative crystals.”

While either solid or liquid at the time of their original entrapment in crystals at high temperatures in the earth,

Figure 7. Fluid inclusions with exsolved gas bubbles and daughter crystals in a beryl host. These fluid inclusions entered the host through a fracture. The fracture healed itself, trapping blebs of this fluid with the negative crystal form seen here. Photomicrograph by Nathan Renfro.





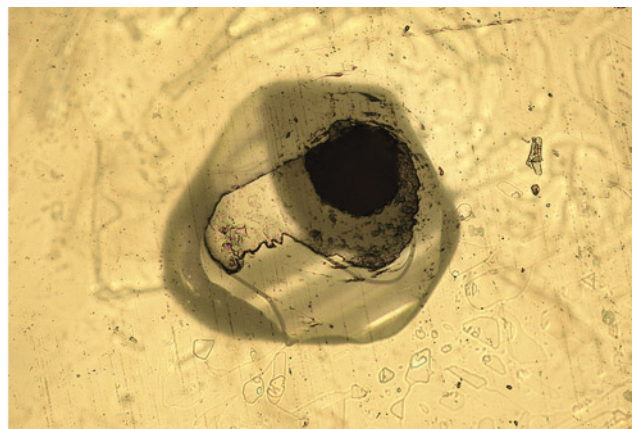
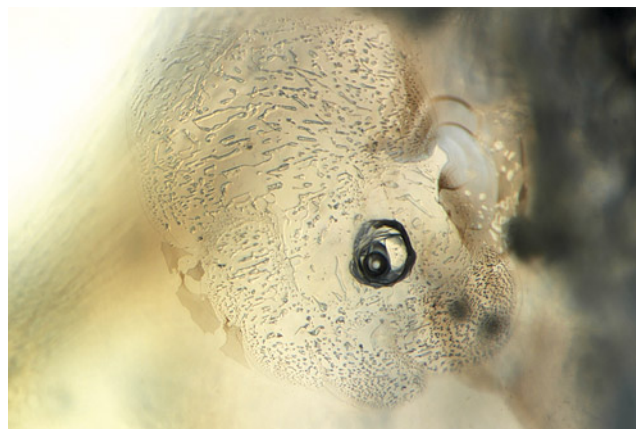


Figure 8. This glassy melt inclusion within a Montana sapphire (left) was originally trapped as a fluid magma that quenched to a glass upon cooling. This can be seen when these inclusions are polished down to the surface. The material inside the inclusion does not flow away, indicating it has quenched to a solid, glassy state (right). Photomicrographs by Aaron Palke; fields of view 1.26 mm (left) and 0.72 mm (right).

inclusions can undergo phase changes during cooling of the host crystals as the host rocks are brought toward the earth's surface. Near the surface, inclusions of fluids normally remain as fluids, while melt inclusions normally solidify to some type of glass or other solid (figure 8). In some cases, a fluid can separate into two fluids that are immiscible (i.e., do not mix with one another at cooler temperatures). Solid inclusions can also undergo changes to lower-density or secondary alteration phases.

At elevated temperatures in the earth, minerals can accommodate greater amounts of foreign impurity elements in their crystal structures. But when the minerals cool in the earth's crust, these impurity elements can no longer be contained, and they are usually expelled from the structure (exsolved) as inclusions of different minerals (such as rutile needles in sapphire). At lower pressures and temperatures near the earth's surface, gases originally dissolved in inclusion fluids can also be exsolved as distinct gas bubbles within water or carbon dioxide or some other fluid. Secondary or "daughter" crystals can also form by coming out of the solution from the fluid in the inclusion (figure 7).

Inclusions occur either individually or in small groups. Sometimes they are abundant enough to affect the transparency of the host mineral. They often occur randomly in the host crystal. But they may also form along certain crystallographic directions, color zones, or healed fractures, or they can occur in geometric patterns related to the crystal symmetry of the host. Solid inclusions can exhibit their own crystal shape, have a rounded or irregular appearance, or adopt the negative crystal shape of the host mineral. Gemologists categorize inclusions based on their appearance (shape, size, transparency, color, luster, contrast with the host, and orientation) and their association with other mineral inclusions.

Inclusions and their host gemstones can have various age relationships with one another, although this forma-

tion relationship cannot always be clearly established based on visual or other evidence. **Protogenetic** primary solid inclusions were present before the host mineral formed, and the mineral grew around and entrapped them—these may display irregular or partly dissolved shapes. **Syngenetic** primary solid, liquid, or gas inclusions formed at the same time as the host mineral by being trapped on growing crystal faces. Solid inclusions sometimes have well-formed crystal shapes that represent either their morphology or a morphology imposed on them by the host. **Epigenetic** secondary inclusions formed after the host by exsolution along a rehealing cleavage or fracture.

### Scientific Study and Geological Importance of Inclusions

The study of solid and fluid inclusions provides a way for the scientist to reconstruct events and processes in the geological past. Fluid inclusions represent actual, and often quite rare, samples of the geological fluids that existed at some time in the history of rocks and minerals. As such, they can provide information on the physical and chemical conditions that were present during and after rock formation. In particular, studies of inclusions can reveal information on:

**Temperature:** When a mineral and the fluid inclusions within it cool over geologic time, they shrink at different rates. The inclusion fluid shrinks faster than the solid crystal host, and this difference is evident in the exsolution over time of a gas bubble within the fluid at temperatures existing near the earth's surface (see figure 9). Through gradual, controlled heating of the crystal sample and observing when the gas bubble disappears back into the fluid (homogenizes), one can estimate the temperature that existed when the inclusion itself first formed.

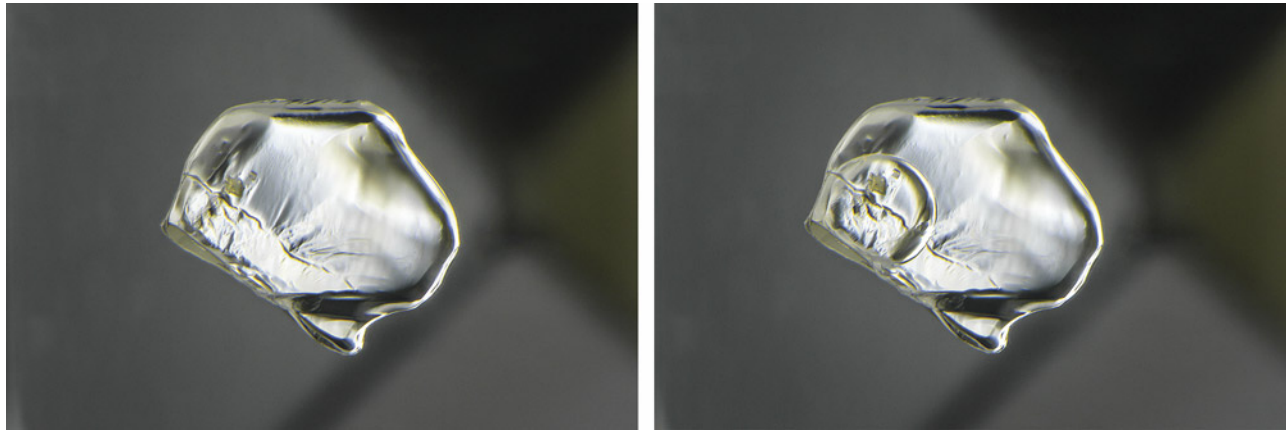


Figure 9. When warmed slightly by the well light of a microscope, the carbon dioxide and gas bubble fluid inclusion in this quartz will homogenize to a single fluid (left). When cooled slightly, this fluid separates into distinct gas and fluid phases (right). Photomicrographs by Nathan Renfro; field of view 2.56 mm.

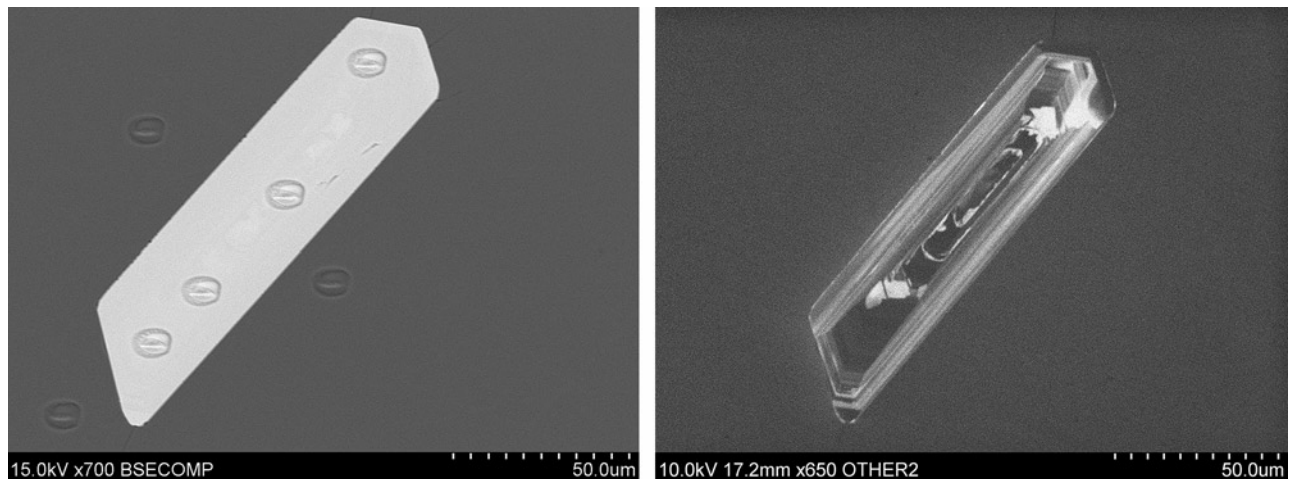
**Pressure:** Once the chemical composition of the fluid inclusions is identified, scientists can use experimental laboratory data on similar fluids to get a sense of the pressures that existed at the time and the environment in which the inclusions were trapped in the host mineral.

**Density:** With data on chemical composition, along with the density and individual volume of the various phases present in a fluid inclusion, the total average density of all the phases in the inclusion can be calculated. This result is important for understanding the types of fluids and their circulation in the earth's crust.

**Chemical Composition:** The liquids, the solids, and in some cases the gases present in inclusions can be analyzed to obtain information on the chemical environment of inclusion formation in the earth's crust and mantle. Inclusions provide important geological information on the deep earth that may not be available from any other source.

**Geologic Age Dating:** When solid inclusions in mineral crystals contain small amounts of radioactive trace elements, it is possible to determine the geologic age of the inclusion (figure 10). Radioactive elements undergo a specific decay over known periods of geologic time, so careful

Figure 10. A zircon inclusion polished down to the surface of the host sapphire, viewed in backscattered electron imaging (left) and cathodoluminescence imaging (right) using scanning electron microscopy (SEM). Secondary ion mass spectrometry (SIMS) analysis pits are seen in the image on the left. These analytical tools are able to determine the age of the zircon inclusion, giving an upper limit on the age of the sapphire host. Images by Rachelle Turnier, University of Wisconsin/GIA.



determination of these elements can be used to calculate mineral formation ages.

*Application of Inclusion Research:* The abundance and frequent occurrence of inclusions in a variety of geologic samples offers numerous opportunities for inclusion studies that support a multitude of geological investigations, such as:

- Verifying the geologic conditions of formation of ore deposits, providing a tool for the field exploration of new deposits
- Determining the conditions of formation, mineralogy, and geologic history of rocks found in many types of crustal and upper mantle environments (some results cannot be obtained any other way)
- Inspecting fluid inclusions that contain hydrocarbons, which can be important for oil exploration
- Determining the metamorphic or magmatic provenance of certain minerals found today in sediments and sedimentary rock formations
- Ascertaining the conditions and geological ages of diamonds and coexisting mineral phases in the lower crust and mantle
- Hypothesizing the conditions of geotectonic events such as crustal formation and subduction, mountain building and erosion, volcanism, metamorphism, and sedimentation
- Studying trapped organisms and vegetation found as fossil inclusions in amber to provide information on the ancient biosphere

- Using gases trapped in inclusion fluids to study the ancient atmosphere

## Gemological Importance of Inclusions

For the gemologist, inclusion studies combined with documentation of standard physical properties provide the basis for gem identification. In some instances, particular inclusions uniquely identify a gemstone and its geographic origin. Observation of inclusions is carried out using a gemological microscope and various lighting configurations. These may include brightfield, darkfield, fiber-optic lighting at different orientations to the sample, shadowing, use of polarizing or colored filters, and other image-processing techniques. Since the 1950s, inclusion photography has been an essential part of gemological education (see Koivula, 1981, 2003; Renfro, 2015a,b).

Inclusions are often the key to determining the geographic origin of gemstones. Some gems contain inclusions that are very specific to certain localities. Parasite inclusions in an emerald are a diagnostic indicator of Colombian origin (figure 11). In other cases, inclusions are one piece of the puzzle, such as the long, slender rutile silk seen in a Sri Lankan sapphire (figure 12).

Inclusions are an important clue in identifying treatments applied to gemstones. The observation of internal diffusion of blue color around relict rutile silk in a sapphire offers evidence of high-temperature heat treatment meant to enhance the stone's blue color (figure 13). Microscopy is arguably the most important way to identify many treatments such as heat treatment, dyes, and clarity enhancement through fracture filling.



*Figure 11. Parasite inclusions in emerald are a diagnostic indicator of a Colombian origin. Photomicrograph by Jonathan Moyal; field of view 0.82 mm.*

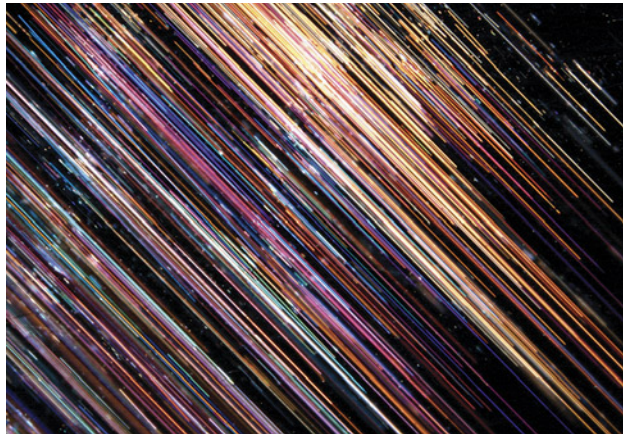


Figure 12. Long, slender rutile silk inclusions in sapphire are an indicator, although not diagnostic, of a Sri Lankan origin. Photomicrograph by Nathan Renfro.

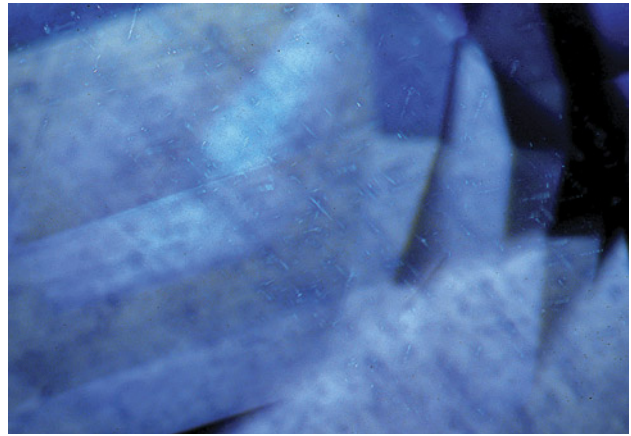


Figure 13. The rutile silk in this sapphire has been dissolved into the corundum lattice by heat treatment at high temperature, creating blue coloration around the partially dissolved silk. Photomicrograph by Nathan Renfro.

### Inclusions as Natural Art

Inclusions in gems serve as visual works of natural art (figure 14). Fortuitous geological processes in the earth created these inclusions in natural, untreated gems without any human intervention. Their shape, appearance, color(s), and in some cases the constraints imposed by the crystal symmetry of the mineral host all combine to create an inclusion “scene” that is entirely unique and never to be repeated. The artistic nature of inclusions is perhaps best illustrated by a series of photomicrograph charts created by Nathan Renfro and others that have appeared in

*Gems & Gemology* since 2016 (Renfro et al., 2016; 2017a,b; 2018; 2019; 2021).

The field of gemological research exists at a fascinating intersection between the cold, dispassionate scientific method and the impassioned and provocative world of aesthetics and art. So perhaps it is fitting that these inclusions that tell us so much about the history and genesis of gems can also move and touch us as works of art. Future installments will further explore the ways in which scientific inquiry of the geology of colored stones can deepen our appreciation of these gems.



Figure 14. Rutile needle inclusions in a quartz host. Cross-polarized light shows off the Brazil-law twinning in the quartz, creating a spectacular display of light. Photomicrograph by Nathan Renfro; field of view 20.05 mm.

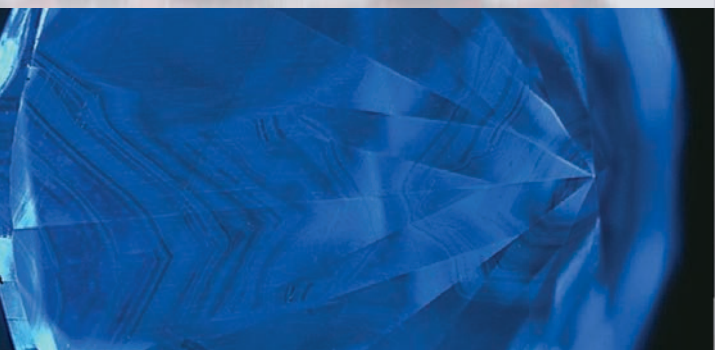
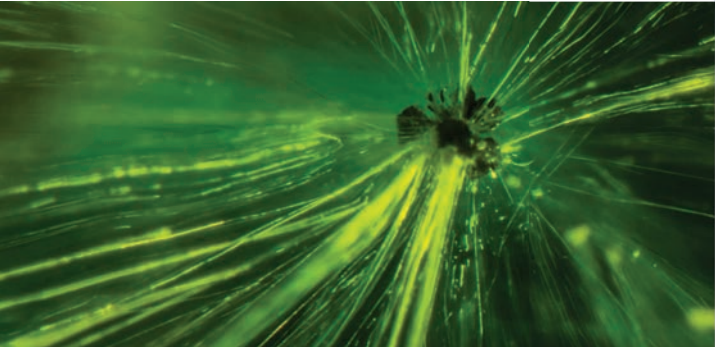
## REFERENCES

- Ball S.H. (1950) *A Roman Book on Precious Stones: Including an English Modernization of the 37th Booke of the Historie of the World by C. Plinius Secundus*. Gemological Institute of America, Los Angeles.
- Blum J.R., Leonhard G., Seyfert A.H., Söchting E. (1854) Die Einschlüsse von Mineralien in Krystallisirten Mineralien. *Naturkundige Verhandlungen van de Hollandsche Maatschappij der Wetenschappen te Haarlem*, Vol. 9, 264 pp.
- Boyle R. (1672) *An Essay about the Origine & Virtues of Gems*. W. Godbid, London, 185 pp.
- Brewster D. (1826) On the existence of two new fluids in the cavities of minerals, which are immiscible, and possess remarkable physical properties. *Philosophical Transactions of the Royal Society of Edinburgh*, Vol. 10, No. 1, pp. 1–41, <http://dx.doi.org/10.1017/S0080456800024133>; Vol. 10, No. 2, pp. 407–427
- (1827) Notice respecting the existence of the new fluid in a large cavity in a specimen of sapphire. *Edinburgh Journal of Science*, Vol. 6, No. 1, pp. 155–156.
- (1844) On crystals in the cavities of topaz, which are dissolved by heat, and re-crystallize on cooling. *Report of the Fourteenth Meeting of the British Association for the Advancement of Science – Notices and Abstracts of Miscellaneous Communications*, pp. 9–10.
- (1845a) On the existence of peculiar crystals in the cavities of topaz. *Proceedings of the Royal Society of Edinburgh*, Vol. 2, No. 26, pp. 23–25.
- (1845b) On the existence of crystals with different primitive forms and physical properties in the cavities of minerals, with additional observations on the new fluids in which they occur. *Transactions of the Royal Society of Edinburgh*, Vol. 16, No. 1, pp. 11–22.
- (1863) On the pressure cavities in topaz, beryl, and diamond, and their bearing on geological theories. *Philosophical Magazine*, Vol. 25, No. 167, pp. 174–180.
- Chi G., Diamond L.W., Lu H., Lai J.Q., Chu H. (2020) Common problems and pitfalls in fluid inclusion study: A review and discussion. *Minerals*, Vol. 11, No. 1, article no. 7, <http://dx.doi.org/10.3390/min11010007>
- Davy H. (1822) On the state of water and aeriform matter in cavities found in certain crystals. *Philosophical Transactions of the Royal Society of London*, Vol. 112, No. 1, pp. 367–376.
- Dewey C. (1819) Sketch of the mineralogy and geology of the vicinity of Williams' College, Williamstown, Massachusetts. *American Journal of Science*, Vol. 1, No. 4, pp. 337–346.
- de Dolomieu D.G. (1792) Sur de l'huile de pétrole dans le cristal de roche et les fluides élastiques tirés du quartz. *Journal de Physique*, Vol. 40, No. 1, pp. 318–319.
- Gübelin E.J. (1944–1946) Gemstone inclusions. *G&G*, Vol. 4, No. 10, pp. 142–149; Vol. 4, No. 11, pp. 158–163; Vol. 4, No. 12, pp. 174–179; Vol. 5, No. 1, pp. 205–210; Vol. 5, No. 5, pp. 294–300; Vol. 5, No. 6, pp. 318–323.
- (1948a) Gemstone inclusions. *Journal of Gemmology*, Vol. 1, No. 7, pp. 7–39.
- (1948b) Die diagnostische Bedeutung der Einschlüsse in Edelsteinen. *Schweizerische Mineralogische und Petrographische Mitteilungen*, Vol. 28, No. 1, pp. 146–156.
- (1950) Diagnostic importance of inclusions in gemstones. *Journal of Gemmology*, Vol. 2, No. 7, pp. 281–303.
- (1953) *Inclusions as a Means of Gemstone Identification*. Gemological Institute of America, Los Angeles, 220 pp.
- (1969) On the nature of mineral inclusions in gemstones. *G&G*, Vol. 13, No. 2, pp. 42–56 and No. 3, pp. 74–88.
- (1974) *Internal World of Gemstones*. ABC Edition, Zurich, 234 pp.
- Gübelin E.J., Koivula J.I. (1986) *Photoatlas of Inclusions in Gemstones*. ABC Edition, Zurich, 532 pp.
- (2005) *Photoatlas of Inclusions in Gemstones, Volume 2*. Opinio Publishers, Basel, Switzerland, 830 pp.
- (2008) *Photoatlas of Inclusions in Gemstones, Volume 3*. Opinio Publishers, Basel, Switzerland, 672 pp.
- Hartley W.N. (1876) On the presence of liquid carbon dioxide in mineral cavities. *Journal of the Chemical Society of London*, Vol. 29, pp. 137–143.
- (1877) Mineral cavities and their contents. *Popular Science Review*, Vol. 16, No. 2, pp. 119–129 (and *Journal of the Chemical Society of London*, Vol. 31, pp. 241–249).
- Hollister L.S., Crawford M.L., Eds. (1981) *Fluid Inclusions—Applications to Petrology*. Topics in Mineral Sciences, Mineralogical Association of Canada, Vol. 6.
- Kile D.E. (2003, 2013) The petrographic microscope: Evolution of a mineralogical research instrument. *Mineralogical Record*, Special Publication 1, pp. 1–96 and Vol. 44, No. 3, pp. 303–322.
- Koivula J.I. (1981) Photographing inclusions. *G&G*, Vol. 17, No. 3, pp. 132–142.
- (2003) Photomicrography for gemologists. *G&G*, Vol. 39, No. 1, pp. 4–23.
- Lea I. (1866, 1869, 1876) Notes on microscopic crystals included in some minerals. *Proceedings of the Academy of Natural Sciences of Philadelphia*, Vol. 18, pp. 110–113; Vol. 21, pp. 4, 119–121; Vol. 28, pp. 98–107.
- Nicol W. (1828) Observations on the fluids contained in crystallized minerals. *Edinburgh New Philosophical Magazine*, Vol. 5, pp. 94–96.
- Renfro N. (2015a) The application of differential interference contrast microscopy to gemmology. *Journal of Gemmology*, Vol. 34, No. 7, pp. 616–620.
- (2015b) Digital photomicrography for gemologists. *G&G*, Vol. 51, No. 2, pp. 144–159. <http://dx.doi.org/10.5741/GEMS.51.2.144>
- Renfro N.D., Koivula J.I., Moyal J., McClure S.F., Schumacher K., Shigley J.E. (2016) Chart: Inclusions in natural, synthetic, and treated emerald. *G&G*, Vol. 52, No. 4, pp. 402–403, <http://dx.doi.org/10.5741/GEMS.52.4.402>
- (2017a) Chart: Inclusions in natural, synthetic, and treated sapphire. *G&G*, Vol. 53, No. 2, pp. 213–214, <http://dx.doi.org/10.5741/GEMS.53.2.213>
- (2017b) Chart: Inclusions in natural, synthetic, and treated ruby. *G&G*, Vol. 53, No. 4, pp. 457–458, <http://dx.doi.org/10.5741/GEMS.53.4.457>
- (2018) Chart: Inclusions in natural, synthetic, and treated diamond. *G&G*, Vol. 54, No. 4, pp. 428–429, <http://dx.doi.org/10.5741/GEMS.54.4.428>
- (2019) Chart: Inclusions in natural, treated, synthetic, and imitation opal. *G&G*, Vol. 55, No. 2, pp. 244–245, <http://dx.doi.org/10.5741/GEMS.55.2.244>
- Renfro N.D., Koivula J.I., McClure S.F., Schumacher K., Shigley J.E. (2021) Chart: Micro-features of spinel. *G&G*, Vol. 57, No. 1, pp. 46–49, <http://dx.doi.org/10.5741/GEMS.57.1.46>
- Roedder E. (1984) Fluid inclusions. *Reviews in Mineralogy*, Vol. 12. Mineralogical Society of America, Chantilly, Virginia, 644 pp.
- Rose G. (1862) Über den Asterismus der Krystalle, insbesondere des Glimmers und des Meteoreisens. *Monatsberichte der Königlich Preussische Akademie der Wissenschaften zu Berlin*, pp. 614–618.
- Samson I., Anderson A., Marshall D., Eds. (2003) *Fluid Inclusions: Analysis and Interpretation*, Topics in Mineral Sciences. Mineralogical Association of Canada, Vol. 32.
- Sorby H.C. (1858) On the microscopical structure of crystals, indicating the origin of minerals and rocks. *Quarterly Journal of the Geological Society of London*, Vol. 14, No. 1/2, pp. 453–500.
- (1869) On the microscopical structure of some precious stones. *Monthly Microscopical Journal*, Vol. 1, pp. 220–224.

# DO YOU DIG GEMOLOGY?

The GIA® G&G Facebook group is a forum where more than 25,000 gemologists and gem lovers share and discuss gemological discoveries, especially the findings published here in *Gems & Gemology*.

If you are mesmerized by gem sources, inclusions and other characteristics, this is the community for you!



Join us today at  
[www.facebook.com/groups/giagemsgemology](https://www.facebook.com/groups/giagemsgemology)



**GIA®**



# GEM NEWS INTERNATIONAL

## Contributing Editors

Gagan Choudhary, *Gem Testing Laboratory, Jaipur, India* (gagan.choudhary@iigjrlc.org)

Christopher M. Breeding, *GIA, Carlsbad* (christopher.breeding@gia.edu)

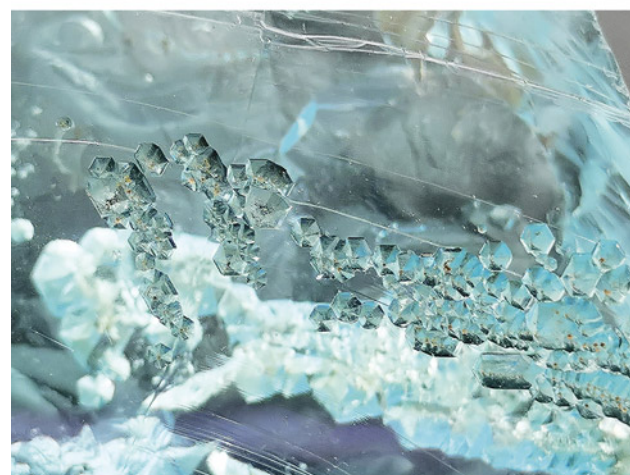
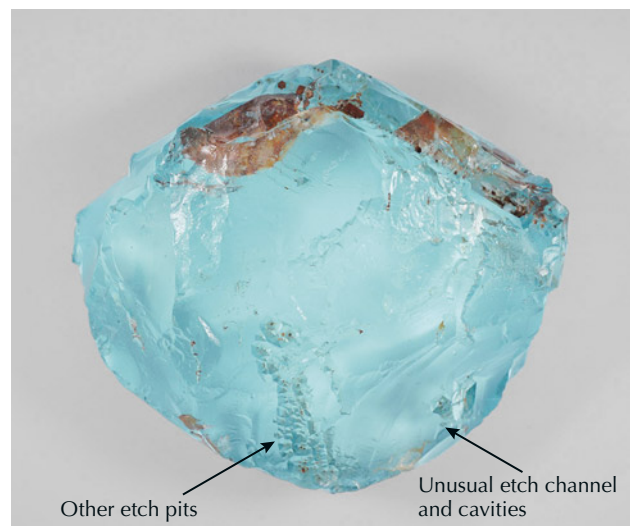
Guanghai Shi, *School of Gemmology, China University of Geosciences, Beijing* (shigh@cugb.edu.cn)

## COLORED STONES AND ORGANIC MATERIALS

**A large aquamarine with unusual etch features from Xinjiang, China.** Etch features are commonly seen in beryl crystals (e.g., T. Lu, "Interesting etch features and cavities in beryl and quartz," Spring 2002 GNI, pp. 102–103). Their formation is related to various factors during or after crystal growth, both internal and external, including chemical composition, lattice defect types and their distribution, pressure-temperature conditions of the forming environment, solvent composition, and dissolution time (R. Kurumathoor and G. Franz, "Etch pits on beryl as indicators of dissolution behaviour," *European Journal of Mineralogy*, Vol. 30, No. 1, 2018, pp. 107–124).

Recently, Shino Gold Jewelry (Shanghai) Co. submitted a large piece of rough aquamarine crystal to the National Gemstone Testing Center (NGTC) lab in Beijing for identification service. The crystal, weighing 778 g (figure 1, top), was claimed to have been mined in the Altay region of Xinjiang, China. Standard gemological testing revealed a refractive index of 1.577–1.583 and a specific gravity of 2.69. These values were typical for aquamarine and were confirmed by the infrared and Raman spectra. The numerous hexagonal etch features on the (0001) crystal face (figure 1, bottom), combined with the contents in the fissures (mainly kaolinite and hematite) identified by Raman spectroscopy, indicate that the crystal is of natural origin. Notably, one of the etch features has not been previously reported to our knowledge—the crystal had two hexagonal dissolution cavities with openings about 3 mm in diame-

Figure 1. This 778 g (approximately 11 × 4 cm) aquamarine crystal from Xinjiang displays a unique natural etch pattern (detail in bottom photo). Photos by Ting Zheng; courtesy of Shino Gold Jewelry (Shanghai) Co.



*Editors' note: Interested contributors should send information and illustrations to Stuart Overlin at [soverlin@gia.edu](mailto:soverlin@gia.edu) or GIA, The Robert Mouawad Campus, 5345 Armada Drive, Carlsbad, CA 92008.*

GEMS & GEMOLOGY, VOL. 58, NO. 2, pp. 244–268.

© 2022 Gemological Institute of America

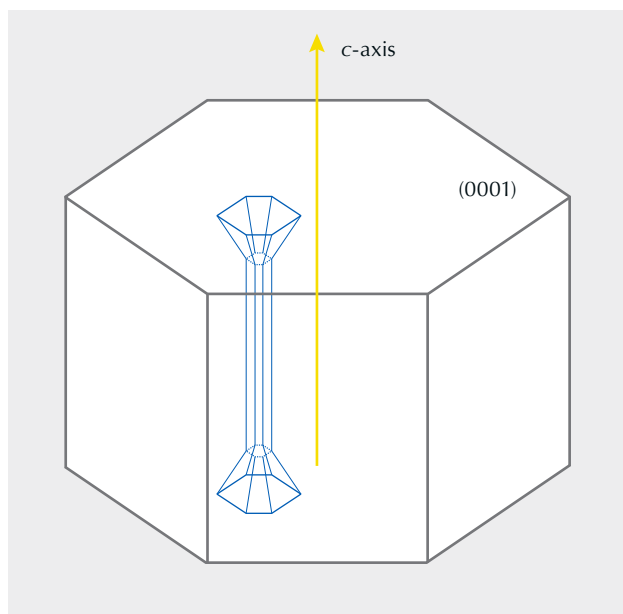


Figure 2. Schematic diagram of the etch feature parallel to the *c*-axis of the aquamarine crystal.

ter, connected by a hexagonal etch channel 4 cm long and parallel to the *c*-axis (figures 2 and 3). Interestingly, the etch channel appeared to be empty and penetrated throughout the crystal.

The formation of this etch feature cannot be fully explained at present. One possible explanation is that it is related to the defects (dislocations) parallel to the *c*-axis, which control the locations of the preferred dissolution process (T. Lu et al., "Observation of etch channels in several natural diamonds," *Diamond & Related Materials*,



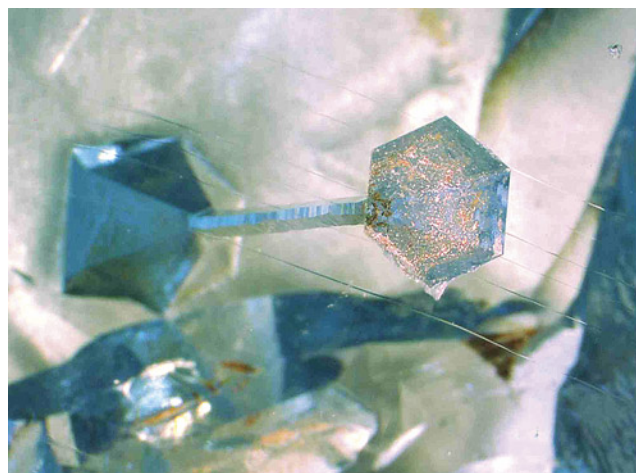
Figure 4. A 0.22 ct emerald-cut red beryl (5.08 × 3.12 × 1.91 mm). Photo by Huixin Zhao.

Vol. 10, No. 1, 2001, pp. 68–75). Also, the formation of these special etch features is affected by different dissolution rates in different directions of the crystal. The selected dissolution on the (0001) plane was very slow, while the dissolution rate along the *c*-axis was significantly faster, resulting in the special funnel-shaped etch pits connected by a very long etch channel.

Ting Zheng (zhengt1990@foxmail.com),  
Qian Deng, and Taijin Lu  
National Gemstone Testing Center, Beijing

**Topaz crystals in red beryl.** Gem-quality beryl comes in various colors, including green, yellow, pink, and rarely red, which has only been mined in the state of Utah to

Figure 3. The etch features of the crystal: two hexagonal dissolution cavities connected by a hexagonal etch channel. The channel (left) is about 4 cm long and empty throughout, and the openings have a hexagonal funnel shape (right). Photomicrographs by Chao Liu (left; field of view 23 mm) and Ting Zheng (right; field of view 6.25 mm).





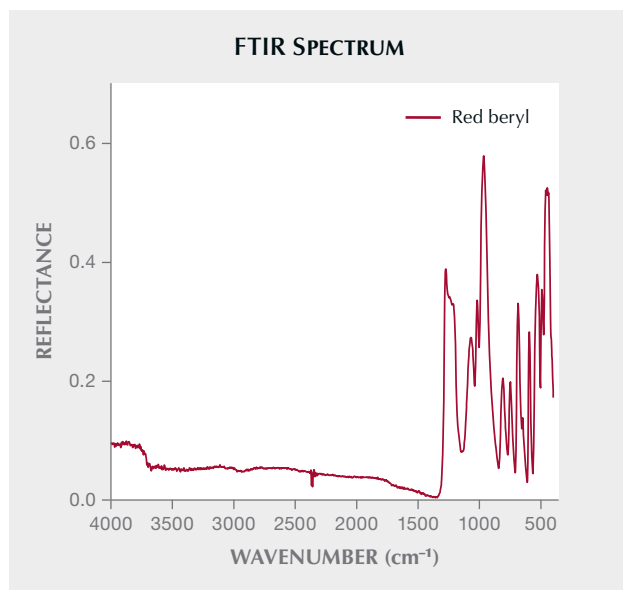


Figure 5. The infrared reflectance spectrum confirmed the identity of the red beryl.

date. Recently, a red beryl (figure 4) was submitted to Guild Gem Laboratories in Shenzhen for identification. This emerald-cut sample weighed 0.22 ct and exhibited a highly saturated red color. The refractive index values of 1.562–1.569 and birefringence of 0.007 were consistent with

Figure 6. The UV-Vis-NIR spectrum of the red beryl shows a weak peak at 370 nm (Fe<sup>3+</sup>) and an intense peak at 540 nm (Mn<sup>3+</sup>).

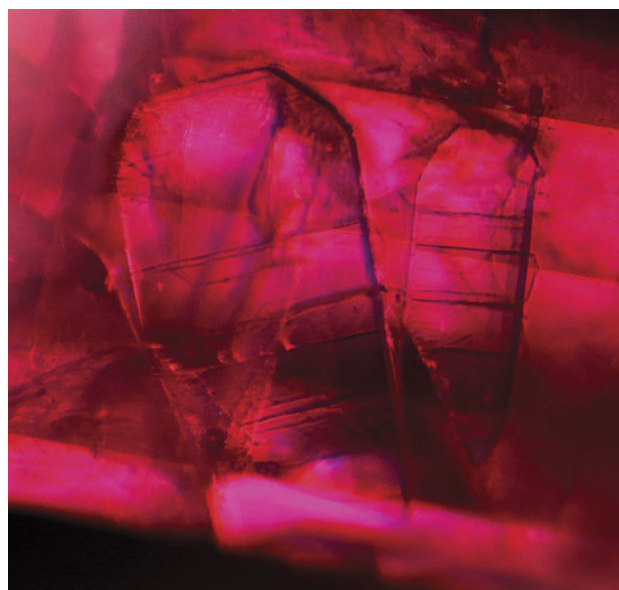
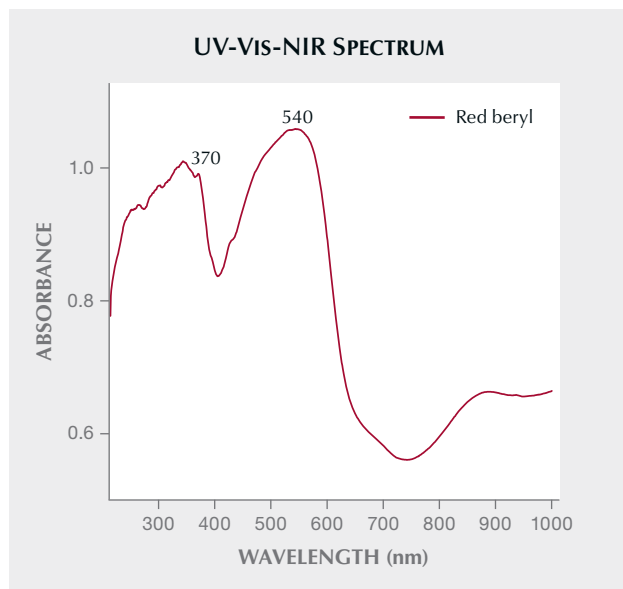


Figure 7. Exposed crystal inclusions in the red beryl showed a fine columnar shape and distinct cleavage fissures. Photomicrograph by Huixin Zhao; field of view 1.6 mm.

beryl. Multiple analytical methods were applied, including FTIR and UV-Vis-NIR spectroscopy, and EDXRF for chemical analysis. FTIR confirmed the sample as beryl (figure 5), and the UV-Vis-NIR spectrum showed a prominent manganese-related broad band centered at 540 nm, as well as a weak iron-induced band at 370 nm (figure 6).

EDXRF results showed that the beryl was rich in iron (16920 ppm) and manganese (2586 ppm), along with a trace amount of zinc (787 ppm). Such results were very close to previously reported values for red beryl from the Wah Wah Mountains of Utah: 15000 ppm iron, 2000 ppm manganese, and 700 ppm zinc, respectively (J.E. Shigley and E.E. Foord, "Gem-quality red beryl from the Wah Wah Mountains, Utah," Winter 1984 *G&G*, pp. 208–221).

Microscopic observation revealed several two-phase fluid inclusions along the healed fissures, and purple-blue flashes were clearly seen within the open fissures, which indicated clarity enhancement by organic fillers. This was confirmed by FTIR, with peaks at 2854, 2871, 2927, and 2963 cm<sup>-1</sup>. Two transparent crystal inclusions were present and exposed to the surface near the girdle, showing a prismatic crystal habit (figure 7). Within the included crystals, a series of cleavage layers were prominent. Further testing by micro-confocal Raman spectroscopy in the 100–1200 cm<sup>-1</sup> range showed distinct peaks at 240, 267, 285, 332, 430, 456, and 927 cm<sup>-1</sup>, results that agree with topaz according to the RRUFF online database (figure 8).

Topaz rhyolites are widely distributed across the western United States, and red beryl occurs in topaz-bearing

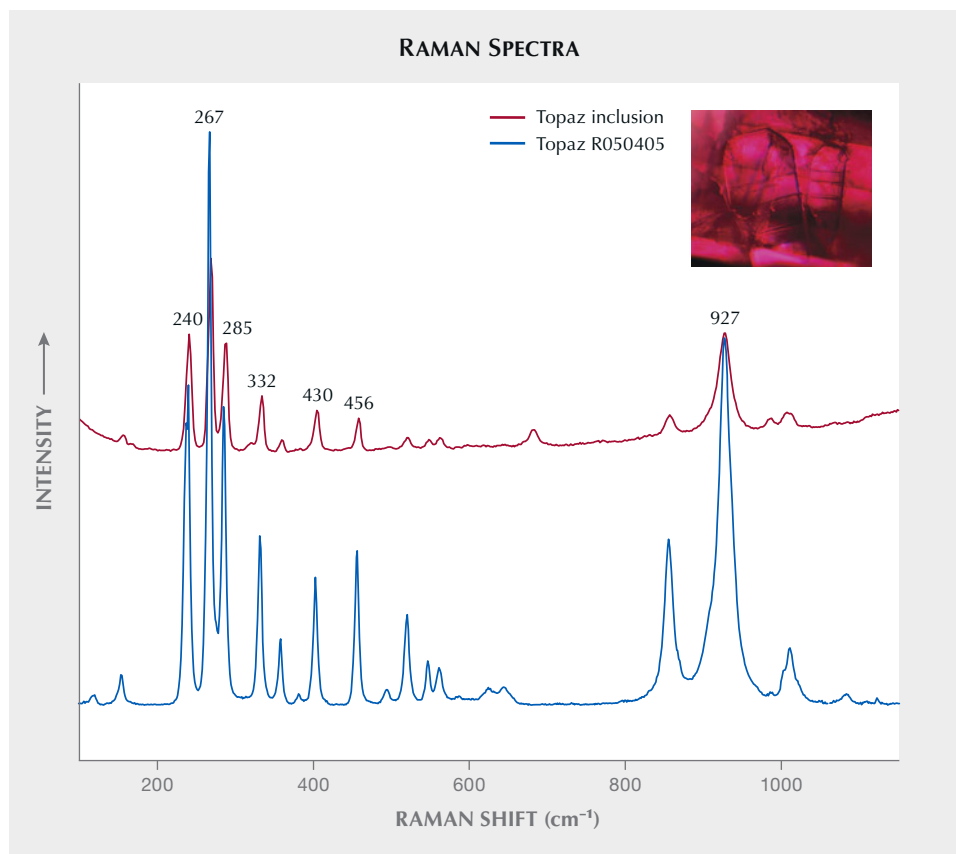


Figure 8. The Raman spectrum of the crystal inclusion agreed with the topaz spectrum in the RRUFF database.

rhyolites (J.E. Shigley et al., “Red beryl from Utah: A review and update,” Winter 2003 *G&G*, pp. 302–313). Hence, it is not surprising to see topaz as a mineral inclusion in red beryl, although such an observation does not appear to have been reported before.

Yujie Gao, Dan Ju ([judan@guildgemlab.com](mailto:judan@guildgemlab.com)), and  
Huixin Zhao  
Guild Gem Laboratories, Shenzhen, China

**Unusual cat’s-eye omphacite *fei cui* jade.** A round cabochon set in a ring with round brilliant and rose-cut diamonds (figure 9) was recently submitted to the National Center of Quality Inspection and Testing on Gold-Silver Products (NGGC) for examination. The center stone, measuring approximately 7.4 × 7.0 mm in diameter, possessed a vivid green bodycolor and exhibited pronounced chatoyancy with a vibrant green sheen. FTIR analysis (figure 10) revealed that the stone was natural untreated omphacite-type *fei cui* jade, with a typical fingerprint spectrum corresponding with omphacite, a broad absorption band centered at 3500 cm<sup>-1</sup> caused by the hydrous interstitial minerals, and the functional group region showing no absorption of any organic filling material commonly used in bleaching and filling treatment, such as Bisphenol A epoxy resin. Subsequent micro-Raman imaging and spectroscopic analysis confirmed the sample as a

fairly pure omphacite aggregate, considering that no other mineral impurity was observed or identified (figure 11).

Figure 9. This green omphacite *fei cui* jade (7.4 × 7.0 mm) displayed chatoyancy under fiber-optic light. Photo by Bowen Zhao.



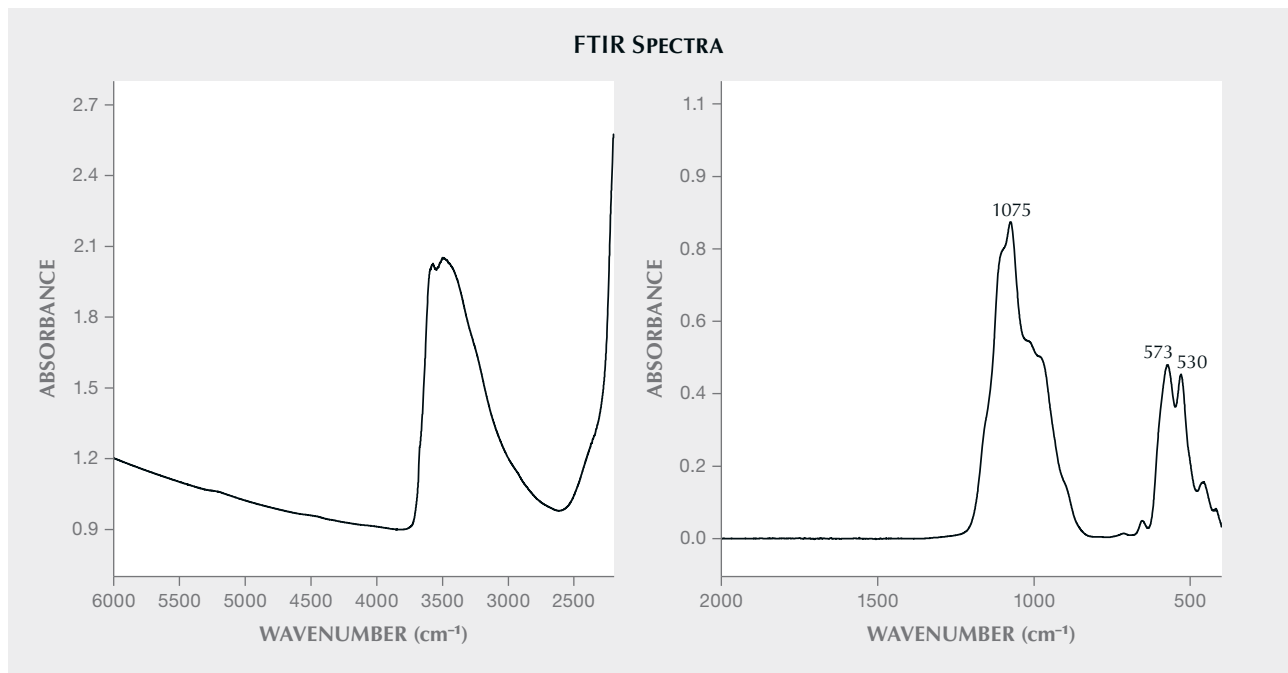


Figure 10. Both the functional group region (left) and the fingerprint region (right) of the sample's IR absorption spectrum were collected with a diffuse reflectance accessory. A K-K transform was applied to the fingerprint spectrum collected.

The strongest Raman peaks at  $682\text{ cm}^{-1}$  and  $1023\text{ cm}^{-1}$  were attributed to symmetrical Si-O<sub>b</sub>-Si stretching/bending and symmetrical Si-O<sub>nb</sub> stretching, respectively. O<sub>b</sub> refers to the bridging oxygens, while O<sub>nb</sub> represents non-bridging oxygens in silicon tetrahedra.

Element analysis with energy-dispersive X-ray fluorescence (EDXRF) showed that the sample's major elements were silicon, calcium, aluminum, magnesium, and iron, consistent with omphacite, whose IMA formula is  $(\text{Ca,Na})[\text{Mg,Fe,Al}]_2\text{Si}_2\text{O}_6$ . It is well known that the Fe<sup>2+</sup>-in-

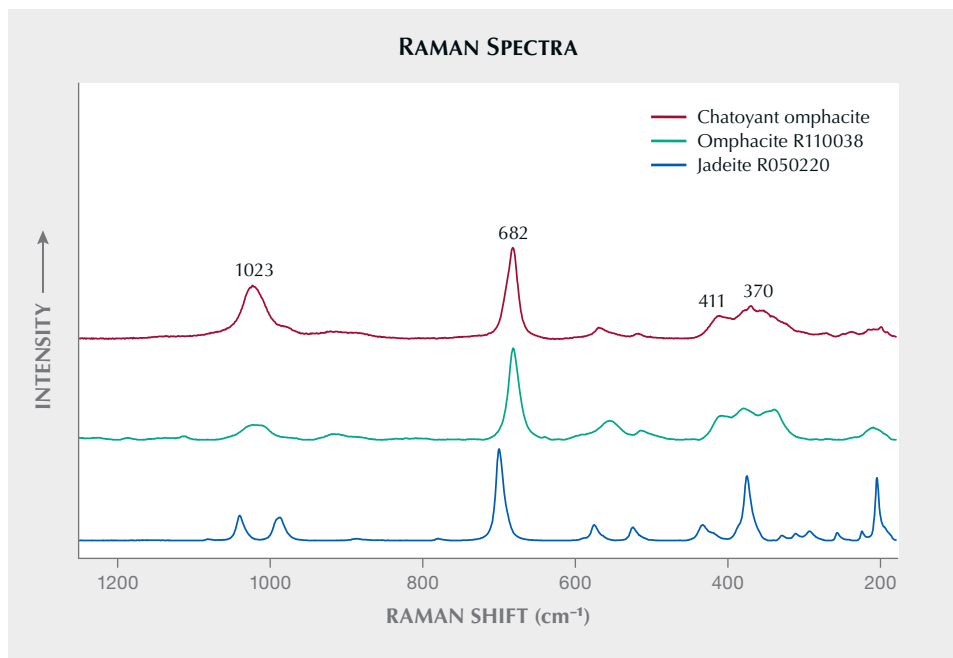


Figure 11. The sample's Raman shift confirmed its mineral species. The sample matched well with the RRUFF spectrum for omphacite but differed considerably from the RRUFF spectrum for jadeite. The spectra are shifted vertically for clarity.

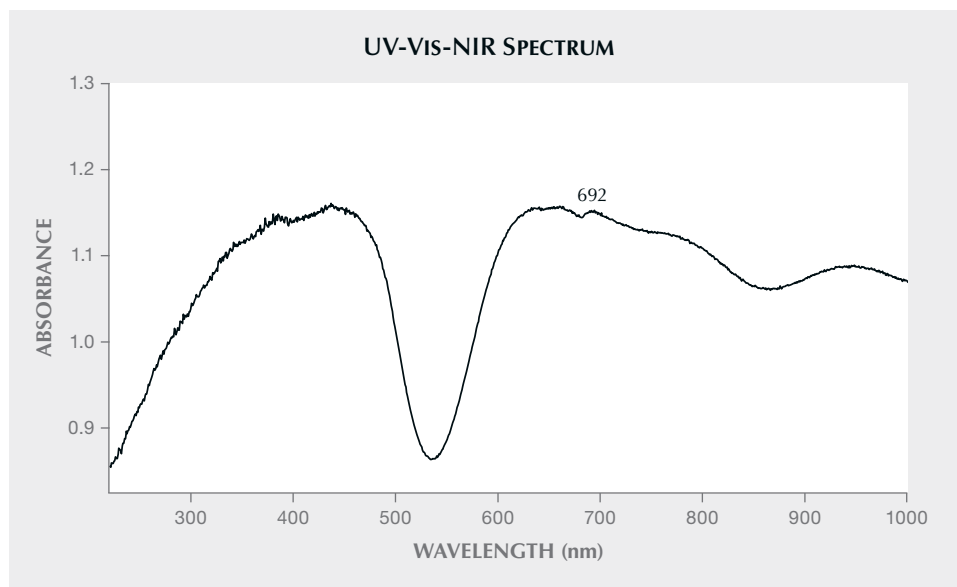


Figure 12. Two broad absorption bands centered around ~430 and ~650 nm were formed with the contributions of both iron and chromium. The 692 nm peak convincingly indicated the presence of Cr<sup>3+</sup>.

duced grayish bluish green bodycolor is most common among the green omphacite varieties. However, this chatoyant sample was characterized by a relatively high chromium content (Cr<sub>2</sub>O<sub>3</sub> ≈ 0.22 wt. %), producing a more saturated and purer green bodycolor rather than a dull green one. This color feature was confirmed by UV-Vis-NIR spectroscopy, with only a single transmittance band centered at 535 nm appearing in the visible range (figure 12).

Microscopic observation with finely tuned fiber-optic light revealed a parallel-arrayed fibrous texture throughout the sample (figure 13). Meanwhile, a vague honeycomb-like pattern was observed at two specific sides near the girdle (the 12 and 6 o'clock positions of the cabochon in figure 9). Thus, under reflected light the stone presented a chatoyant sheen parallel to the ring band.

Based on our current knowledge, this green omphacite *fei cui* jade was probably from Guatemala. Translucent *fei cui* jade with such fine texture, vivid green bodycolor, and

even color distribution has always been considered of high quality and rarity, but the chatoyancy of this sample offered additional value.

*Xiaoyu Lv, Bowen Zhao, and Xiaoying Lu  
National Center of Quality Inspection and Testing on  
Gold-Silver Products (NGGC), Shanghai*

**Three-rayed asterism in quartz.** Asterism is a well-known (if not the most familiar) optical phenomenon observed in numerous gem species. In transparent or translucent gemstones, a series of parallel inclusions consisting of tiny needles or channels produces a distinct light band by a complex process of scattering and reflection of light. If the gemstone is cut as a cabochon, the light band, which is oriented perpendicular to the needle or channel axis, generally produces a sharp light line on the surface of the gemstone, an effect known as chatoyancy. If several series of parallel inclusions

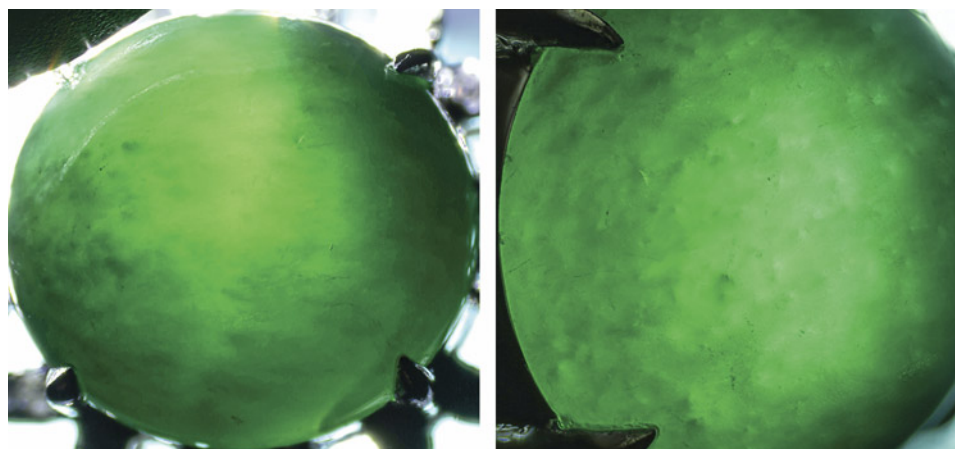


Figure 13. The omphacite *fei cui* jade's parallel-arrayed fibrous texture (left) and vague honeycomb-like pattern (right), shown in fiber-optic illumination. Photomicrographs by Bowen Zhao; fields of view 10.45 mm (left) and 8.81 mm (right).

**TABLE 1.** Properties of quartz samples showing a network of three-rayed stars.

Sample	Transparency	Weight (ct)	Shape	Size	Orientation of c-axis
A	Transparent	287	Round	45 mm diameter 21 mm height	About 45° inclined to the base
B	Transparent	463	Round	52 mm diameter 24 mm height	Approximately parallel to the base
C	Transparent	69.5	Oval	32 × 22 mm diameter 15 mm height	Not determined
D	Transparent	93.5	Irregular	34 × 28 mm diameter 13 mm height	Approximately parallel to the base

are present, we observe several intersecting light bands producing asterism. The number of rays in a star depends on the number of intersecting light bands. For example, two intersecting light bands produce four-rayed stars, three intersecting light bands produce six-rayed stars, and so on.

A single star is observed if all needles or channels are oriented parallel to a single plane. If the inclusions are found in different planes, we might observe several stars on the surface of a cabochon or sphere (K. Schmetzer et al., "Dual-color double stars in ruby, sapphire, and quartz: Cause and historical account," Summer 2015 *G&G*, pp. 112–143). This effect can be due to the symmetry of the host, which causes several series of non-planar needles (e.g., in cubic spinel or garnet). Multi-asterism is also produced by several series of needles that are independent of each other, as in quartz or beryl (K. Schmetzer and M. Glas, "Multi-star quartzes from Sri Lanka," *Journal of Gemmology*, Vol. 28, No. 6, 2003, pp. 321–332). A combination of these two variants is observed in garnet. All different variants may be designated as a "network of stars."

The present contribution describes three-rayed asterism, a phenomenon that does not really fit into the generally accepted knowledge about the formation of asterism and multi-asterism. This variant of asterism in quartz is a rare optical phenomenon mentioned briefly by Gübelin and Koivula (*Photoatlas of Inclusions in Gemstones, Volume 2*, 2005, Opinio-Verlag, Basel, Switzerland, p. 548) and by Steinbach (*Asterism: Gems with a Star*, 2016, MPS Publishing and Media, Idar-Oberstein, Germany, pp. 649–651). Hainschwang (Fall 2007 GNI, pp. 261–262) observed two three-rayed stars on quartz cabochons with chlorite inclusions. The two stars had one ray in common and were observed upon rotation of the cabochon, with one of the three-rayed stars observed at another end of the ray that is shared by both stars. Hainschwang assumed that the optical phenomenon was caused by the chlorite inclusions, but the formation mechanism is not completely understood.

Our observation is based on the examination of four star quartz samples, which came from the private collection of one of the authors (MPS). The quartz cabochons

were purchased at various gem and mineral fairs and were said by the vendors to originate from Brazil; further details on locality are unknown. The properties of the cabochons are summarized in table 1.

Upon first view, the samples showed broad light bands forming a three-rayed star, with all branches of the star originating from a center (figure 14). The single branches of the three-rayed stars move along the surface of the cabochons after rotation of the stone or a change of the position of the light source or the observer. So far, this observation is consistent with the features of light bands generally observed in asteriated gemstones. But in "normal" gemstones (e.g., star rubies or star sapphires), we see three intersecting light bands forming a six-rayed star.

Figure 14. Asterism with a three-rayed star seen on a quartz cabochon (sample B) in reflected light with fiber-optic illumination. Photo by Martin P. Steinbach.



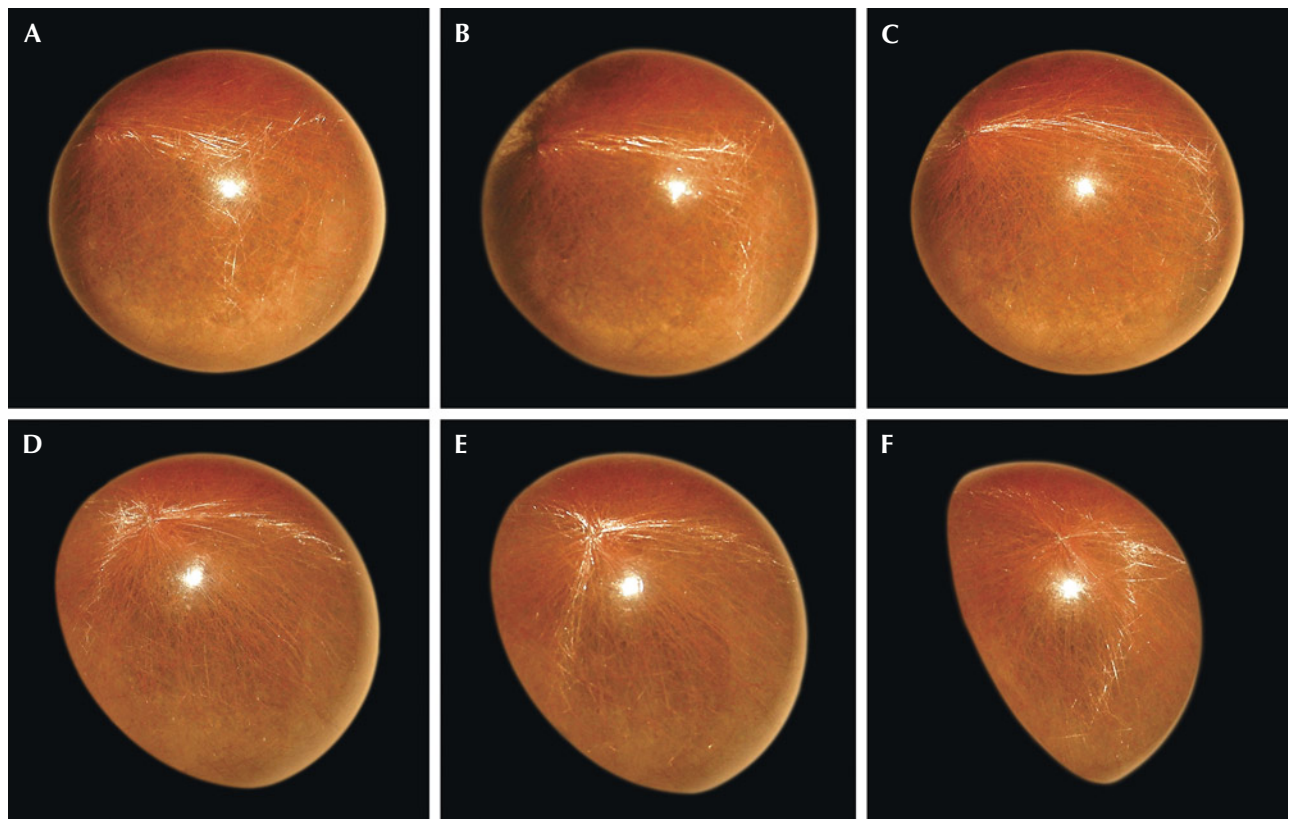


Figure 15. Upon rotation of sample A, the center of a three-rayed star moves to the girdle and another center of a three-rayed star comes into sight (D); upon further rotation, this star is also moved. The sequence A to F shows the optical phenomenon described. Photos by Karl Schmetzer; reflected light, fiber-optic illumination.

Surprisingly, upon rotation of the cabochons it was detected that the samples did not show a single three-rayed star but a multi-star network. Rotating each quartz cabochon in a direction in which it was possible to follow one of the light bands on the cabochon's surface, at some point this branch of the star ended in another center of a three-rayed star. Repeating this procedure, another center of a three-rayed star was occasionally detected, unless the branches of the three-rayed star ended at the girdle (figure 15).

Figure 16 shows a schematic representation of the multi-star networks observed in the four samples. It must be underscored that the different patterns drawn represent lines on curved domes of the different cabochons. If the branches of the stars are in a position close to the girdle, some lines

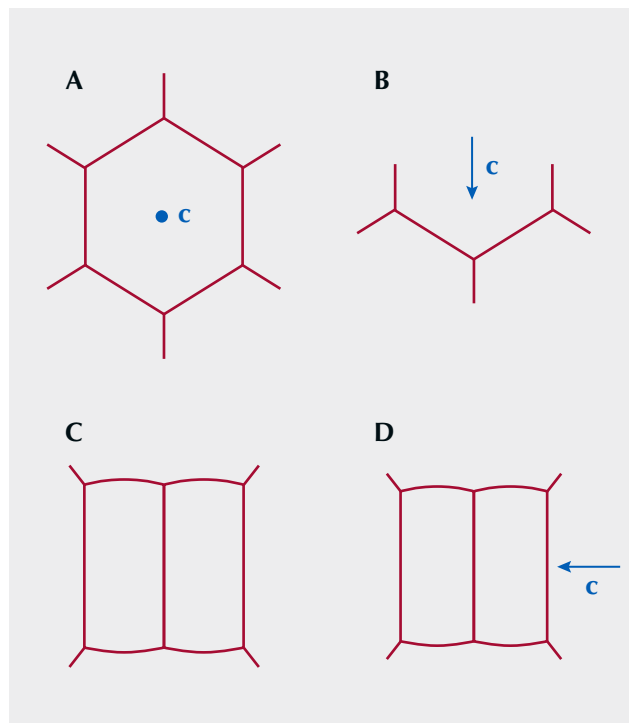


Figure 16. Schematic representation of the multi-star network observed on the four quartz cabochons (samples A–D in table 1). The red lines represent the light bands observed on the surface upon various rotations. The patterns in A and B were observed on the round cabochons; sample C was an oval cabochon, while sample D was an irregularly shaped cabochon. The direction of the c-axis for the three transparent samples is also indicated.



Figure 17. Fibrous inclusions in a quartz cabochon from Brazil showing three-rayed asterism. Photomicrograph by Karl Schmetzer; immersion, field of view 7.6 mm.

that appear almost straight in the middle of the cabochon will appear more or less curved. So far, due to the different orientations of the cabochons and the different shapes, each sample represents only part of a full star network that would be seen on the surface of a complete sphere.

All the samples revealed a dense pattern of needle-like to fibrous inclusions (figure 17) typically described as rutile (J. Hyršl and G. Niedermayr, *Magic World: Inclusions in Quartz*, 2003, Bode Verlag, Haltern, Germany, pp. 82–139). However, these inclusions are mostly bent or curved, and no series of parallel needles or channels were seen under the magnification of a gemological microscope (up to 100×). It is uncertain how these curved rutile inclusions, sometimes described as “fibers” or “hairs,” contribute to the phenomenal pattern observed.

The mechanism responsible for the observed multi-star network is unknown; it could be caused by structural features or inclusions. However, quartzes with similar rutile inclusion patterns from Brazil (as shown in figure 17) and elsewhere generally do not show three-rayed asterism or the type of three-rayed asterism network described here. It is possible to create a single three-dimensional network by a combination of the variants seen in figure 16, A–D. But this would be highly speculative, since we cannot (based on the samples available) prove that all variants seen so far contribute to one single pattern.

*Karl Schmetzer  
Petershausen, Germany  
Martin P. Steinbach  
Idar-Oberstein, Germany*

**A zircon with strong photochromic effect.** Recently, a 6.54 ct oval faceted gemstone with greenish blue color (figure 18, left) was sent to Taiwan Union Lab of Gem Research (TULAB) for identification. The specific gravity of this stone was 4.68, and the refractive index was over the limit of the refractometer. Microscopic observation showed strong birefringence. In addition to standard gemological testing, Raman spectroscopy and comparison with the zircon reference spectrum R050203 from the RRUFF database (figure 19) confirmed it was a zircon. It was particularly worth noting that this zircon showed a significant color change from greenish blue to very dark yellowish green (figure 18) when exposed to a long-wave ultraviolet lamp.

To determine the extent of the color change and whether it was permanent or reversible, the zircon was first exposed to long-wave UV light for one minute and then under 10W white LED light for another minute (the light sources were placed approximately 3 cm away from the gemstone). After repeating this process several times with each exposure one minute longer than the previous time, we confirmed that the color changed from medium light greenish blue with strong saturation to a medium dark greenish yellow with lower saturation after two minutes of long-wave UV light exposure. However, the greenish yellow color gradually returned to the stable greenish blue color after photobleaching with LED white light for 30 minutes. Therefore, the stone was a photochromic zircon with reversible color change (as reported in N.D. Renfro, “Reversible color modification of blue zircon by long-wave ultraviolet radiation,” Fall 2016 *G&G*, pp. 246–251). After the color change reached its full extent under long-wave UV light, the zircon was analyzed by visible spec-

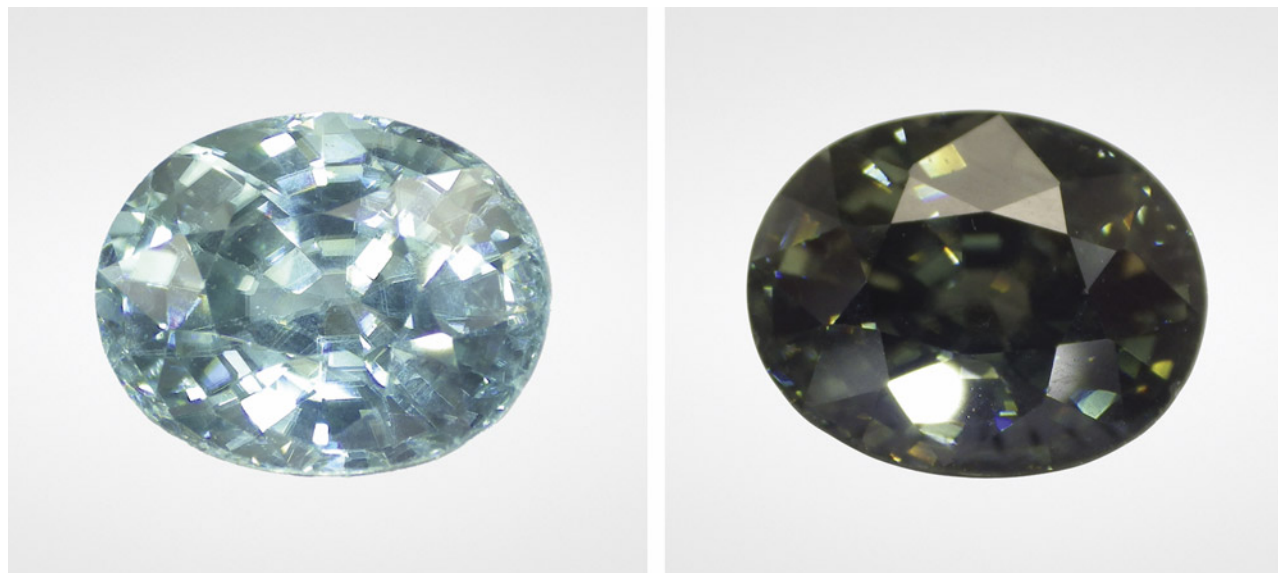


Figure 18. This 6.54 ct zircon showed a significant color change from medium light greenish blue (left) to very dark yellowish green (right) after exposure to long-wave UV for two minutes, and the color was reversible during the photobleaching process with LED white light. Photos by Kai-Yun Huang.

troscopy to record its continuous spectral change during the photobleaching process every six minutes (figure 20). The resulting spectra revealed that the light transmittance in the

range between 450 nm and 550 nm gradually increased during the photobleaching process, and the greenish blue color finally returned to a stable state after 30 minutes.

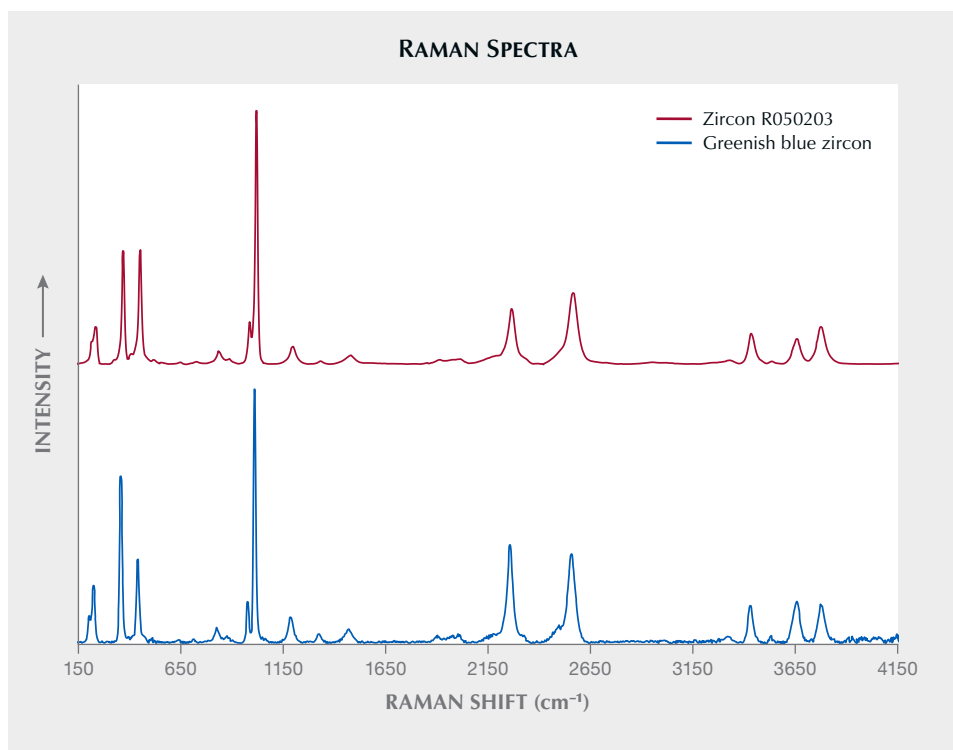


Figure 19. The stacked Raman spectra of the greenish blue zircon and a zircon reference spectrum from the RRUFF database; spectra are normalized and baseline-corrected.



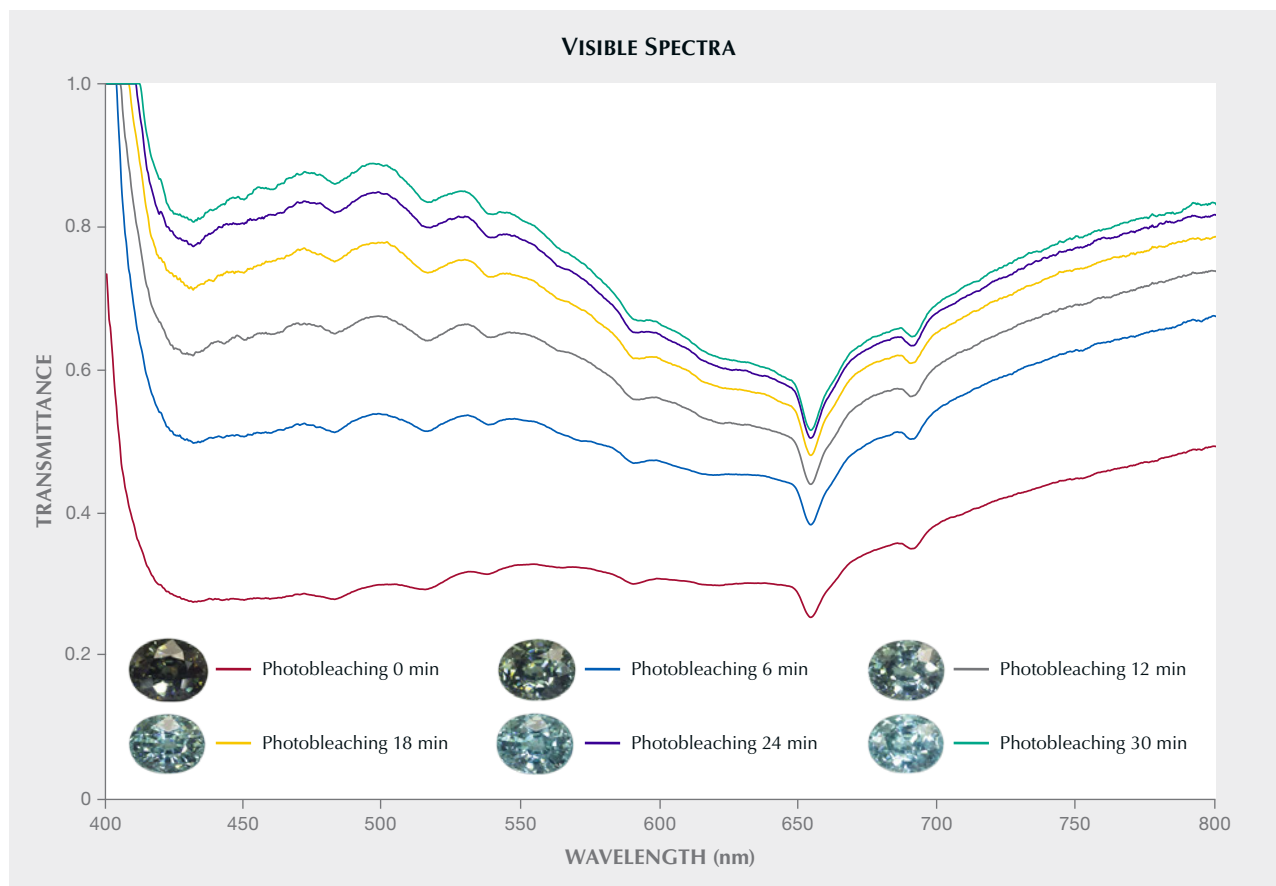


Figure 20. Visible spectra of the zircon (after UV light exposure) during the photobleaching process were recorded every six minutes. The gradually decreasing spectral change implied that the color tended to stabilize.

Although this type of photochromic zircon has previously been reported, a zircon over 6 ct with such a significant photochromic effect is still rare and worth noting, especially since it exhibited a distinct difference in hue, tone, and saturation.

*Shu-Hong Lin*  
*Institute of Earth Sciences,*  
*National Taiwan Ocean University*  
*Taiwan Union Lab of Gem Research, Taipei*  
*Yu-Shan Chou and Kai-Yun Huang*  
*Taiwan Union Lab of Gem Research, Taipei*

## RESPONSIBLE PRACTICES

**Myne London: Sourcing emeralds with a mission.** In 2018, sisters Fiona Wellington and Kate Murray Gordos founded Myne London ([www.mynelondon.co.uk](http://www.mynelondon.co.uk)), a London-based ethical emerald supplier with a goal of supporting women in the gem trade. Their emeralds are sourced from lesser-known mines in Swat Valley, Pakistan, where they aim to create a sustainable and responsible emerald industry and a lasting positive economic impact in the

community. Inspired by their childhood memories of Pakistan, Wellington and Gordos are dedicated to making Swat Valley’s emeralds globally recognized for their traceability and intense vivid green color (figure 21), all while empowering women.

Myne London partners with local groups in the Swat Valley region, including miners and mine owners. In addition to sourcing the emeralds directly from the miners, Myne London is committed to keeping the lapidary work in Islamabad and providing opportunities for women. Partnering with a local company, they train and hire Pakistani women to cut and polish the emeralds (figure 22), a profession traditionally dominated in the region by men. Myne London, which employs a 75% female workforce, collaborates with jewelry designers worldwide—mainly women—to create exquisite pieces featuring the high-quality emerald melee, in addition to designing its own fine jewelry collections.

But Wellington and Gordos aspire to do even more for their female lapidaries. In 2021, they started the Myne London Foundation, a charitable organization designed to give their employees better access to education, which is limited for girls in the country. Illiteracy rates are higher than



Figure 21. Emerald rough from Swat Valley, Pakistan.  
Photo courtesy of Myne London.

50% for adult women in Pakistan. The money raised by the foundation assists the daughters of female employees with tuition costs, school uniforms, and transportation. Without money to pay for these costs, children in the northern regions of Pakistan often do not attend school. The foundation receives 10% of Myne London's profits.

In March 2022, Myne London hosted an inaugural charity ball for the foundation, raising nearly \$20,000, which has already been put to good use in Pakistan. "We immediately actioned to pay for the daughter of one of our lapidary workers to attend school from now on in Islamabad. She is six years old. We plan to provide this for her for as long as she wishes to stay in education," said Wellington. "We also are committed to find ways to support girls in sport, because that is a great leveler and improves confidence as well as health."

Outside of Pakistan, Myne London continues its ethos of women's economic empowerment by collaborating with women around the world in jewelry design. Last year, the company partnered with Los Angeles-based jewelry designer Octavia Zamagias of Octavia Elizabeth, who shares the same social goals. Using 18K gold, Zamagias created several stunning pieces featuring Swat Valley emeralds (figure 23). Looking ahead, Myne London is planning jewelry collaborations with three other talented women—two based in London and the other in Florence.

The firm recently partnered with Opsydia, a gemstone security specialist, to permanently place its brand logo beneath the surface of the Swat Valley emerald melee. Encouraged by Opsydia's success placing identifiers in melee diamonds, Myne London aims to promote traceability using this innovative technology.

With all their success in Swat Valley, Myne London hopes to expand to other areas of the world someday, using the same model for ethics, traceability, and women's em-



Figure 22. Eighty percent of the Pakistani lapidaries working in the Myne London workshop are women.  
Photo courtesy of Myne London.

powerment. But for now, they remain focused on the women and emeralds of Swat Valley.

Erica Zaidman  
GIA, Carlsbad

Figure 23. Ring designed by Octavia Elizabeth in 18K gold featuring 1.24 carats of Swat Valley emerald.  
Photo courtesy of Octavia Elizabeth/Myne London.





Figure 24. This 11.30 ct sample (18.9 × 14.0 × 8.8 mm) was found to be a triplet composed of colorless glass and quartz held together by green cement. Photo by Biqian Xing.

## SYNTHETICS AND SIMULANTS

**Unusual glass-and-quartz triplet imitation of emerald.** Recently, an 11.30 ct emerald-cut sample sold as an emerald (figure 24) was provided by an anonymous jewelry manufacturer, who suspected an imitation. It resembled a natural emerald with its vivid bluish green color, inclusion abundance, and a vitreous luster. However, examination identified it as a glass-and-quartz triplet, an occasionally convincing imitation of emerald.

When examined via water immersion in a direction parallel to the girdle plane, one can observe that this triplet was made of two pieces of colorless material (crown and pavilion), with a green cement slice in between (figure 25). Using water for the immersion test to observe the internal characteristics did not corrode the sample and yielded better experimental results. No inclusions were observed in the crown. Microscopic examination revealed two-phase (liquid and gas) inclusions, cracks (figure 26A), and lace-like partially healed fissures in the pavilion (figure 26B). In the middle cement layer, no gas bubbles were observed along the separation plane in the assemblage, unlike doublets previously described (H.A. Hänni and U. Henn, “Modern doublets, manufactured in Germany and India,” *Journal of Gemmology*, Vol. 34, No. 6, 2015, pp. 479–482; Spring 2019 Lab Notes, p. 92). However, the very thin layer of solidified cement (approximately 10 μm thick; figure 26C) showed a maze-like pattern under the microscope (figure 26D).

This triplet had refractive indexes of 1.515 (crown) and 1.544–1.553 (pavilion) and a hydrostatic specific gravity of 2.59. Its fluorescence under long-wave UV radiation was green for the crown and blue-white for the pavilion (affected by the fluorescence of the cement) and inert for both the crown and pavilion under short-wave UV radiation. No obvious absorption was observed with a handheld portable spectroscope, and no reaction was observed with the Chelsea filter.

The EDXRF and FTIR results identified the crown as soda-lime-silica glass (69.97 wt.% SiO<sub>2</sub>, 15.25 wt.% Na<sub>2</sub>O, and 8.94 wt.% CaO) with characteristic peaks at 1061 (asymmetric vibration modes of the Si-O-Si network), 770 (symmetric vibration modes of the Si-O-Si network), 968 (stretching vibration of the Si-O non-bridging oxygen group),

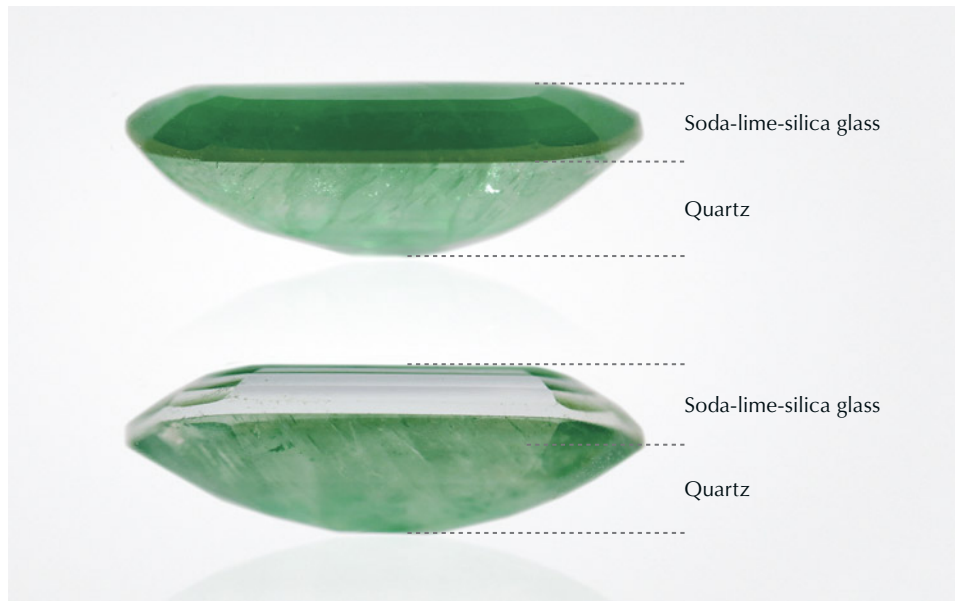


Figure 25. Illuminated with diffused transmitted light with water immersion, the assembled nature of this 11.30 ct triplet was obvious in profile view (top image shows a slight downward view, and bottom image shows a slight upward view). The pavilion is nearly colorless (both top and bottom images) due to the refraction and scattering of the green cement by a large number of inclusions, while the crown is colorless and clean under a certain observation angle (bottom image). Photo by Biqian Xing.

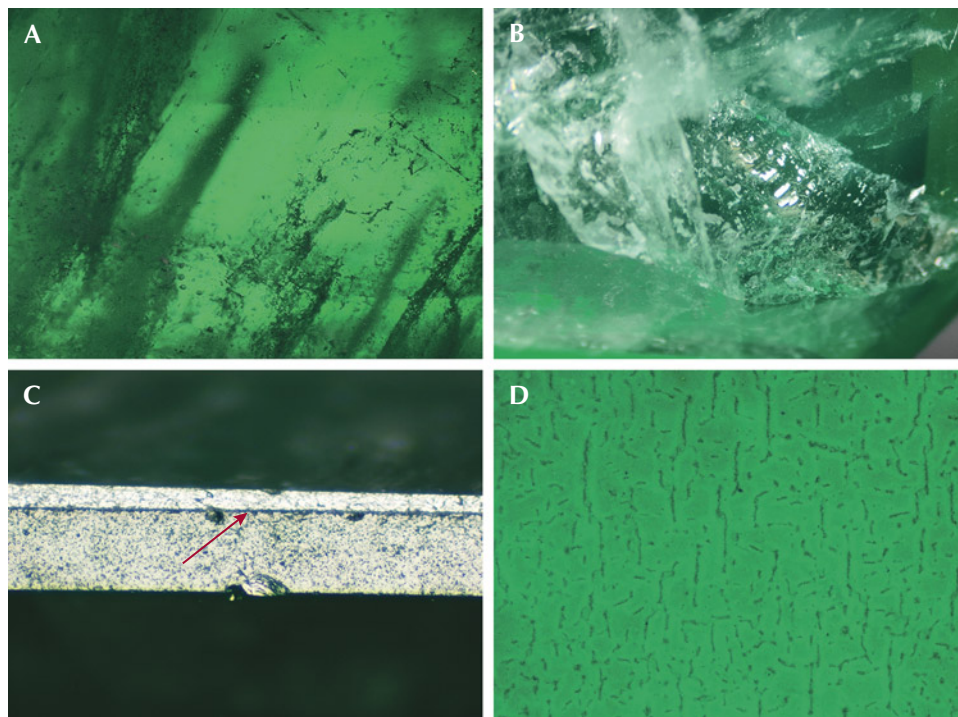


Figure 26. Microscopic observation of the triplet revealed numerous cracks (A), fluid inclusions, and lace-like partially healed fissures (B) in the pavilion. C: The cement slice could be seen under reflected light (as shown by the arrow). D: A maze-like pattern in the cement slice. Photomicrographs by Biqian Xing; fields of view 2.51 mm (A), 10.37 mm (B), 2.71 mm (C), and 1.15 mm (D).

and  $465\text{ cm}^{-1}$  (Si-O-Si and O-Si-O bending modes) (figure 27) (A. Agarwal and M. Tomozawa, "Determination of fictive

temperature of soda-lime silicate glass," *Journal of the American Ceramic Society*, Vol. 78, No. 3, 1995, pp. 827–829; S.I.

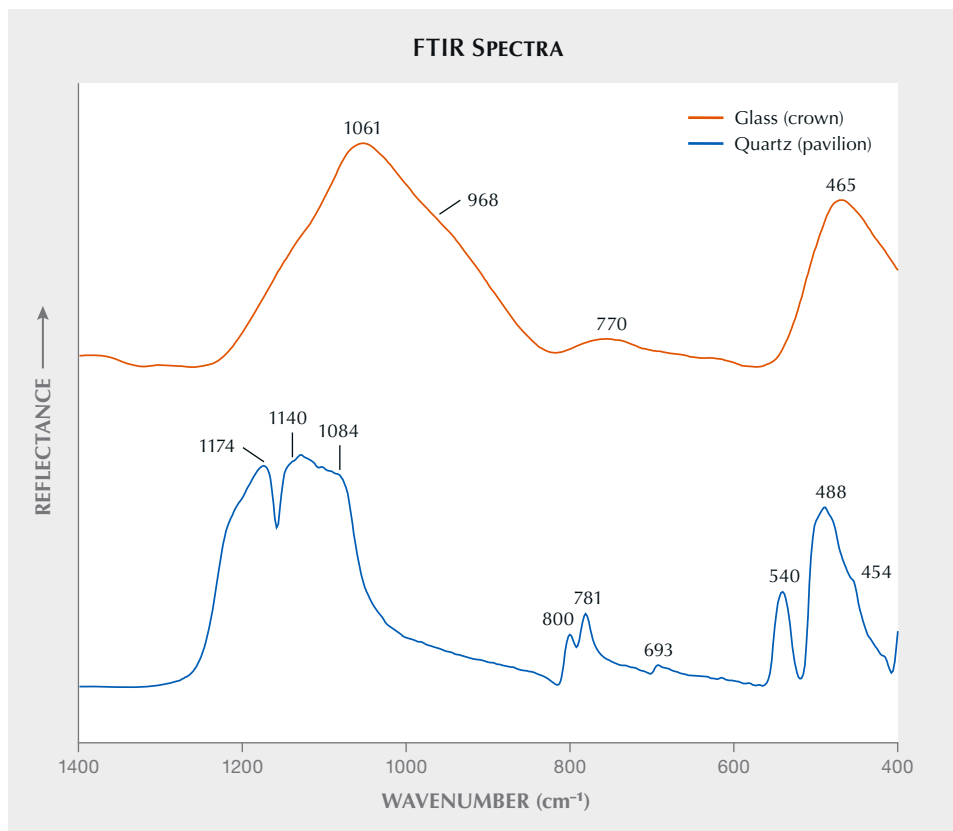


Figure 27. FTIR spectroscopy identified the crown of the triplet as glass (peaks at  $1061$ ,  $968$ ,  $770$ , and  $465\text{ cm}^{-1}$ ) and the pavilion as quartz (peaks at  $1174$ ,  $1140$ ,  $1084$ ,  $800$ ,  $781$ ,  $693$ ,  $540$ ,  $488$ , and  $454\text{ cm}^{-1}$ ). Spectra are stacked for clarity.

Amma et al., "Specular reflectance (SR) and attenuated total reflectance (ATR) infrared (IR) spectroscopy of transparent flat glass surfaces: A case study for soda lime float glass," *Journal of Non-Crystalline Solids*, Vol. 428, 2015, pp. 189–196). The pavilion was identified as quartz, with 99.54 wt. % SiO<sub>2</sub> and characteristic FTIR peaks at 1174, 1140, 1084 (antisymmetric stretching vibrations of the SiO<sub>4</sub> tetrahedron), 800 (SiO<sub>4</sub> symmetric stretching), 781 (SiO<sub>4</sub> symmetric stretching), 693 (Si-O-Si bending transition modes), 540, 488, and 454 cm<sup>-1</sup> (figure 27) (A. Hahn et al., "Using Fourier transform infrared spectroscopy to determine mineral phases in sediments," *Sedimentary Geology*, Vol. 375, 2018, pp. 27–35). Unfortunately, the green cement was too thin to analyze with a micro-infrared spectrometer or Raman spectrometer.

The triplet was a typical imitation of emerald but surprisingly convincing when viewed table-up with the unaided eye. With its extremely thin cement slice, maze-like pattern, and lack of bubbles, even a jewelry manufacturer might mistake it for emerald. This investigation reminds us that the examination of potentially composite stones cannot be ignored.

*Biqian Xing, Guanghai Shi, and Wenqing Liu  
China University of Geosciences, Beijing*

## TREATMENTS

**Ruby: An expensive mistake.** Gemologists at Bangkok's Lotus Gemology recently received a 6 ct ruby for identification. Declared to be an untreated ruby from Mozambique, the stone featured a superb vivid red color of a type that is often termed "pigeon's blood" in the trade. As it was also of good clarity and well cut, it was obvious we were dealing with a gem of potentially high value.

The UV-Vis-NIR spectrum was typical for ruby/synthetic ruby. The infrared spectrum revealed peaks at 3309 and 3232 cm<sup>-1</sup>. The 3232 cm<sup>-1</sup> peak generally indicates that

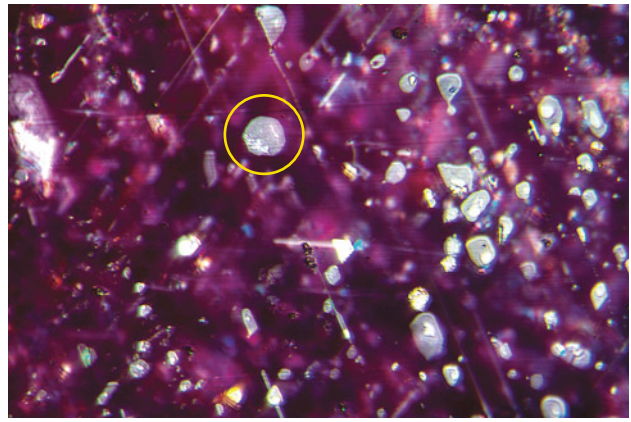


Figure 28. Silk in corundum often unmixes into two different solid phases, one highly reflective (rutile) and the other of lower relief (ilmenite or hematite-ilmenite). When the Mozambique ruby was heated, the lower-relief crystals began to break down, developing irregular white patches, as shown in the yellow circle. Photomicrograph by Richard W. Hughes; field of view 1 mm.

a stone has been subjected to artificial heat treatment. We proceeded to examine the gem in the microscope, where we found two additional pieces of evidence of heat treatment.

The first feature was rutile silk of a type that is typical of rubies from East Africa. In these stones, the silk consists of high-relief needles of rutile with attached unidentified "daughter" crystals of another substance of lower relief. In the case of heat-treated stones, the daughter crystals will sometimes show a partial breakdown ("GIA Lab reports on low-temperature heat treatment of Mozambique ruby," *GIA Research News*, April 28, 2015). Small amounts of breakdown in the form of irregular white patches were found in this stone (figure 28).

But the most obvious evidence of heat treatment was the presence of spall marks (figure 29), which are solidified

Figure 29. Spall marks on the surface of the Mozambique ruby prove it was heat treated after cutting and polishing. Note that some of the spall marks have dark halos around them. Photomicrographs by Richard W. Hughes; fields of view 2.0 and 2.5 mm.

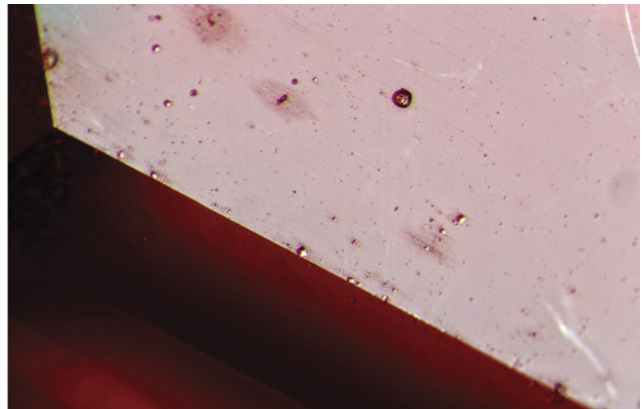




Figure 30. Left: Before a fade test, this approximately 10 ct sapphire displayed a strong orange hue. Right: After the fade test, the orange color became less pronounced and the stone appeared yellow. Photos by Ronnakorn Manorotkul.

droplets of material on the surface that melted or were dissolved during heating. These spall marks across the stone showed that the ruby had been heated after cutting and not repolished following the treatment. We can only guess about the reasons for heating such a valuable gem, but there is no doubt that this particular roll of the dice was a losing gamble because the potential improvement in appearance is slight compared to the large price difference between untreated and heated ruby. We concluded that this was a heat-treated Mozambique ruby.

Richard W. Hughes  
Lotus Gemology, Bangkok

**Yellow sapphires with unstable color.** In recent years, one concern our laboratory has heard from clients and from other gemologists is the issue of color stability in corun-

dum. Some sapphires, particularly those with a strong yellow component (including *padparadscha* sapphire), contain unstable color centers that may fade when the stone is exposed to light and/or heat (K. Nassau and G.K. Valente, "The seven types of yellow sapphire and their stability to light," Winter 1987 *G&G*, pp. 222–231). We regularly test for this in the laboratory by conducting a fade test. Most of the sapphires we encounter that have an unstable color are unheated stones.

Recently an orange sapphire of approximately 10 ct was submitted for testing (figure 30). Microscopic examination revealed signs of heat treatment, with partially dissolved silk, several glassy discoids (figure 31), and melted crystals (figure 32). A fade test was conducted by placing the stone approximately 5 cm under a 120-watt incandescent spotlight for at least an hour, and a dramatic difference was ob-

Figure 31. A cluster of glassy discoids suggests that this sapphire has been heat treated. Photomicrograph by E. Billie Hughes; field of view 4.0 mm.

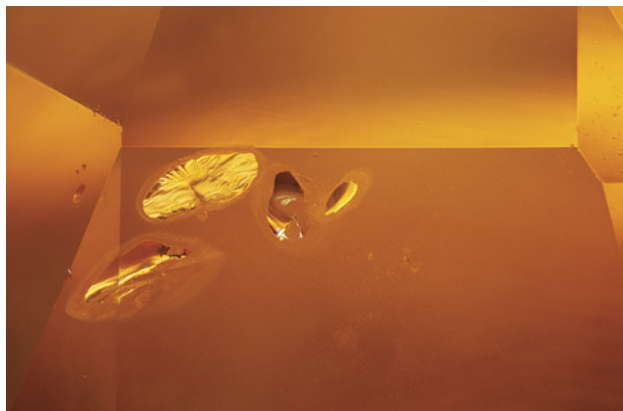


Figure 32. This small crystal with a melted appearance provides evidence that the specimen has undergone heat treatment. Photomicrograph by E. Billie Hughes; field of view 3.5 mm.

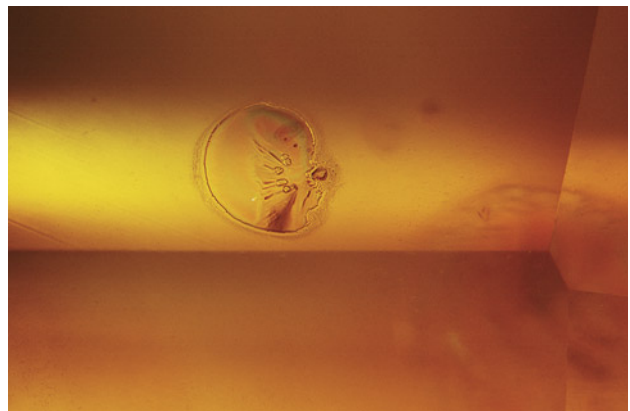




Figure 33. Before a fade test, the unheated sapphire of approximately 18 ct displayed a highly saturated yellow hue (left). After a fade test involving light and mild heat, the color faded to a pale yellow (right). Once the stone was exposed to sunlight for 30 minutes, the more intense yellow color displayed before the fade test came back. The sapphire was then subjected to a light-only fade test, and the more saturated yellow color remained stable. Photos by Ronnakorn Manorotkul.

served. The color had changed from orange to a vivid yellow (again, see figure 30).

Under normal conditions, high-temperature heat treatment (at least 1200–1300°C) will bleach any color centers that might be present. This suggests that the orange color was activated after the heat treatment. It is possible that this occurred either by subjecting the stone to artificial irradiation or by placing it in sunlight (Nassau and Valente, 1987). However, we are unable to state definitively what process was used to activate the orange color.

Several weeks later, we tested another yellow sapphire of approximately 18 ct (figure 33). In this instance, the stone's features were consistent with those of unheated sapphire. Again, a fade test was performed with the 120-watt spotlight, which mildly warmed the stone to approximately 100°C. Its color also faded after the fade test, and the owner was informed. The owner explained that they had previously put the sapphire in direct sunlight, which would have brought the color back to what was likely its stable state, a process described by Nassau.

To test this, we placed the stone in direct sunlight for 30 minutes, and the more intense yellow color did return. Unfortunately, placing the gem in direct sunlight behind a window in our office did not have the same effect.

Upon seeing the color return after being placed in direct sunlight, we decided to try another fade test, this time using a light source that would not warm up the stone. An XD-300 xenon light source was used, and the stone was placed within 5 cm of a fiber-optic light guide connected to this source. After exposure to this cooler light source for over an hour, the color did not fade. This suggests that the mild heat of the 120-watt spotlight, not just the light, faded the stone's color

and that the more intense yellow color displayed after exposure to sunlight could indeed be considered the stable color.

We have since adjusted our fade tests to be light-only by switching to this cooler light source to avoid the heat generated with the 120-watt spotlight.

Our experience with these sapphires has been a fascinating case study in the color stability of yellow sapphire. This example reinforces the importance of considering all possibilities when testing stones in the laboratory. We do not fully understand the exact causes of these changes, and much remains to be learned.

*E. Billie Hughes  
Lotus Gemology, Bangkok*

## AUCTION REPORTS

**Spring 2022 auction highlights.** The De Beers Cullinan Blue was the early buzz of the spring 2022 auction season, with the 15.10 ct Fancy Vivid blue step-cut diamond far surpassing Sotheby's presale estimate of \$48 million. Bringing \$57.5 million, the diamond was the largest of its color to ever appear at auction and also the third most valuable diamond of any color to sell at auction. (To read more about GIA's examination of the De Beers Cullinan Blue, see Lab Notes in this issue, pp. 216–217.)

The season continued in Geneva, with Christie's auctioning two diamonds weighing more than 200 ct each at the Magnificent Jewels sale on May 11, beginning with the largest white diamond ever sold at auction. Named the Rock (figure 34), the GIA-graded 228.31 ct, G-color, VS<sub>1</sub> pear-shaped diamond sold for \$21.9 million, or \$96,000 per



*Figure 34. At 228.31 ct, the Rock is the largest white diamond ever sold at auction. Photo courtesy of Christie's.*

carat. The previous record holder for the largest white diamond sold at auction weighed 163.41 ct and was sold by Christie's in 2017.

The second diamond, the Red Cross (figure 35), returned to Christie's for a third time at auction. It was first sold at Christie's in 1918 to benefit the British Red Cross

during World War I. At 205.07 ct, the GIA-graded Fancy Intense yellow cushion cut fetched \$14.3 million, or \$70,000 per carat, after 11 minutes of competitive bidding, setting an auction record price for a Fancy Intense yellow diamond. A portion of the proceeds benefited the International Committee of the Red Cross.





*Figure 35. The 205.07 ct Red Cross diamond set an auction record price for a Fancy Intense yellow diamond at Christie's Geneva Magnificent Jewels sale. Photo courtesy of Christie's.*

A jadeite necklace (figure 36; opposite page) was the top lot at Christie's May 25 Hong Kong sale, selling for \$8.8 million after 11 minutes of bidding. The stunning piece features 33 perfectly round, exceptionally large jadeite beads ranging from 12.3 to 15.0 mm in diameter, with an 11 ct Burmese ruby clasp surrounded by oval brilliant diamonds.

In June, the focus returned to diamonds at Christie's final Magnificent Jewels auction of the season in New

York. The 103.49 ct Light of Africa (figure 37), the fifth most valuable colorless diamond ever offered at Christie's, surpassed its presale estimate of \$18 million, with the winning bid coming in at just over \$20 million—an incredible \$195,000 per carat. The GIA-graded emerald-cut type IIa diamond was cut and polished from a 299 ct rough stone unearthed from the Cullinan mine.

*Erica Zaidman*



*Figure 37. The 103.49 ct Light of Africa diamond sold for an impressive \$195,000 per carat at Christie's Magnificent Jewels sale in New York. Photo courtesy of Christie's.*



*Figure 36. This necklace featuring 33 jadeite beads was the top lot at Christie's Magnificent Jewels sale in Hong Kong. Photo courtesy of Christie's.*



Figure 38. These 12 tourmalines from *The Big Find* will be featured in one-of-a-kind jewelry pieces. Photos courtesy of the Maine Mineral & Gem Museum.

**MUSEUM EXHIBITIONS**

**The Big Find: Celebrating 50 years of Maine tourmaline.** October 2022 will mark 50 years since North America's largest and most significant unearthing of gem-quality

tourmaline. The astounding 1972 discovery, known as "The Big Find," unveiled vast pockets of tourmaline of every color at an abandoned mine near the top of Plumbago Mountain in Newry, Maine. Yielding more than a ton of tourmaline rough from 1972 to 1974, The Big Find



*Figure 39. Tourmaline bears on a frosted quartz base, carved by Gerhard Becker using tourmaline from The Big Find in Newry, Maine. Gifted to GIA by John Staver and currently on loan to the Maine Mineral & Gem Museum. (See more tourmaline carvings from GIA's collection at [www.gia.edu/gia-museum-tourmaline-carvings](http://www.gia.edu/gia-museum-tourmaline-carvings).) Photo by Orasa Weldon.*

reawakened gem mining in the state of Maine. To celebrate the 50th anniversary of this historic discovery, the newly opened Maine Mineral & Gem Museum has big plans underway.

*The Big Find: A Legend Continues* began last year when the museum sought jewelry designers from across the country to create jewelry using 12 stones from the 1972 find, ranging in weight from 9.78 to 49.30 ct (figure 38). Twelve designers selected by jury are now at work crafting one-of-a-kind pieces to be presented on October 8, 2022, at a runway extravaganza in Newry. Event and

ticket information can be found at <https://mainemineral-museum.org/the-big-find/>.

The museum is also commemorating the anniversary with special tourmaline exhibits and guest lectures all year, including various Maine tourmaline carvings on loan from the GIA Museum (figure 39). After the event, all 12 pieces of tourmaline jewelry will be on display at the Maine Mineral & Gem Museum and then at the 2023 Tucson Gem & Mineral Show before being auctioned off to raise money for the museum.

*Erica Zaidman*



Figure 40. Inside the vault room of the *Brilliance: The Art and Science of Rare Jewels* exhibit. Photo courtesy of the Natural History Museum of Los Angeles County.

**Brilliance Exhibit at the Natural History Museum of Los Angeles County.** A special exhibit of rare gems and minerals, entitled *Brilliance: The Art and Science of Rare Jewels*, was recently displayed at the Natural History Museum of Los Angeles County. The exhibit was available for viewing

from December 8, 2021, through February 21, 2022, in the Gem Vault in the museum's Gem and Mineral Hall (figure 40). Over one hundred spectacular objects—necklaces, bracelets, rings, earrings, and unmounted gems (many the creations of master jewelry designer Robert Procop)—were



Figure 41. Left: The 46.39 ct Fancy blue Celeste diamond and a 100.92 ct colorless diamond were but two of the exquisite gems on display at the Natural History Museum of Los Angeles County. Right: This 108.03 ct blue sapphire from Sri Lanka is exceptional in terms of its clarity, color, and size. Photos courtesy of the Natural History Museum of Los Angeles County; courtesy of Robert Procop.



Figure 42. The 79.39 ct Royal Pink sapphire is, according to the designer, the largest vivid natural pink sapphire in the world. Courtesy of Robert Procop.

on display along with mineral specimens from the museum's collection. Colorless and fancy-color diamonds, rubies, sapphires, emeralds, as well as color-change and asteriated gems and other spectacular specimens, were represented (figures 41 and 42). By allowing the public to view

and appreciate these unique treasures, this museum event provided an understanding of how gems and minerals are used today in a variety of fields, from jewelry design to scientific research. Crystals of gem minerals represent products of some optimum conditions for natural mineral formation, and the study of rough and faceted gems is increasingly used by scientists today to better understand Earth's history.

*James E. Shigley and Brooke Goedert  
GIA, Carlsbad*

**Smithsonian's Great American Diamonds exhibit.** Two extraordinary American diamonds (figure 43) have found a home at the Smithsonian's National Museum of Natural History, where they were unveiled as part of the new *Great American Diamonds* exhibit in June. The 16.87 ct Freedom diamond, the largest faceted diamond of U.S. origin, was fashioned from a 28 ct crystal unearthed at Colorado's Kelsey Lake mine in 1997. The cushion-cut diamond is now set in a ring donated by Robert E. and Kathy G. Mau. The second diamond on exhibit, the emerald-cut Uncle Sam, was faceted from the largest uncut American diamond crystal ever discovered at 40.23 ct. Uncovered at Arkansas' Crater of Diamonds in 1924, the flawless 12.42 ct pinkish brown stone was recently recovered from a private collection (after being missing for decades) and donated by Peter Buck. This is the first time the Uncle Sam has been exhibited in more than 50 years.

While diamonds from the United States are exceptionally rare, the two mines in Colorado and Arkansas produced tens of thousands of carats of rough diamonds, from 1919 to 1926 at the Crater of Diamonds and 1996 to 2001 at Kelsey Lake. "Most people are surprised to learn that diamonds have been mined in the United States, and as the



Figure 43. Left: The 16.87 ct Freedom, from Kelsey Lake in Colorado, is the largest faceted diamond from the U.S. Right: The 12.42 ct Uncle Sam is the largest faceted diamond from Arkansas, cut from a 40.23 ct crystal uncovered at the Crater of Diamonds. Photo by James Tiller and Brittany M. Hance; courtesy of Department of Mineral Sciences, Smithsonian Institution.

# GIA Alumni Collective™



Figure 44. The new GIA Alumni Collective offers a robust educational and networking platform for GIA graduates worldwide.

national museum, we are delighted to introduce these great American diamonds to our visitors,” said Dr. Jeffrey Post, the museum’s curator-in-charge of gems and minerals.

Joining these two impressive donations in the *Great American Diamonds* exhibit are two uncut diamonds from the museum’s existing collection. The Canary, a golden yellow crystal weighing 17.85 ct, is one of the largest uncut diamonds from Arkansas. The 6.45 ct Colorado, which displays the typical octahedral shape of a natural diamond crystal, was recovered from the kimberlite host rock during mining operations at Kelsey Lake. As part of the Smithsonian’s National Gem and Mineral Collection, these four stones are among more than 10,000 precious stones and pieces of jewelry, including the iconic Hope diamond.

*Erica Zaidman*

## ANNOUNCEMENTS

**GIA Alumni Collective.** GIA’s alumni association has a new name, a fresh look, and up-to-date features. With a mission to connect GIA graduates around the world, provide opportunities for continuing education, and foster networking throughout the gem and jewelry industry, the GIA Alumni Collective (figure 44) builds on the association’s long history with updates that better reflect the creativity, technical savvy, entrepreneurship, and vitality of GIA’s alumni.

After successfully completing a GIA program or course, alumni can register for the Collective and stay informed about all the resources available to them by visiting the new GIA Alumni Collective website. The new online community, [collective.gia.edu](https://collective.gia.edu), serves as a “central hub” where members can add their profile to the directory, engage and connect directly with other members and global chapters, join “virtual” chapters, register to attend professional events, access more than 20 Continuing Education seminars at a 10% discount, and more.

“The new GIA Alumni Collective website and online community is a reflection of our diverse alumni network. The collaboration with chapter leaders and other members brings new energy and a modern look that connects our global network and provides a space to experience the future of gems and jewelry,” says Cathryn Ramirez, executive director of alumni development and continuing education at GIA.

GIA has more than 155,000 active alumni in 58 chapters spanning the globe—33 in the Americas, 16 in Asia, and three apiece in Europe, the Middle East, and Africa. While chapters host their own meetings and events, chapters often co-host to provide additional networking opportunities. The GIA Alumni Collective hosts annual events at the AGTA Tucson and JCK Las Vegas trade shows where hundreds of alumni from all over the world meet up with longtime friends and colleagues and foster new relationships.